

MAHATMA GANDHI UNIVERSITY

**Radio and optical studies of a
selected sample of giant radio
galaxies and a merging galaxy
cluster Abell 407**

BIJU KG

*A thesis submitted in partial fulfilment of the
requirements for the award of the degree of
Doctor of Philosophy in Physics
under the Faculty of Science*



Department of Physics
NEWMAN College
Thodupuzha, Kerala, India.
November 2016

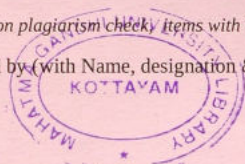
MAHATMA GANDHI UNIVERSITY

CERTIFICATE ON PLAGIARISM CHECK

1. Name of the Research Scholar	BIJU K G
2. Title of the Thesis/Dissertation	<i>Radio and Optical Studies of a Selected Sample of Giant Radiogalaxies and a Merging Galaxy Cluster Abell 407</i>
3. Name of the Supervisor	Dr. Joe Jacob
4. Department/Institution/ Research Centre	<i>Department of Physics, Newman College, Thodupuzha.</i>
5. Similar Content (%) identified	1% (One)
6. Acceptable Maximum Limit	25%
7. Software Used	Urkund
8. Date of Verification	23-11-2016

*Report on plagiarism check items with % of similarity is attached

Checked by (with Name, designation & signature):



Murli K. P. M.
 Assistant Librarian
 M.G. University Library
 Kottayam

Name & Signature of the Researcher:

BIJU K.G.

BIJU K.G.

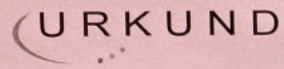
Name & Signature of the Supervisor:

JOE JACOB

Name & Signature of the HoD/HoI (Chairperson of the Doctoral Committee):

Vincent Joseph
 Rev. Dr. VINCENT JOSEPH
 PRINCIPAL
 NEWMAN COLLEGE
 THODUPUZHA





Urkund Analysis Result

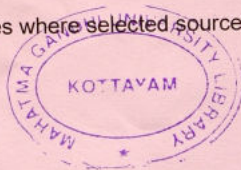
Analysed Document: BIJU KG -Radio and Optical Studies of a Selected Sample of Giant Radiogalaxies and a Merging Galaxy Cluster Abell 407.pdf (D23670073)
Submitted: 2016-11-23 10:49:00
Submitted By: library@mgu.ac.in
Significance: 1 %

Sources included in the report:

http://cxc.harvard.edu/cda/bibstats/biblists/ref_papers.html
<http://www.iucaa.in/~library/pp2014.html>

Instances where selected sources appear:

4



Murali K. K.
 Murali K. K.
 Assistant Librarian
 M.G. University Library
 Kottayam

BIJU K.G.

Dr. Joe Jacob
 DR. JOE JACOB
 Supervising Guide



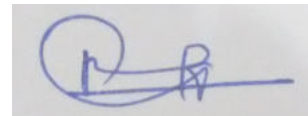
Vincent
 REV. DR. VINCENT JOSEPH
 PRINCIPAL
 NEWMAN COLLEGE
 THOUPUZHA

Declaration

I, BIJU KG, hereby declare that the thesis entitled, “Radio and optical studies of a selected sample of giant radio galaxies and a merging galaxy cluster Abell 407.”, submitted for the award of Doctor of Philosophy is the record of work carried out by me under the supervision and guidance of Dr Joe Jacob, Assistant Professor, Newman College, Thodupuzha, Kerala.

This has not formed the basis for the award of any degree, diploma, associateship, fellowship, titles in this or any other university or other institution of higher learning.

I further declare that the materials obtained from other sources have been clearly acknowledged in this thesis.



Date: 30/11/2016

Place: Thodupuzha

BIJU KG

Newman College

Newman College

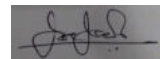


Dr. Joe Jacob
Assistant Professor & Research Guide
Department of Physics
Thodupuzha, 686635
Telephone : 09846015011

Certificate

This is to certify that the thesis entitled “Radio and optical studies of a selected sample of giant radio galaxies and a merging galaxy cluster Abell 407” is a bona fide record of the research work done by Biju KG, under my supervision and guidance, at the Department of Physics, Newman College, Thodupuzha. The work presented in this thesis has not been published or submitted to any other University/Society for any other Degree/Diploma/Associateship or any other titles.

Also certified that the materials obtained from other sources have been explicitly cited in the thesis.



Date: 30/11/2016
Place: Thodupuzha

Dr Joe Jacob
Newman College

“Nothing in life is to be feared, it is only to be understood. Now is the time to understand more, so that we may fear less.”

— Marie Curie

*Dedicated to my
Family*

Acknowledgements

I am happy to thank all the people who supported me during my Ph D life. I am immensely grateful to my research supervisor Dr Joe Jacob for his invaluable guidance, loving encouragement and continuous support throughout my research career.

I express my deep sense of gratitude to Dr Joydeep Bagchi, Professor of Astrophysics, Scientist F, IUCAA, Pune for his inspirational academic support to complete this work. Many of the key ideas in this thesis arose in conversation with Dr Joydeep, and this work would have been impossible without his help.

I remember with gratitude the support of Prof. Iswara Chandra C H, NCRA, Pune through his valuable advices and guidance. I learned the AIPS radio data Analysis mainly through the workshops led by him.

I am very much indebted to Dr Vivek M for the time he spent and the knowledge he shared, right from the beginning of my research.

I would like to express my sincere gratitude to Professor Sri Anand and Dr Vijaya Mohan who taught me the first lessons of Astrophysics during the IGO training school in 2010.

I am happy to acknowledge Reju Sam John, Pratik Dhabade, Nayana, Sunil Kumar, Mahadev, Madhuri and Sheelu for their scholarly inputs and support at various phases of the programme.

I am indebted to the University Grants Commission (UGC) for granting Teacher Fellowship, under Faculty Development Programme.

I express my gratitude to the Inter-University Centre for Astronomy and Astrophysics, Pune for being my second home during the research, providing generous support and unique environment for research. I specially thank the Director, Dean of visitor services Prof. Kandaswamy Subramaniam, Samuel, Santosh Khadilkar for all the help provided during my visits.

I would also place on record my sincere thanks to the staff at GMRT and IGO for their help in observing the objects discussed in this thesis.

I am grateful to the Principal, Management and Staff of Newman College, Thodupuzha for providing facility and support for successful completion of this thesis.

I am indebted to the Management, the Principal, my colleagues and students of W. M. O. Arts and Science College for their support and encouragement to complete my research work.

I would like to acknowledge Sri. K.P. Aliyas for introducing the world of astronomy to me, through the talks he delivered on this subject as a part of the programmes of Kerala Sasthra Sahithya Parishath (KSSP).

I record and acknowledge the invaluable support and encouragement rendered by my collaborators and fellow research scholars. I extend my sincere thanks to Sheelu, Savithri, Nayana, Biny, Atul, Karthik, Samir Dhurde, Mahadev, Pratik, Madhuri, Sisir, Jameer, Ashish, Reju, Charles, Avinash, Rinku, Krishnamohan, Sonia, Nikhil, Archana, Vinu Vikram, Minu Joy, Saji Augustne, Dhanya, Preetha, Jithesh, Azad, Veena, Sachin, Jishnu and Prof. Sajeeth Ninan Philip for joyful gatherings and happiest moments at IUCAA. I wish to acknowledge the support rendered by my family, relatives and friends in the form of encouragement, personal support, prayers and concern along my way.

Biju KG

Preface

The emissions from galaxies are normally contributed by the thermal radiations from its constituent stars and dust. But there are galaxies which can emit energy in a wide range of wavelengths, i.e. from radio to γ -rays, which are non-thermal. Moreover, these emissions are from the central region of the galaxy ($\sim 100pc$) and these regions appear as more luminous than an entire galaxy. Such regions/galaxies are called ‘Active Galactic Nuclei’ (AGN). Radio AGNs ($L_{1.4GHZ} \geq 10^{24}WHz^{-1}$) are a major sub-class of the overall AGN population. Large-scale jets from radio galaxies is directly connected to mass accreting, spinning supermassive black holes (SMBH) found at the centers AGNs.

The linear sizes of radio sources are found to vary from few parsecs to Mpc scales. The radio galaxies having linear sizes of more than 1 Mpc are defined as Giant Radio Galaxies (GRGs) and are the largest single objects in the Universe.

Centres of galaxy clusters dominated by the massive, luminous elliptical galaxies are intense sites of mergers, which are believed to be the main mechanism for the growth of some extremely massive (mass $> 10^{12}M_{\odot}$) and bright ellipticals, which are known as the cD galaxies. Previous studies have shown that cD galaxies are almost always radio loud and quite often they eject powerful radio jets. During merger of galaxies, there is a high chance of gas flow towards the central SMBH, thereby triggering the activity of the central engine. As a result, cluster central cD galaxies are more likely to be radio-loud above radio luminosity $10^{24.5} W Hz^{-1}$ at 1.4 GHz.

The first part of the thesis has taken up the detailed study, emphasising on the radio emissions emanating out, from such multiple merger processes in progress at the center of the Abell cluster A 407. The second part of the thesis focus on the radio and optical properties of a sample of GRGs which are being studied for the first time at low radio frequencies.

After the introduction we discuss the results of our radio and optical studies of a peculiar radio source 4C 35.06, an extended radio-loud AGN found at the center of galaxy cluster Abell 407 ($z = 0.047$). The central region of Abell 407 also hosts a remarkably tight ensemble of nine galaxies within an ~ 1 arcmin (50 kpc) region, surrounded by a very faint, diffuse stellar halo. This remarkable system (named the ‘Zwicky’s Nonet’) provides a unique and compelling evidence for an ongoing formation of a giant cD galaxy at the cluster center. Multi-frequency deep radio observations carried out with Giant Meterwave Radio Telescope (GMRT) at 610, 235 and 150 MHz reveal a system of 400 kpc scale helically twisted and kinked radio jets and outer relic lobes associated with 4C 35.06 in ‘Zwicky’s Nonet’. The outer extremities of jets show extremely steep spectrum (spectral index -1.7 to -2.5) relic/fossil radio plasma with a relatively short spectral age of $\text{few} \times (10^6 - 10^7)$ years. Such ultra-steep spectrum relic radio plasma lobes without definitive hot-spots are very rare, and they provide an interesting opportunity towards understanding the life-cycle of relativistic jets and the physics of black hole mergers.

In the second part of the thesis, we discuss the results obtained from the studies of GRGs in the radio and optical wavelengths. We have selected a sample of six GRGs which are not studied so far at lower radio frequencies.

It is well known that powerful radio jets above 100 kpc scale are nearly always launched from the nuclei of elliptical galaxies, and the typical radio luminosity

of spiral galaxies with AGN is much lower than that of ellipticals. We have discovered a counter example of this paradigm through the analysis of a GRG source, which is having a linear size of ~ 1.6 Mpc hosted by a spiral galaxy *2MASX J23453268 – 0449256* (J2345-0449).

J2345-0449 is a double-double radio source where relativistic jets are ejected from a luminous and massive spiral galaxy on a scale of ~ 1.6 megaparsecs, the largest known so far. Extreme physical properties observed for this spiral galaxy, such as its high mass, large angular momentum (fast disk rotation) and episodic relativistic radio jet activity are discussed. The launch of these powerful jets is likely facilitated by an advection-dominated accretion flow (ADAF) at low Eddington rate onto this unusually massive and possibly fast spinning central black hole. These findings show that J2345-0449 is an extremely rare and unusual galactic system whose properties challenge the standard paradigms for black hole growth in disk galaxies and formation of relativistic jets in them.

Following the discussion on the radio emissions from the spiral host J2345-0449, we are discussing the results on the GRG *2MASX J10212421+1217060* at redshift $z = 0.129$, which is having a linear size of ~ 2 Mpc. From the GMRT observations of this source, we found that the radio jet to the southern side is having a length of ~ 650 kpc. Radio sources with long uninterrupted jets in a scale of hundreds of kpc are very rare, and hence such sources are interesting in that sense itself. Bagchi et al.(2007) reported a one-sided radio source *CGCG 049-033*, having a ~ 440 kpc long jet, which was the longest radio jet reported till the date. Thus the analysed source is found to gain the status of the longest uninterrupted radio jet reported so far. It is observed that the radio images show clear signatures of episodic activity, and the jet from the second episode of activity is travelling through the diffused relics of the previous epoch.

We observed four more GRGs using GMRT at different frequencies. Their spectral index properties, morphologies, luminosities and linear sizes are studied. The black hole masses of these sources are also estimated. All these sources have been observed at 325 and 610 MHz frequencies using GMRT.

1. 2MASXJ102131.5+0519011 : This is a double-lobed radio source at redshift, $z=0.156$, with diffuse relic regions, extending up to ~ 2.2 Mpc.
2. 2MASXJ15261183+2939048: This is a giant radio source at a redshift, $z=0.1169$, with a total linear size of ~ 2.0 Mpc.
3. 2MASXJ22561507-3617589 : This source is at a redshift of 0.090 with diffuse lobes. The linear size of the source is ~ 1.5 Mpc.
4. 2MASXJ12070524-2741466: This is a Wide-angle tailed (WAT) radio source at a redshift, $z=0.025$, with a linear size of ~ 1 Mpc. This source carries the signatures of recurrent activity of the central AGN.

The thesis concludes with a summary of the results and future possibilities.

PUBLICATIONS

1. *GMRT observations of the radio source 4C 35.06: precessing jets from a cD galaxy under assembly?*, **Biju, K.G**; Pandey-Pommier, M.; Sunilkumar, P.; Dhurde, Samir; Bagchi, Joydeep; Ishwara-Chandra C., H.; Jacob, Joe; BASI, ASI Conference Series, 2014, Vol. 13, pp. 155-156; 2014arXiv1411.7261G.
2. *Megaparsec Relativistic Jets Launched from an Accreting Supermassive Black Hole in an Extreme Spiral Galaxy*, Bagchi, Joydeep; Vivek, M.; Vikram, Vinu; Hota, Ananda; **Biju, K. G.**; Sirothia, S. K.; Srianand, Raghunathan; Gopal-Krishna & Jacob, Joe, ApJ, 788, 2014.
3. *Zwicky's Nonet': a compact merging ensemble of nine galaxies and 4C 35.06, a peculiar radio galaxy with dancing radio jets*, **K.G. Biju.**; Joydeep Bagchi.; M. Pandey-Pommier.; Ishwara Chandra C.H.; Joe Jacob.; M.K. Patil.; Sunil Kumar P.; Mahadev Pandge.; Samir Dhurde.; Pratik Dabhade.; Madhuri Gaikwad.; Sheelu Abraham.; M. Vivek.; Ashish A. Mahabal.; S. G. Djorgovski., MNRAS, Volume 471, Issue 1, p.617-628
4. *NVSS J102124+121702: A 2.2 mega parsec scale Giant Radio Galaxy, with a 650 Kpc uninterrupted jet.*, **K.G. Biju.**; Bagchi, Joydeep; Madhuri Gaikwad.; Mahadev Pandge.; Pratik Dabhade.; Ishwara Chandra C.H.; Joe Jacob., Paper in preparation.

Contents

Declaration	vii
Acknowledgements	xv
Preface	xvii
Contents	xxii
List of Figures	xxvii
List of Tables	xxxii
1 Introduction	1
1.1 Classification of galaxies	2
1.1.1 Elliptical galaxies	3
1.1.2 Spiral galaxies and Lenticulars	5
1.2 AGNs and Radio Galaxies	5
1.2.1 Radio galaxy classification	8
1.2.1.1 Morphological classification	9
1.2.1.2 Classification based on optical properties of the host galaxies.	12
1.2.1.3 Classification based on linear sizes.	13
1.2.1.4 Giant Radio Galaxies	14
1.3 Motivation of the thesis	15
1.4 Outline of the thesis	17

2	Radio and Optical data analysis	19
2.1	GMRT radio data analysis	20
2.1.1	Sequence of steps in GMRT data analysis	22
2.1.1.1	Imaging	27
2.1.1.2	Note 1: Robust parameter	30
2.1.1.3	Note 2: Thermal RMS noise in the radio maps	30
2.1.1.4	Angular size of a radio core	31
2.1.2	Preparation of spectral index maps	31
2.2	IGO data analysis	34
2.2.1	Bias subtraction and Flatfield deduction	34
2.2.2	Spectroscopic data analysis	35
2.2.3	Velocity dispersion	40
3	‘Zwicky’s Nonet’: a compact merging ensemble of nine galaxies and 4C 35.06, a peculiar radio galaxy with precessing radio jets	43
3.1	‘Zwicky’s Nonet’: Previous optical, X-ray and radio observations	47
3.1.1	Optical observations	47
3.1.2	Previous X-ray studies	50
3.1.3	Previous radio observations of 4C 35.06	51
3.2	GMRT, IGO and Palomar observations	52
3.3	Results and Discussion	54
3.3.1	GMRT images of 4C 35.06 and map parameters	54
3.3.2	AGN radio core	56
3.3.3	Spectral index maps and spectral ageing results	59
3.3.4	Twists and kinks in the jet: Dynamical signatures of a perturbed AGN?	65
3.3.5	Interaction of jet system with the ambient intra-cluster medium	70
3.3.6	Optical spectroscopic results: AGN signature and black hole mass estimation	75
3.4	Conclusions	82
4	Radio and optical studies of the largest radio source hosted by a spiral galaxy 2MASX J23453268-0449256	87

4.1	Previous observations	89
4.2	GMRT and IGO observations	91
4.3	Results	92
4.3.1	GMRT images of J2345-449	92
4.3.2	Optical spectroscopic results	97
4.3.2.1	Central velocity dispersion and black hole mass	97
4.3.2.2	Galaxy rotation curve	99
4.3.3	WISE mid-infrared colours.	103
4.4	Discussion	106
4.4.1	Mass of the galaxy	106
4.4.2	SMBH in J2345-0449	107
4.4.3	Jet power and magnetic field	108
4.4.4	Astrophysical processes behind the radio emission	110
4.5	Conclusions	112
5	NVSS J102124+121702: A 2.2 mega parsec scale Giant Radio Galaxy, with a 650 kpc uninterrupted jet	115
5.1	Previous observations	116
5.2	Results	118
5.2.1	GMRT radio images and map parameters	118
5.2.2	Spectral index maps and radio spectral properties	125
5.2.3	Jet power of J1021+1217	131
5.2.4	WISE mid infrared colours	131
5.2.5	Optical spectroscopic results	134
5.3	Discussion	137
5.4	Conclusions	139
6	Four Giant Radio Galaxies with diffuse relic regions.	143
6.1	Previous observations	147
6.2	GMRT observations	150
6.3	Results	153
6.3.1	GMRT radio images and map parameters	153
6.3.2	Spectral index maps and radio spectral properties	164
6.3.2.1	Jet power	174

6.3.3	WISE mid infrared colours	175
6.3.4	Optical spectroscopic results	180
6.4	Discussion	183
6.4.1	Black hole mass and linear size of GRG	183
6.4.2	Effect of environment on linear size	184
6.4.3	Spectral age and linear sizes	185
6.4.4	PD diagram	186
6.4.5	LERG nature of the GRGs	188
6.5	Conclusions	188
7	Conclusion and Future Work	193
7.1	Future works	197

List of Figures

1.1	Hubble tuning fork diagram.	3
1.2	AGN Unification diagram.	6
1.3	The radio galaxy 3C 48	10
2.1	Feige110 CCD spectrum image.	36
3.1	SDSS colour composite image of the galaxy cluster Abell 407	46
3.2	A pseudo-colour, near infra-red image of ‘Zwicky’s Nonet’	48
3.3	The DSS r-band image of Abell 407 cluster, with X-ray contours.	50
3.4	i-band image of the galaxy cluster Abell 407, overlaid with 610 MHz radio contours	54
3.5	GMRT radio maps of 4C 35.06 at 610, 235 and 150 MHz frequencies, with NVSS and VLSS images.	56
3.6	zwicky’s nonet: Optical and radio images	58
3.7	The integrated spectrum of 4C 35.06.	60
3.8	The spectral index maps between different frequencies.	61
3.9	spectral break in the relic regions.	63
3.10	The high-resolution grey scale image of the source 4C 35.06 at 610 MHz (GMRT) showing the twisted, helical jet structure.	66
3.11	GMRT 150 MHz radio image of 4C 35.06, superposed on the ROSAT 0.5 - 2.4 keV X-ray contours.	71
3.12	The optical spectra of galaxies G1, G2, G5 and G6.	77
3.13	The optical spectra of galaxies G3, G4, G7 and G9 all taken from IGO.	78
4.1	NVSS image at 1.4 GHz and contour plots	89

4.2	SDSS image of the galactic environment of J2345-0449.	91
4.3	GMRT images and contour plots at 325 and 610 MHz	93
4.4	The integrated spectral index plots of J2345-0449.	94
4.5	The spectral index map between 1.4 GHz and 325 MHz	95
4.6	Spectral break frequency.	96
4.7	The Optical spectrum of the central region	98
4.8	Two-dimensional images showing the long-slit spectrum near the H_{α} and NII emission lines of galaxy J2345 - 0449.	99
4.9	one -dimensional spectra extracted at different sub-apertures and Gaussian fits to H_{α} and NII lines	100
4.10	The rotation curve of the galaxy J2345-0449	102
4.11	WISE colour-colour plots	104
4.12	WISE-Radio Luminosity plot	105
5.1	SDSS image of the galactic environment of J1021+1217	117
5.2	NVSS image and contour plots of J1021+1217	119
5.3	610 MHz GMRT map	120
5.4	610 MHz radio contour map with GMRT	121
5.5	325 MHz GMRT map and contour plots	122
5.6	610 MHz inner radio contours	124
5.7	Spectral index plots of J1021+1217	125
5.8	Break frequency NII and SII regions:second order polynomial fit.	128
5.9	Spectral index maps 1.4GHz vs 325 MHz	129
5.10	Spectral index maps 610 vs 325	130
5.11	WISE colour-colour plots	133
5.12	WISE -radio luminosity plot	134
5.13	The optical spectrum of J1021+1217, from SDSS	135
5.14	Galaxies around the GRG, J1021+1217	138
6.1	SDSS r band images of the galactic environment around J1021+0519 and J1526+2939	148
6.2	DSS2 r band images of the galactic environment around J2256-3617 and J1207-2741	149
6.3	NVSS 1.4GHZ contour plots of four GRGs	152
6.4	610 and 325 MHz GMRT maps of J1021+0519	154

6.5	610 and 325 MHz GMRT map of J1526+2939	157
6.6	610 MHz GMRT map of J2256-3617	159
6.7	610 and 325 MHz GMRT map of J1207-2741	161
6.8	J1207-2741 image with positions marked	163
6.9	Spectral index plots of J1021+0519	165
6.10	Spectral index maps 1.4GHz vs 325 MHz of J1021+0519	167
6.11	Spectral index plots of J1526+2939	168
6.12	Spectral index maps 1.4GHz vs 325 MHz (source J1526+2939)	169
6.13	Spectral index plots of J2256-3617	170
6.14	Spectral index maps 1.4GHz vs 610 MHz (source J2256-3617)	171
6.15	Spectral index plots of J1207-2741	172
6.16	Spectral index maps 1.4GHz vs 610 MHz (source J1207-2741)	174
6.17	WISE colour-colour plots	176
6.18	WISE -radio luminosity plot	179
6.19	The optical spectrum of J1021+0519, from SDSS	180
6.20	The optical spectrum of J1526+2939, from SDSS	181
6.21	P-D diagram	187

List of Tables

3.1	Galaxy properties in central region of Abell 407 cluster.	47
3.2	Details of GMRT observations.	53
3.3	Equipartition magnetic field B_{eq} for different regions of the radio source.	65
3.4	SMBH masses obtained from stellar velocity dispersion	80
3.5	SMBH masses (from K band absolute magnitudes), of the members of ‘Zwicky’s Nonet’.	81
4.1	Flux density values at different frequencies.	94
4.2	Rotation velocities relative to the galactic centre	101
4.3	WISE mid-infrared magnitudes and luminosities for J2345-0449	106
5.1	Global parameters of NVSS J102124+121702	118
5.2	SDSS magnitudes and SDSS colours	118
5.3	Flux values at different frequencies of J1021+1217.	127
5.4	WISE:Mid infrared magnitudes and luminosities	132
5.5	Optical emission line paprameters	135
6.1	Global parameters of Sources J1021+0519 and J1526+2939	150
6.2	Global parameters of Sources J2256-3617 and J1207-2741	151
6.3	SDSS magnitudes and SDSS colours	151
6.4	1.4 GHz radio flux density of four GRGs	151
6.5	Details of the GMRT observations GRGs	153
6.6	Radio Map parameters of J1021+0519	155
6.7	Radio Map parameters of J1526+2939	158
6.8	Radio Map parameters of J2256-3617	159

6.9	Radio Map parameters of J1526+2939	163
6.10	Radio flux densities at different frequencies of the GRGs	164
6.11	Jet Power	175
6.12	WISE:Mid infrared magnitudes and luminosities	177
6.13	WISE mid-infrared colours for all the four sources.	177
6.14	Optical emission line parameters J1021+0519	178
6.15	Optical emission line parameters of J1526+2939	179
6.16	Black hole mass from K band absolute magnitudes	182
6.17	Black hole masses all six GRGs	183
6.18	Galactic environment of host galaxies	184
6.19	Nearest galaxy clusters to the host galaxies	185
6.20	Spectral ages of the GRGS.	186

Chapter 1

Introduction

Galaxies are considered as the building blocks of the Universe. The hierarchical nature of buildup of the Universe from galaxies to Galaxy clusters, Superclusters and the cosmic web is well known today. However, until the end of the nineteenth century, it was believed that the Universe is limited to our Galaxy, the Milky Way. After Galileo, the observation by astronomers through bigger and better telescopes had revealed the presence of faint fuzzy objects in the sky. It was Messier who made the first catalogue of fuzzy objects in the sky in a bid to avoid the menace of these objects while studying comets. This serves as the first record of non-stellar objects in the sky. Later, William Herschel made an extensive catalogue of these fuzzy objects, the updated version of which is the new general catalogue (NGC). The path-breaking observations by Edwin Hubble in 1930s on the spectra of some of these fuzzy objects and the associated determination of their distances confirmed that the Universe extends beyond our Galaxy and that there are galaxies outside ours. Now with, further advancement

of knowledge regarding extragalactic objects, we understand our Milky Way is one among the billions of galaxies in this Universe.

Currently, it is established with irrefutable dynamical evidence that most of the galaxies are hosting super-massive black holes (SMBHs) of masses $10^6 - 10^{10} M_{\odot}$ at their centers (Kormendy & Richstone, 1995; Kormendy & Ho, 2013; Magorrian et al., 1998). Now there exist strong correlations between black hole masses and galaxy bulge properties such as bulge luminosity, bulge mass and stellar velocity dispersion (Gebhardt et al., 2000; Ferrarese & Merritt, 2000; Gültekin et al., 2009a; Merritt & Ferrarese, 2001; Nelson, 2000; Tremaine et al., 2002; Marconi & Hunt, 2003a). These black holes are believed to be the central engines of active galactic nuclei (AGNs) and the accretion of matter onto it is responsible for the huge power output from these sources. (Lynden-Bell, 1969; Soltan, 1982; Begelman et al., 1984). Some of the AGNs manifest themselves as extremely luminous quasars and radio galaxies which eject large-scale relativistic bipolar jets. The physics of black hole formation and the launching of relativistic jets are major areas of research in modern astrophysics.

1.1 Classification of galaxies

Depending on their morphology and other internal properties, galaxies are classified into many classes. The well known ‘Hubble classification’ is based on the morphology of the galaxies in optical wavelengths. In the Hubble classification scheme, there are mainly three different classes of galaxies: Ellipticals,

Lenticulars and Spirals. Hubble proposed ‘irregulars’ as the fourth class of galaxies, which lack any specific morphology. In the Hubble’s morphological classification scheme, the different classes are usually represented in a tuning fork-shaped diagram, which is called Hubble tuning fork diagram (Figure 1.1).

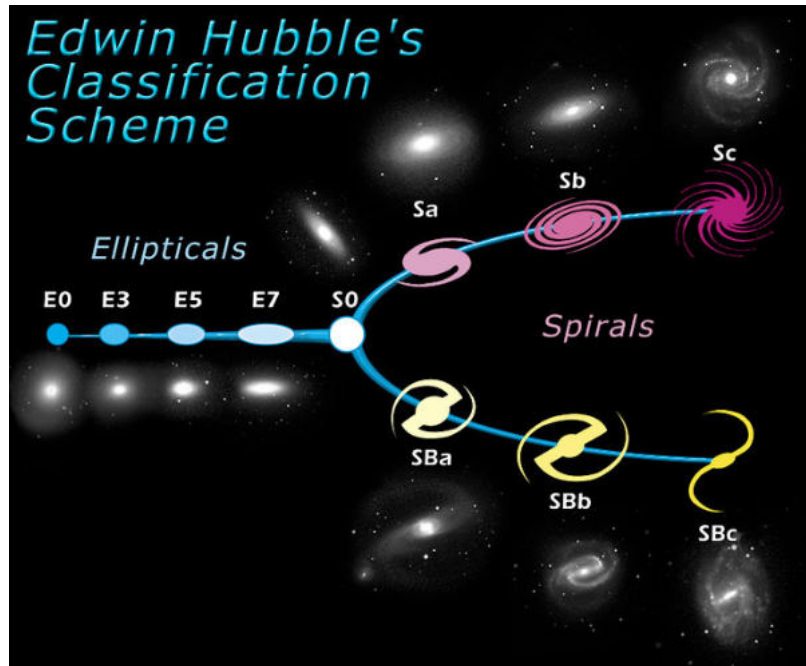


FIGURE 1.1: Hubble tuning fork diagram. Credit: NASA & ESA.
(Image from <https://www.spacetelescope.org/images/heic9902o/>)

1.1.1 Elliptical galaxies

Galaxies with elliptical isophotes belong to the category of elliptical galaxies. Depending on the ellipticity of the isophotes they can be classified into different subgroups. If ‘a’ and ‘b’ are the semi-major and semi-minor axes, the ellipticity $\epsilon = 1 - \frac{b}{a}$. The elliptical galaxies are subclassified according to their ellipticity

and are represented as E_n where $n = 10\epsilon$. Elliptical galaxies can also be classified according to their luminosities and colour as Normal ellipticals, Dwarf ellipticals, cD galaxies, Blue compact dwarf galaxies and Dwarf spheroids.

Elliptical galaxies are believed to have evolved by multiple mergers (Toomre & Toomre, 1972; Farouki & Shapiro, 1982; Negroponte & White, 1983; De Lucia et al., 2006). A large number of observable properties of ellipticals can be explained by the merger model. Also, ellipticals are more abundant in galaxy clusters and groups, where the conditions during their collapse and mergers are favourable for their formation (Dressler, 1980a,b). Galaxy clusters are considered as the largest gravitationally bound structures, existing mostly in the dense regions of the Universe. It is known that clusters harbour giant elliptical galaxies, called Brightest Cluster Galaxies (BCGs) at their centers. Some of the BCGs are classified as cD galaxies because of its very peculiar properties. cD galaxies are characterised by their huge mass and size, with diffuse stellar halo extending 100s of kpc into the intracluster medium. Also, they are characterised by the presence of multiple nuclei embedded in the diffuse stellar halo (Tovmassian & Andernach, 2012; Garijo et al., 1997; Kormendy & Djorgovski, 1989).

It is observed that elliptical galaxies are hosting more massive SMBHs at their centers compared to spirals and lenticulars. The masses of SMBHs in BCGs and cDs are still higher than that of normal ellipticals. Many studies have shown that radio sources with large-scale jets are generally hosted by elliptical galaxies. Also, a large-fraction of BCGs and cDs are found to be radio-loud compared to that of normal ellipticals. The minimum value of black hole mass suggested for the production of large-scale relativistic jets in radio galaxies, and radio quasars is $\gtrsim 10^8 M_\odot$ (Chiaberge & Marconi, 2011; Laor, 2000; Gopal-Krishna et al., 2008; Sikora et al., 2007).

1.1.2 Spiral galaxies and Lenticulars

The spiral galaxies are characterised by a disk with spiral structure and a central bulge. They are subclassified as normal spirals (S's) and barred spirals (SB's). 'S' type spirals have a central bulge, and 'SB's' have a central bar. Also, letters a, b and c are used to label these spiral galaxies depending on the tightness of the spiral arms (see Figure 1.1).

Morphologically Lenticular galaxies appear as a transition stage between ellipticals and spirals, but it is suggested that their formation history may be different (Barway et al., 2009). They have a bulge and a disk but lacks spiral arms. Ellipticals and lenticulars are generally termed as early-type galaxies while spirals are called as late type-galaxies. These names have no connection with the evolutionary track of these galaxies.

The mass and spin of SMBHs in spiral galaxies are estimated to be less than that of elliptical galaxies (Chiaberge & Marconi, 2011; Bagchi et al., 2014; Gopal-Krishna et al., 2008). It is also found that powerful radio jets on $\gtrsim 100$ kpc scale are almost always launched from the nuclei of elliptical galaxies and not of spirals. The typical radio luminosity of spiral galaxies with AGN is observed to be about 10^3 - 10^4 times feebler than ellipticals, making them comparatively radio-quiet (Bagchi et al., 2014; Singh et al., 2015; Hota et al., 2011).

1.2 AGNs and Radio Galaxies

The luminosity of galaxies is mainly contributed by stars with only a very small fraction coming from gases and dust. However, there are galaxies which emit enormous amounts of energy in a wide range of wavelengths, i.e. from radio

wavelengths to γ -rays. It is also observed that this radiation is coming from a very small central region (AGNs) (~ 100 pc) of the galaxies. AGNs are powered by accreting SMBHs. The accretion of matter into the SMBH results in the release of gravitational potential energy, leading to the outpour of energy in a wide range of wavelengths (Lynden-Bell, 1969; Soltan, 1982; Begelman et al., 1984). Radio galaxies are a subclass of AGNs. Other classes of AGNs are Seyfert Galaxies, Quasars, LINERs, BL Lac objects & Optically Violently Variable (OVV), and Narrow Line X-ray Galaxies (NLXGs).

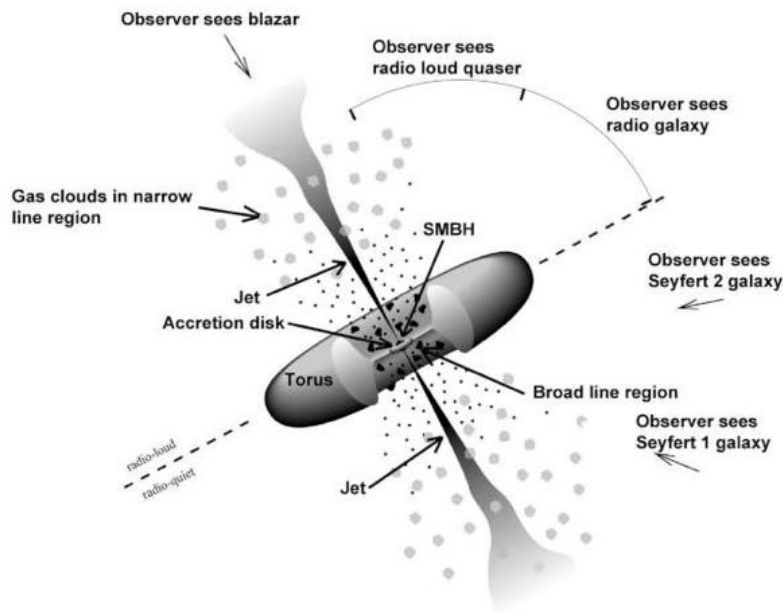


FIGURE 1.2: AGN ‘orientation-based’ Unification diagram (Urry & Padovani, 1995). Image credit: <https://fermi.gsfc.nasa.gov/science/etev/agn/>.

Historically there were attempts to explain various observational properties of AGN in terms of its orientation effects. The basic idea was that all of the active galaxies (quasars, Seyfert, radio galaxies) which we observe have the same internal structure in their nucleus. Unified models of AGN unite all these classes

of objects (quasars, radio galaxies, Seyferts and others) by conjecturing that they are a single type of physical object, just observed from different conditions. The currently favoured model is an ‘orientation-based unified model’ meaning the differences arise because of different viewing angles of the observer (See Figure 1.2). Since AGN are not spherically symmetric, what we see depends on from where we view them (Urry & Padovani, 1995; Rowan-Robinson, 1977).

The generally accepted criteria for classifying an AGN as Radio AGN is based on its radio luminosity at 1.4 GHz ($L_{1.4\text{GHz}}$). i.e. if

$$L_{1.4\text{GHz}} \geq 10^{24} \text{WHz}^{-1},$$

it is considered as a radio-loud AGN (Tadhunter, 2016). The complete orientation based unification of radio-loud and radio-quiet objects remains problematic, particularly in explaining the vast range in radio power and jet extents. The physical origin of the radio-loud and radio-quiet dichotomy and the mechanisms by which relativistic jets are launched in AGNs is still under investigation. Many studies have shown that the major difference between radio-loud and radio-quiet AGNs is related to the black hole properties, such as its mass, spin, and accretion rate (Blandford & Znajek, 1977; Blandford & Payne, 1982; Wilson & Colbert, 1995), in addition to the orientation effects.

At present, there are two popular theories or mechanisms by which jets are produced in AGNs, the Blandford-Znajek (BZ) mechanism and the Blandford-Payne (BP) mechanism (Blandford & Znajek, 1977; Blandford & Payne, 1982). The BZ process requires a fast rotating black hole for jet production. Here the black hole’s rotational energy is converted into jets, making use of the magnetic field created at the inner edges of the accretion disk. According to the BP process, a rotating black hole is not necessary for the production of jets. Here the jets are

guided by the magnetic fields generated by the fast rotating accretion disk, and the energy is extracted from the accretion disk itself. So, in short, we can say

$$\textit{Disk rotation} + \textit{vertical field} \rightarrow \textit{BP type jet}$$

$$\textit{Black Hole rotation} + \textit{vertical field} \rightarrow \textit{BZ type jet}$$

However, in both the mechanisms the presence of a strong magnetic field is essential near the black hole horizon. Also, the intensity and geometry of the magnetic field can strongly influence the emerging jet (Beckwith et al., 2008).

It is suggested that if a geometrically thick disk produces a jet, it can be represented by Advection-Dominated Accretion Flow (ADAF) models (Narayan & Yi, 1994, 1995). Also, it is found from numerical simulations that BZ mechanism can produce relativistic jets from thick disk systems (McKinney, 2005). So BZ mechanism is more probable in AGNs, which are in ADAF state. An ADAF state is characterised by the strong magnetic flux anchored to an ion-supported torus of optically thin, geometrically thick, extremely hot gas with poor radiative efficiency (Rees et al., 1982). In such systems, the accretion flow of matter will be dominated by advection process, and the accretion will be sub-Eddington. As the disk is geometrically thick, the radiative efficiency will be lower than its kinetic efficiency. Thus large-scale jets can be launched from such systems (Narayan & Yi, 1994, 1995).

1.2.1 Radio galaxy classification

Radio galaxies are generally synchrotron emitting symmetric double lobes that are connected by jets to the radio core (See Figure 1.3). The jet connecting

the core and the lobes may not be visible in many cases. Small regions of strong synchrotron emissions called hot spots, created when the jet head hits dense intergalactic medium, also might be observed in the lobes of some radio galaxies. The position of the core of the radio galaxy may be coinciding with the optical host galaxy. Radio sources in many cases may have an extension much more than the host galaxies.

As these galaxies have high luminosities in the radio band, they are observable even at high redshifts. So, they serve as signposts of the early Universe, helping to study the evolution of galaxies (Miley & De Breuck, 2008). Another important observation regarding radio galaxies is that a vast majority of them are hosted by elliptical galaxies. There are Seyfert galaxies which are usually associated with spirals, and are characterised by radio emissions up to few parsecs only (Adams, 1977; Bagchi et al., 2014; Singh et al., 2015; Hota et al., 2011).

Radio galaxies are classified into different groups according to their morphology, optical host properties and linear sizes. Such classifications are important because the underlying physical processes are different in each class.

1.2.1.1 Morphological classification

One of the well-known classification of radio AGNs as FR I/ FR II is based on their radio morphology (Fanaroff & Riley, 1974; De Young, 1993). This classification is based on the value of r_s , which is the ratio of the separation between the brightest points on both sides of the radio core to the total size of the radio galaxy. If the value of $r_s > 0.5$, the source is considered as FR II and if $r_s < 0.5$, it will be termed as an FR I source (Fanaroff & Riley, 1974). FR II radio sources are usually characterised by hot spots at the ends of the lobes. So

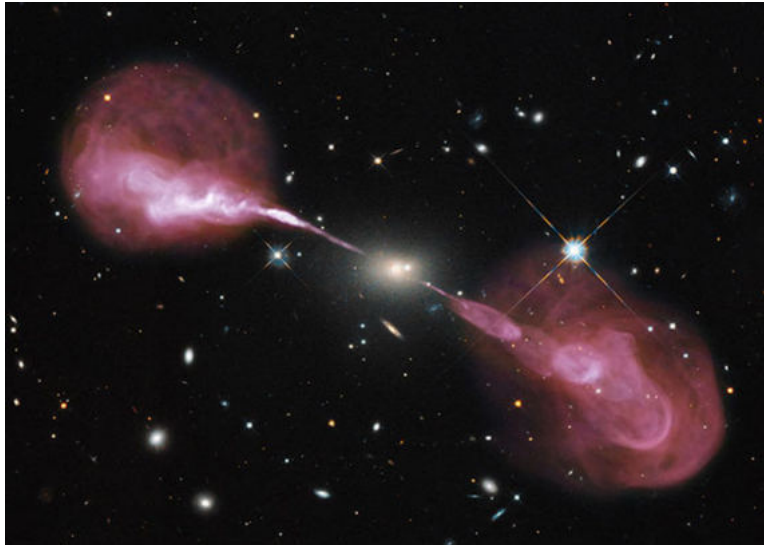


FIGURE 1.3: The radio image of 3C 48, which is overlaid on the optical images from the Hubble Space Telescope’s Wide Field Camera 3. The radio core, jets and lobes can be seen. Credit: NASA, ESA, S. Baum and C. O’Dea (RIT), R. Perley and W. Cotton (NRAO/AUI/NSF), and the Hubble Heritage Team (STScI/AURA)

they are also called ‘edge-brightened sources’. Similarly, FRI radio sources are called ‘edge-darkened’. The radio luminosity at the 178MHz frequency is also used to classify them. FRII radio sources are generally more powerful with their radio luminosity at the 178 MHz ($L_{178} \geq 2 \times 10^{25} \text{ WHz}^{-1}$) (Fanaroff & Riley, 1974). The morphological classification of radio galaxies as FRI or FRII is still debatable but could be connected to the environment, so that jet interaction with the intergalactic medium (IGM) plays an important role in it (De Young, 1993; Lin et al., 2010; Kawakatu et al., 2009). Supporting this argument FRII galaxies are usually found in less dense environments. They are also classified according to the jet kinetic power. However, it is known that almost 17% of radio sources cannot be classified either as FRI or FRII.

Apart from FRI/FRII classification, radio galaxies generally show four distinct types of structures: (a) Linear (b) ‘C’ shaped (c) ‘S’ or ‘Z’ shaped and (d) the ‘X’ shaped ones. The linear morphology is most common with symmetric jets feeding lobes to either side of the radio core. The formation of ‘C’ type morphology can be attributed to the movement of the source through the dense ICM, where the ram pressure of it bends the jets (Mguda et al., 2015; Miley et al., 1972; Owen & Rudnick, 1976; Begelman et al., 1979). The inversion symmetry found in ‘S’ or ‘Z’ shaped radio sources are possibly related to the precession of the spinning black hole (Begelman et al., 1980) and the associated tilting/perturbation in the accretion disk (Lu, 1990; Janiuk et al., 2008). These radio morphologies may be an indicator of the presence of a merging super massive black hole binary in the center of the host galaxy (Begelman et al., 1980; Deane et al., 2014) or disk driven precession, and have been observed in jet systems from several radio sources (van Breugel et al., 1984; Ge & Owen, 1993; Crawford et al., 2003; Condon & Mitchell, 1984; Walker et al., 2000). The last group, the ‘X’ shaped radio galaxies (XRGs) are believed to be due to a rapid flip of the spin axis of the SMBH (Rottmann, 2001; Merritt & Ekers, 2002; Hodges-Kluck et al., 2010; Lal et al., 2008) due to the perturbative influence of another black hole of higher mass merging with it. Alternatively, the interactions of the jet with the ambient gaseous medium has also been suggested as the cause of the unusual ‘X’ shaped morphology (Leahy & Williams, 1984; Capetti et al., 2002).

Rare cases of existence of multiple lobes due to different epochs of radio activity have also been observed (Kuźmicz et al., 2017; Saikia & Jamrozy, 2009a; Nandi & Saikia, 2012; Schoenmakers et al., 2000c) in many radio galaxies. In Double Double Radio Galaxies (DDRGs), two radio lobes each on either side of the core can be observed (Schoenmakers et al., 2000c,a). Here the outer lobe is produced by the AGN activity from an earlier epoch, and the inner lobes are

produced by recent AGN activity. Initially the AGN in the active phase has produced radio jets and lobes, which later on had shut down and then restarted its activity after some time. This recurrent activity of the AGN is responsible for the morphology of DDRGs. There are also examples of three episodes of activity in radio AGNs (Brocksopp et al., 2007; Hota et al., 2011).

1.2.1.2 Classification based on optical properties of the host galaxies.

Radio galaxies having large scale jets are generally hosted by elliptical galaxies having SMBH of masses $\geq 10^8 M_\odot$ (Laor, 2000; Gopal-Krishna et al., 2008). The optical spectroscopic properties of host galaxies generally reflect its internal properties. Based on the width of the emission lines they are classified as Narrow Line Radio Galaxies (NLRGs; with FWHM $< 2000\text{km/s}$) (Costero & Osterbrock, 1977), and Broad Line Radio Galaxies (BLRGs; with FWHM $> 2000\text{km/s}$) (Osterbrock et al., 1976). Also, there is another class of radio galaxies called Weak Line Radio Galaxy (WLRG) where $O[III]\lambda 5007$ line is absent or very weak (Tadhunter et al., 1998).

FRII galaxies, usually found in less dense environments, are generally characterized by strong emission lines in the optical spectra (Zirbel & Baum, 1995; Zirbel, 1997; Kauffmann et al., 2008). On the other hand, FRI radio sources are found more in galaxy clusters and are hosted by galaxies showing very weak or no optical emission lines (Zirbel & Baum, 1995; Hine & Longair, 1979; Best & Heckman, 2012).

The NLRGs or WLRGs are further classified as Low Excitation or High Excitation Radio Galaxies (LERGs & HERGs). LERGs are with weak or without emission lines (Laing et al., 1994; Tadhunter et al., 1998; Best & Heckman, 2012;

Lin et al., 2010). Buttiglione et al. (2010) studied a sample of radio galaxies ($\sim 92\%$ of galaxies in the 3CR survey) and classified them according to their emission line properties as LERGs and HERGs. He defined a quantity called the Excitation Index (EI) as,

$$EI = \text{Log}[O III]/H\beta - 1/3(\text{Log}[N II]/H\alpha + \text{Log}[S II]/H\alpha + \text{Log}[O I]/H\alpha). \quad (1.1)$$

According to this LERGs have been defined as those galaxies for which $EI \lesssim 0.95$ and HERGs as those having $E.I. \gtrsim 0.95$. But to calculate the EI, we must know the flux values of many emission lines.

The LERG/ HERG classification of radio galaxies are also possible using the 1.4GHz radio luminosity. Best & Heckman (2012) studied a sample of 18,286 radio-loud AGNs to differentiate between the low-excitation and high-excitation radio sources. They found that most of the low-excitation radio sources are having radio luminosity at 1.4GHz ($L_{1.4GHz}$) lower than $10^{26} WHz^{-1}$, while high-excitation sources are found to have values above this. So this value of radio luminosity is considered as a dividing value to classify the low-excitation and high excitation nature of radio sources. This classification is also possible with Wide-field Infrared Survey Explorer (WISE) colour-colour plots and the luminosity plots (Gürkan et al., 2014). Detailed discussion on this is given in the forthcoming chapters.

1.2.1.3 Classification based on linear sizes.

One of the important classifications of radio galaxies is based on their linear sizes. There are radio galaxies with projected linear sizes $\lesssim 100pc$ which are called Giga Hertz Peaked Spectrum (GPS) sources because they have peak in

their radio spectrum at Giga Hertz frequencies. Similarly, radio sources having linear sizes between 100pc-10kpc are called Compact Steep spectrum Sources (CSS). The spectral index of such sources is observed to be ≤ -0.7 . The radio sources having linear sizes between 10kpc and 1Mpc are not specifically grouped into any class. Radio galaxies with a projected linear size ≥ 1 Mpc are termed as Giant Radio Galaxies (GRGs) (Ishwara-Chandra & Saikia, 1999). They are the largest single objects in the Universe.

Still, the evolution of radio galaxies over cosmic time is not fully deciphered. The current understanding proposes an evolutionary route of $GPS \rightarrow CSS \rightarrow FRI/FRII \rightarrow GRG$, (Schoenmakers et al., 2000c). However, still, we do not know what percentage of GPS finally end up as GRGs.

1.2.1.4 Giant Radio Galaxies

The GRGs discovered so far is only around 300, which is only a tiny fraction of the total number of radio galaxies (Subrahmanyan et al., 1996; Ishwara-Chandra & Saikia, 1999; Lara et al., 2001; Schoenmakers et al., 2001; Machalski et al., 2001; Saripalli et al., 2005; Machalski et al., 2006, 2007; Kuźmicz & Jamrozy, 2012; Dabhade et al., 2017). The first GRGs discovered are 3C 326 and DA240, of which 3C 236 is still ranked as the second largest GRG ever discovered (Willis et al., 1974). Using the present Λ CDM cosmology model the linear size of 3C236 is 4.62 Mpc. The Largest GRG known to date is J1420-0545 with a linear size of 4.95Mpc (Machalski et al., 2008). GRGs are interesting typical candidates which enable the study of the evolution of a radio galaxy in cosmic time and the ambient intergalactic medium which confines the lobes far away from the parent galaxy. However, detecting such giant radio sources becomes difficult because the jet connecting the core to the lobes may not be seen in

most cases. One reason for it is the sensitivity limit of the telescopes. It is also observed that there is a paucity of GRGs at redshifts ≥ 1 (Ishwara-Chandra & Saikia, 1999; Saikia & Jamrozy, 2009b; Konar et al., 2008). It is expected that at high redshifts CMBR density is high and hence more will be the energy losses due to inverse Compton scattering. The most distant giant radio source reported so far is J031151.7-313001.0 at the redshift of 2.420 with a linear size of ~ 1 Mpc (Amirkhanyan, 2016). By the introduction of highly sensitive instruments like Low-Frequency Array (LOFAR), more giant sources may be revealed, even at high redshifts.

There are many reasons proposed for the evolution of GRGs. The important ones are the effect of environment (Subrahmanyan et al., 2008), advanced age of the radio sources (Jamrozy et al., 2008), Recurrent radio activity (Subrahmanyan et al., 1996) and properties of the central engine (Kuźmicz & Jamrozy, 2012). As the number of well-studied GRGs is very few, more multi-frequency studies are required to get a clear picture regarding the evolution of GRGs. These points are discussed in detail in chapter 6

1.3 Motivation of the thesis

In this thesis, we study a peculiar radio source 4C 35.06, with precessing radio jets hosted by the central region of the galaxy cluster Abell 407 and a sample of six GRGs, which are not studied so far at low radio frequencies.

The radio source 4C 35.06 is hosted by an ensemble of nine galaxies (Named by us ‘Zwicky’s Nonet’) embedded in a very diffuse stellar halo. The system ‘Zwicky’s Nonent’ is most probably in the stage of forming a cD galaxy. This radio source 4C 35.06 is characterised by diffuse relic regions. Many studies have

proposed that systems hosting helically modulated symmetric jets are promising sites for the search of close black hole systems. The galactic members in Zwicky's Nonet are very close in projection as well as in redshift. We compare this system with the helically twisted jet morphology of the famous micro-quasar SS433. Here we study the special morphology of the radio source, with reference to the galactic environment, from where it has originated.

Out of the six GRGs which are discussed in this thesis two are found to be extremely special. One of these two sources is hosted by a spiral galaxy and has a linear size of 1.6 Mpc. Till now this is the largest radio source associated with any spiral galaxy. Radio sources with linear sizes $> 100kpc$ from spiral hosts are extremely rare. We study the rotation curve of the host galaxy to confirm the spiral nature. The galaxy is also found to have very high values of rotation velocity and stellar velocity dispersion. In this thesis, we study the unusual properties of this source from the radio and optical observations.

The second special GRG discussed in this thesis is having a total linear size of 2.4 Mpc. This radio source is found to host an uninterrupted radio jet of linear size ~ 650 kpc, qualifying to be the longest one reported so far. We study the source at radio and optical wavelengths.

In this study, we discuss the morphological peculiarities, radio spectral properties and ages of six GRGs. We also discuss the properties of the host galaxies from optical spectra and infrared magnitudes. Here we compare our results with the available theories on the evolution of GRGs, such as the influence of environment, mass of the SMBH, the age of the source, and the recurrent activity.

As the number of GRGs, which are studied at multi-frequencies are small ([Dabhade et al., 2017](#); [Konar et al., 2004](#)), a detailed statistical analysis of such

sources is not possible. This thesis will contribute six more GRGs, with multi-frequency radio observations for a better understanding of the GRG population.

1.4 Outline of the thesis

This thesis has been organised as follows:

- **Chapter 1:** This provides the general overview of the galaxies, classification of galaxies, radio galaxies, different radio morphologies, the motivation of the thesis and thesis outline.
- **Chapter 2:** This chapter discusses the observations and data analysis.
- **Chapter 3:** Here we discuss radio and optical studies on ‘Zwicky’s Nonet’, the cD galaxy under formation at the center of the galaxy cluster Abell 407.
- **Chapter 4:** In this chapter, we discuss radio and optical properties of ‘J2345-0449’, the longest radio source associated with a spiral host.
- **Chapter 5:** Here we study the longest uninterrupted radio jet in the giant radio galaxy, NVSS J102124+121702 using radio observations and discuss the other properties of it using data from various sky surveys.
- **Chapter 6:** This chapter discusses the results obtained from the radio and optical studies on four giant radio galaxies. The properties of the host galaxies are also discussed. We also discuss the theories on the evolution of GRGs, by comparing the results obtained for our sample of six GRGs.
- **Chapter 7:** summarise our results and discuss future possibilities.

In this work we adopt a Λ CDM cosmology model with $H_0 = 69.6 \text{ km s}^{-1} \text{ Mpc}^{-1}$, $\Omega_M = 0.286$ and $\Omega_\Lambda = 0.714$. The radio spectral index α is defined as: flux density (S_ν) \propto frequency (ν) $^\alpha$.

Chapter 2

Radio and Optical data analysis

We carried out the radio observations, with the Giant Metrewave Radio Telescope (GMRT)¹, located at Narayangaon about 80 km from Pune. GMRT is one of the biggest and most successful experimental/ observational facility available in India. It is operated under National Centre for Radio Astrophysics (NCRA), Pune of Tata Institute of Fundamental Research (TIFR)

The optical spectroscopic observations are done using IUCAA Girawali Observatory, (IGO)² owned and operated by Inter University Center for Astronomy and Astrophysics (IUCAA). Three faint galaxies in the ‘Zwicky’s Nonet’ are observed using the 200-inch (5.1-meter) Hale Telescope of Mount Palomar Observatory.

We used Image Reduction and Analysis Facility (IRAF), developed by the National Optical Astronomy Observatories (NOAO), for the optical spectroscopic

¹<http://www.gmrt.ncra.tifr.res.in>

²<http://igo.iucaa.in>

data analysis. The GMRT radio data are analysed using the Astronomical Image processing Software (AIPS), developed by the National Radio Astronomy Observatory (NRAO).

In the radio studies we have also used the data available in Very Large Array (VLA), Faint Images of the Radio Sky at Twenty-cm (FIRST),³ and NRAO VLA Sky Survey (NVSS)⁴ radio sky surveys. We have also made use of the NASA/IPAC Extragalactic Database (NED)⁵ and NASA's Astrophysics Data System (NASA ADS)⁶.

For the optical and infrared studies, we used data from Sloan Digital Sky Survey (SDSS)⁷, Two Micron All Sky Survey (2MASS)⁸ (Skrutskie et al., 2006a) and the Wide-field Infrared Survey Explorer (WISE)⁹ (Wright et al., 2010).

2.1 GMRT radio data analysis

GMRT is an interferometric array of 30 dishes of 45m diameter each, offering a maximum baseline of 25km. Radio interferometry is used to increase the resolution of the telescope. The angular resolution of a telescope $\sim \frac{\lambda}{D}$, where D is the diameter of the telescope and λ is the wavelength of observation. As radio wavelengths are very large, the resolution that can be achieved by a single dish will be small. The interferometric array of small telescopes can solve this problem. The signals from each of the telescope pairs are combined to produce

³<http://sundog.stsci.edu/>

⁴<https://www.cv.nrao.edu/nvss/>

⁵<https://ned.ipac.caltech.edu/>

⁶<http://adsabs.harvard.edu/>

⁷SDSS is the Data base <http://www.sdss.org>

⁸<http://irsa.ipac.caltech.edu/Missions/2mass.html>

⁹[//wise.ssl.berkeley.edu/](http://wise.ssl.berkeley.edu/)

an interference pattern, which carries all the details of the object. For interferometers the angular resolution is $\sim \frac{\lambda}{b_{max}}$, where b_{max} is the maximum separation between the dishes called the maximum baseline.

In radio interferometry, images of astronomical sources are produced by the Fourier synthesis of measured complex visibility. The signals from the antennas are passed through amplifiers, which are tuned to the specific frequency at which the source to be observed. The signals (voltages) from any two antennas are joined in a correlator, and the correlator will give the time average of the product of the voltages. As the signals from antennas changes with time, they will interfere constructively or destructively in time, and as a result, the correlator output from each of the antenna pairs will be an interference pattern. According to the van Cittert-Zernike theorem, this interferometric data (the complex visibility) is proportional to the Fourier component of the sky brightness distribution. Therefore on performing inverse Fourier transform on the interferometric data, the brightness distribution on small sky planes can be reproduced. This is the basic principle of radio-interferometry.

The radio observations with GMRT is possible in the frequency bands centered at 150, 325, 610, 235 and the 1000 - 1450 MHz. The 1000 - 1450 MHz, L - band feed is subdivided into four sub-bands each centered at 1060, 1170, 1280 and 1390 MHz. Simultaneous dual frequency observations are possible at 610 and 235 MHz frequencies. Radio data from the GMRT is in the lta format. This raw data in the lta format is to be first converted to FITS format for importing to AIPS.

The general observation pattern is the following. The radio observation includes observation of the target source, the flux calibrator and the phase calibrator. The radio sources 3C 48 (0137+331, J2000), 3C 147 (0542+498, J2000)

and 3C 286 (or 1331+305,J2000) are used as the flux density calibrators. Phase calibrators are taken from the available list of phase calibrators, which are close to the target source. If the flux calibrators are close to the source, they can be used as phase calibrators.

Radio observations begin with the observation of any one of the flux calibrators 3C48, 3C 286 or 3C 147 for \sim ten minutes. After this \sim 30 minutes, scan on target source will be done, alternated by \sim 5-minute scans on the phase calibrator.

2.1.1 Sequence of steps in GMRT data analysis

The general procedure associated with any task in AIPS:

task \rightarrow 'Enter task name'

default \rightarrow It will set all parameters to the default values.

getn i \rightarrow where 'i' is the catalogue number of the uv data.

inp \rightarrow it will display all input parameters.

go \rightarrow Run the task.

The various AIPS tasks used for GMRT data analysis are the following.

1. FITLD

This task is used to load FITS data into AIPS. Once the task is selected, set the parameter values to the default values and run the task.

INTAPE \rightarrow Enter the data directory which is usually 1.

DATAIN \rightarrow Enter the FITS file name with the path of the input data file

OUTNAME \rightarrow Enter the desired output name of fitld

DOHIST \rightarrow 1 to enable the history

Go FITLD

2. INDXR

It creates an index(NX) table and index the uv data file. It also creates a Calibration table (CL) for entering the calibration solutions later. The calibration solution interval can be selected by changing c parameters.

C Parm(3) =1. → Here the solution interval is 1 minute.

3. LISTR

LISTR gives the list of each scan from the NX table.

OPTYPE 'SCAN'

It will list all the sources and their scan times in the terminal window.

4. QUACK

This task will flag selected portions of scans in a multi-source UV data set.

OPCODE 'BEG'

APARM(2) 0.25.

This will clip 0.25 seconds of data from the beginning of each scan. Usually, the beginning data for each scan are corrupted by the cache data from the previous scan. To get rid of this, it is a usual practice to clip the first visibility data points for a small interval of time. This will also create an FG table.

5. TVFLG

This task is used to view and edit data points. Before doing processing the data, we have to remove all the zero visibility points in the data. This will be mainly from non-working antennas.

SOURCES 'all'

D Parm(6) → Enter the integration time used in the data.

6. SETJY

This task is used to set the flux densities of the flux calibrators (3C48, 3C147 or 3C286) before proceeding for further calibration.

SOURCES '3C48, 3C147 or 3C286' → Use all the flux calibrators observed.

OPTYPE CALC → It uses the standard Baars et al. formulae ([Baars et al., 1977](#)) and frequency information from the header and determines the flux densities of 3C286, 3C48 and 3C147.

7. CALIB

This task is used to compute the antenna based complex gain solution for the flux density calibrator. This will generate an SN table containing complex gain solutions.

CALSOURCE → all flux and phase calibrators

ICHANSEL 150 150 1 0 → Choose a good channel as the reference. Usually, a channel in the middle is selected, which is not affected by Radio Frequency Interference (RFI).

REFANT → Choose a working antenna with least RFI as reference antenna.

SOLINT 1 (solution interval to be 1 min)

SOLTYPE 'LIR' → interpolation algorithm

SOLMOD 'A & P' → Amplitude and Phase

SNVER → 0

The SN, table created here is used to apply the calibration.

8. GETJY

This task is used to get the flux density values of phase calibrators.

SOURCES 'Phase calibrators'.

CALSOUR 'Flux calibrators.'

9. CLCAL

Here we apply the calibration to the sources.

SOURCES ”

CALSOUR ”

First, we do CLCAL with SOURCES as ‘flux calibrator’ and CALSOUR as ‘flux calibrator’. Repeat it with SOURCES as ‘phase calibrator’ and CALSOUR as ‘phase calibrator’.

OPCODE ‘CALI’

SAMPTYPE ‘MWF’

INTERPOL ‘2pt’

GAINVER 1

GAINUSE 2

It will apply the calibration solutions to the channel which we have selected as the reference channel for the sources we have used. The task will create a new CL table (CL table version 2).

After CLCAL, plot the data using TVFLG or UVPLT and flag the bad data from Radio Frequency Interference (RFI), using TVFLG or UVFLG. After satisfactory flagging remove the SN and CL (version 2) Tables and redo the tasks,

CALIB → GETJY → CLCAL.

While doing the task CLCAL this time, we have to apply the calibration to the target source also. For this, run the task ‘CLCAL’ with SOURCES ‘Target source’ and CALSOUR ‘Phase Calibrator’.

10. BPASS

In this task single channel calibration is applied to all the channels of the data.

CALSOUR ‘flux calibrators only.’

DOCALIB 1

SOLINT 0

BPASSPRM(5) 1

ICHANSEL 150 150 1 0 → here use the reference channel used before.

It will create the BP table. We can plot this BP table using the task POSSM. From the plots, we have to check for bad channels. If there are any bad channels, they need to be flagged using task SPFLG.

11. SPLAT

In an observation with 256 channels, in each integration time, we will get 256 data points. In SPLAT, we are averaging few points, without affecting the data quality. This task will reduce the data volume. The channel averaging helps to improve the Signal to Noise Ratio (SNR).

SOURCE 'all'

BCHAN → beginning channel to average

ECHAN → End channel to average

DOCALIB 1

FLAGVER 0

APARM(1) 3

CHANNEL → number of channels to average.

For 1280MHz the BW of a channel after averaging is 4MHz For 610 MHz the BW of a channel after averaging is 2-3 MHz.

12. SPLIT

The calibrated target source data can be now separated out from the multi-source data. This is done through the task 'SPLIT'.

DATAIN .splat file

SOURCE → 'Target source only.'

DOBAND 3

DOCAL 1

APARM 0

Here a file with extension .SPLIT will be created. Examine the split file using the tasks TVFLG, UVPLOT or VPLOT. If there is any clear bad data it can be flagged. Then imaging can be made using the task IMAGR.

2.1.1.1 Imaging

The radio interferometric imaging works under the principle of 2D Fourier transform, and this assumes a flat sky plane. Depending on the size of the primary beam, multi-facet imaging needs to be done to hold this assumption. Task 'SETFC' is used to calculate the number of facets. We use AIPS task 'IMAGR' to do the multi-facet imaging.

13. SETFC

DATAIN .split file

SOURCES 'all'

BOXFILE → enter the path to the box file '.box'

Cellsize * * → $* = \frac{1}{3} \frac{\lambda}{D} \times 206265$ arcsec

Imsize 1024 1024

Bparm(1) → This is 1.6 times of the $\frac{HPBW}{2}$ in degree

SETFC task will give the number of facets. This should be used in the next task imaging.

14. IMAGR

DATAIN is .split file

DOCAL -1

FLAGVER 0

GAINUSE 0

STOKES ”

BCHAN 1 → Beginning channel

ECHAN → End channel

NCHAV 10 → enter the total channels

CELLSIZE * * → use the values used in SETFC

IMSIZE 1024 1024

NFIELD → enter the value obtained from the task SETFC

DO3DIMAG 1

Robust 0 → select 0 initially.

According to the van Cittert-Zernike theorem, the interference pattern is directly related to the source brightness. In this case, for small field of view, the complex visibility is the 2D Fourier transform of the brightness on the sky. So the task IMAGR does inverse Fourier transform of the uvdata and produces a model image. After the first round of imaging, phase-only self-calibration is performed to correct for phase errors using the first image as a model. The task used for self-calibration is ‘CALIB’.

15. CALIB (Self calibration)

In self Calibration, we are using the same task ‘CALIB’. Self-calibration (here on ”self-cal”) is used to explain the process for procuring a time series of complex gains which are antenna-based (phase and amplitude) that minimises the deviation of the observed visibilities from a model of the source visibilities. The concept of self-cal forms the basis of radio interferometric calibration. Indeed, the standard procedure of calibrating interferometric data, by solving for these gains on a point-like calibrator of precisely known position, is simply a special case of self-cal where the model is assumed to have zero phase and equal amplitude on all baselines. When

the morphology of the target is not known a priori, such as for a science target, one can use an iterative process to construct a better and better image (model) gradually of the target, after standard calibration has been applied. The technique for doing self-cal on such targets was developed in the 1970's for long baseline interferometry (see the review by [Pearson & Readhead \(1984\)](#)).

Here we are providing the image produced in the previous task 'IMAGR' as a model. So this task improves the calibration of the target source, using its own image as the model. The initial self-calibrations should be used to improve the phase of the source.

DATAIN 'split file'

INNAME → The first 'ICL file, ie. ICL001

ICHANSEL 1 10* 1 0 → if there are 10 channels

NMAPS → Enter the number of fields (number from SETFC).

SOLMOD P → phase only.

The calib will create an SN file. check the file using SNPLT. Flag if there is any large phase change associated with any antenna. Then repeat the process as under (The new calib should be the datain in the next IMAGR).

→ *IMAGR* → *CALIB* → *SNPLT/UVFLG* → *IMAGR* → *CALIB* → *IMAGR* →

When the antenna based phase changes are minimum, a final round of amplitude and phase calibration can be done. For this, we have to change the 'SOLMOD' to 'A& P'. The image from this final self-calibrated data is being used in this thesis.

2.1.1.2 Note 1: Robust parameter

The robust parameter is used to decide the weightage that should be given to the baselines. If the robust parameter is zero, it will give equal weightage to all baselines. If the robust parameter is -ve, it will give more weightage to longer baselines (In GMRT, we know the longest baseline is 25kms). As a result, when we use -ve robust parameters the resolution will be high. Similarly when we use robust +ve, it will give more weightage to shorter baselines, and as a result, the resolution will be low. However, when we have high resolution, the diffuse extended regions and relic regions may resolve out. So the value of robustness should be decided by our science goal. When we want to image some diffuse relic regions, we must give more weightage to shorter baselines and hence the robustness should be +ve. When our science goal is such as to resolve the core, we have to go for high resolution, and we should use -ve robustness.

2.1.1.3 Note 2: Thermal RMS noise in the radio maps

The thermal RMS noise in GMRT is given by

$$\Delta S = \frac{T_{sys}}{\sqrt{2G\eta_c\sqrt{n_b n_{IF}}\Delta\nu T}}$$

Here T_{sys} is the system temperature (K), η_c correlator efficiency, n_b is the number of baselines, n_{IF} is the number of IF channels, and $\Delta\nu$ (Hz) is the bandwidth of each sideband (or channel width for spectral line observations). $n_{IF} = n_{pol} + n_{SB}$, where n_{pol} is the number of polarisations (2 for the GMRT) and n_{SB} is the number of sidebands. ‘T’ is the time in seconds for which the source is observed. ‘G’ is the antenna gain. In GMRT the

values of ‘G’ and η_c are taken as 1.

The theoretical limit to RMS noise in any frequency is given by the above expression. However, the actual RMS noise level that can be achieved in radio maps is more than this, due to the presence RFI from the local environment.

2.1.1.4 Angular size of a radio core

The angular sizes of compact radio cores can be determined using the AIPS task ‘JMFIT’. It is commonly used to derive the position, peak and integrated flux density and angular size of compact sources. The parameters used are,
 NGAUSS → Enter the number of Gaussians to fit.

NITER → it is $20 \times NGAUSS$

The source area can be specified by TVWIN.

The values of ‘NGAUSS’ and ‘NITER’ should be changed, until the solution converges to some constant value.

2.1.2 Spectral index map

Spectral index maps are prepared from images of the same resolution, which are prepared from data of the same UV coverage. But in GMRT the UV coverage at different frequencies are different. For 325 MHz the UV maximum is $27k\lambda$, and in 610 MHz it is $50k\lambda$. So to prepare spectral index maps between these two frequencies we have to image the 610 MHz data with UVtapper at 27×27 (To make U_{max} and V_{max} equal to $27k\lambda$). Then the map should be convolved to the same resolution as that of the 325 MHz map.

Similarly, the NVSS 1.4 GHz maps are produced with the VLA-D array data of U_{max} and V_{max} equal to $\sim 5k\lambda$. In VLA-D array all the 27 antennas are arranged within the 1km range. To produce spectral index maps with NVSS and GMRT maps, we have imaged the GMRT data with UVtapper 5 5 ($U_{max}=5k\lambda$ and $V_{max}=5k\lambda$). Though the maps produced like this are found to have high background RMS (\approx Three times more than the original maps), the integrated flux density variation was $\approx 10\%$ only from the maps that are prepared without any ‘uvtaper’ value. In GMRT, out of the 30 antennas, 14 are in the central one km region. So, there will be sufficient flux from shorter baselines of GMRT. After this, the GMRT maps are convolved to the same resolution as that of 1.4 GHz NVSS maps. Such radio images are used to produce the spectral index maps.

Following are the steps (AIPS tasks) we have used for it.

1. SUBIM

This task is used to prepare a sub-image of the relevant portion of the sky. This is to be done for both the images. The area can be selected by TVWIN.

2. CONVL

Using this task, we can make the resolution of the high-resolution map to that of the low-resolution map.

GETN \rightarrow catalogue number of high-resolution map.

bmaj \rightarrow FWHM of major axis - Enter the value in low-resolution map

bmin \rightarrow FWHM of minor axis -Enter the value in low-resolution map

opcode ‘Gaus’

It will create a map with extension .CNVL. Now the high-resolution map is converted into a low-resolution that we have specified through the input values of ‘bmaj’ and ‘bmin’.

3. OHGEO

This will make both the sub-images to the same size.

GETN → catalogue number of big image (Usually higher frequency).

GET2N → catalogue number of smaller image (Usually lower frequency).

axref 0

This will make the bigger image to the same size as that of the smaller image. The new map will have an extension .OHGEO.

4. COMB

Here the two images of the same size can be used. Before doing this task, measure the background RMS noise (σ) level in both the maps.

GETN → first image

GET2N → second image

APARM(9) → enter 3σ of the first map

APARM(10) → enter 3σ of the second map

OPCODE 'SPIX'

BPARM(1) → enter σ of the first map

BPARM(2) → enter σ of the second map

BPARM(3) 1 → To get noise map.

This task will produce two maps one with extension .SPIX and the other with extension .SPIXN. The first is spectral index map and the second is the error map.

2.2 IGO data analysis

We obtained the spectra of seven galaxies using IGO, using the IUCAA Faint Object Spectrograph and Camera (IFOSC). IFOSC employs an EEV $2K \times 2K$, thinned, back-illuminated CCD with $13.5\mu\text{m}$ pixels. The spatial sampling scale at the detector is $44\mu\text{m}$ per arcsecond giving a field of view of about 10.5 arcminutes on the side. For all observations we used two IFOSC grisms; grism 7 and grism 8 in combination with a 1.5-arcsec slit. This combination has a wavelength coverage of $3800\text{--}6840\text{ \AA}$ and $5800\text{--}8350\text{ \AA}$ and spectral resolution of 300 km/s and 240 km/s respectively.

We have used the software IRAF for the reduction of astronomical images in pixel array form. A CCD is an electronic detector made of many photosensitive ‘pixels’. When light (photon) falls on these pixels, it will liberate electrons, and the information about the photons is stored as charges in these pixels. To get the image or spectrum of the object to which the CCD is exposed, it should undergo many processes. Following are the processes used in the optical spectroscopic data analysis. (In each task we have mentioned the parameters that are needed to be changed. For others default values are sufficient.)

2.2.1 Bias subtraction and Flatfield deduction

Usually, in CCDs, there will be some initial charge in each of the pixels, even when it is not exposed to light. This should be taken in to account when we make an image of the source. So the first data one has to take in any optical telescope are the bias frames (or zero frames), which gives the readings in each pixel without any exposure. These values to be deducted from each science frame. This is similar to the zero correction in any measurement. Usually, we take many

bias frames and they are combined to form an average bias frame called master bias frame, using the IRAF task `zerocombine` (In the IRAF package `ccdred`).

In any CCD, the response of each pixel to light will not be the same. This pixel to pixel variation to light is taken into account using the process called flat field deduction. For this, we have to expose the CCD to an area of equal illumination. For imaging, we expose the CCD to the evening sky before the stars are just visible or to the morning sky after the stars just disappear. In spectroscopy, we usually use Halogen lamps to take flat frames. We take five to ten flatfield frames and are then combined to form an average flatfield frame through the task ‘`flatcombine`’. This frame is then normalised using the task ‘`Response`’. Here we create a new frame by dividing each pixel of the flatfield frame by the average pixel value. Using this normalised flatfield, we perform the process called flatfield deduction on the science frames.

2.2.2 Spectroscopic data analysis

The bias subtraction and flat field deduction are pre-requisites for both the spectroscopic and photometric data analysis. In spectroscopic observations, we have to study the variation of the source flux with the wavelength of emission. Here, other than the source of interest we have to observe a standard star for flux calibration and some arc-lamp spectrum for the wavelength calibration. We have used He-Ne lamp spectrum for wavelength calibration and standard stars Feige-110 and Hiltner-600 were observed for flux calibration. The CCD pre-processes such as the bias subtraction, and flat field deduction should be done on all these frames. Also, we can remove cosmic rays from all these frames using a task named ‘`crmedian`’. Once all these pre-processes are done on the science frames, the spectrum can be extracted using the task ‘`DOSLIT`’ in IRAF.

In spectroscopic observations, the slit length will be made parallel to the spatial axis (axis 2 in Figure 2.1), and width will be parallel to the dispersion axis (axis 1 in Figure 2.1). So the slit width should be adjusted to accommodate only one target along the width. But more sources can be in different spatial positions of the slit. Figure 2.1 shows how the light from the source is dispersed along axis '1' (wavelength direction) after passing through the grism.

DOSLIT is an IRAF task in the package 'SPECRED'. This task combines the functions and parameters of many tasks to provide a single, complete data reduction path. The aperture selection, wavelength calibration and flux calibration all can be done using this task. Various tasks and the parameters used are all listed below.

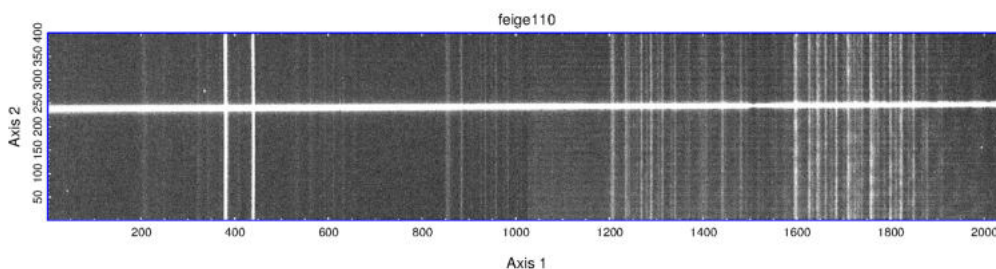


FIGURE 2.1: Feige110 CCD spectrum image. The light from the star is dispersed along axis '1' (wavelength direction, increasing to the right). The spatial direction is vertical.

1. zerocombine

This task is used to combine the bias frames to produce a master bias frame.

input = bias*.fits List of zero level images to combine

(output = Zero.fits) Output zero level name

(combine= average) Type of combine operation

(ccdtype=) CCD image type to combine
(rdnoise= 4) ccclip: CCD readout noise (electrons)

2. flatcombine.

Flatcombine is the task used to combine the flat frames to produce a master flat frame.

input = flat*.fits) List of flat field images to combine
(output = masterflat.fits) Output flat field name
(combine= average) Type of combine operation
(ccdtype=) CCD image type to combine
(process= no) Process images before combining?

3. response

calibrat= masterflat.fits) Longslit calibration images
normaliz= masterflat.fits) Normalization spectrum images
response= Nmasterflat.fits) Response function images- normalised master flat.
(interac= yes) Fit normalization spectrum interactively?
It will create a normalised master flat frame named Nmasterflat.fits.

4. crmedian

Here we can remove cosmic rays from all the science frames. This task detects cosmic rays from pixels deviating by a specified statistical amount from the median at each pixel.

input = Image name.fits) Input image name
output = Outputimage.fits) Output image name

5. ccdproc

This task is used for bias subtraction and flat field deduction from all

science frames.

images = science frame*.fits) List of CCD images to correct

(output =) List of output CCD images

(ccdtype=) CCD image type to correct

(zerocor= yes) Apply zero level correction?

(flatcor= yes) Apply flat field correction?

(zero = Zero.fits) Zero combined frame

(flat = Nmasterflat.fits) normalised master flat frame

All the standard star frames and science frames should go through this process. After `ccdproc`, the images will be saved in the same name itself. All the operations done on the frame can be obtained from the image header.

6. `specred`

(extinct= onedstds\$kpnoextinct.dat) Extinction file

(caldir = onedstds\$spec16redcal/) Standard star calibration directory

(observa= observatory) Observatory of data

(dispaxi= 1) Image axis for 2D/3D images

Here we have to specify the two files, one for extinction correction and the other the standard star directory, which contains the standard star that we have observed. The ‘dispaxi’ means the dispersion axis and, here the dispersion axis is ‘1’ (see Figure 2.1). In some Observatories, the dispersion axis may be ‘2’.

7. `doslit`

objects = targetsource.fits) List of object spectra

(arcs = arc-lamp.fits) List of arc-lamp spectra

(standar= standardstar.fits) List of standard star spectra

(readnoi= 4) Read out noise sigma (photons)

(dispcor= yes) Dispersion correct spectra?
(extcor = yes) Extinction correct spectra?
(fluxcal= yes) Flux calibrate spectra?
(splot = yes) Plot the final spectrum?
(redo = yes) Redo operations if previously done?
(sparams=) Algorithm parameters
Enter ‘:e’ in the line of sparameters. Then edit as follows.
(weights= variance) Extraction weights (none—variance)
(coordli= linelists\$idhenear.dat) Line list
(select = nearest) Selection method for reference spectra

Once you run the task doslit, an IRAF window will open, where a graph is displayed in such a way that the x-axis gives the pixels along the spatial axis (axis ‘2’ in Figure 2.1) and the y-axis represents the flux values. Here we can interactively specify the aperture (stars/galaxy position) and the background region. Once this is done the traces of the object is displayed, and we can interactively modify it. The same thing will be repeated for the standard star also. After that, we can identify the lines in the arc-lamp spectra. Once this is also satisfactorily done, we have to enter the observatory name, standard star name, airmass etc. The task doslit uses the flux values of the standard star and wavelength values of arc lamp lines from the corresponding directories and gives the flux and wavelength calibrated spectrum of the source.

2.2.3 Velocity dispersion

To measure the stellar velocity dispersions of the galaxies, we have fitted a Gaussian to the D1 and D2 absorption lines in the optical spectrum. The FWHM of the combined lines (D1 & D2) is related to the individual FWHM by the relation,

$$FWHM_{D1D2}^2 = FWHM_{D1}^2 + FWHM_{D2}^2.$$

As sodium D1(5890Å) and D2 (5890Å) lines are very close, the $FWHM_{D1} \approx FWHM_{D2}$. So the FWHM of the sodium D1 or D2 line will be,

$$FWHM = \frac{FWHM_{D1D2}}{\sqrt{2}}.$$

In addition to the broadening of the spectral lines due to the motion of the stars around the centre of the galaxy, there may be a contribution from the instrument itself. From the various lines in the arc-lamp spectra, we can measure the $FWHM_{instr}$, due to the instrumental broadening of the lines. So the corrected FWHM will be,

$$FWHM_{corrected} = \sqrt{FWHM^2 - FWHM_{instr}^2}.$$

The instrumental broadening of the lines in the IGO spectra are found to be $\approx 6.2 \text{ \AA}$, and those in the Palomar spectra are found to be $\approx 5 \text{ \AA}$. With this corrected FWHM, we have estimated the stellar velocity dispersion using the equation given below.

$$\sigma = \frac{\sqrt{FWHM^2 - FWHM_{instr}^2}}{2.354 \times (1 + z) \lambda_{rest}} 3 \times 10^5 km s^{-1} \quad (2.1)$$

The stellar velocity dispersion values quoted in the text are obtained through this procedure.

Chapter 3

‘Zwicky’s Nonet’: a compact merging ensemble of nine galaxies and 4C 35.06, a peculiar radio galaxy with precessing radio jets

Galaxy mergers play a pivotal role in the assembly of galaxies in the Universe across cosmic time, and these are most prevalent in high-density regions at the centers of galaxy clusters. The merger dynamics is influenced by various factors such as the size, mass, impact parameter, relative velocity, gas content and the relative inclination of the merging galaxies within the cluster. Merger phenomena occur on different physical scales, which strongly affects the properties of galaxies. Mergers on the galactic scale ($\sim 10 - 100$ kpcs) may result

in ram pressure stripping of gas, the formation of long tidal tails and enhanced star formation, as well as the transformation of the morphology of galaxies. This makes cluster centers fascinating laboratories to study galaxy evolution. The merger of the galaxies is also thought to be a major factor in the growth of black holes and triggering of AGN activity resulting in the occasional powerful relativistic jet ejection, which may transport matter and energy from the interiors to the surrounding ambient medium through various feedback processes. On smallest scales ($\ll \text{pc}$) the final inspiral stage of black hole merger results in powerful gravitational wave emission. On very large scales ($\sim 100 - 1000 \text{ kpc}$) the shocks and turbulence induced into the intracluster medium (ICM) during galaxy or group mergers are believed to inject large amounts of turbulent energy and giving rise to subsequent shock heating of the ICM to X-ray temperatures with disruption of cooling-cores (Roettiger et al., 1996; Paul et al., 2011).

It is observed that centres of rich galaxy clusters are usually dominated by massive, luminous elliptical galaxies known as Brightest cluster galaxies (BCG). Alternatively, there are some cases where extremely massive ($> 10^{12} M_{\odot}$) and bright ellipticals, which are known as the cD galaxies dominate the cluster centers (Tovmassian & Andernach, 2012; Garijo et al., 1997; Kormendy & Djorgovski, 1989). The most prominent property which distinguishes cD galaxies from common giant ellipticals is the presence of a diffuse, faint halo of stellar light surrounding it that extends up to 100s of kpc to Mpc scales, well into the intracluster medium (Oemler, 1976; Tonry, 1987; Garijo et al., 1997; Kormendy & Djorgovski, 1989; Tovmassian & Andernach, 2012; Jordán et al., 2004). Though it is well known that cD galaxies are almost always located at the densest and innermost regions of rich clusters, it is still not clearly understood how these galaxies assemble and evolve in such a special galactic environment, because very few clusters with a cD galaxy in the process of forming have been identified.

It is believed that formation of a cD galaxy may take place via four distinct routes (Garijo et al., 1997; Tovmassian & Andernach, 2012; Jordán et al., 2004); Galactic ‘cannibalism’, tidal stripping, cooling flows and cluster collapse. The presence of multiple nuclei observed in many cD galaxies are strong evidence in favour of galactic cannibalism model (Hausman & Ostriker, 1978) while the tidal stripping theory supports the formation of the halo of cD galaxies (Garijo et al., 1997; Merrifield & Kent, 1991; Jordán et al., 2004; Ostriker & Tremaine, 1975; Ostriker & Hausman, 1977). Cluster cooling flows have been suggested as a possible method by which a cD galaxy acquires mass by accretion of gas and grows, while a small portion of it results in star formation in cluster cores (Cowie & Binney, 1977; Fabian & Nulsen, 1977; Fabian, 1994). Alternatively, another hypothesis on the formation of cD galaxies invokes a rapid merging of galaxies during cluster collapse, suggesting that cD galaxies appear to have formed rapidly at early cosmic times, via hierarchical merging before cluster virialization (Merritt, 1983, 1985; Jordán et al., 2004).

Galaxy interactions and major galaxy mergers remove significant amounts of angular momentum by gravitational torques and drive the gas towards SMBHs, thereby triggering the activity of the central engines (Wilson & Colbert, 1995). As a result, cluster central cD galaxies are more likely to be radio-loud above radio luminosity $10^{24.5} \text{ W Hz}^{-1}$ at 1.4 GHz. Past studies have shown that cD galaxies are almost always radio-loud, and quite often they eject powerful radio jets with clear signatures of feedback of their supermassive black hole on the surrounding gas (Bagchi & Kapahi, 1994; Burns et al., 1981, 1983; Best et al., 2007; McNamara & Nulsen, 2007).

The presence of multiple nuclei are highly probable in cluster center galaxies which evolve through multiple mergers (Volonteri et al., 2003; Kulkarni & Loeb, 2012; Deane et al., 2014). Here the perturbations in the accretion disc due to

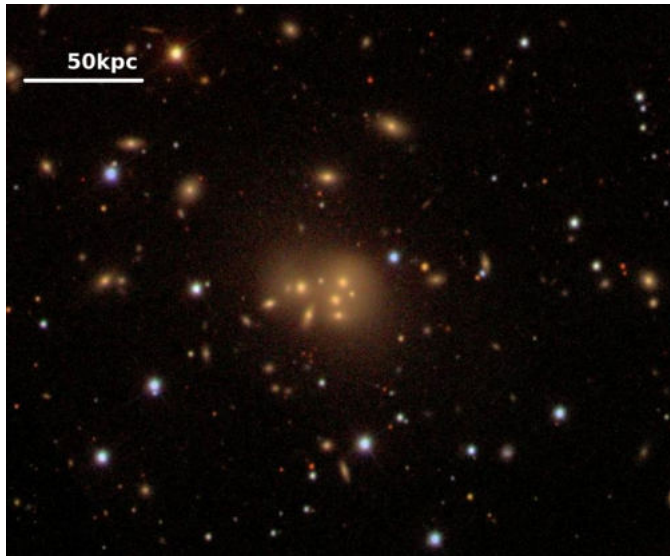


FIGURE 3.1: Colour image of the galaxy cluster Abell 407 taken from the Sloan Digital Sky Survey (SDSS). The central region is host to a striking group of nine close-packed galaxy like condensations (the ‘Zwicky’s Nonet’), embedded within a diffuse stellar halo of intra-cluster light. This system possibly represents an exceptional multiple-nucleus cD galaxy precursor assembling in a rich galaxy cluster environment.

the presence of closely spaced interacting massive black hole pairs may result in the occurrence of distorted radio jets. The inversion symmetry found in ‘S’ or ‘Z’ shaped radio sources is possibly related to the precession of the spinning black hole (Deane et al., 2014; Begelman et al., 1980; Merritt & Ekers, 2002) and the associated tilting/perturbation in the accretion disk (Lu, 1990; Janiuk et al., 2008).

Here, we study the radio and optical properties of the extraordinary radio source 4C 35.06 (B2 0258+35B) located at the center of the rich Abell cluster A 407. The central region of Abell 407 also hosts a remarkably tight ensemble of nine galaxies surrounded by a faint, diffuse stellar halo. In the adopted cosmology

at the redshift $z = 0.047$ implies a linear scale of $0.885 \text{ kpc arcsec}^{-1}$ and a luminosity distance of 200.1 Mpc (Wright, 2006).

TABLE 3.1: Galaxy properties in central region of Abell 407 cluster.

Source ^a	Coordinates (J2000) (from SDSS)	Redshift ^b	SDSS Magnitudes					SDSS Colours		
			<i>u</i>	<i>g</i>	<i>r</i>	<i>i</i>	<i>z</i>	<i>g - r</i>	<i>r - i</i>	<i>i - z</i>
G1 (B)	03h 01m 51.5s +35d 50m 30s	0.0483	18.23	15.84	14.72	14.23	13.84	1.12	0.49	0.39
G2 (A)	03h 01m 51.2s +35d 50m 22s	0.0454	21.09	19.04	18.46	17.95	17.54	0.58	0.51	0.41
G3 (D)	03h 01m 51.8s +35d 50m 20s	0.0471	18.11	16.00	15.00	14.44	13.97	1.00	0.56	0.47
G4 (C)	03h 01m 51.7s +35d 50m 12s	0.0501	20.91	18.81	17.76	17.37	16.90	1.05	0.39	0.47
G5 (F)	03h 01m 51.5s +35d 50m 12s	0.0478	20.02	17.93	16.86	16.31	15.85	1.07	0.55	0.46
G6 (E)	03h 01m 52.4s +35d 50m 29s	0.0444	21.33	19.93	19.11	18.70	18.18	0.82	0.41	0.52
G7 (G)	03h 01m 53.2s +35d 50m 26s	0.0471	18.37	16.34	15.31	14.80	14.39	1.03	0.51	0.41
G8 (H)	03h 01m 53.7s +35d 50m 28s	-	-	-	-	-	-	-	-	-
G9 (I)	03h 01m 54.5s +35d 50m 18s	0.0451	20.27	18.68	17.59	17.23	16.68	1.09	0.36	0.55

^aZwicky's original nomenclature within brackets.

^bSchneider & Gunn (1982)

3.1 ‘Zwicky’s Nonet’: Previous optical, X-ray and radio observations

3.1.1 Optical observations

Abell 407 is a rich galaxy cluster (Bautz Morgan class II) at a redshift of 0.047, listed in the Abell catalogue of galaxy clusters (Abell et al., 1989). In the Uppsala General Catalogue (UGC) this multiple galactic system is confusingly labelled as a single galaxy UGC 2489, with its position coinciding with the brightest cluster member G1 at $03^{\text{h}}01^{\text{m}}51.5^{\text{s}}, +35^{\text{d}}50^{\text{m}}30^{\text{s}}$ (Cotton et al., 1999). The optical image of the central region of this cluster from Sloan Digital Sky Survey (SDSS) shows a complex ensemble of at least nine galaxy like condensations within a region $\sim 1 \text{ arcmin}$ across ($\sim 50 \text{ kpc}$), embedded within a low surface brightness, diffuse stellar halo, reminiscent of a cD galaxy (Figure 3.1)

(Biju et al., 2017). The 2MASS near-IR image of this region is shown in Figure 3.2. The SDSS magnitudes in optical bands with the redshifts, the colours and the Zwicky’s original nomenclature for the nine galaxies are listed in Table 3.1. The $g - r$ colour index of ~ 1 indicates they are passive, early type red galaxies.

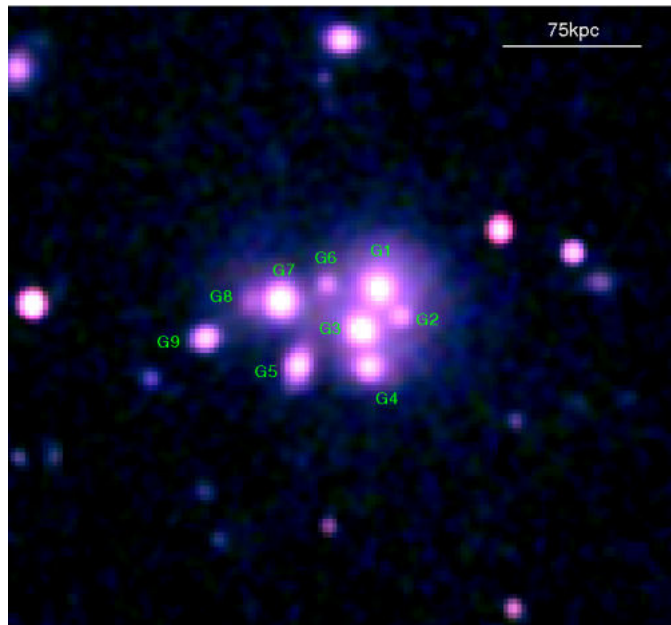


FIGURE 3.2: A pseudo-color near infra-red image of the compact group ‘Zwicky’s Nonet’ obtained by combining the J, H, and K band images available in the 2MASS 6X deep survey. All the nine central galaxies are marked on the image and Table 3.5 showed their magnitudes and derived black hole masses.

This extraordinary galactic configuration (V Zw 311) was first noted by Fritz Zwicky in 1971 (Zwicky & Zwicky, 1971) which was later studied in more detail by Schneider & Gunn (1982) using Palomar 200-inch and Palomar 60-inch telescopes. Schneider & Gunn (1982) described it as the “most nightmarish known multiple-nucleus system” and concluded that this galactic system possibly represents an extremely rare and unique snapshot of a giant cD galaxy in formation. They proposed that the multiple galaxy mergers, assisted by the orbital

decay from dynamical friction in the background of stellar and dark matter halos (Chandrasekhar, 1943) would possibly result in the emergence of a first rank cD galaxy ¹ in about 2 billion years. There were no further investigations undertaken to understand the formation and evolution of this unusual galactic system. Here we propose to name this extraordinary galaxy group of nine galaxies as the ‘Zwicky’s Nonet,’ honouring Fritz Zwicky who discovered this galaxy group. To our knowledge, this is the most compact and rich system of multiple galaxies known till date. Other famous compact groups are the ‘Stephen’s Quintet’ and ‘Seyfert’s Sextet’, and the lesser known ‘Zwicky’s Triplet’ (Arp 103).

The Stephen’s Quintet (Arp 319/ VV228) is a compact group of five galaxies at a redshift of 0.0215, spread over a region of ~ 3 arcmin across, which corresponds to a linear size of ~ 77 kpc (Arp, 1973; Vorontsov-Velyaminov, 1959). The Seyfert’s Sextet (VV 115) is another group of six galaxies in the constellation Serpens at a redshift of 0.0145. These galaxies are spread over a region of ~ 2 arcmin across, which corresponds to a linear size of ~ 18 kpc, and was first observed by Seyfert (1951). The Zwicky’s Triplet(Arp 103) is a small group of three galaxies, which was first identified in 1961 by Zwicky & Humason (1961) and Burbidge & Burbidge (1961). Not much literature is available on this galaxy group.

¹First-ranked galaxies are the brightest galaxies in clusters of galaxies. They usually occupy the central region of the cluster(Thuan & Puschell, 1989). If the cluster has a first rank galaxy with extended light envelope, it can be considered as a cD galaxy (Lugger, 1984). Here as the central region of A 407 is hosting a cD galaxy in formation we used the phrase first rank cD galaxy in formation.

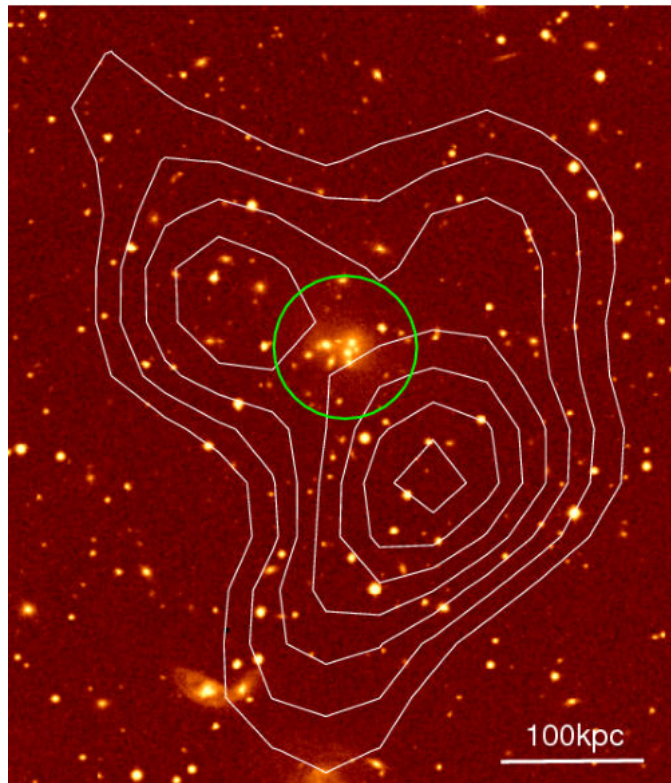


FIGURE 3.3: The DSS r-band image of Abell 407 cluster, with X-ray iso-intensity contours (0.42, 0.55, 0.68, 0.81, 0.94, 1.07, 1.25 sigma) above the background from ROSAT 0.5 - 2.4 keV band data overlaid in white. The green circle has a radius of 1 arcmin around the optical position. The field of view of DSS image is 8 arcmin \times 8 arcmin centered on the brightest galaxy of the group, G1.

3.1.2 Previous X-ray studies

The Abell 407 galaxy cluster is detected in the ROSAT All-Sky Survey (RASS), with estimated X-ray luminosity and temperature in the 0.1-2.4 keV energy band of 5×10^{44} ergs/s and 2.5 keV respectively (Ebeling et al., 1998). In MCXC (Meta Catalogue of X-ray Galaxy Clusters) it is listed as MCXC

J0301.8+3550 (Piffaretti et al., 2011) with estimated cluster mass $M_{500} = 9.16 \times 10^{13} M_{\odot}$, where M_{500} is total mass enclosed inside a radius $R_{500} = 675.4$ kpc. (Here R_{500} is the radius within which the mean over-density of the cluster is 500 times the critical density at the cluster redshift.) We used the archival X-ray data in RASS hard band (0.5 -2.4 keV), and the extracted surface brightness contours are overlaid on SDSS r-band image as shown in Fig. 3.3. The projected separation of optical center and brighter X-ray peak to the south-west is ~ 1.7 arcmin or ~ 90 kpc.

In dynamically active and merging clusters, there is a significant offset between the X-ray emission peaks and the position of BCGs (Rykoff et al., 2008). The dynamical behaviour of galaxies and the intracluster gas are different during cluster mergers. The intracluster gas is highly collisional and will be subjected to intense ram pressure and shock heating. The X-ray peaks at the regions of shock-heated gas can be offset from the optical center. Mann & Ebeling (2012) found that in very extreme cases of active mergers the offset between X-ray peaks and BCGs will be more than 42 kpc. In our case, the offset is 90 kpc, which indicates an extreme merger state of the cluster.

3.1.3 Previous radio observations of 4C 35.06

The central region of galaxy cluster Abell 407 hosts a peculiar radio source 4C 35.06. One of the earliest detections of this source is at 1.4 GHz frequency with the Cambridge one-mile telescope with fairly poor resolution (Riley, 1975). Subsequently, this source has been studied using VLA at two frequencies 1.4 GHz and 5 GHz by Bondi et al. (1993), finding a bi-lobed structure at ~ 5 arcsec² resolution. The total flux density of 4C 35.06 is 728 mJy at 1.4 GHz, with a core flux density of 10 mJy, an eastern lobe of 305 mJy, and a western lobe of 416

mJy. At 5 GHz the total flux density obtained was 170 mJy, with a core flux of 4 mJy, an eastern lobe of 55 mJy and a western lobe of 114 mJy. A 5 GHz Very Long Baseline Array (VLBA) observation at $4.87 \times 2.23 \text{ mas}^2$ resolution detected a compact radio core of 2.6 mJy peak flux (3.5 mJy total) associated with the galaxy G3, which is the second brightest member of the group (Liuzzo et al., 2010). The VLBA scale is only about 3 pc across, while the large-scale radio structure extends over 200 kpc, leaving a vast gap in our understanding of the connection between the compact AGN and larger radio morphology. Moreover, the large-scale jet structure and ultra steep spectrum outer regions of this source were missed in previous high-frequency VLA maps. Using the high resolution (5 arcsec^2 FWHM) and high sensitivity ($70 \mu\text{Jy}/\text{beam rms}$) GMRT observations taken at 610 MHz frequency, Biju et al. (2014) for the first time drew attention to the complete radio structure of an extraordinary helically twisted, kinked jet system powering the radio source 4C 35.06. Shulevski et al. (2015) also studied the radio source at a very low radio frequency of 62 MHz with LOFAR at a broad resolution of $50''$ FWHM. We discuss these observations further, along with our new GMRT observations in the sections below.

3.2 GMRT, IGO and Palomar observations

We have observed 4C 35.06 using GMRT at three frequencies of 610, 235 and 150 MHz. The details of radio observations are given in Table 3.2. For flux and bandpass calibrations 3C 48 was observed at the beginning and end of the observational runs for 10-minutes. The 30-minute scans on target source were alternated by 5-minute scans on the phase calibrator. The same source 3C 48 was observed for phase calibrations also. The data reduction details are explained in chapter 2. At 610, 235 MHz and 150 MHz, rms noise levels of

70 $\mu\text{Jy}/\text{beam}$, 0.90 mJy/beam and 1 mJy/beam were achieved respectively. In Fig. 3.4 the GMRT 610 MHz radio image of 4C 35.06 is shown overlaid on SDSS i-band optical image.

TABLE 3.2: Details of GMRT observations.

Telescope	Observed frequency	Band width	Obs.time	Beam (arc sec)	RMS
GMRT	610MHz	32MHz	9hrs	5.83×4.78	70 $\mu\text{Jy}/\text{b}$
GMRT	235MHz	6MHz	9hrs	20.86×16.68	900 $\mu\text{Jy}/\text{b}$
GMRT	150MHz	16MHz	10hrs	19.87×15.77	1mJy/b
VLA(NVSS) ^a	1.4GHz	100MHz	survey	45×45	400 $\mu\text{Jy}/\text{b}$
VLA(VLSS) ^b	74MHz	1.56 MHz	survey	80×80	100mJy/b

^a (Condon et al., 1998) ^b (Cohen et al., 2007)

We obtained good quality spectra for eight galaxies of ‘Zwicky’s Nonet’. The optical spectroscopic observations of the brighter galaxy members G1, G3, G4, G7 and G9, were taken with IGO 2m telescope and that of fainter galaxies G2, G5 and G6 with the Palomar 200-inch telescope. The IGO observations were on 20-22 November 2011. The aim was to characterize their AGN and star-forming activity, and obtain the central velocity dispersions (σ) and estimate the black hole masses using the well known $M_{BH} - \sigma$ correlation. The Palomar 200-inch observations were carried out on January 23, 2014.

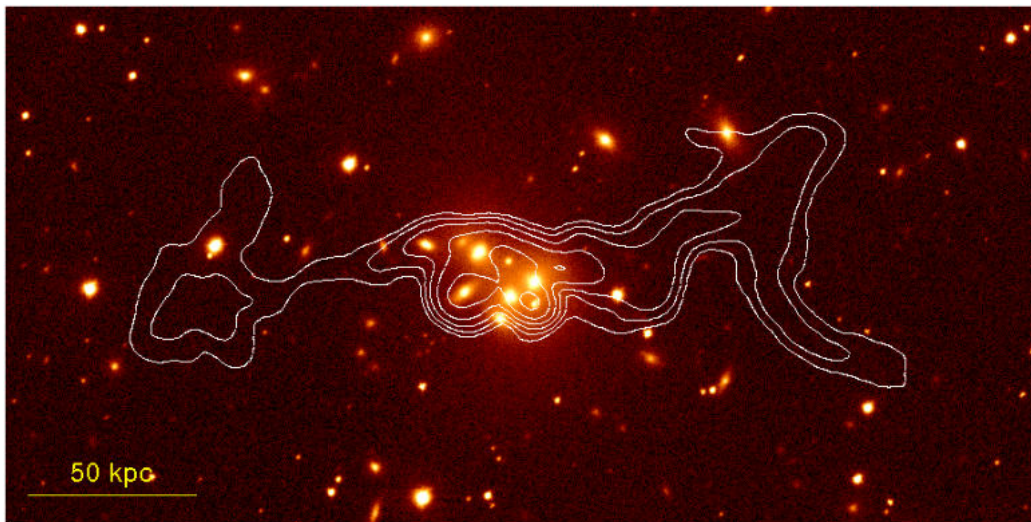


FIGURE 3.4: Optical i-band image of the galaxy cluster Abell 407 taken from the Sloan Digital Sky Survey (SDSS). The white contours show the 610 MHz radio emission morphology of 4C 35.06 as imaged with GMRT at 5 arcsec^2 resolution. Both the radio and optical images have been rotated for convenience.

3.3 Results and Discussion

3.3.1 GMRT images of 4C 35.06 and map parameters

Figure 3.5 upper row presents the GMRT low-frequency radio images at 610, 235 and 150 MHz. The regions marked A1, B1 and A2, B2 represent the features on jets while C denotes the core region. The regions D1 and D2 indicate the outer diffuse structures of the source. The forthcoming sections give a detailed discussion of these regions. We also show the radio images from the NVSS (1420 MHz) and VLA Low-frequency Sky Survey (VLSS, 74 MHz) in the bottom panel of Figure 3.5. The contours of the GMRT 150 MHz image are plotted over the NVSS and VLSS images for size comparison. The highest resolution (5

arcsec²) and currently the deepest yet GMRT image at 610 MHz shows a bright, complex core region and associated double sided twisted/helical jet structure, while the NVSS 1.4 GHz image does not resolve these structures due to its poor resolution (45 arcsec²). The VLA 1.4 GHz image at 15 arcsec² resolution detects the extended, twisting-turning jet structure (Figure 3.5, bottom left panel). The low-frequency 235 and 150 MHz GMRT maps show extended, steep spectrum 'relic' plasma emission features (Figure 3.5, Top Panel) at the extremities of the helically twisted jet structure. These features were also detected in 62 MHz Low-Frequency Array (LOFAR) map (Shulevski et al., 2015).

At 610 MHz the source is found to have a total flux density of 1.7 ± 0.12 Jy. All the fluxes are measured above the 3 sigma limit. The flux densities along the western and eastern jets are found to be 580 mJy and 193 mJy respectively. The angular size of the source is 260 arcsec, which translates to a linear size of ~ 220 kpc. The radio maps at 150 MHz and 235 MHz show extended emission regions beyond the jet structure seen at 610 MHz, which are clear from the contour plots shown in Figure 3.5. The maximum extent of the source at 235 MHz is 430 arcsec, which corresponds to a linear size of ~ 380 kpc. At 150 MHz the source is found to have the largest extended angular size of 460 arcsec and a corresponding linear size of ~ 400 kpc. This implies that the linear extent of the source grows larger with lowering of frequency. At these frequencies, the western jet is brighter than the eastern jet (2.37 Jy and 1.18 Jy at 150 MHz, and 1.72 Jy and 800 mJy at 235 MHz respectively). The total flux densities at 150 MHz and 235 MHz are obtained as 6.0 ± 0.18 Jy and 4.7 ± 0.13 Jy, respectively.

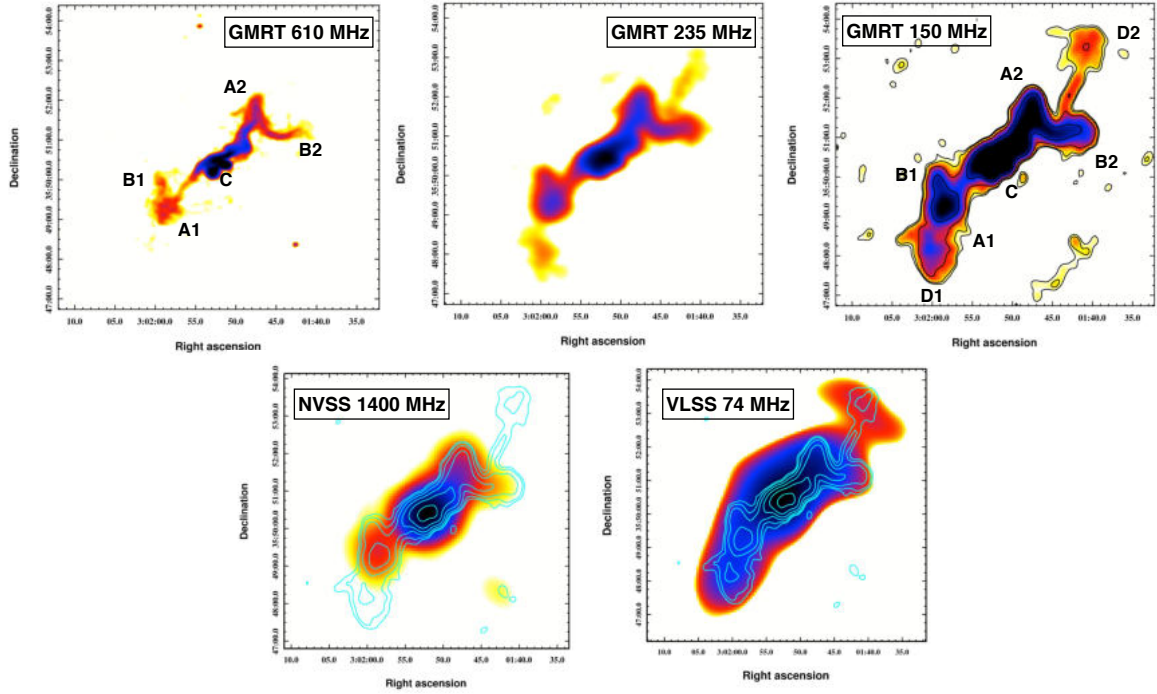


FIGURE 3.5: Colour scale GMRT images (Top Panel, left to right): at 610 MHz at resolution $5.83 \text{ arcsec} \times 4.78 \text{ arcsec}$, 235 MHz at resolution $20.86 \text{ arcsec} \times 16.68 \text{ arcsec}$, and 150 MHz (contour plot) with levels $[1, 2, 4, 8, 16, \dots] \times 4 \text{ mJy/beam}$ and resolution $23.9 \text{ arcsec} \times 19.36 \text{ arcsec}$. Bottom Panel: Colour scale images showing 150 MHz GMRT contours plotted over 1400 MHz NVSS image (Bottom left) and 74 MHz VLSS image (Bottom right).

3.3.2 AGN radio core

GMRT 610 MHz map of 4C 35.06 with 5 arcsec^2 resolution is shown in the left panel of Figure 3.6. Here we can see that there are three radio peaks near the center of the jet, marked with $+$ signs centered on the optical galaxies G2, G5 and G6. Zoomed image of the Zwicky's nonet in SDSS i band, overplotted with 610 MHz radio contours are shown in the right panel of Figure 3.6, with all galaxy

positions marked. From these figures, it is clear that two of the radio peaks (on G2 and G5) are shifted south from the principal jet direction, while that on G6 is on the jet axis. Previous VLBA observation (Liuzzo et al., 2010) has detected a compact AGN core in the galaxy G3 at $03^h01^m51.8^s +35^d50^m19.59^s$ on parsec scale (The position of G3 is marked with + in the left panel of Figure 3.6). But no radio peak is observed on the galaxy G3, in the GMRT radio maps. This suggests that the most probable AGN host galaxy emitting the bipolar jet could be G6 rather than G3, which is shifted southward from the jet direction. The galaxy G6 is very faint both in optical and infrared (Table 3.3 and Table 3.5). From the spectroscopic analysis, we obtained a velocity dispersion of (143 ± 40) km s^{-1} for G6 (from Palomar 200-inch telescope), which yielded a black hole mass of $(0.52 \pm 0.65) \times 10^8 M_\odot$ (using equation 3.5; detailed discussion given in Section 3.3.6; Table 3.4). However, the error margin is high due to the low SNR of the spectrum. Even though it is improbable (but not impossible) for a faint galaxy like G6 to host such a large scale radio jet, it is a possibility that this now faint galaxy has been stripped off the majority of its outer halo stars in multiple tidal encounters while still retaining a massive black hole and a dense stellar core near the centre. This is possibly also reflected in even smaller black hole mass of $(0.15 \pm 0.07) \times 10^8 M_\odot$ derived from its K-band magnitude of $M_K = -21.16$ (using equation 3.6; Table 3.5; detailed discussion given in Section 3.3.6).

In an alternative scenario, Shulevski et al. (2015) have suggested that the rapid movement of radio-loud galaxy G3 and its episodic AGN radio activity is the reason for the observed peculiar radio morphology of 4C 35.06. The large-scale jet morphology is interpreted as due to the earlier phase of activity of G3, which has switched off and then restarted after moving to its current position, resulting in the offset inner double lobed morphology and steep spectrum larger jet structure, similar to dying radio galaxies (Murgia et al., 2011). Thus, at present,

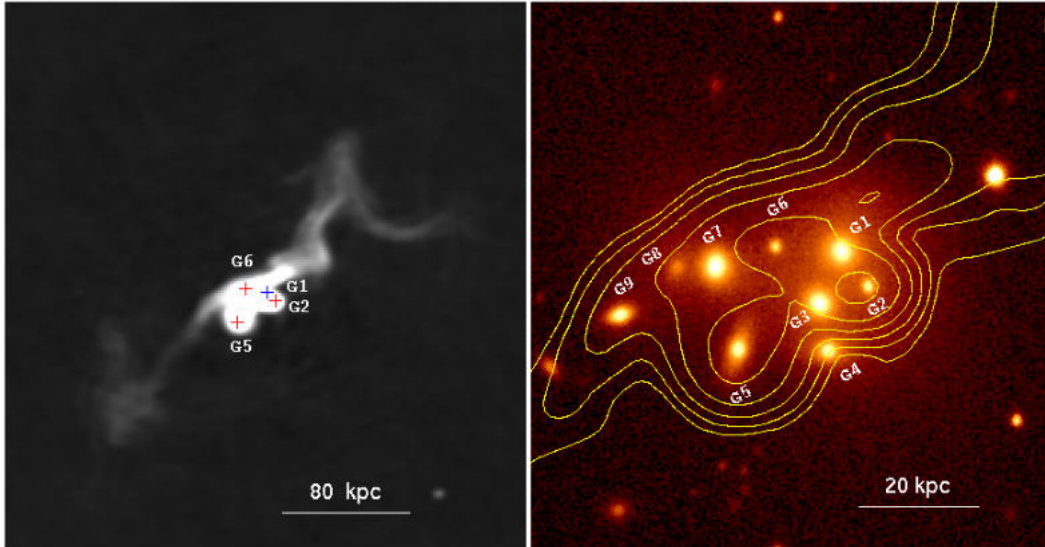


FIGURE 3.6: Left panel: grey scale depiction of 4C 35.06 at 610 MHz imaged with GMRT at 5 arcsec^2 resolution, with the positions of central galaxies G1 (the brightest member), and G2, G5 and G6 (possible radio sources) marked on it. Right panel: the SDSS i band zoomed image of the central region with the 610 MHz radio contours plotted on it. In this figure all the nine galaxies comprising ‘Zwicky’s Nonet’ have been marked. North is up and east is to the left.

we observe an aged FRI-like large-scale structure with an embedded restarted radio source. However, in our GMRT 610 MHz map the optical positions of galaxies G2 and G5 are found to be close to the radio peaks of proposed inner lobes (see Fig.3.6). Moreover, galaxy G6 is observed near the center of symmetry of large-scale bipolar jets, and therefore in our different interpretation, the inner double lobed structure suggested by [Shulevski et al. \(2015\)](#) can be due to the superposition of two radio cores associated with galaxies G2 and G5 in the ‘Zwicky’s Nonet’, while the overall large-scale structure of twisted/helical jets and relic regions (Section 3.3.4) signifies precession of the jet system associated with faint galaxy G6. However, in our radio data, we could not resolve the core

radio emission of G6 from the extended jet. However, much higher resolution radio or X-ray data are still necessary to firmly identify the compact AGN core and the progenitor galaxy of the large-scale jet structure.

3.3.3 Spectral index maps and spectral ageing results

Spectral index studies in radio galaxies are important, as it conveys information about the energy gain and loss processes in the emission regions of the source. Steep (e.g. relic/fossil) spectral index with $\alpha < -1.0$ and power-law/curved spectra (e.g. lobes, jets) with typical, $\alpha = -0.6$ to -0.8 , in the spectrum indicates emission from different regions and epochs of jet activity. Multiple low-frequency observations are best tracers for such activities in the jet (Sirothia et al., 2013).

The broad-band integrated spectra of 4C 35.06 clearly show an overall steep spectrum from 4.9 GHz down to 26 MHz (Fig. 3.7). The new GMRT observations fit with the archival data giving a best fit integrated spectral index of -0.99 ± 0.028 , thereby indicating an overall steep spectral nature of the source, as compared to typical radio galaxies with lobes/jets. Further, the spectral indices for the extended, diffuse outer most regions, D1 and D2 are -1.79 and -2.10 respectively, suggesting their very steep and ultra steep ($\alpha < -2.0$) spectral nature respectively. Furthermore, the extremely steep spectral nature of both D1 and D2 regions suggest that the radio emission originates from an ageing (relic) plasma, possibly from a previous phase of energy injection in the region. These very steep spectral regions were also seen in the recent LOFAR observations at 61 MHz (Shulevski et al., 2015), but much less clearly defined compared to the present higher resolution GMRT data.

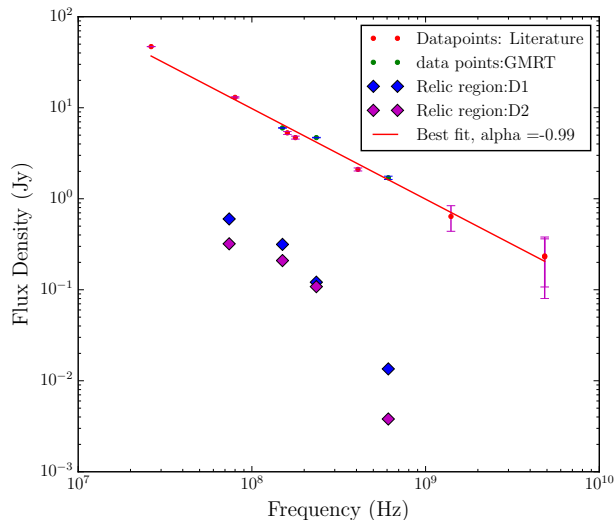


FIGURE 3.7: The integrated spectrum of 4C 35.06. The power law fit is represented by the red line with red points indicating the data from literature and green points from the GMRT observations. The spectra with blue and pink data points represent the diffuse, relic regions D1 and D2 detected in GMRT low-frequency images (Fig. 3.5).

To further clarify the nature of this radio source, we created spectral index maps at low and high frequency ends, using radio maps convolved to the same resolution. The dual frequency spectral index maps produced between 235 vs 610 MHz and 150 vs 235 MHz are shown in Figure 3.8 (top panels respectively) along with the respective error maps (bottom panels). The figures suggest that the emission in the central region of complex core ejecting helical/twisted jets show spectral indices in the range of $\alpha = -0.5$ to -0.9 , whereas the emission from the relic regions dominate at the outer extremities with $\alpha \sim -2.5$ on 235-610 MHz map and $\alpha \sim -3$ on the 150-235 MHz map. Further, the contours of 235-610 MHz map are overlaid on the 150-235 MHz map to highlight the extended relic regions visible only at lowest frequencies. The errors estimated in the central

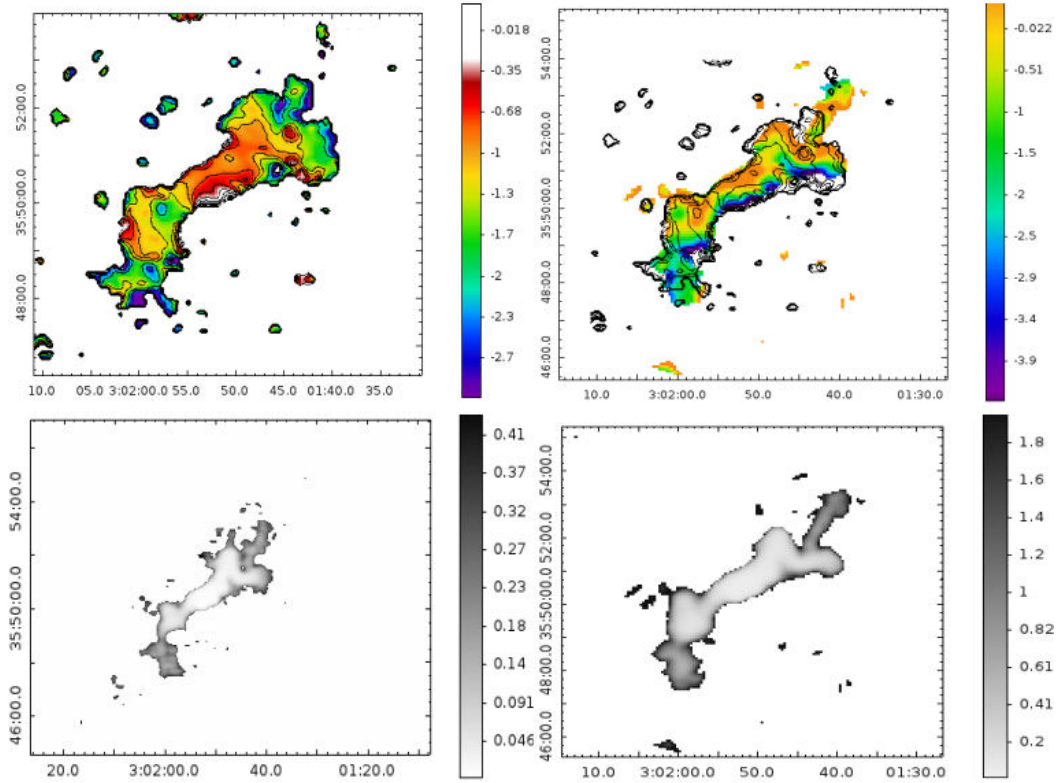


FIGURE 3.8: The spectral index maps obtained from 235 MHz vs 610 MHz and 235 MHz vs 150 MHz GMRT images (Top Panel) using matched resolutions. The contours of 235 vs 610 MHz spectral index map (top left) are shown plotted over the 235 vs 150 MHz map (top right) for reference. Bottom panel shows the error estimates in these maps.

region are much lower than that near the edge, as the diffuse relic regions are fainter and not detected at the same size for the three frequencies. The central region shows flat spectrum, possibly due to the superposition of emission from a few radio emitting galaxies, which become steeper on moving away from the center, up to the outer most extremities of the jet. This indicates that there is no fresh injection of accelerated particles into the relic regions, and hence the extreme steepness of the spectra therein.

The spectral index represents a powerful tool to study the properties of the relativistic electrons and the magnetic field in which they radiate and also to investigate the connection between the electron energy and the ICM. We have estimated the radiative age of the radio plasma by determining the spectral breaks (or slope change) in the radio spectra of the outer most regions marked D1 and D2. The Figure 3.9 top panel shows the integrated radio spectrum of the region D1 and the bottom panel shows that of the region D2. The spectra are fitted with second-order polynomials and tangents are drawn to the curves at frequencies 610 MHz and 150 MHz. The intersection point of these tangents is taken as the break frequency ν_b . We obtained very close values for the break frequencies; for the D1 region $\nu_b = 308$ MHz and the D2 region, we calculate $\nu_b = 302$ MHz (Figure 3.9). Beyond the spectral breaks, a sharp steepening or possible cut-off in the spectra is suggested, which is consistent with the scenario of radio emission from a rapidly cooling electron population.

The electron spectral age t_{sp} (cooling time scale) of the source is then estimated from the synchrotron radio spectrum using the equation given by (Murgia et al., 2011)

$$t_{sp} = 1.59 \times 10^9 \left[\frac{B^{1/2}}{[B^2 + B_{IC}^2] [\nu_b(1+z)]^{1/2}} \right] yrs \quad (3.1)$$

This formula is obtained for a uniform magnetic field, neglecting the expansion losses over the radiative age. Here B is the magnetic field in μG , z is the redshift, $B_{IC} = 3.25(1+z)^2 \mu\text{G}$ is the inverse Compton equivalent magnetic field, and ν_b is the cooling break frequency in GHz. For $\nu_b = 0.3$ GHz, as applicable in relic plasma regions D1 and D2, and magnetic field range $B = 1 - 10 \mu\text{G}$, the electron spectral age is obtained to be $t_{sp} = (2.11 - 0.79) \times 10^8$ y (using equation

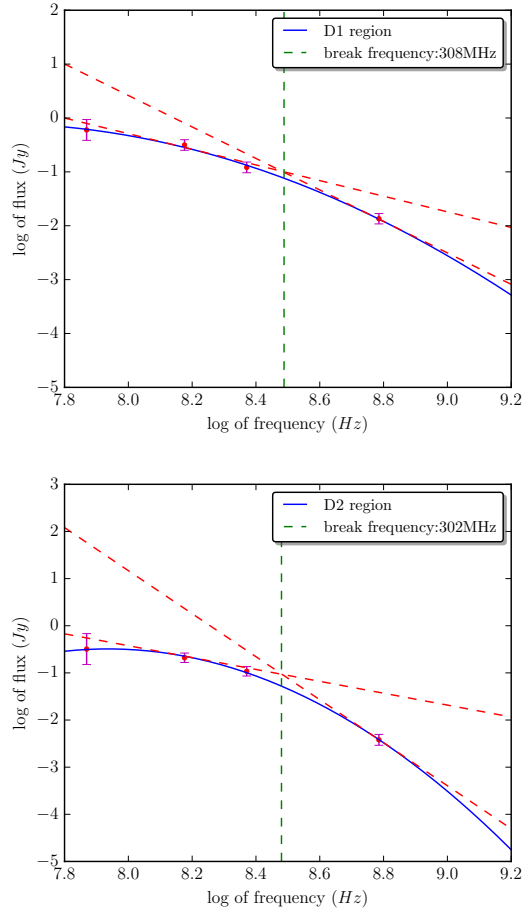


FIGURE 3.9: Top panel: The second order polynomial spectral fit (blue line) for the outer most region D1. The break frequency (green dotted line) is obtained as 308 MHz. Bottom panel: The second order polynomial fit (blue line) for the outermost region D2. The break frequency obtained here is 302 MHz (green dotted line). In both the regions, the flux values are taken at frequencies 610, 235, 150 (GMRT) and 74 MHz (VLSS). The dashed red lines represent the tangents drawn at higher (610 MHz) and lower frequency (150 MHz) ends of spectra, and the vertical dashed green line at the intersection point denotes the estimated break frequency.

3.1), which can be taken as the elapsed time since the last injection of relativistic particles in the emission regions.

In the above analysis, while estimating the spectral age, we assumed a magnetic field between 1 - 10 μG , which is the usual value of magnetic field associated with radio galaxies with relic regions. The exact estimation of the magnetic field is a very tedious process. The total energy of a synchrotron source is the sum of the energies associated with the relativistic particles- electrons and heavier particles, mainly protons- and the magnetic field. So the total energy can be written as

$$U_{tot} = U_p + U_B$$

$$i.e. U_{tot} = U_{electron} + U_{proton} + U_B.$$

At the minimum energy conditions, the energy associated with magnetic field and particles will be almost the same. In this case, $U_p = U_B$. The ratio of the energy associated with protons to that of electrons is $\frac{U_{proton}}{U_{electron}} = k$. We cannot exactly determine the value of k. From theoretical considerations, its value is taken as between 1 to 100 (Govoni & Feretti, 2004).

Assuming minimum energy condition, we calculate the energy density and magnetic field in the regions A1, A2 and D1, D2. The minimum energy density u_{min} is given by (Govoni & Feretti, 2004):

$$u_{min} = \xi(\alpha, \nu_1, \nu_2)(1 + k)^{4/7}(\nu_o)^{4\alpha/7}(1 + z)^{(12+4\alpha)/7}(I_o/d)^{4/7} \quad (3.2)$$

where α is the spectral index; ν_1 and ν_2 are lower and higher limits of frequency; ν_o is the frequency at which surface brightness I_o is measured; and function $\xi(\alpha, \nu_1, \nu_2)$ is tabulated in Govoni & Feretti (2004). $\nu_1 = 10$ MHz, $\nu_2 = 10$ GHz, $\nu_o = 150$ MHz and $z = 0.047$.

TABLE 3.3: Equipartition magnetic field B_{eq} for different regions of the radio source. Here k is the ratio of energy in relativistic protons to that in electrons and α is the spectral index.

Regions	$B_{eq}(\mu G)$		α
	$k=1$	$k=100$	
A1	5.63	17.25	1.5
A2	5.51	16.92	1.5
D1	5.58	17.12	2
D2	4.74	14.54	2

The magnetic field then can be expressed by :

$$B_{eq} = \left(\frac{24\pi}{7} u_{min}\right)^{1/2} \quad (3.3)$$

The magnetic field values calculated for different regions are given in Table 3.3. In fossil/relic regions D1 and D2, the mean $B_{eq} \sim 16 \mu G$, for $k = 100$ (equation 3.3). Using this value of magnetic field, the spectral age of electrons comes out to be 1.1×10^7 y (equation 3.1), suggesting a relatively short radiative lifetime. For $k = 1$ the spectral ages of D1 and D2 turn out to be 7.5×10^7 y, for mean $B_{eq} \sim 5 \mu G$ (equation 3.3).

3.3.4 Twists and kinks in the jet: Dynamical signatures of a perturbed AGN?

Due to the excellent dynamic range and resolution capabilities of GMRT at low frequencies, the radio morphology of the source 4C 35.06 could be imaged

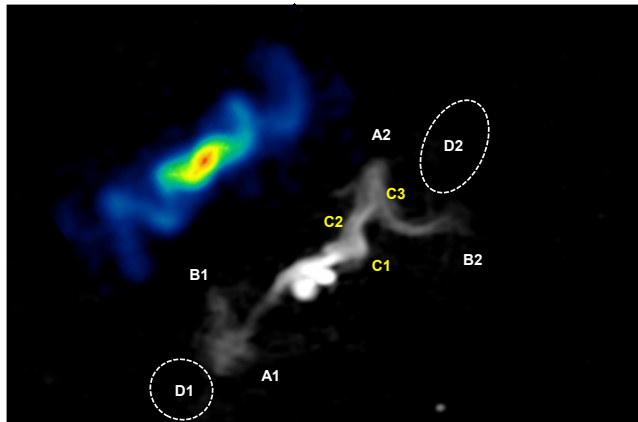


FIGURE 3.10: The high resolution grey scale image of the source 4C 35.06 at 610 MHz (GMRT) showing the twisted, helical jet structure. Different regions of the source are marked and the extensions D1 and D2 observed at lower frequencies 235 MHz and, 150 MHz are indicated with dotted lines. The colour image shows, for comparison, the cork-screw shaped precessing jets observed in galactic XRB ‘microquasar’ SS433, which is the total intensity image at 4.85 GHz observed with the VLA in A configuration (Blundell & Bowler, 2004). Note the linear size of SS 433 jet system is only 0.26 pc while that of 4C 35.06 at 610 MHz is 230 kpc.

up to 400 kpc from the center. We discuss here many interesting, faint features which were not observed in the previous radio images. This has provided much insight into the possible dynamics of the central-engine as well as the origin of its unusual jet structure. The GMRT map at 610 MHz reveals a striking, helically twisted (and kinked) jet morphology, first mentioned in Biju et al. (2014), and suggested by Shulevski et al. (2015) using low-resolution LOFAR data at 62 MHz.

From the large-scale jet structure shown in GMRT 610 MHz maps (Fig. 3.6 and Fig. 3.5), one observes that the bipolar jet twists helically with inversion symmetry, on either side of the core C at the points marked A1 and A2 in Fig. 3.5

and Fig. 3.10. Moreover, the North-Western (N-W) arm of the jet is observed to be brighter, bending into a prominent loop/arc from A2 to the point B2. A similar feature from A1 to B1 is seen in the South- East (S-E) arm as well, but relatively fainter and diffuse compared to the N-W counterpart. This difference appears to be due to projection effects making western loop more prominent on the sky plane compared to the eastern one, which is possibly oriented more along the line of sight away from the observer.

The GMRT images at 235 MHz and 150 MHz show diffuse extended emission regions farther beyond those seen at 610 MHz, the positions of which are marked as D1 and D2 in Fig. 3.5 and Fig. 3.10. In both the frequencies, region D2 in the western arm shows further bending in the jet from B2, with possibly an added cycle of a helical structure (refer Fig. 3.5; top panel). In the 150 MHz map, the extension D2 is observed to be capped by a ‘knot’ or a ‘mushroom’ like feature at the end. The symmetric counterpart of this knot/mushroom could be the feature D1 in the S-E arm but again seen in projection along the line of sight. Alternatively, the mushroom structure could be a terminal radio lobe at the end of a jet associated with another AGN in the system, not yet identified.

The extremely steep high-frequency radio spectra of the mushroom feature at D2 (and also D1), located 200 kpc from the centre, indicate significant energy losses, thus suggesting an absence of freshly injected particles. One possibility is that are buoyant non-thermal plasma bubbles rising into the hot intra-cluster medium inflated by the radio jet in the past, as observed around some BCG/cD galaxies in several clusters or groups (Bagchi et al., 2009; David et al., 2009; McNamara & Nulsen, 2012). Future observations at lower frequencies with enhanced resolution are needed to check whether more of the helical jet cycles and associated fading radio structures can be traced further out from regions D1 and D2. In addition to these interesting features, one can see a few sharp kinks or

steps in the western arm of the jet at points marked C1, C2 and C3 (Fig. 3.10). In the eastern side of the jet, these kinks/steps are not clearly visible, possibly due to the projection effects or maybe because they are absent on this side. In our present work, lacking detailed modelling, it is difficult to decipher what these kinks in the jet flow represent physically.

The deciphering of the radio morphology of jet structure gains added impetus when compared with a precessing radio jet structure observed in the well known galactic ‘microquasar’ SS 433. Figure 3.10 shows the radio image of SS433 at 4.8 GHz (Blundell & Bowler, 2004) in colour, above the grey scale image of 4C 35.06. SS 433 is an X-ray binary (XRB) system in the center of supernova remnant W50 consisting of a stellar-mass black hole or neutron star accreting matter from an A-type super-giant donor star. The most unusual aspect of this object, modelled through radial velocity measurements of ‘shifting’ H_α lines and high-resolution radio imaging, is that the accretion disk around the compact object precesses with a regular period of ~ 164 days (Milgrom, 1979; Abell & Margon, 1979). Consequently, the axis of the jet-ejection-nozzle also precesses with the same period and the ejected radio plasma traces out a dynamically changing ‘cork-screw’ pattern on the sky (see Figure 3.10 and Blundell & Bowler (2004)). The kinematic modelling also reveals jet bulk Lorentz factor $\gamma = 1.035$ ($v = 0.26c$), precession cone half angle ~ 20 deg and the central axis of rotational cone inclined by ~ 79 deg from the line of sight. It is noticeable that large-scale jet structure in 4C 35.06 is analogous to that of SS 433 if we ignore the kinks (C1, C2 and C3) for the time being. Here the loop portions A2 to B2 and A1 to B1 are suggestive of the cork-screw pattern as a result of the continuous change of the jet axis due to the possible precessing motion of jet-ejection-nozzle coupled to the accretion disk. Further, no flat spectrum terminal hotspots are found in

the jet extremities of 4C 35.06, which is another indication for the continuous shifting of the jet direction, instead of a linear propagation.

Even though the jet as a whole precesses, the relativistic fluid elements in the jet continue to follow a radial (ballistic) trajectory. In contrast to a static case, the matter in a precessing jet interacts not only with the surrounding medium when it reaches the jet head, but also all along its path. As a result, the farther away from the accelerating source a fluid element of the jet is, the more decelerated it is and also fades out faster. The very steep spectral indices of regions D1 and D2 located at the extremities of the jet might indicate such energy losses in adiabatic expansion and radiative processes since the last injection of fresh particles, due to the change in the jet axis in precessional motion, analogous to spectral steepening observed along the jets in SS 433 (Bell et al., 2011).

The GMRT images also reveal that only the outer extremities of the jets show the precession signature. Thus it may be indicating an earlier stage of the precession of the jet, which has ended with the stabilization of the accretion disk in alignment with the black hole spin (McKinney et al., 2013). The precession of radio jets may be due to two mechanisms. First, due to the presence of a binary black hole system (Begelman et al., 1980; Merritt & Ekers, 2002; Deane et al., 2014), where the accretion disk of the AGN can be precessed by the torque exerted by the companion black hole, leading to jet precession. Second, due to the Lense-Thirring frame dragging effect (Bardeen & Petterson, 1975).

In Bardeen-Peterson model, if the angular momentum vector of the accretion disk becomes misaligned with that of a fast-spinning Kerr black hole, say due to a merger-induced strong perturbation in accretion flow, the black hole will try to frame drag the inner accretion disk in alignment with its spin vector. This will lead to the precession of the accretion disk, and the radio jets launched orthogonal

to it (McKinney et al., 2013). If this is the reason for the helically twisted jets in 4C 35.06, an interesting corollary is that the accreting supermassive black hole must be spinning. Moreover, the observed close resemblance of the morphology of 4C 35.06 with the precessing relativistic jet system of X-ray binary SS 433 supports the fundamental paradigm, that, in spite of a vast difference in involved black hole masses, length and time scales, almost all relativistic disk-jet coupled phenomena happen in a scale-invariant manner in radio-loud AGNs and the galactic microquasars.

3.3.5 Interaction of jet system with the ambient intra-cluster medium

In section 3.3.1 we saw that the flux density of the western arm of the jet is nearly double that of the eastern arm. Depending on the inclination of the jet direction with our line of sight, the precession cone angle and the jet bulk velocity, the projected radio morphology and brightness can appear to be quite different on the approaching and receding sides, as shown by Gower et al. (1982) in numerical simulation of relativistic effects in precessing jets. The differences in the eastern and western arms of the observed jet morphology can possibly be attributed due to this.

Moreover, in Figure 3.11 the GMRT 150 MHz radio image of 4C 35.06 is shown superposed on the ROSAT X-ray map in 0.5 - 2.4 keV band. In section 3.1.2 an offset between the X-ray peak and the position of the BCG is explained as a consequence of cluster merger (Mann & Ebeling, 2012). In figure 3.11, it can be seen that the jet is advancing in a direction of lower ambient gas density. In radio sources, the X-ray surface brightness along the jets and the lobes are found to be very small, due to the uplifting and displacing of the thermal gas from the

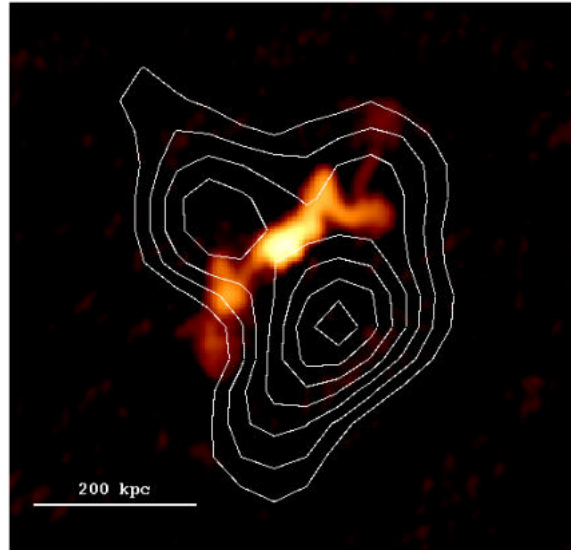


FIGURE 3.11: GMRT 150 MHz radio image of 4C 35.06 is superposed on the ROSAT 0.5 - 2.4 keV band smoothed X-ray data shown in contours.

jet flow direction (Carilli et al., 1994). Here it is observed that the behaviour of the jet system in 4C 35.06 is similar. Such radio mode feedback effect could be analogous to the distorted, extended lobes of supernova remnant W50 (the ‘Manatee’ nebula), apparently shaped by the interaction of powerful jets from the central-engine in SS 433 with the ambient ISM (Dubner et al., 1998). We need much deeper X-ray observations of the A407 cluster to investigate the AGN feedback signatures better.

Observationally, kinetic power of a jet (\bar{Q}) is a key descriptor of the state of an accreting SMBH system; its mass, spin and the magnetic field of the accretion disk. Despite a wealth of observations the exact mechanism of jet launching is still unclear in radio-loud galaxies (Bagchi et al., 2014). One of the most promising and widely used models is the Blandford-Znajek (BZ) mechanism that extracts much of the rotational energy of the BH and the orbital energy of the accretion

flow into an intense, Poynting flux dominated electromagnetic jet (Blandford & Znajek, 1977). In the BZ process, the jet launching requires a massive, spinning Kerr BH, and an accretion disk threaded with strong poloidal magnetic field lines advected near the hole's outer horizon at $R_H = (GM_{\text{BH}}/c^2)[1 + (1 - a^2)]^{1/2}$. In the classic BZ process the electromagnetic luminosity of jet \bar{Q} scales with BH properties as

$$\bar{Q}_{44} \approx 0.2 M_8^2 a^2 B_4^2, \quad (3.4)$$

where, $\bar{Q}_{44} = \bar{Q}/10^{44} \text{ erg s}^{-1}$, the BH mass $M_8 = M_{\text{BH}}/10^8 M_\odot$ and the poloidal magnetic field $B_4 = B/10^4 \text{ Gauss}$ and the dimensionless spin parameter is $a = cJ_{\text{BH}}/GM_{\text{BH}}^2$ for BH's angular momentum is J_{BH} (Blandford & Znajek, 1977; MacDonald & Thorne, 1982a; Tchekhovskoy et al., 2010). Thus, the jet power depends strongly on the BH mass, spin and the magnetic flux at the horizon. This prediction is confirmed by numerical general relativistic magneto-hydrodynamic (GRMHD) simulations which show that the efficiency of conversion of accretion luminosity to the jet (including coronal wind) luminosity (η) could be as high as $\eta = (\bar{Q}/\dot{M}c^2) \sim 30 - 140\%$ for spin $a = 0.5 - 0.99$, if the magnetized accretion flow manages to accumulate (via advection and turbulent amplification) large magnetic flux near the black hole's horizon (Tchekhovskoy et al., 2010; Penna et al., 2013). Similar results have been found (Hawley & Krolik, 2006) which demonstrate that the electromagnetic extraction of spin energy of a Kerr black hole is very much feasible.

Correlation of low-frequency ($\nu \sim 150 \text{ MHz}$) radiative power of radio sources against their jet power shows that the radio luminosity of the jet constitutes only a small fraction ($< 1\%$) of the total kinetic power (Punsly, 2005; Daly et al., 2012). Here we use the low-frequency radio flux, which usually originates

in diffuse, optically thin plasma (diffuse lobes) moving at low velocities, thus the relativistic beaming effects are negligible. Using GMRT 150 MHz radio flux density of 6.0 ± 0.18 Jy, the time-averaged kinetic power of jets in 4C 35.06 is $\bar{Q} \approx 3 \times 10^{43} \text{ erg s}^{-1}$ (Punsly, 2005). We have not corrected for the (unknown) loss of energy in the outer radio lobes and thus \bar{Q} is likely to be a lower limit. This power is below the transition value of $5.0 \times 10^{43} \text{ erg s}^{-1}$ between FR I and II classes, but if the jet continues to operate between $10^7 - 10^8$ yr, the injected mechanical energy is $\sim 10^{58} - 10^{59}$ erg; large enough to strongly affect or even quench any cooling flow, and to drive large-scale outflows that redistribute and heat the gas on cluster-wide scales. If we further assume this jet power is derived from accretion flow onto a black hole at the rate \dot{M} and $\bar{Q} \sim 0.1 \dot{M} c^2$, we obtain $\dot{M} \sim 5.3 \times 10^{-3} M_{\odot} \text{ y}^{-1}$. This number is only representative, but it suggests accretion at sub-Eddington rate $\lambda = \bar{Q}/L_{\text{edd}} = 0.0024 \times (10^8/M_{\text{BH}})$, where L_{edd} is Eddington luminosity and M_{BH} is mass of black hole. This low accretion rate signifies a radiatively inefficient accretion flow (RIAF) and a low luminosity active galactic nuclei (so-called LLAGN or LINER), which is also confirmed by the optical spectra of the central galaxies in this galaxy group (refer section 3.3.6).

Even though the symmetric helical pattern observed in the jet structure might be explained with precession model, there are some small-scale asymmetries like the presence of kinks or steps C1, C2 and C3 in the western arm that pose a challenge. The precession model alone may be insufficient to explain these features. Usually while studying the jet morphology the effect of surrounding medium also has to be taken in to account, especially when the system is in a dense environment (like 4C 35.06). However, it is highly unlikely that the environment interacts with the jet system to produce large-scale symmetric features like A1-B1 and A2-B2, as this would require inhomogeneities to be placed

symmetrically at large-scales, which is very improbable. Therefore the smaller scale asymmetries like C1, C2, C3 could be due to the inhomogeneities in the surrounding external medium causing instabilities in jet flow on one side.

It is already known that the very close SMBH pairs are capable of introducing a rotationally symmetric helical modulation or precession on the structure of large-scale radio jets (Begelman et al., 1980). With precessing jet models, it is indeed possible to fit highly complex image maps of many extended radio sources (Gower et al., 1982). Therefore systems hosting helically modulated symmetric jets are the most promising sites of close black hole systems (triple or binary)(Deane et al., 2014; Begelman et al., 1980). Figure 3.2 shows the near-IR image of the central region of the ‘Zwicky’s Nonet’ in Abell 407 where nine galaxies are embedded in a compact region. It is observed that seven galaxy pairs are separated by distances less than 10 kpc in projection. They appear fairly close not only in projection but their redshift values are also close with mean $\bar{z} = 0.0469$ and standard deviation $\sigma_z = 0.00176$, or $v \sim 520 \text{ km s}^{-1}$. The number of binary or triple black hole systems discovered with projected separations less than 10 kpc are very few due to observational constraints (Deane et al., 2014). In the present dense system of nine galaxies packed within a radius of only 25 kpc, the smallest projected separation between galaxy pair combinations is observed to be about 5 kpc (between G7 and G8). So the closeness of the galactic members and the rotationally symmetric helically modulated large-scale jet structure together suggests the importance of this galaxy group for the search of multiple supermassive black hole systems and their electromagnetic merger signatures.

In 4C 35.06, a slow conical precession of jet axis due to gravitational perturbation effects is very likely, as it occurs in the extremely dense central region

of a cD galaxy under assembly. In such an unusual galactic environment, orbital decay assisted by dynamical friction causes the central binary black holes of galaxies to merge. While, gravitational torque in the binary phase may cause the accretion disk of AGN to precess (Katz, 1997), resulting in a helical jet which projected on to sky plane may give rise to the observed morphology. We note that C-shaped twisted paired jet system in radio source 3C 75 in Abell 400 cluster is indeed ejected from a binary black hole pair separated by only 7 kpc (Owen et al., 1985). Both the jets in 3C 75 also show prominent kinks or wiggled structures which have been modelled as due to the translatory and orbital motion of the bound binary black hole pair (Yokosawa & Inoue, 1985). As mentioned above, in 4C 35.05 we can find similar kinks at points C1, C2 and C3 in the western arm of the jet, which could arise from a binary orbiting jet system, where a black hole with radio jets is orbiting another one at high speed and with large orbital eccentricity. It is also necessary to investigate with high-resolution imaging whether a pair of jet systems are entwined in this radio source, analogous to 3C 75.

3.3.6 Optical spectroscopic results: AGN signature and black hole mass estimation

In the spectroscopic studies of the galaxies in the central region of Abell 407, Schneider & Gunn (1982) have measured the redshifts and stellar velocity dispersions (σ) for a few of the galaxies, covering a wavelength range from 3700Å to 5250Å. They could not obtain σ for any of the nine core galaxies. In our present study, we have obtained decent SNR spectra over the wavelength range of 3800Å to 8500Å for eight out of the nine galaxies comprising ‘Zwicky’s Nonet’ (Figure 3.12 and 3.13). However, attempt to obtain a fair spectrum for galaxy G8 failed due to it being very faint. Our main aim was to

search for any AGN signatures or star-forming activity in the optical spectra of these central galaxies and estimate their black hole masses from the stellar velocity dispersion of the central bulge component. The most commonly observed AGN lines are those of Ly_α (1216Å), $CIII$ (1909Å), CIV (1549Å), $MgII$ (2798Å), $OIII$ (4363Å, 4959Å, 5007Å), and the hydrogen Balmer series (Kellermann & Owen, 1988). The star formation rate can be estimated if there exist H_α or OII lines (Argence & Lamareille, 2009; Kennicutt, 1998). In none of these eight galaxies we could detect any major emission lines related to AGN or star-forming activity, and it is observed that the spectra of eight galaxies resemble that of passive, early type red ellipticals (refer Figure 3.12 and 3.13). AGNs with $H\alpha$ luminosity smaller than 10^{40} erg s⁻¹ and weak emission lines are classified as low-luminosity active galactic nuclei (LLAGN) type (Ho et al., 1997). Accordingly here the AGN can be classified as an LLAGN. We note this is not unusual as optical emission lines are found to be absent in many AGN showing radio emission and large-scale radio jets. Also in many cases, it has been observed that FRI radio sources in galaxy clusters are hosted by galaxies showing very weak or no optical emission lines (Zirbel & Baum, 1995; Hine & Longair, 1979; Best & Heckman, 2012).

The nuclear emission lines of a galaxy better reflect its internal properties such as the mass and accretion rate of the SMBH, or the physical conditions prevailing in the accretion disk (Kauffmann et al., 2008). Accordingly, radio galaxies are classified into two groups based on the emission line properties; viz. the low excitation and high excitation radio galaxies (LERGs and HERGs). The spectra in Figure 3.12 and 3.13 show that all the suspected radio-loud galaxies (G2, G3, G5 and G6) belong to the low excitation class (Lin et al., 2010; Hardcastle et al., 2006; Laing et al., 1994). Quite frequently LERGs are found to be hosted by central galaxies of groups or clusters having extended cD like light profiles

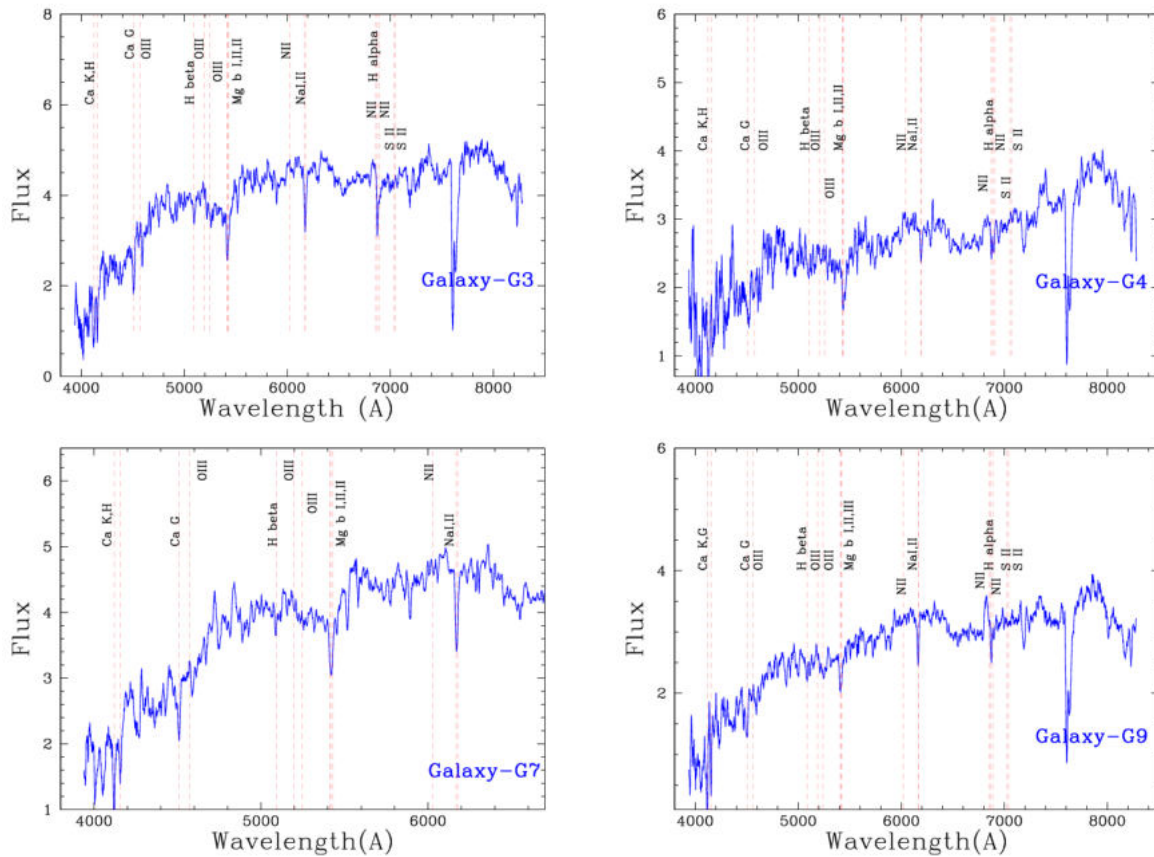


FIGURE 3.13: The optical spectra of galaxies G3, G4, G7 and G9 all taken using the 2-meter Telescope at IUCAA Girawali Observatory. Flux scale in the y-axis is $\times 10^{-16}$ ergs cm^{-2} s^{-1} \AA^{-1} .

(Best & Heckman, 2012), similar to what we see in ‘Zwicky’s Nonet’, a putative precursor of a cD galaxy.

Once the existence of SMBHs was established with dynamical evidence, researchers had been searching for the relation between the properties of the BH with that of the host galaxies. The first such attempt was made by Kormendy & Richstone (1995) to find a relation between the black hole mass and the bulge

luminosity of the host galaxy. Later on, in 2000 two papers were published investigating the connection between BH mass and the stellar velocity dispersion (σ) of the host galaxies. Using a sample of 10 galaxies with known BH mass [Ferrarese & Merritt \(2000\)](#) obtained a best fit linear relation between BH mass and σ as

$$\log(M_{BH}) = 4.8(\pm 0.54)\log(\sigma) - 2.9 \pm (1.3)$$

In the same year itself, [Gebhardt et al. \(2000\)](#) obtained a similar relation from a sample of 26 galaxies with known BH mass and σ . The relation obtained by [Gebhardt et al. \(2000\)](#) was

$$M_{BH} = 1.2(\pm 0.2) \times 10^8 \left(\frac{\sigma}{200 \text{ km s}^{-1}} \right)^{3.75 \pm 0.3} M_{\odot}.$$

With the increase in the sample of galaxies with known black hole masses, these relations were modified many times ([Gültekin et al., 2009a](#); [Merritt & Ferrarese, 2001](#); [Nelson, 2000](#); [Tremaine et al., 2002](#); [Marconi & Hunt, 2003a](#)). Now the general expression which connects the mass of the central black hole M_{BH} to the galaxy's bulge stellar velocity dispersion is given by

$$\log_{10} \left(\frac{M_{BH}}{M_{\odot}} \right) = \alpha + \beta \log_{10} \left(\frac{\sigma}{200 \text{ km s}^{-1}} \right) \quad (3.5)$$

where σ is expressed in km s^{-1} . Here we have used $\alpha = 8.38$ and $\beta = 4.53$ as derived in [McConnell et al. \(2011\)](#). The SMBH masses estimated are tabulated in Table 3.4. The masses are also calculated using the slightly different α and β values taken from [Gültekin et al. \(2009a\)](#) and [McConnell & Ma \(2013\)](#). These masses are consistent with the numbers given in Table 3.4. These results show that galaxies G1, G3, G5, G7, and G9 all host supermassive black holes ($M_{BH} \approx \text{few} \times 10^8 M_{\odot}$) at their centers while for the other galaxies G2, G4,

TABLE 3.4: The redshifts and masses of the SMBHs (([McConnell et al., 2011](#)) using equation 3.5) associated with the galaxy like condensations in ‘Zwicky’s Nonet’.

Galaxy	Redshift	Velocity dispersion ($km s^{-1}$)	Mass of the SMBH $M_{BH,\sigma}(10^8 M_{\odot})$
G1	0.0473	222 ± 16	3.88 ± 1.23
G2	0.0476	143 ± 27	0.53 ± 0.44
G3	0.0470	273 ± 18	9.83 ± 2.96
G4	0.0503	135 ± 33	0.40 ± 0.45
G5	0.0476	230 ± 8	4.52 ± 0.74
G6	0.0454	143 ± 40	0.52 ± 0.65
G7	0.0468	211 ± 16	3.08 ± 1.00
G9	0.0445	176 ± 20	1.34 ± 0.68

and G6 we have obtained only approximate black hole masses with large errors. Interestingly, the most massive black hole of mass $M_{BH} \approx 10^9 M_{\odot}$ resides in galaxy G3 which showed a radio-loud AGN core in previous VLBA observations ([Liuzzo et al., 2010](#)).

Using the luminosity based method, the black hole masses of the galaxies were calculated from their K band absolute magnitudes. We used 6 times deeper data for A407 available from the 2MASS survey. We have used the equation connecting K band absolute magnitude of bulge component to the central black hole mass given by ([Graham, 2007](#))

$$\log_{10} \left(\frac{M_{BH}}{M_{\odot}} \right) = -0.38(\pm 0.06) (M_K + 24) + 8.26(\pm 0.11) \quad (3.6)$$

TABLE 3.5: K band absolute magnitudes and masses of the SMBHs associated with the nine galaxies of ‘Zwicky’s Nonet’ (Graham, 2007). See equation 3.6. The last column shows the ratio of the SMBH black hole masses obtained from stellar velocity dispersion and K band magnitude.

Source	K Band absolute magnitude	Mass of the SMBH. $M_{BH,K}(10^8 M_{\odot})$	SMBH mass ratio $M_{BH,\sigma}/M_{BH,K}$
G1	-23.46 ± 0.039	1.13 ± 0.30	2.76
G2	-21.99 ± 0.085	0.31 ± 0.12	1.71
G3	-23.49 ± 0.034	1.16 ± 0.30	8.47
G4	-22.60 ± 0.028	0.53 ± 0.17	0.76
G5	-22.73 ± 0.031	0.60 ± 0.18	7.5
G6	-21.16 ± 0.089	0.15 ± 0.07	3.47
G7	-23.56 ± 0.031	1.23 ± 0.30	2.5
G8	-20.06 ± 0.113	0.06 ± 0.03	–
G9	-22.50 ± 0.039	0.49 ± 0.16	2.74

The black hole masses thus obtained for all the nine galaxies are listed in Table 3.5. The following caveats are worth mentioning here: It is unclear whether the canonical $M_{BH}-\sigma$ relation will suffice to galaxies in such hostile environment, undergoing violent mergers and stripping of stars in multiple tidal encounters, as clearly evidenced by the formation of a large-scale stellar halo of stripped matter in ‘Zwicky’s Nonet’ (Figure 3.1 and Figure 3.2). The same concern applies if one were to obtain M_{BH} using the K-band magnitude of the bulge and the $M_{BH}-M_K$ correlation shown above.

The effect of the gravitational potential of the background stellar halo (which is highly dark matter dominated; (Schneider & Gunn, 1982)) and close merging galaxies on the bulge stellar velocity dispersion of a galaxy are possible factors which need to be accounted while calculating black hole masses. Here we have not attempted to do so. But, for checking this issue, in Table 3.5 last column we

show the ratio of black hole mass estimated from $M_{BH}-\sigma$ correlation ($M_{BH,\sigma}$) to that obtained from $M_{BH}-M_K$ method ($M_{BH,K}$). The ratio $M_{BH,\sigma}/M_{BH,K}$ is > 2 for galaxies with well determined black hole masses, which suggests that possibly $M_{BH}-M_K$ method gives smaller black hole masses due to the tidal stripping of the outer envelope of some galaxies. This results in the reduction of their K band luminosity or else, $M_{BH}-\sigma$ black hole masses are overestimated. The stripped away matter from the presently observed nuclei will be providing a large fraction of the total luminosity to the observed stellar halo. The main parameters of the stellar halo which is detectable up to the r-band surface brightness limit of ~ 24 mag arcsec $^{-2}$ (and possibly beyond), quoted by [Schneider & Gunn \(1982\)](#) are; central mass density $\rho(0) = 0.63 \pm 0.25 M_{\odot} \text{ pc}^{-3}$, the mass-to-light ratio in r-band $M/L = 90 \pm 35$, and halo radial velocity dispersion $\sigma_{halo} = 610 \pm 200 \text{ km s}^{-1}$. From this value of σ_{halo} and taking halo radius $r = 30 \text{ arcsec}$ ($\sim 26.5 \text{ kpc}$), we obtain the total dynamical mass as $2.2 \times 10^{12} M_{\odot}$, interestingly which is of the same order as that of a supergiant cD galaxy.

3.4 Conclusions

We have presented the analysis of radio, optical and infra-red imaging observations of the extraordinary radio source 4C 35.06 found in Abell 407 galaxy cluster, and have also presented spectroscopic observations of the central group of galaxies in which it resides. Our main results are as follows :

1. The central region of Abell 407 hosts a remarkably tight ensemble of nine passive, early type red ellipticals galaxies within $\sim 1 \text{ arcmin}$ ($\sim 50 \text{ kpc}$) region, embedded within a faint, diffuse stellar halo. This unique galactic

system, named as the ‘Zwicky’s Nonet’, provides compelling evidence for a rare ongoing formation of a giant cD galaxy at the cluster center.

2. The radio observations of 4C 35.06 at 150, 235 and 610 MHz with GMRT reveals the complete radio structure. A complex central core region along with a helically twisted and kinked bipolar radio jet structure extend to ~ 400 kpc, which terminates into diffuse, ultra-steep spectrum regions at the jet extremities are found.
3. The linear size of the large-scale jet system grows from 230 kpc at 610 MHz to 400 kpc at 150MHz, therefore implying steep spectrum emission at outer regions, that is better detected at lower frequencies. GMRT flux density measurement gives a total flux density of 1.7 Jy at 610 MHz, 4.7 Jy at 235 MHz and 6.0 Jy at 150 MHz respectively, with overall steep spectral index $\alpha \sim -1$.
4. The central core region shows flat spectrum, due to the superposition of possibly a few compact radio-loud AGNs, that becomes gradually steeper along the jet away from the center, up to the outer most extremities of the jet. This indicates that there is no fresh injection of accelerated particles in relic regions, and hence the extreme steepness of the spectra therein.
5. GMRT has provided the clear images of the radio jet at 610 MHz and of diffused steep spectrum relic/fossil regions (D1 and D2) in the 235 MHz and 150 MHz for 4C 35.06. These regions are also hinted in 74 MHz VLSS and LOFAR 61 MHz maps. Both the regions, D1 and D2, show very steep radio spectra ($\alpha \leq -2$) and spectral breaks which are clear indicators of an ageing nonthermal plasma undergoing radiative cooling. In the case of western region D2 an ultra-steep spectrum of $\alpha < -2$ was measured down to 150 MHz.

6. In fossil/relic regions D1 and D2, the average minimum energy magnetic field is $B \sim 16 \mu\text{G}$ for $k = 100$. The corresponding spectral age of electrons is estimated at 1.1×10^7 y. For $k = 1$ the average minimum energy magnetic field is $B \sim 5 \mu\text{G}$ and the radiative lifetime 7.5×10^7 y respectively, where k is the ratio of energy in relativistic particles to that in electrons.
7. The GMRT images of helically twisted and kinked jet system embedding a very tight condensation of nine galactic nuclei near its center point to the possibility of precessional and orbital motion of the AGN. This also suggests possible gravitational perturbation effects of multiple black holes in closely interacting galaxies.
8. The GMRT map at 610 MHz shows three radio peaks at the central region, of which two (near the optical positions of galaxies G5 and G2) exhibit offset with the jet direction, while the other (near to G6) falls in the middle of the jet. Thus the fainter member G6 appears to host the large scale radio jet. However, in our present radio observations, we can not pin-point conclusively which one (or more) of the nine close galaxies give rise to the overall large-scale radio jet system.
9. The morphological similarity of the jet system in 4C 35.06 with that of precessing jets in galactic microquasar SS 433 is noted, which supports a precessional scenario. The absence of terminal hot spots and presence of ultra-steep spectrum regions on both ends of the jet strongly suggest the continuous shifting of the jet direction, further supporting the precessional model. However, better modelling is required to investigate this scenario.
10. The optical spectra of eight galaxies in ‘Zwicky’s Nonet’ fail to show any prominent emission lines due to AGN, indicating a radiatively inefficient mass accretion flow onto central black holes at sub-Eddington rates. No

strong star-formation/star-burst activity is detected either in any of the galaxy spectra.

11. The time-averaged kinetic power of jets in 4C 35.06 is obtained as $\bar{Q} \approx 3 \times 10^{43} \text{ erg s}^{-1}$. This is below the transition value $5.0 \times 10^{43} \text{ erg s}^{-1}$ between FR I and II classes.
12. Black hole masses of the central galaxies have been obtained from the bulge velocity dispersion ($M_{BH,\sigma} - \sigma$) and K-band magnitude ($M_{BH,K} - M_K$) correlations. Galaxies G1, G3, G5, G7, and G9 all host SMBHs at their centers ($M_{BH} \approx \text{few} \times 10^8 M_\odot$), whereas for the fainter members G2, G4, and G6 we could only obtain approximate black hole masses within large error bars. The most massive black hole of mass $M_{BH} \approx 9.8 \times 10^8 M_\odot$ resides in galaxy G3 which showed a radio-loud AGN core in previous VLBA observations.
13. The black hole mass ratio from two methods, i.e. $M_{BH,\sigma}/M_{BH,K}$, is found to be > 2 for galaxies with well-determined masses. This suggests that possibly $M_{BH}-M_K$ method gives systematically smaller black hole masses due to the stripping of the outer envelope of some galaxies and thus a reduction in their K-band stellar luminosity. This is indicative of strong evolution in a hostile galactic environment where violent mergers and stripping of stars in multiple tidal encounters are common, as clearly evidenced by the formation of a large-scale stellar halo of stripped matter in ‘Zwicky’s Nonet’.
14. 4C 35.06, with its rare, bipolar morphology of helically twisted and kinked jets and possessing other striking properties as revealed in our observations, provides an excellent opportunity to understand the energetics and

the dynamical evolution of radio jets ejected from AGN hosted in closely interacting multiple galaxy systems.

Chapter 4

Radio and optical studies of the largest radio source hosted by a spiral galaxy 2MASX J23453268-0449256

The radio jets are believed to be formed by extracting the rotational energy from the spinning black hole and the accretion disc through the magnetic fields. The relativistic particles (mainly the electrons and the protons) ejected out of the AGN, through the jets, helps to drag the accreting matter into the BH by removing their angular momentum (Blandford & Znajek, 1977; Blandford & Payne, 1982). The phenomena of ejection of collimated jets of relativistic plasma spanning hundreds or even thousands of kilo parsec scale are still not understood fully. It is found that radio galaxies in the local Universe are always hosted by massive, gas-poor elliptical galaxies, not by spiral galaxies (Best et al.,

2005). The reasons why radio jets are always launched from the nuclei of bulge dominated elliptical galaxies and not from flat spirals is elusive. This chapter describes the study of a giant radio source 2MASX J23453268-0449256, from which the relativistic jets are ejected from a luminous and massive spiral galaxy on a scale of ~ 1.6 megaparsecs. This is the largest known radio galaxy hosted by a spiral galaxy (Bagchi et al., 2014).

The factors which differentiate the radio loud and radio quiet states of an AGN are the fundamental BH properties such as its mass, spin and the accretion rate. Many studies have shown that the minimum BH mass required for an AGN to produce large-scale jets is $\geq 10^8 M_{\odot}$ (Chiaberge & Marconi, 2011; Laor, 2000; Best et al., 2005). Sikora et al. (2007) have proposed that as ellipticals have a different merger history than that of the spirals, the spin of the BHs in them may attain higher values. Alternatively, Gallimore et al. (2006) propose that the denser Inter-Stellar Medium (ISM) in spiral galaxies impedes the jets and confines them to within the host galaxy as often seen in Seyfert galaxies.

Probably because of these, there are only a few reports of disk galaxies ejecting large-scale (>100 kpc) bipolar radio jets: The first such object reported was the radio source J031552-190644 in the galaxy cluster Abell 428 (Ledlow et al., 1998), which is having a linear size of ~ 200 kpc. The first megaparsec (~ 1 Mpc) scale episodic radio source hosted by a spiral was reported by Hota et al. (2011) and, they named the source as SPiral-host Episodic Cluster-dominant AGN or Speca. In 2015 Singh et al. (2015) conducted a study to search for radio galaxies from spiral hosts, by cross-matching a large sample of 187005 spiral galaxies from SDSS DR7 to the full catalogues of FIRST and NVSS. In this study, they could identify only four spiral-host double-lobed radio galaxies. The estimated linear size of two of the detected radio galaxies in this sample was ~ 400 kpc, and the others were smaller sources.

The source J2345 is having a luminosity distance of 344 Mpc at the redshift $z = 0.0755$, with an angular separation scale of $1.442 \text{ kpc arcsec}^{-1}$.

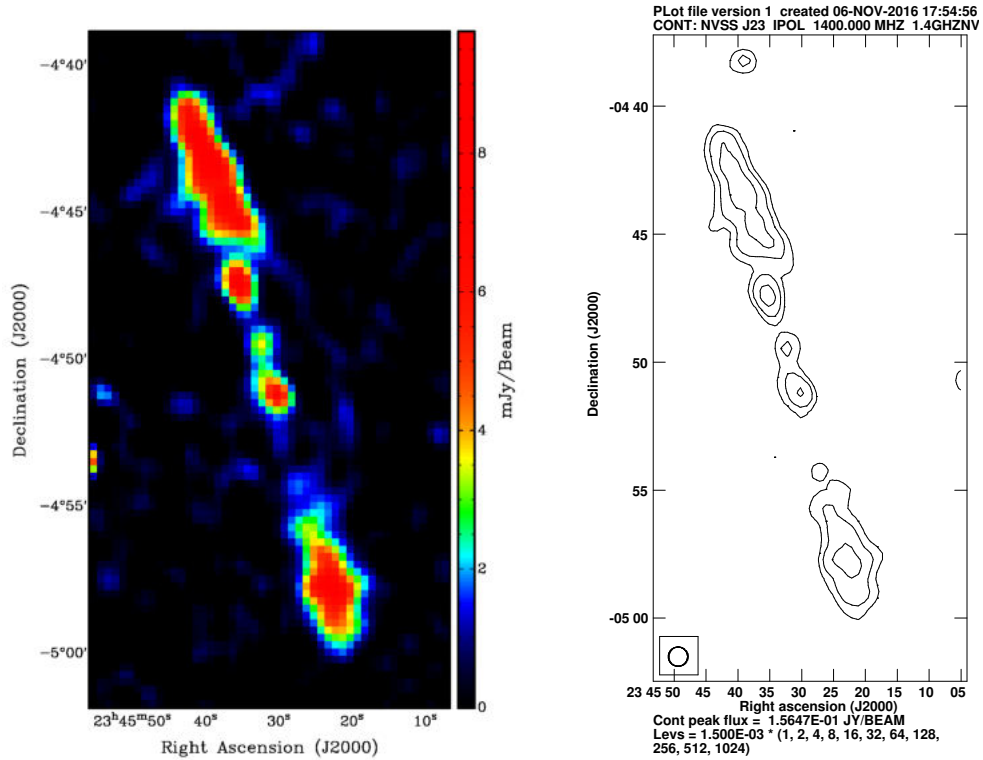


FIGURE 4.1: left panel:NVSS VLA Image of the radio source at 1.4GHz with resolution $45'' \times 45''$. Right panel: The contour plot of NVSS image, with contour levels $[1,2,4,8,16,\dots] \times 1.5 \text{ mJy}$

4.1 Previous observations.

The NVSS radio image in Figure 4.1 shows the radio galaxy J2345-0449 (with a linear size of $\sim 1.6 \text{ Mpc}$) with two pairs of lobes on either side of the core. The two pairs of radio lobes on each side of the core almost symmetrically aligned in a

line is a clear indication of that it is a ‘double-double’ radio galaxy (DDRG). (The inner radio lobe pair extends over ~ 415 kpc.) The integrated flux density and radio luminosity of the source, at 1.4 GHz are $S_{1.4} = 180.60 \pm 0.02$ mJy and $L_{1.4} = 2.5 \times 10^{24}$ Watts Hz^{-1} , respectively. This value of $L_{1.4}$ is moderate, but it is above the rough divide between the radio-quiet and radio-loud galaxies, which is usually taken at $L_{1.4} \geq 10^{24}$ W Hz^{-1} (Tadhunter, 2016). Also, the source is a LERG since the 1.4GHz radio luminosity is below the dividing value ($\sim 10^{26} \text{W Hz}^{-1}$) between LERGs and HERGs (Best & Heckman, 2012). Forthcoming discussions on WISE magnitudes and optical spectrum support that this is a LERG.

This radio galaxy was first mentioned by Machalski et al. (2007) as a megaparsec-scale object located at redshift $z = 0.0757$, but they did not discuss anything about the spiral nature of the host galaxy. From the optical spectroscopic studies, we could reveal the spiral nature of the galaxy J2345-0449 (Bagchi et al., 2014).

The SDSS r band image of the galactic environment of J2345-0449 is shown in Figure 4.2. Positions of the nearest neighbour galaxies are also marked in this figure. It is clear that J2345-0449 is located in a sparsely populated galactic environment. The nearest cluster to this galaxy is RBS 2042 (redshift $z = 0.07860$) which is 33 arcmin (~ 2.8 Mpc) away from it. So, it seems that J2345-0449 is a peripheral member of this galaxy cluster.

In the previously reported spiral galaxy Speca with megaparsec-scale radio jets (Hota et al., 2011), the galactic disk is viewed nearly edge-on, and a clear view of its spiral arms is not possible. The discussed radio source J2345-0449 is the most unambiguous example of a spiral galaxy hosting large-scale jets. This galaxy also displays several other remarkable properties which are quite unusual, and are discussed in the following sections.

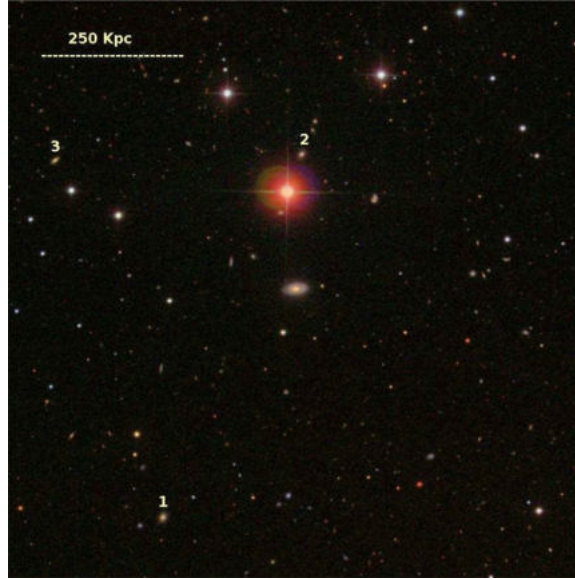


FIGURE 4.2: Large-scale galactic environment around J2345 - 0449. The colour image, taken from the Sloan Digital Sky Survey-III, shows a field of view of $\sim 1 \text{ Mpc} \times 1 \text{ Mpc}$ centered on J2345- 0449. The three nearest and brightest galaxies are marked in the descending order of their brightness in r-band

4.2 GMRT and IGO observations

The source J2345-0449 has been studied at 610 and 325 MHz frequencies using GMRT. For 610 MHz imaging, we have used the GMRT archival data with Project code: 15JMA01, which was observed on 04-12-2008. The 325 MHz GMRT data was obtained from our observation on 06 November 2015 with project code:29_061. We have used 3C48 as flux calibrator. For 610 MHz observation 02212+018 and 0116-208 were used as phase calibrators. In 325 MHz observation, 0022+0021 was used as the phase calibrator.

We were allotted two nights observing time in IGO on 21-22 November 2011

by the Time Allocation Committee in IGO cycle 2011B, and we have carried out spectroscopic observations of J2345-0449 along with the constituent galaxies of Zwicky's Nonet, discussed in chapter 3. In the spectroscopic observation, we placed the slit along the major axis and the along the minor axis of the galaxy. We have four exposures of 30 minutes duration in grism 7 and grism 8, in both the slit arrangements. The data analysis details are given in chapter 2.

4.3 Results

4.3.1 GMRT Radio maps and parameters

The low-frequency radio maps produced from GMRT observations at 325 and 610 MHz frequencies are shown in Figure 4.3. At 325 MHz, a radio map with $20'' \times 15''$ resolution and with a background rms value of $400 \mu\text{Jy}/\text{beam}$ (σ) was obtained. The 610 MHz data analysis resulted in a map with a resolution of $12'' \times 12''$ and an rms noise level of $250 \mu\text{Jy}/\text{beam}$ (σ). The integrated flux density of this source at 325 MHz above 3σ limit was 940 mJy, while at 610 MHz it is obtained as 850 mJy. The fluxes for the source at different regions at different frequencies are given in Table 4.1.

The low-frequency GMRT 325 MHz image shows that the outer lobes are more diffuse, lacking prominent hot spots. The diffuse radio emission near inner lobes is better visible at the 325 MHz frequency image, tracing the back flowing plasma of outer lobes. The radio luminosity at 325 MHz is $L_{325} = 1.33 \times 10^{25}$ Watts Hz^{-1} and that at 610 MHz is $L_{610} = 1.20 \times 10^{25}$ Watts Hz^{-1} . Using the three data points at 1.4GHz, 325 MHz and 610 MHz (See Table 4.1) overall steep spectral index of the source is obtained as $\sim -1.16 \pm 0.27$. Similarly, the spectral

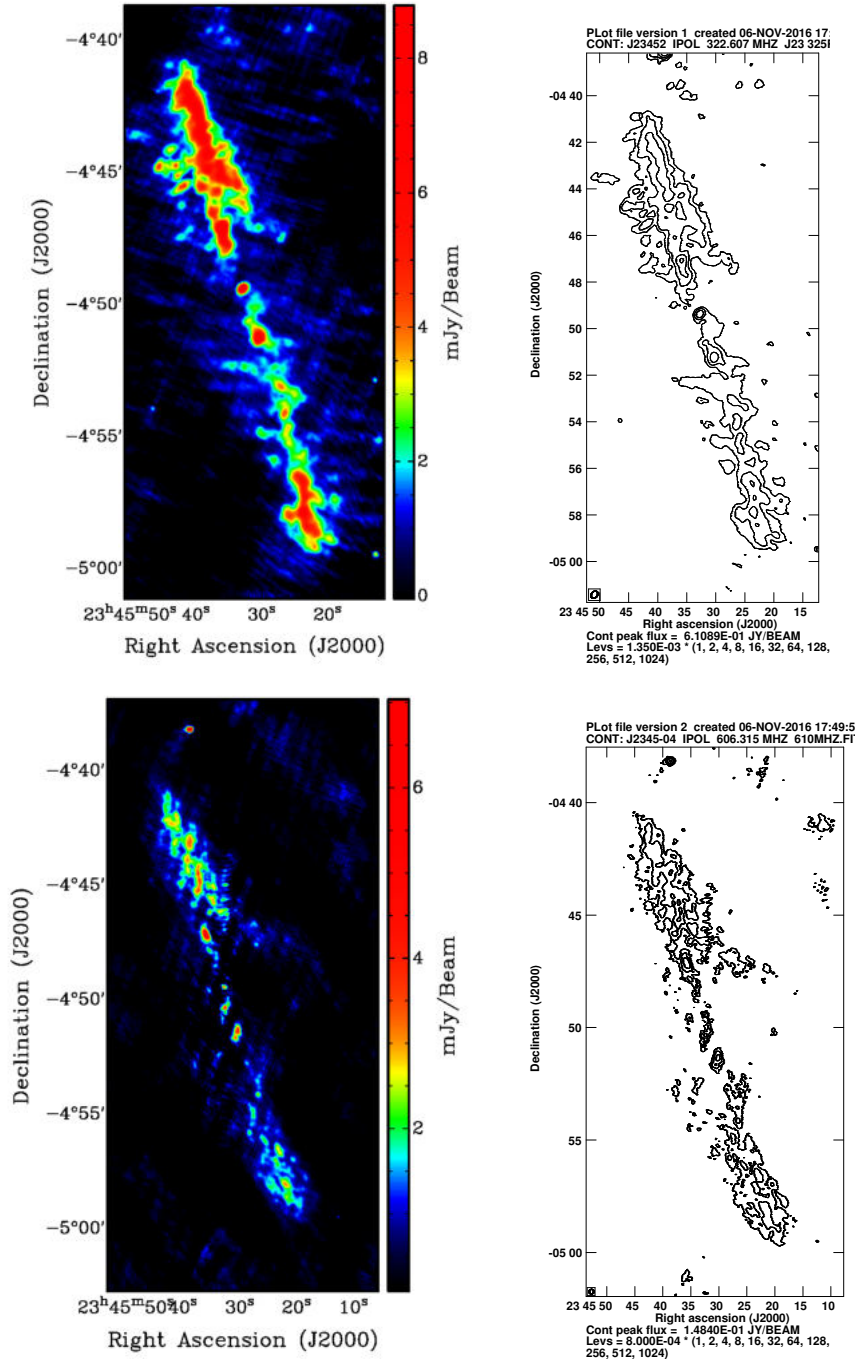
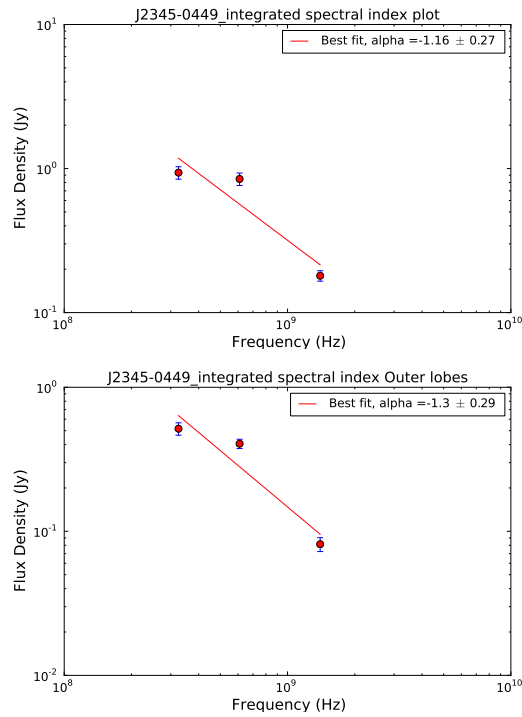


FIGURE 4.3: Top panel : GMRT 325 MHz image (Left) and contour plots(right) with contour levels $[1,2,4,8,16,\dots,1024] \times 1.35$ mJy. Bottom panel: GMRT 610 MHz image (Left) and contour plots(right) with contour levels $[1,2,4,8,16,\dots,1024] \times 0.8$ mJy.

TABLE 4.1: The Flux density (S_ν (mJy)) is shown below for different regions at various frequencies.

Region	S_ν (mJy) 1.4 GHz	S_ν (mJy) 610 MHz	S_ν (mJy) 325 MHz
Northern outer lobe	81	405	515
Northern inner lobe	17	47	55
core	5	5	14
Southern inner lobe	14	41	45
Southern outer lobe	62	289	310
Total flux	180	850	940

FIGURE 4.4: The integrated spectral index plot of J2345-0449 (Top panel) and that of the outer lobes (bottom panel). The integrated spectral index of the source is $\sim -1.16 \pm 0.27$ and, that of the outer lobe regions are $\sim -1.3 \pm 0.29$.

index corresponding to the outer lobes is obtained as $\sim -1.3 \pm 0.29$ (See Figure 4.4). The spectral index map is created between the 1.4GHz (NVSS map) and 325 MHz (GMRT map) shows regions with the steep spectral index up to -1.6. This validates the episodic radio jet activity scenario mentioned above (Figure 4.5).

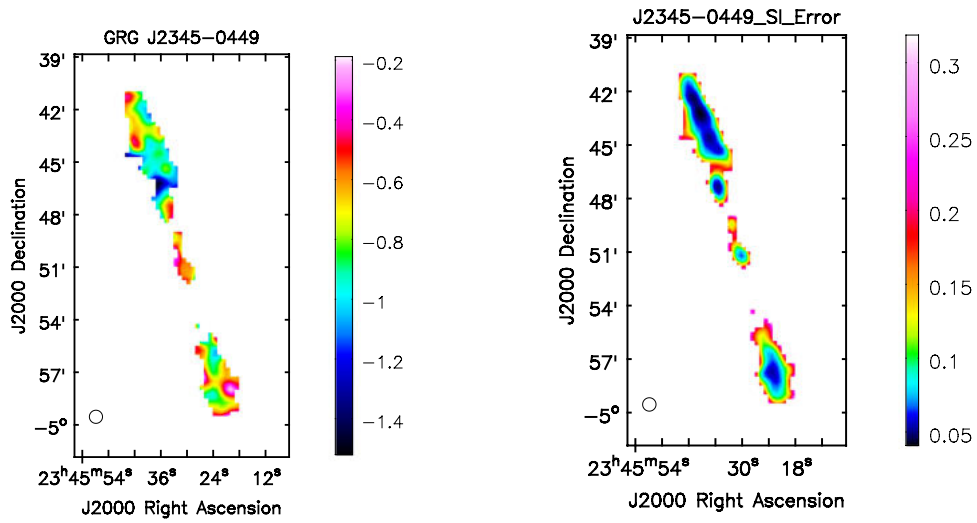


FIGURE 4.5: The spectral index image between 325 MHz (GMRT) and 1400 MHz (VLA/NVSS) frequency (Left) and error map (right).

Using the overall spectral index $\alpha = -1.16$ the luminosity of the sources at 178 MHz is estimated as $L_{178} = 2.78 \times 10^{25} WHz^{-1}$, which is above the distinguishing line between FRI and FRII radio sources ($\sim L_{178} = 2 \times 10^{25} WHz^{-1}$) (Fanaroff & Riley, 1974).

The steep spectral nature of the outer region can be seen from Figure 4.6, where we have plotted the data from Table 4.1 and fitted with second order polynomial to illustrate the aged plasma. The second order polynomial fits for the data points from northern outer lobe and southern outer lobe regions show

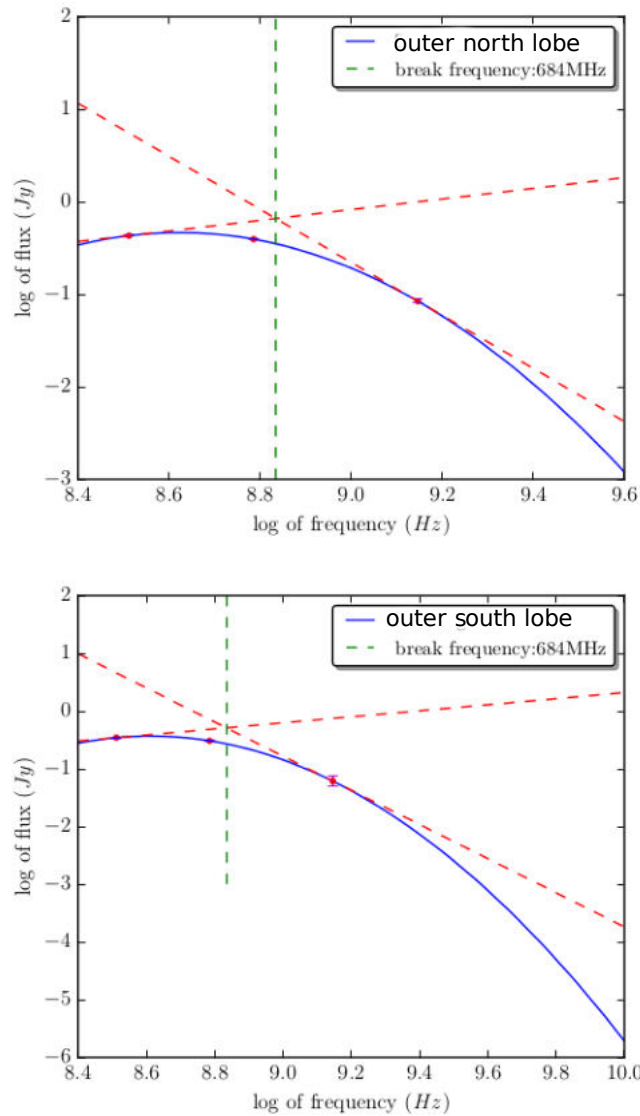


FIGURE 4.6: The data points corresponding to the North and south outer lobes are fitted with second order polynomial to show the curvature. The break frequency shall be between the end values of frequencies (300 MHz and 1.4 GHz). The approximate value is taken at the intersection of the tangents drawn at 325 MHz and 1.4 GHz data points. It is obtained as ~ 680 MHz (see the green dotted line).

clear curvatures. This indicates that the spectral break frequency is somewhere between 600 MHz and 1.4GHz. From Figure 4.6 we estimated it as ~ 680 MHz. Using this the electron spectral age t_{sp} (cooling time scale) of the source is then calculated using the equation given by (Murgia et al., 2011) (same as equation 3.1 given in chapter 3)

$$t_{sp} = 1.59 \times 10^9 \left[\frac{B^{1/2}}{[B^2 + B_{IC}^2] [\nu_b(1+z)]^{1/2}} \right] yrs \quad (4.1)$$

Using $\sim \nu_b = 0.68$ GHz, and magnetic field range $B = 1 - 10 \mu G$, the electron spectral age is obtained to be $t_{sp} = (50 - 120) \times 10^6$ years.

4.3.2 Optical spectroscopic results

The spectrum extracted from the nuclear region of the galaxy is shown in Figure 4.7. It shows no prominent emission lines except the weak lines of $H\alpha$ $\lambda 6562.81\text{\AA}$ and $[N II]\lambda 6585.27\text{\AA}$. The redshift of the galaxy is estimated as $z = 0.0755$.

4.3.2.1 Central velocity dispersion and black hole mass

The stellar velocity dispersion of the galaxy is estimated as discussed in the section 2.2.3, by fitting the Sodium D1 and D2 absorption lines with a Gaussian, and velocity dispersion of $326(\pm 26)$ kms^{-1} (Using equation 2.1) is estimated.

As discussed in chapter 3, section 3.3.6, the general expression which connects the mass of the central black hole M_{BH} to the galaxy's bulge stellar velocity dispersion is,

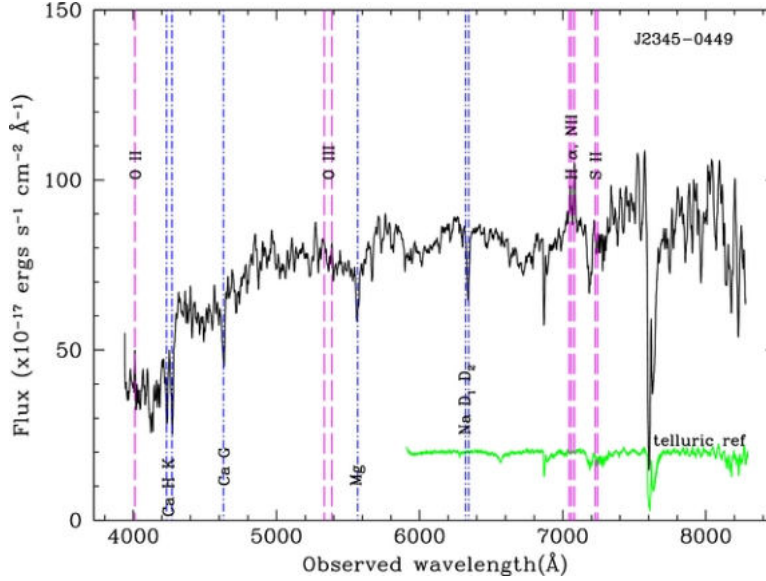


FIGURE 4.7: The Optical spectrum of the central region.

$$\log_{10} \left(\frac{M_{BH}}{M_{\odot}} \right) = \alpha + \beta \log_{10} \left(\frac{\sigma}{200 \text{ kms}^{-1}} \right) \quad (4.2)$$

where σ is expressed in km s^{-1} . [Bagchi et al. \(2014\)](#) found that the galaxy J2345-0449 is a pseudo-bulge galaxy. For pseudo-bulge systems, the values of α and β are 7.50 ± 0.18 and 4.5 ± 1.3 respectively ([Hu, 2008](#)). On substituting these values the black hole mass of the source is obtained as $M_{BH} = 3.88(\pm 0.40) \times 10^8 M_{\odot}$. Estimation of the black hole mass using the $M - \sigma$ relations of [McConnell et al. \(2011\)](#) yields a value of $2.1(\pm 0.70) \times 10^9 M_{\odot}$.

From the measured flux density of the H_{α} emission line, the H_{α} luminosity of the source is calculated as $3.02 \times 10^{40} \text{ erg s}^{-1}$. If the H_{α} luminosity is $\leq 10^{40} \text{ erg s}^{-1}$ the AGN will be of Low luminosity type (LLAGN) ([Ho et al., 1997](#)).

4.3.2.2 Galaxy rotation curve

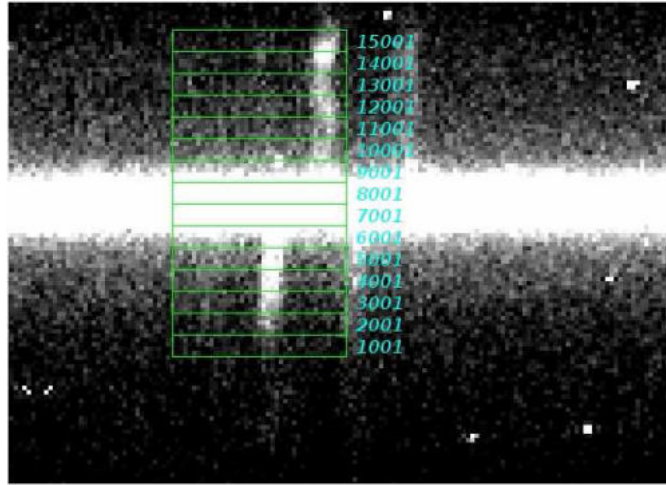


FIGURE 4.8: Two-dimensional images showing the long-slit spectrum near the H_{α} and $[\text{N II}]$ emission lines of galaxy J2345 - 0449. Locations of different sub-apertures (numbers 1 - 15) used to derive the rotation curve of the galaxy are marked in the image. The wavelength direction is horizontal, increasing to the right, and the spatial direction is vertical. A sharply rising flat rotation curve is clearly evident in the shape of both H_{α} and $[\text{N II}]$ lines marked here.

The rotational properties of spiral galaxies can be studied by the rotation curves, which is the plot between the radial distance from the center of the galaxy with the corresponding rotational velocity. The rotation curve for J2345-0449 is derived from the optical spectra taken from IGO. To derive the rotation curve the spectrum from gr8 was used, as the only two emission lines from the galaxy are falling in the wavelength range covered by this grism. We have extracted 1D spectra from sub-apertures of 5 pixel width (spatial direction) placed symmetrically around the center of the galaxy (Figure 4.8, shows the spectrum image around the H_{α} and $[\text{N II}]$ emission lines with different sub-apertures marked.). This has resulted in 15 individual spectra. The width of the sub-aperture corresponds to an angular scale of ~ 1.5 arcsec (2.1 kpc) .

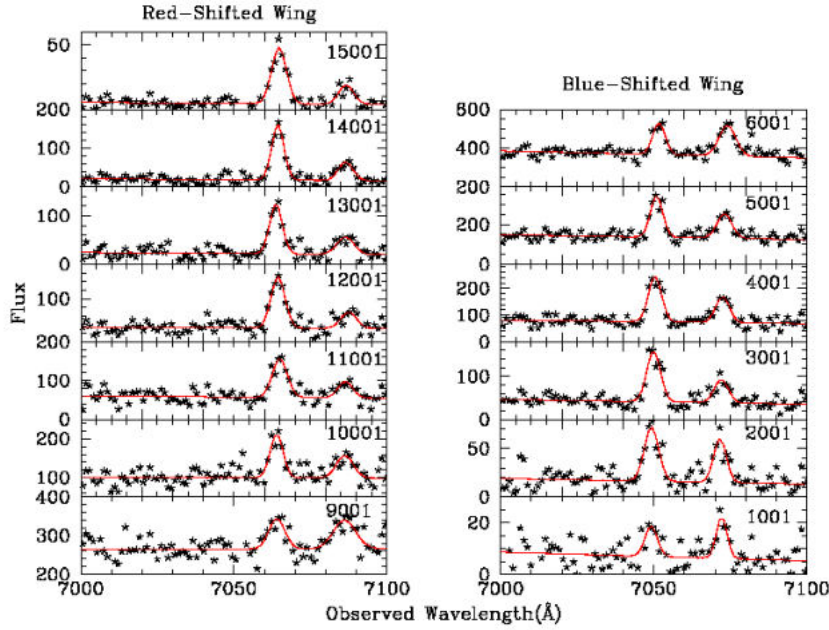


FIGURE 4.9: one -dimensional spectra extracted at different sub-apertures as indicated in figure 4.8. Gaussian fits to $H\alpha$ and $[N II]$ lines are shown for the blueshifted and redshifted wings of the spectra. The flux scale is arbitrary. No significant $H\alpha$ emission was detected in the central apertures numbered 7 and 8 (shown in figure 4.8). The parameters derived from the Gaussian fits (Table 4.2) are used to obtain the rotation curve.

We fitted the $H\alpha$ $\lambda 6562.81\text{\AA}$ and $[N II]\lambda 6585.27\text{\AA}$ lines using Gaussians and χ^2 minimization. Other $[N II]\lambda 6549.86\text{\AA}$ line to the blue side of $H\alpha$ line was faint, well within the noise, and thus we did not attempt to fit it (See figure 4.9. We obtained the rotational velocity V at each sub-aperture position using the equation,

$$V = \frac{z_{ap} - z_{cen}}{(1 + z_{cen})} 3 \times 10^5 \text{ km s}^{-1} \quad (4.3)$$

and plotted it against the distance from the nucleus to obtain the rotation curve (See Table 4.2). Here z_{ap} is the fitted redshift of the $H\alpha$ line in a given aperture,

TABLE 4.2: The redshift values corresponding to the H_α lines at different apertures shown in figure 4.8 and 4.9 The last column shows the velocity of the region relative to the galactic centre.

Aperture	ID	Center λ	Redshift	$\times c$ (km/s)
7	1001	7049.1298 \pm 0.821	0.07381 \pm 1.25e-04	-346 \pm 37.52
6	2001	7049.2569 \pm 0.758	0.07383 \pm 1.15e-04	-340 \pm 34.64
5	3001	7049.9527 \pm 0.840	0.07393 \pm 1.27e-04	-313 \pm 38.39
4	4001	7050.3916 \pm 0.698	0.07400 \pm 1.06e-04	-293 \pm 31.9
3	5001	7050.8901 \pm 0.599	0.07408 \pm 9.12e-05	-271 \pm 27.3
2	6001	7051.6811 \pm 0.831	0.07420 \pm 1.20e-04	-237 \pm 37.90
1	7001	—	—	—
0	8001	—	—	—
-1	9001	7064.0366 \pm 0.880	0.07608 \pm 1.30e-04	287 \pm 40.7
-2	10001	7063.9835 \pm 0.811	0.07607 \pm 1.23e-04	285 \pm 27.07
-3	11001	7065.0165 \pm 0.789	0.07623 \pm 1.20e-04	329 \pm 36.0
-4	12001	7064.4256 \pm 0.553	0.07614 \pm 8.55e-05	304 \pm 25.65
-5	13001	7063.7688 \pm 0.788	0.07604 \pm 1.20e-04	276 \pm 36.02
-6	14001	7064.3826 \pm 0.864	0.07613 \pm 1.30e-04	301 \pm 39.49
-7	15001	7064.7690 \pm 0.822	0.07619 \pm 1.25e-04	318 \pm 37.52

and $z_{cen} = 0.07505$, the redshift at the dynamical center of the galaxy. The table 4.2 gives the redshift values and the estimated rotation velocities at different radial distance from the centre of the galaxy. Similarly, the spectral extraction is carried out for the minor axis data, but no variation in redshift is observed.

In Figure 4.10, we show the derived rotation curves for the major (red points) and minor (blue points) axis. It can be seen that the rotation is evident along the major axis while no such signature is seen along the minor axis. It is evident from here that, the emission lines originate in a tilted rotating disk. The rotational

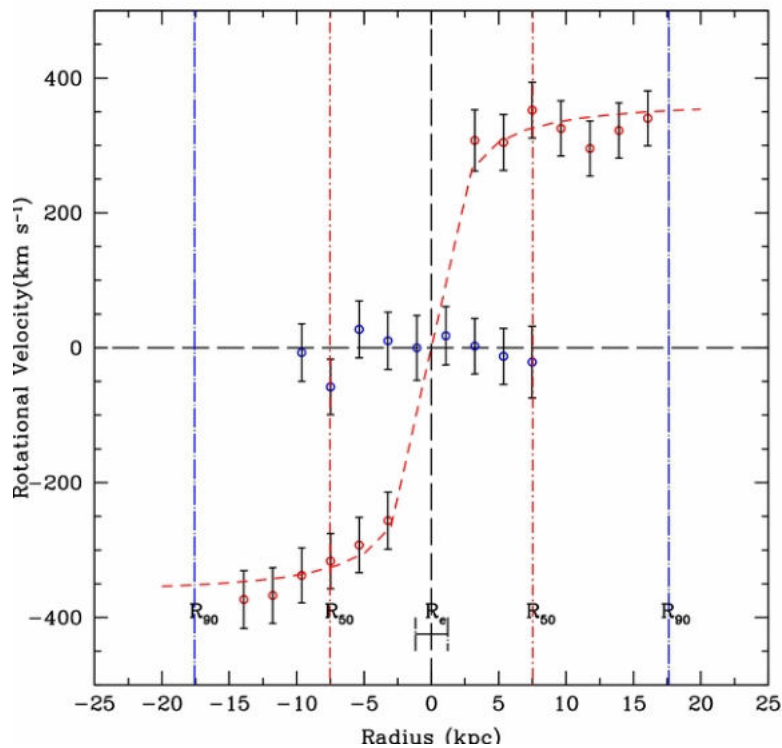


FIGURE 4.10: The rotation curve of the galaxy (red dashed curve) derived from the kinematics of the Balmer H_α line in the long slit spectrum taken along the major axis (red data points) and minor axis (blue data points). The rotational velocity is shown without the $\sin(i)$ correction for inclination. The major axis data shows a clear rotation signature, while no such rotation is evident across the minor axis, which is clear evidence that the emission originates in a tilted rotating disk

curve shown in Figure 4.10 is fitted with an analytical function (Courteau, 1997)

$$V(R) = V_0 + \frac{2}{\pi} V_{c,obs} \times \arctan^{-1} \left(\frac{R}{R_{turn}} \right) \quad (4.4)$$

where, R is radial distance, V_0 is the systemic velocity, $V_{c,obs}$ is the asymptotic circular velocity, and R_{turn} is the turn-over radius. The fitting results in the

following values: $V_0 = 0 \text{ km s}^{-1}$, $V_{c,obs} = 370.8 \pm 25.8 \text{ km s}^{-1}$ and $R_{turn} = 1.4 \pm 0.7 \text{ kpc}$. The inclination corrected ($i \sim 58^\circ$ (Bagchi et al., 2014)) circular velocity is $V_{c,incl} = 432.6 \pm 25.8 \text{ km s}^{-1}$.

4.3.3 WISE mid-infrared colours.

The magnitudes, luminosities and SNR of the spiral galaxy J2345-0449, in the WISE mid-IR (MIR) bands, are listed in Table 4.3. WISE mid-IR colours can be used to obtain the properties of a dust obscured galactic nucleus and to determine the radiative efficiency of the AGN. In a dust-obscured galactic nucleus, optical-UV radiation from the AGN accretion disk is absorbed by the dusty-torus and re-radiated in MIR bands. The WISE MIR colours can distinguish within AGN, concerning the accretion modes, as HERGs and LERGs. In the WISE colour-colour plots they occupy different positions. Wright et al. (2010); Stern et al. (2012); Gürkan et al. (2014). The derived MIR colours for J2345-0449 are:

$$[W1 - W2] = 0.064, [W2 - W3] = 2.817, [W2 - W4] = 4.722 \quad (4.5)$$

Figure 4.11 shows the wise colour-colour plots for different classes of AGNs such as LERGs, HERGs, NLRGs, BLRGs and QSOs. In the WISE colour- colour plot of W1-W2 vs W2-W3 (top panel of Figure 4.11), J2345-0449 is identified in the position of LERGs (Gürkan et al., 2014). Similarly in the W1-W2 vs W2-W4 plot (bottom panel of Figure 4.11) , the galaxy falls on the region where LERG's and NLRGs cluster (Gürkan et al., 2014).

From the $22 \mu\text{m}$ luminosity versus L_{151} radio luminosity plot Gürkan et al. (2014) it can be observed that the empirical cut off between LERGs and HERGs

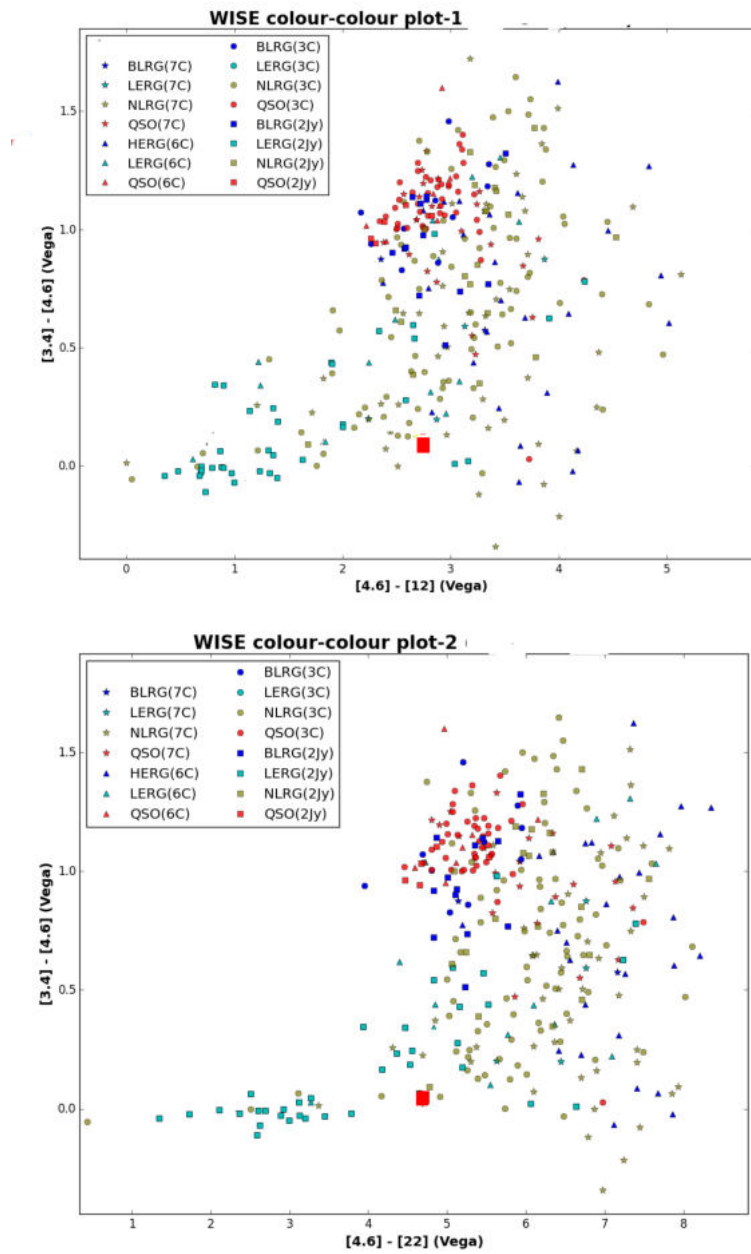


FIGURE 4.11: Top panel: WISE colour-colour plot between W1-W2 and W2-W3. Bottom Panel: WISE colour-colour plot between W1-W2 and W2-W4. In both the plots the red square shows the position of j2345-0449

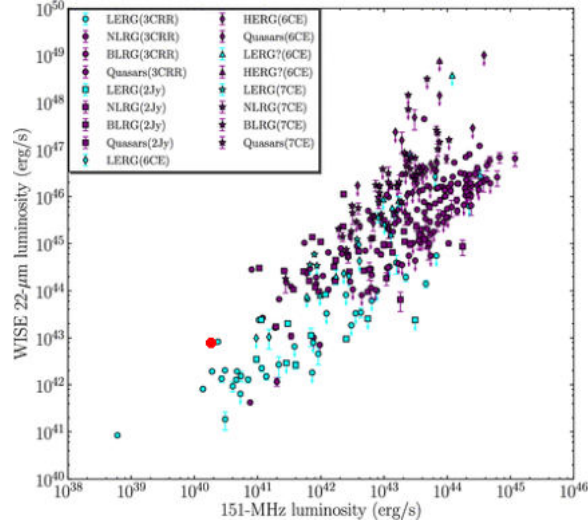


FIGURE 4.12: $22\ \mu\text{m}$ luminosity versus L_{151} radio luminosity plot. The position of j2345-0449 is marked in red.

corresponds to a $22\ \mu\text{m}$ luminosity of $5 \times 10^{43}\ \text{erg s}^{-1}$. The $22\ \mu\text{m}$ luminosity of J2345-0449 is $2.26 \times 10^{43}\ \text{erg s}^{-1}$, much below the cut off value. From the integrated spectral index of $\alpha = -1.16$ the radio luminosity of the source at 151 MHz is calculated as $L_{151} = 5.31 \times 10^{40}\ \text{ergs S}^{-1}$. In the $22\ \mu\text{m}$ luminosity versus L_{151} radio luminosity plot J2345-0449 is in the group of LERGs (see Figure 4.12). The above points show that, J2345-0449 is a low-excitation radio galaxy, its SMBH possibly residing in a radiatively inefficient ADAF state. This is also indicated by the small core $\text{H}\alpha$ luminosity and the lack of broad emission lines in the AGN optical spectrum.

TABLE 4.3: WISE mid-infrared magnitudes and luminosities for J2345-0449. Magnitudes with their errors are given in the first row for the four mid-IR bands. Second row shows the derived luminosities in erg s^{-1} . The third row shows the signal-to-noise ratios of detection in four bands.

WISE band (Wavelength)	W1 3.4 μm	W2 4.6 μm	W3 12 μm	W4 22 μm
Magnitude	11.882 ± 0.023	11.818 ± 0.023	9.001 ± 0.028	7.096 ± 0.100
Luminosity	6.71×10^{43}	2.88×10^{43}	2.62×10^{43}	2.26×10^{43}
SNR	47.9	47.8	38.7	10.9

4.4 Discussion

4.4.1 Mass of the galaxy

One of the important property of this galaxy is its high rotational velocity. In section 4.3.2.2 from the rotation curve (Figure 4.10), we found that the galaxy is having a rotational velocity of $370 \pm 25.8 \text{ km s}^{-1}$ at a distance of 1.4 kpc from the galactic centre. The inclination corrected rotational velocity of this galaxy will be $V_{\text{rot}} = 430 (\pm 30) \text{ km s}^{-1}$. [The inclination of the galaxy plane to the line of sight is estimated by Bagchi et al. (2014), and the value obtained is $i \sim 58^\circ$. So the inclination corrected rotational velocity will be $\frac{370 \pm 25.8}{\sin i}$]. Such a rapid disk rotation of ($V_{\text{rot}} \sim 400 - 500 \text{ km s}^{-1}$) is rare and has been reported earlier for just a few exceptionally massive spirals (Giovanelli et al., 1986; Rigopoulou et al., 2002; Bogdán et al., 2013).

The Rotation curves are the major tool for determining the mass distribution in spiral galaxies (Sofue & Rubin, 2001). Assuming a quasi-spherical halo, the dynamical mass (luminous plus dark-matter) enclosed within a radius r is

$M_{\text{dyn}} = \kappa r V_{\text{rot}}^2 / G$, where κ is a correction factor, in range 0.6 – 1 for a thin-disk to a spherical halo mass distribution model (Lequeux, 1983), and G is the gravitational constant. We obtain $M_{\text{dyn}} = 1.07(\pm 0.13) \times 10^{12} M_{\odot}$, for $\kappa = 1$ and $V_{\text{rot}} \sim 430 \text{ km s}^{-1}$ at $r = 25 \text{ kpc}$, i.e. ~ 3.5 times the scale radius of the exponential disk. This places J2345-0449 amongst the brightest and most massive spirals known, having ~ 7 times the mass of the Milky Way within an equivalent radius.

4.4.2 SMBH in J2345-0449

Another unusual property displayed by this disk galaxy is its exceptionally large stellar velocity dispersion $\sigma_* = 326.2(\pm 26) \text{ km s}^{-1}$. This indicates a large central concentration of mass, including a putative SMBH. As discussed in section 4.3.2.1, the mass of the SMBH estimated in J2345-0449, by considering its pseudobulge nature is $3.88(\pm 0.40) \times 10^8 M_{\odot}$ (Hu, 2008). Similarly, black hole mass calculated using the correlation by McConnell et al. (2011), (which is derived using a sample of both ellipticals and spirals), the value of M_{BH} obtained is $2.1(\pm 0.70) \times 10^9 M_{\odot}$. These values suggest that J2345-0449 hosts an SMBH as massive as those found in giant elliptical galaxies; not expected in normal disk galaxies.

The estimated values of BH mass of J2345-0449 shows that, though it lacks a classical bulge, it is likely to host a massive and accreting black hole of mass $M_{\text{BH}} > 10^8 M_{\odot}$. There are strong correlations between M_{BH} and stellar velocity distribution (σ) in systems with classical bulges (Häring & Rix, 2004; Marconi & Hunt, 2003b; Gültekin et al., 2009b; McConnell et al., 2011). Many studies have shown that (Hu, 2008; Graham et al., 2011; Shankar et al., 2012) that pseudobulge and barred galaxies may host black holes that are about 3 - 10 times less massive than pure ellipticals with the same σ . So it will be an

important result if J2345-0449 harbours an SMBH of mass $\sim 10^8 M_\odot$. However, some studies have shown that pseudo-bulgesystems may also host fairly massive black holes of masses 10^3 – $10^7 M_\odot$ (Kormendy et al., 2011; Shankar et al., 2012).

The estimated value of black hole mass ($M_{BH} > 10^8 M_\odot$) satisfies the minimum criteria required for the production of large-scale radio jets (Laor, 2000; Gopal-Krishna et al., 2008; Sikora et al., 2007; Chiaberge & Marconi, 2011). From the unusual radio properties, high dynamical mass and the stellar velocity dispersion value of $326.2(\pm 26)$ kms^{-1} of J2345-0449, we can expect a more massive black hole in this galaxy. van den Bosch et al. (2012) observed that the compact disk galaxy NGC 1277 (having a total mass of $1.2 \times 10^{11} M_\odot$) is hosting an SMBH of mass $1.7 \times 10^{10} M_\odot$. They have estimated this black hole mass by studying the stellar or gas kinematics within the region of the sphere of influence of the black hole. The stellar velocity dispersion of this disk galaxy was $\sim 333 \text{ km s}^{-1}$, and the $M - \sigma$ relation predicted a black hole mass value of $2.4 \times 10^9 M_\odot$ only. It should be noted that the σ value of this galaxy is comparable to that of J2345-0449.

4.4.3 Jet power and magnetic field.

The jet power of a radio source is an important parameter, which is connected to the state of an accreting SMBH system; its mass, spin and the magnetic field of the accretion disk. We have used the calibration relation (Punsly & Zhang, 2011; Daly et al., 2012) for estimating jet power, using the 151 MHz lobe flux density of the source. The 151 MHz flux density is obtained as 3.3 Jy, using the spectral index value of $\alpha = -1.3$, which is obtained for the outer lobes (This spectral value is estimated using the 0.3, 0.6 and 1.4 GHz radio data, excluding the inner jet/lobe pair and core. Refer section 4.3.1). The value of jet power

obtained for J2345-0449 was $\bar{Q} \approx 5 \times 10^{43} \text{erg s}^{-1}$. This value of \bar{Q} in J2345-0449 falls on the dividing value between FRI/FRII sources (Rawlings & Saunders, 1991).

In the classic BZ process the electromagnetic luminosity of jet \bar{Q} scales with BH properties as (This equation is given in chapter 3; equation 3.4)

$$\bar{Q}_{44} \approx 0.2 M_8^2 a^2 B_4^2, \quad (4.6)$$

where, $\bar{Q}_{44} = \bar{Q}/10^{44} \text{ erg s}^{-1}$, the BH mass $M_8 = M_{\text{BH}}/10^8 M_\odot$ and the poloidal magnetic field $B_4 = B/10^4 \text{ Gauss}$ (Blandford & Znajek, 1977; MacDonald & Thorne, 1982b; Tchekhovskoy et al., 2010). Thus, the jet power depends strongly on the BH mass, spin and the magnetic flux at the horizon.

On assuming a lower limit of black hole mass $M_{\text{BH}} \sim 2 \times 10^8 M_\odot$ for J2345-0449, the magnetic field required to launch a jet of this power for a slow spinning black hole ($a=0.1$) is $B \sim 0.8 \times 10^5 \text{ Gauss}$. The maximum magnetic field, that will be produced near the inner accretion disk, when the accretion is at the Eddington rate is given by $B_{\text{Edd}} \approx 6 \times 10^4 M_8^{-1/2} \text{ Gauss}$. The value of the Eddington magnetic field of J2345-0449 is $\approx 0.8 \times 10^5 \text{ Gauss}$. This shows that the estimated jet power can be extracted via the BZ process, if the specific angular momentum $a > 0.1$. That means, if the jet formation in J2345-0449 is through the BZ process, the BH in it should be spinning fast.

4.4.4 Astrophysical processes behind the radio emission from J2345-0449

The observed peculiarities of J2345-0449, such as the huge dynamical mass ($\sim 1.07 \times 10^{12} M_{\odot}$), the 1.6 Mpc scale relativistic emissions and the presence of a huge black hole ($\sim 3.88 \times 10^8 M_{\odot}$), makes it unusual as these are uncommon in spiral galaxies. So it is important to discuss, the reason for the efficient fueling and sustained collimated jet ejection activity in J2345 - 0449. It requires a detailed knowledge of the properties of the central engine, such as its mass, spin, accretion rate and the magnetic field. An explanation for the formation of large-scale jets is the Blandford-Znajek(BZ) process (Blandford & Znajek, 1977) that efficiently extracts the rotational energy of the black hole and the orbital energy of the accretion flow into an intense outflow of charged plasma at relativistic speeds along the axis of rotation. In the BZ process, the jet launching requires a massive, spinning Kerr black hole and an accretion disk threaded with strong poloidal magnetic field lines advected near the hole's outer horizon at the radius $R_H = (GM_{BH}/c^2)[1 + (1 - a^2)]^{1/2}$. Here 'a' is the specific angular momentum of the black hole.

In the previous section 4.4.3, we found that the jet power estimated for J2345-0449 can be achieved with a fast spinning, very massive black hole through the pure BZ process. There are other complex hybrid models of jet production mechanisms, which are combinations of Blandford-Payne (BP) (Blandford & Payne, 1982) and BZ mechanisms (Blandford & Znajek, 1977).

The results in the previous sections such as the WISE colour-colour plots, the optical spectrum, the low H_{α} and the 1.4 GHz radio luminosity values, all strongly supports a radiatively inefficient, low luminosity AGN (LLAGN) and LERG nature of J2345-0449. This strongly demands that the accretion process

in this galaxy is in the sub-Eddington rate. As ADAF states are characterised by geometrically thick disks, the favourable mechanism for jet launching is BZ process (McKinney, 2005).

So it is plausible that the unusual jet activity of J2345 - 0449 may have been triggered by the AGN accretion state switching from a previous high Eddington rate ($\lambda \gtrsim 10^{-2} - 10^{-3}$) to a sub - Eddington rate, where

$$\lambda = \dot{M}/\dot{M}_{Edd} \quad (4.7)$$

denotes the dimensionless mass accretion rate in units of the Eddington accretion rate \dot{M}_{Edd} . Many studies have supported strong relations between the accretion rates and jet formation. (Rees et al., 1982; Meier, 2001)

If accretion rate is above the critical value $\lambda_{crit} \sim 10^{-2} - 10^{-3}$, the disk structure is a standard Shakura and Sunyaev, radiatively efficient, geometrically thin disk (Shakura & Sunyaev, 1973), whereas at reduced accretion rates ($\lambda \ll \lambda_{crit}$), it leads to an ADAF state. In ADAF most of the heat generated by the local, turbulent viscous heating is rapidly advected inside the black hole horizon or released in a wind or radio jet. Thus, the radiative cooling efficiency of the geometrically thick, optically thin disk is greatly diminished (Narayan & Yi, 1994, 1995). In ADAF the inner region of the accretion disk gets extremely hot, forming a thick ion torus that helps to collimate the relativistic outflow into the “funnel” regions at the poles (Rees et al., 1982).

In J2345-0449 as the AGN is showing low-excitation and low-luminosity (LERG / LLAGN), and at the same time presenting very high kinetic luminosity in jetted outflows, establish the fact that the AGN is in an ADAF state.

4.5 Conclusions

The major results on the radio source J2345-0449 are summarised here.

1. The giant radio source J2345-0449 is a rare case of a megaparsec-scale radio jet launched by a spiral galaxy. It is the longest radio source observed so far, hosted by a spiral galaxy.
2. This radio source is DDRG, with a total linear size of 1.6 Mpc.
3. The flux density of the galaxy at 1.4 GHz, 610 MHz and 325 MHz are respectively 180mJy, 850 mJy and 940 mJy.
4. The integrated spectral index of the source is -1.16 ± 0.27 and the that of the outer lobe region is -1.3 ± 0.29 .
5. The spectral age of the source is obtained as $(50 - 120) \times 10^6$ years.
6. The radio morphology, luminosity value at 178 MHz ($L_{178} = 2.8 \times 10^{25} \text{ W Hz}^{-1}$) and the jet power suggest the FR II nature of this radio source.
7. The spiral nature of the host galaxy is revealed by the galaxy rotation curve.
8. The rotational velocity of the galaxy is very high and, its inclination corrected value is ~ 430 km/s.
9. The central velocity dispersion calculated for this galaxy is also high ($\sim 326 \pm 26$ km/s), suggesting the possibility of a huge black hole (up to $2.1 \times 10^9 M_{\odot}$) at its center. In this scenario, the pseudo-bulge nature of the galaxy is also very unusual.

10. The H_α luminosity of the source is small, suggesting the AGN as an LLAGN.
11. In the optical spectrum, the presence of very weak emission lines of H_α and NII alone are detected.
12. The WISE colour-colour plots, the absence of strong emission lines in the optical spectrum and the radio luminosity at 1.4 GHz, all propose the low excitation nature of the galaxy.
13. The extreme rotational velocity of the galaxy and the large-scale radio jets tempts to speculate the possibility of a more massive black hole at its center.
14. The low luminosity AGN and low excitation nature of this radio galaxy, together with the large-scale radio jets propose that AGN may be in an ADAF state.

Chapter 5

NVSS J102124+121702: A 2.2 mega parsec scale Giant Radio Galaxy, with a 650 kpc uninterrupted jet.

Radio sources with long uninterrupted radio jets in a scale of hundreds of kpc are rare, and hence are interesting. Understanding the driving force behind such highly collimated jets capable of proceeding through the Inter Galactic Medium (IGM) without invoking the onset of instabilities and subsequent disruption have been an enigma in jet science. [Bagchi et al. \(2007\)](#) reported an one-sided radio source CGCG 049-033, having a long uninterrupted radio jet to the extent of ~ 440 kpc, which is the longest one reported till date. Later [Hocuk & Barthel \(2010\)](#) reported a straight quasar jet in 4C 34.47, with a projected length of ~ 380 kpc. In this chapter we report the study of a source *2MASX J10212421 +*

1217060, (hereafter J1021+1217) at redshift $z = 0.129$ coinciding with a 15' radio source in the NVSS VLA database (Condon et al., 1998), with a projected linear size of ~ 2 Mpc. This source has been identified as an FRII radio galaxy by Koziel-Wierzbowska & Stasińska (2011). We proposed deep observations on this source using GMRT at two frequencies 610 MHz and 325 MHz, to produce high resolution maps to study the structural details. Our radio observations and further analysis have revealed that this source is very unusual due to its jet size and morphology. A redshift of 0.129 implies a scale of $2.318 \text{ kpc arcsec}^{-1}$ and a luminosity distance of 609 Mpc.

5.1 Previous observations

The galactic environment of J1021+1217 is shown in the $15' \times 15'$ colour composite image from the SDSS (Figure 5.1). This source is ~ 12 arcmin (~ 1.66 Mpc) away from the galaxy cluster GMBCG J102053.2+120749 (Hao et al., 2010), which is at a redshift of 0.1289 with a mass of $2.9 \times 10^{14} M_{\odot}$ and a virial radius of 1.29 Mpc. Since this GRG is well beyond the virial radius of 1.29 Mpc, it is not part of this cluster, but is a field galaxy at the periphery. We have marked 14 galactic cluster members in figure 5.1, for which spectroscopic redshift values available in SDSS.

J1021+1217 is identified as an Elliptical galaxy (type E2) with an angular size of $0.28' \times 0.20'$ corresponding to a linear size of 39×28 kpc. The global parameters of the source are given in Table 5.1 and SDSS magnitudes and colours are in Table 5.2. This source is also detected in WISE and 2MASS wavelength bands.

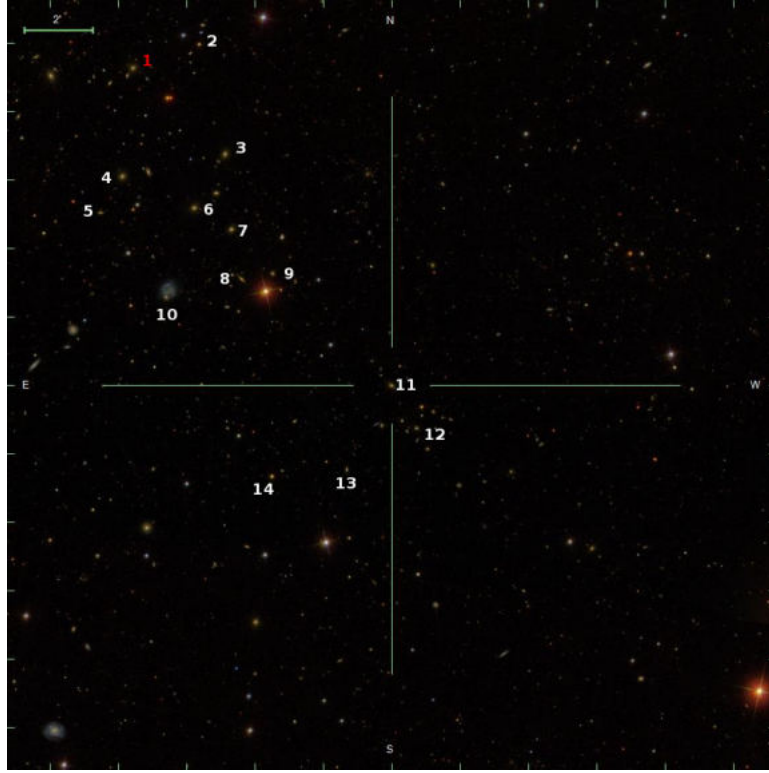


FIGURE 5.1: $22' \times 22'$ colour composite image of J1021+1217 from SDSS . J1021+1217 is labelled as '1'. The image center coincides with the cluster center galaxy. All the 14 galaxies labelled in the image are having redshift values around 0.130.

The radio image at 1.4GHz is available in the NVSS VLA data base (See Figure 5.2), with a resolution of $45'' \times 45''$ (Condon et al., 1998). The radio source appears as a double double radio galaxy with two lobes each on either side of the core. The total flux density is obtained as 138 ± 12 mJy. (All flux values are measured above 3σ cut off) The northern inner lobe and southern inner jet are found to have flux densities 24mJy and 44 mJy respectively. Similarly, the northern and southern outer lobes are found to have flux densities 37mJy and 15 mJy respectively. The core flux density is 18mJy (see Table 5.3). The total

TABLE 5.1: Global parameters of NVSS J102124+121702. Ref. <https://ned.ipac.caltech.edu/>; (Skrutskie et al., 2006b; Best & Heckman, 2012; Koziel-Wierzbowska & Stasińska, 2011)

RA& DEC	$10^h 21^m 24.2^s; +12^d 17^m 05^s$
Morph	E2
Magnitude(<i>SDSSg</i>)	17.6
Size	$0.28'' \times 0.20''$
Distance(Mpc)	609
Redshift(<i>z</i>)	0.129
Radial Velocity(km s ⁻¹)	38787

TABLE 5.2: SDSS magnitudes and SDSS colours of the Galaxy J1021+1217. Ref: SDSS Data base <http://www.sdss.org>

SDSS Magnitudes					SDSS Colours		
<i>u</i>	<i>g</i>	<i>r</i>	<i>i</i>	<i>z</i>	<i>g - r</i>	<i>r - i</i>	<i>i - z</i>
19.63±0.7	17.61 ±0.01	16.5±0.0	15.99±0.0	15.59 ± 0.01	1.11	0.51	0.40

linear size of the source at this frequency is ~ 2.1 Mpc. This corresponds to a radio luminosity of $L_{1.4} = 6.33 \times 10^{24} W Hz^{-1}$.

5.2 Results

5.2.1 GMRT radio images and map parameters

We observed the source at frequencies 610 MHz and 325 MHz respectively on 7th and 14th of January 2014, using GMRT. We used the 512 channel correlator with a total bandwidth of 32 MHz. Flux calibrators 3C147 and 3C286 were

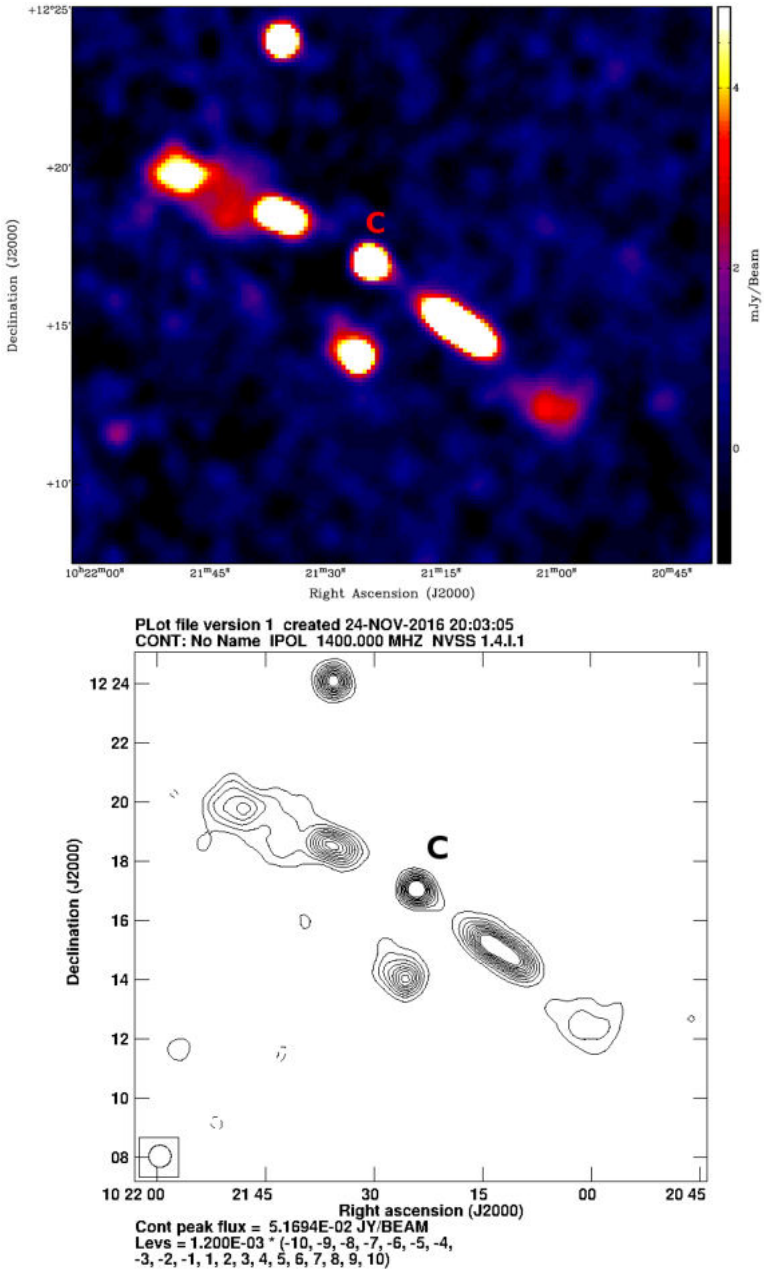


FIGURE 5.2: Top panel: NVSS VLA Image of the radio source at 1.4GHz with resolution $45'' \times 45''$. Bottom panel: The contour plot of NVSS image. The core is marked as 'C' in both the images.

observed for ten minutes each at the beginning and end of the observations to compute flux and to do bandpass calibration. The sources J1021+219 and J1123+055 were used as phase calibrators. The data are analysed as discussed in chapter 2.

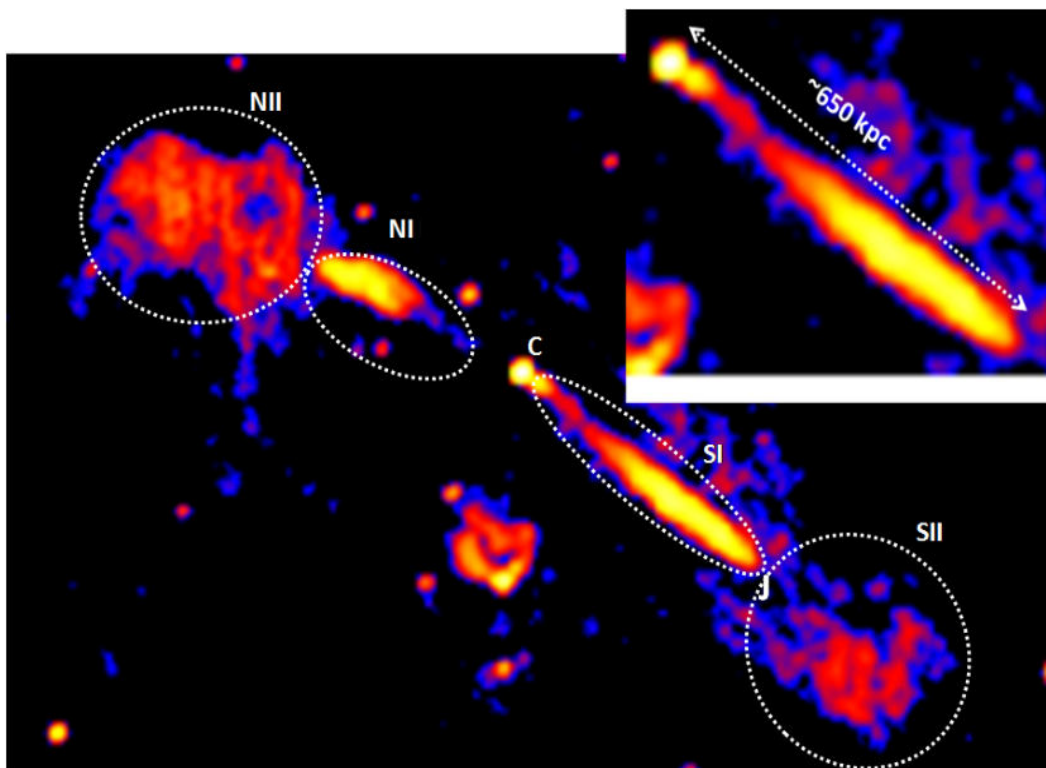


FIGURE 5.3: 610 MHz GMRT map of J1021+1217 with $12'' \times 12''$ resolution and $70 \mu\text{Jy beam}^{-1}$ rms.; The inset image shows the uninterrupted jet of linear size 650 kpc towards south. The core is marked as 'c'.

The low-frequency radio map obtained from GMRT observations at 610 MHz is shown in Figure 5.3 and the corresponding contour plot in Figure 5.4. The resolution of 610 MHz map is $12'' \times 12''$ and the background rms is $70 \mu\text{Jy beam}^{-1}$. The total flux density at this frequency is obtained as 336 mJy . The flux densities of the northern and southern inner regions (NI and SI) are

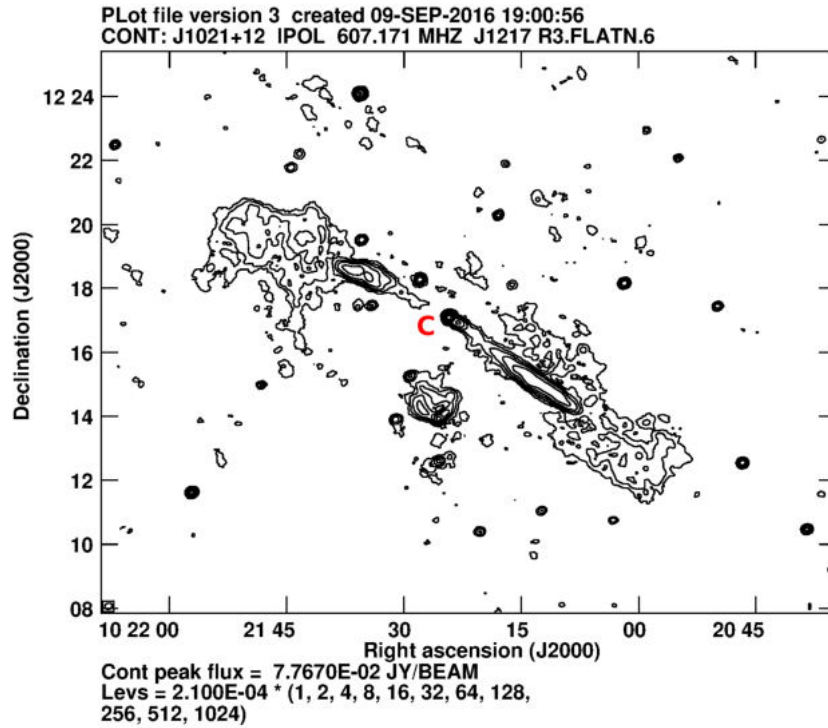


FIGURE 5.4: GMRT 610 MHz radio contour map of J1021+1217 with levels [1, 2, 4, 8, 16,...] $\times 210 \mu\text{Jy}/\text{beam}$ and resolution $12'' \times 12''$.

measured to be 47 and 103 mJy respectively. The outer diffuse relic lobes on the north(NII) and south(SII) have flux densities 107 mJy and 62 mJy respectively. The total angular size of the source is 947 arcsecs, and the corresponding linear size is 2.2 Mpc. The core size of this source is determined using JMFIT and is obtained as $3.84'' \times 3.58''$ (see section 2.1.1.4).

The 325 MHz GMRT map with a resolution of $20'' \times 20''$ and background $\text{rms} = 200 \mu\text{Jy beam}^{-1}$ is shown in Figure 5.5. At this frequency, the total flux density is obtained as 527 mJy. The flux densities of the the NI and SI regions are 75 mJy and 168 mJy respectively. The outer relic lobes NII and SII

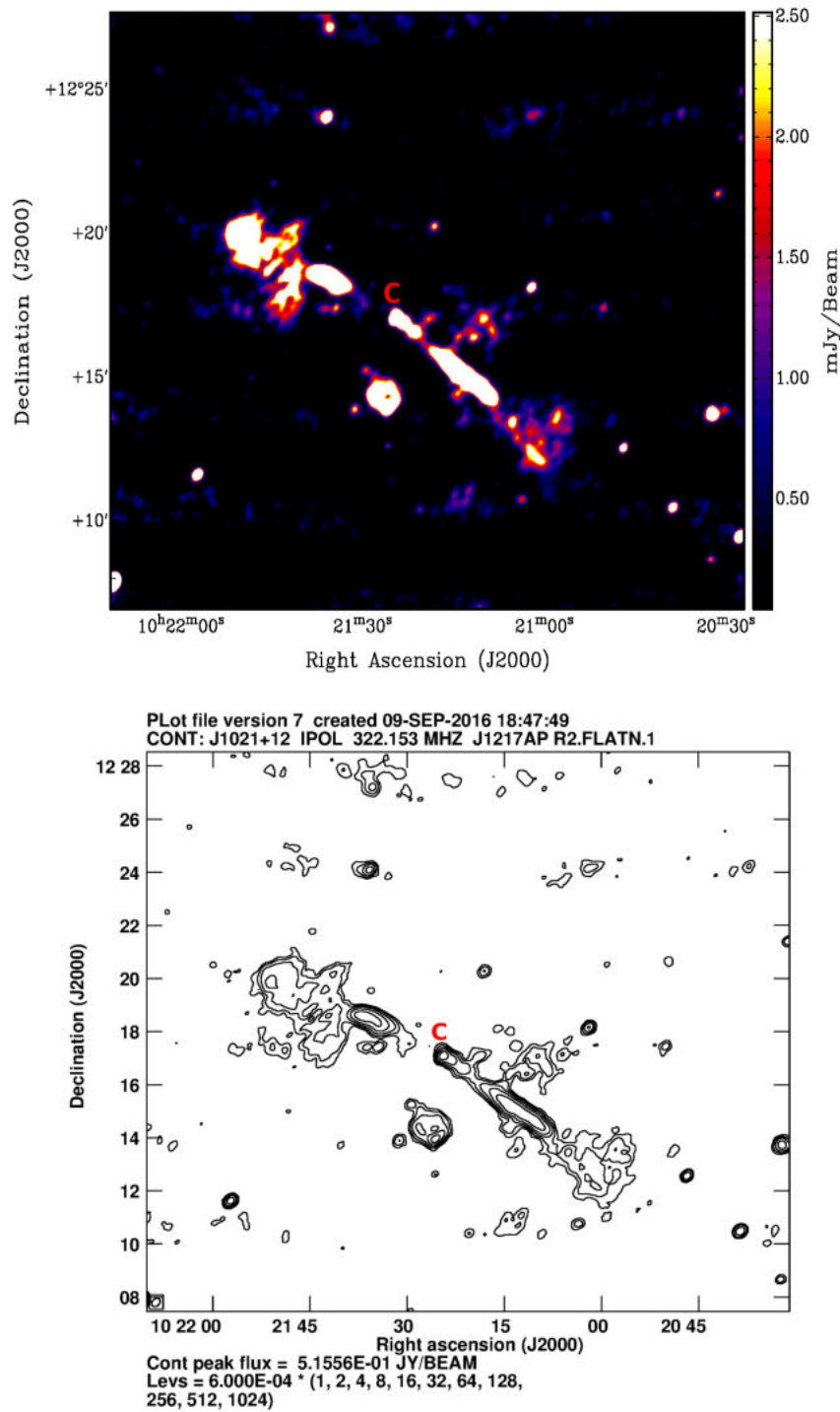


FIGURE 5.5: Top Panel: Coloured GMRT image at 325 MHz with $20'' \times 20''$ resolution. Bottom Panel: contour plot with levels $[1, 2, 4, 8, \dots, 1024] \times 600 \mu\text{Jy}$

are having flux densities 194 mJy and 73 mJy respectively while the core flux density is found to be 17 mJy (see Table 5.3). The total angular size of the source is 940 arcsecs and, the corresponding linear size is 2.2 Mpc.

In 610 MHz GMRT map (see Figure 5.3) the entire radio source extends from the region NII to SII. There are relatively diffuse low surface brightness lobes (NII and SII) on either extremity of the source. Of these lobes, the southern lobe SII is observed to be more diffuse than the northern lobe NII. We can see a compact inner lobe (NI) of high surface brightness, in the north of the core. There is also a high surface brightness jet structure seen towards the south, extending from C to ‘J’ in the region SI.

The jet formation in radio galaxies is related to the gravitational accretion of matter onto the SMBH (Lynden-Bell, 1969; Soltan, 1982). This process can be intermittent, and as a result of which, the newly formed jet will propagate through the cocoon material left over by the earlier episode. And this may create a new pair of lobes inside this cocoon material (Konar et al., 2012, 2013). Which can be observed from the structural details and the spectral ageing analysis of the source. In the case of J1021+1217, the structural details and the difference in surface brightness between the inner and outer regions, indicates that they have originated from different epochs AGN activity. This can be further confirmed by the observed steep spectral index values (up to -2) of the outer lobes, observed in the spectral index maps (discussed in the next section 5.2.2).

Though the end of the southern inner jet is brighter, it is not ending up to a clear lobe, due to the lack of significant backflow. The Figure 5.6 shows contour plots of the inner southern jet at 610 MHz from images with $6'' \times 6''$ and $12'' \times 12''$ resolutions (These are prepared with AIPS Robust parameter ‘0’ and ‘2’ while imaging. Refer section 2.1.1.2 in chapter 2). The source can not be

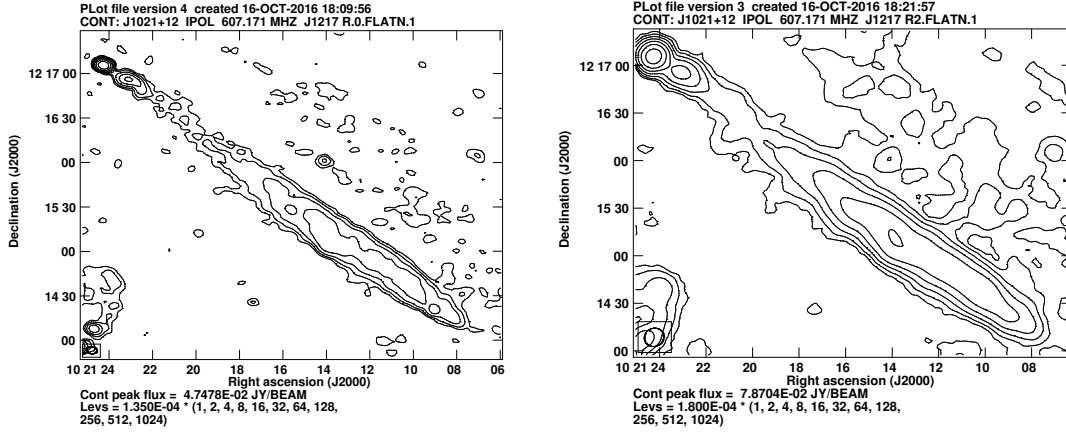


FIGURE 5.6: Radio contours of the inner southern lobe of J1021+1217 at 610 MHz, from maps of different resolution. Left panel is that from an image with a resolution of $6'' \times 6''$ (Robust=0) and the Right panel is that from a map with a resolution of $12'' \times 12''$ (Robust=2).

attributed the status of a DDRG since an edge brightened lobe is not formed in the southern jet.

From the radio maps it is observed that the southern jet is having an angular size of $\sim 286''$ which corresponds to a linear size of $663kpc$ (in the scale $1'' = 2.318kpc$). This gives it the status of the longest uninterrupted radio jet reported so far (Bagchi et al., 2007; Hocuk & Barthel, 2010; Conway et al., 1993; Willis et al., 1982). At present the longest radio jet reported is in a one-sided radio source CGCG 049-033, having an uninterrupted radio jet to the extent of ~ 440 kpc (Bagchi et al., 2007). The jet associated with J1021+1217 is having $\sim 200kpc$ more length than that of CGCG 049-033.

The luminosities of the source at 610 and 325 MHz frequencies are given by $L_{610} = 1.85 \times 10^{32} \text{ ergs sec}^{-1} Hz^{-1}$ and $L_{325} = 2.7 \times 10^{32} \text{ ergs sec}^{-1} Hz^{-1}$ respectively. The source can be classified as a LERG since the radio luminosity at

1.4GHz, $L_{1.4} = 6.33 \times 10^{24} \text{ W Hz}^{-1}$, is below the dividing value ($\sim 10^{26} \text{ W Hz}^{-1}$) between LERGs and HERGs (Best & Heckman, 2012). Further discussions on WISE magnitudes and optical spectrum support this (sections 5.2.5 & 5.2.4).

5.2.2 Spectral index maps and radio spectral properties

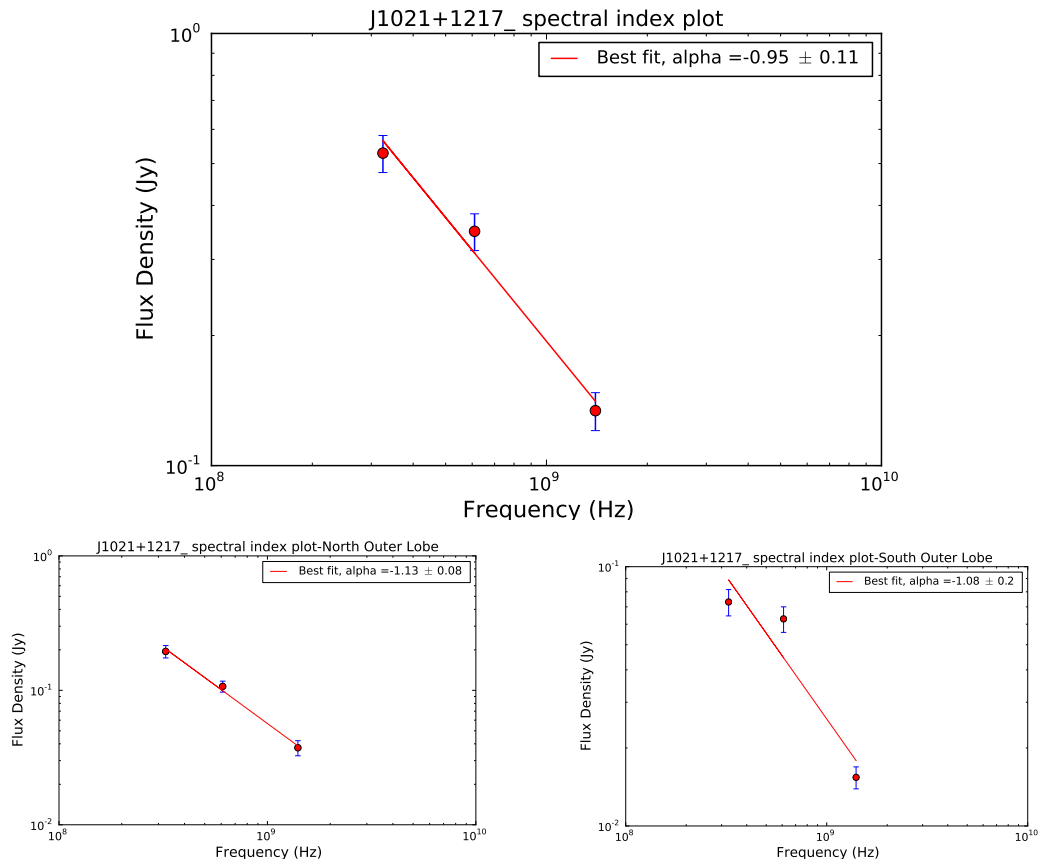


FIGURE 5.7: Top panel: The integrated spectral index of J1021+1217 is -0.95 ± 0.11 (See Top Panel). Integrated Spectral index of the northern outer lobe is -1.13 ± 0.08 (See Bottom left Panel). Integrated Spectral index of the southern outer lobe is -1.08 ± 0.20 (See Bottom right Panel).

The integrated spectrum of J1021+1217 shows an overall steep spectrum from 1.4 GHz to 325 MHz. The 1.4 GHz data point is obtained from the archive and the other rest from GMRT observations. The best fit integrated spectral index is obtained as -0.95 ± 0.11 . The spectral indices of the northern and southern diffuse outer lobes (NII and SII) are estimated as -1.13 ± 0.08 and -1.08 ± 0.20 respectively (see Figure 5.7). Similarly the integrated spectral indices of the SI and NI regions are obtained as -0.91 ± 0.07 and -0.77 ± 0.02 respectively. The average spectral index of the outer regions (NII and SII) is ~ -1.1 , while that of the inner regions (SI and NI) is ~ -0.84 , indicating that they are from different epochs of AGN activity. Table 5.3 shows the flux values corresponding to different regions of the source at various frequencies.

The steep spectral nature of the northern and southern outer relic regions can be observed from Figure 5.8 (see Table 5.3). The second order polynomial fit for the data points from NII and SII regions shows clear curvature. A rough estimate of the spectral break frequency is obtained from the intersecting points of the tangents drawn at 1.4 GHz and 325 MHz. The values obtained are 670 MHz and 684 MHz for the NII and SII regions respectively (see Figure 5.8).

The electron spectral age t_{sp} (cooling time scale) of the source can be estimated from the synchrotron radio spectrum using the equation 3.1 (Murgia et al., 2011).

$$t_{sp} = 1.59 \times 10^9 \left[\frac{B^{1/2}}{[B^2 + B_{IC}^2] [\nu_b(1+z)]^{1/2}} \right] yrs \quad (5.1)$$

With a break frequency, $\nu_b = 0.68$ GHz, obtained from the relic plasma regions NII and SII, and using a magnetic field range $B = 1 - 10 \mu G$ (applicable to relic regions), the electron spectral age is obtained to be $t_{sp} = (99 - 48) \times 10^6$ years.

If the time interval between the two consecutive ON periods of an AGN with recurrent activity is small, the jet produced in the second episode may advance through the medium with a speed in between 0.19c to 0.57c, for angle θ between 45° and 135° (Here θ is the angle between the jet direction and the line of sight) [Schoenmakers et al. \(2000b\)](#). From the knowledge of the speed of jet head and assuming that the OFF period of the AGN is very small, we can estimate a lower limit to the age of the AGN ([Schoenmakers et al., 2000b](#)) as the time required by it to reach the end of the lobes from its core. For J1021+1217, the radio structure extends to ~ 500 arcsecs from the core to either direction in 610 and 325 MHz GMRT maps. This corresponds to a linear distance of $500 \times 2.318 \text{ kpc} = 1159 \text{ kpc}$. If the jet is assumed to have a speed of $\sim 0.5c$, the time required by the jet to cover the distance 1159 kpc is $\sim 7.56 \times 10^6$ years. This gives only a lower limit to the age of the source.

TABLE 5.3: S_ν (Jy) is shown below for different regions at various frequencies.

Region	S_ν (mJy) 1.4 GHz	S_ν (mJy) 610 MHz	S_ν (mJy) 325 MHz
Northern outer region (NII)	37	107	194
Northern inner region (NI)	24	47	75
core (C)	18	17	17
Southern inner region (SI)	44	103	168
Southern outer region (SII)	15	62	73
Total flux	138	336	527

For a better understanding of the physical nature of the source the spectral index maps are created after convolving the radio maps to the same resolution. The spectral index maps between 1.4GHz vs 325 MHz and 325 MHz vs 610 MHz along with the error maps are given in figure [5.9](#) and [5.10](#) respectively. The core region shows flat-spectral index of ~ -0.5 while the inner regions(NI & SI)

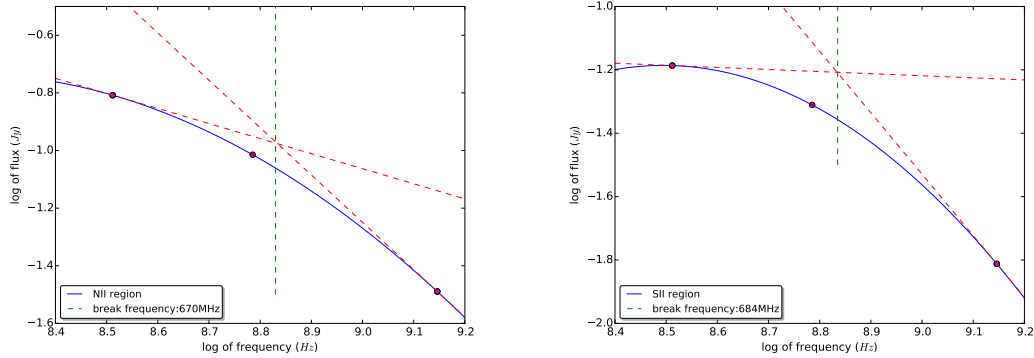


FIGURE 5.8: Second order polynomial fit for region NII with tangents drawn at 1.4 GHz and 325 MHz. Left panel: NII region Right panel: SII region.

exhibit a spectral index between -0.5 and -0.8. It can be noted that in both the maps the southern relic lobe exhibits a flat-spectrum spot, while this feature is absent in its counter part. This may be due to the jet from the earlier episode still reaching the relic lobe. The steep spectral index values up to -2 observed in the outer lobes indicate the presence of old plasma.

Some earlier studies have shown that, if the jet feeding the hotspots are interrupted (ie. when AGN activity stops), the hotspots may fade away in a relatively smaller time of 10^4 to 10^5 years (Schoenmakers et al., 2000b,c). If a hotspot appears on the outer lobe of a radio source with recurrent activity, it indicates that the jet from the previous epoch had been reaching there very recently (Schoenmakers et al., 2000b,c). This can happen when the AGN off time is relatively small (Schoenmakers et al., 2000b). It is proposed that J1021+1217 is a similar case.

J1021+1217 can be classified as an FR II radio source since its radio luminosity $L_{178} = 4.34 \times 10^{25} \text{ WHz}^{-1}$ (derived using the integrated spectral index $\alpha = -0.95$), is above $2 \times 10^{25} \text{ WHz}^{-1}$ (Fanaroff & Riley, 1974).

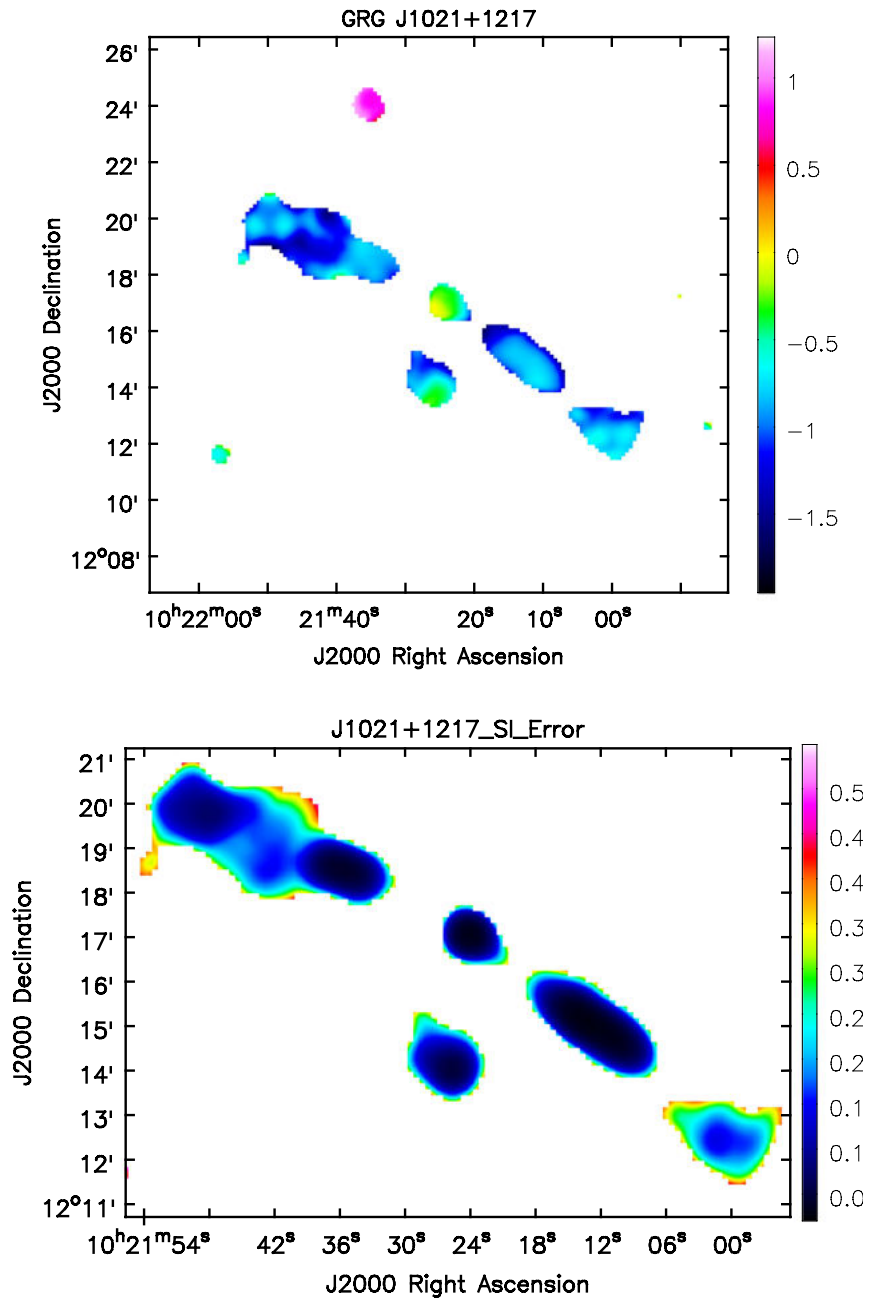


FIGURE 5.9: **Top panel:** The spectral index map generated between 1.4 GHz and 610 MHz GMRT images. **Bottom Panel:** The error map.

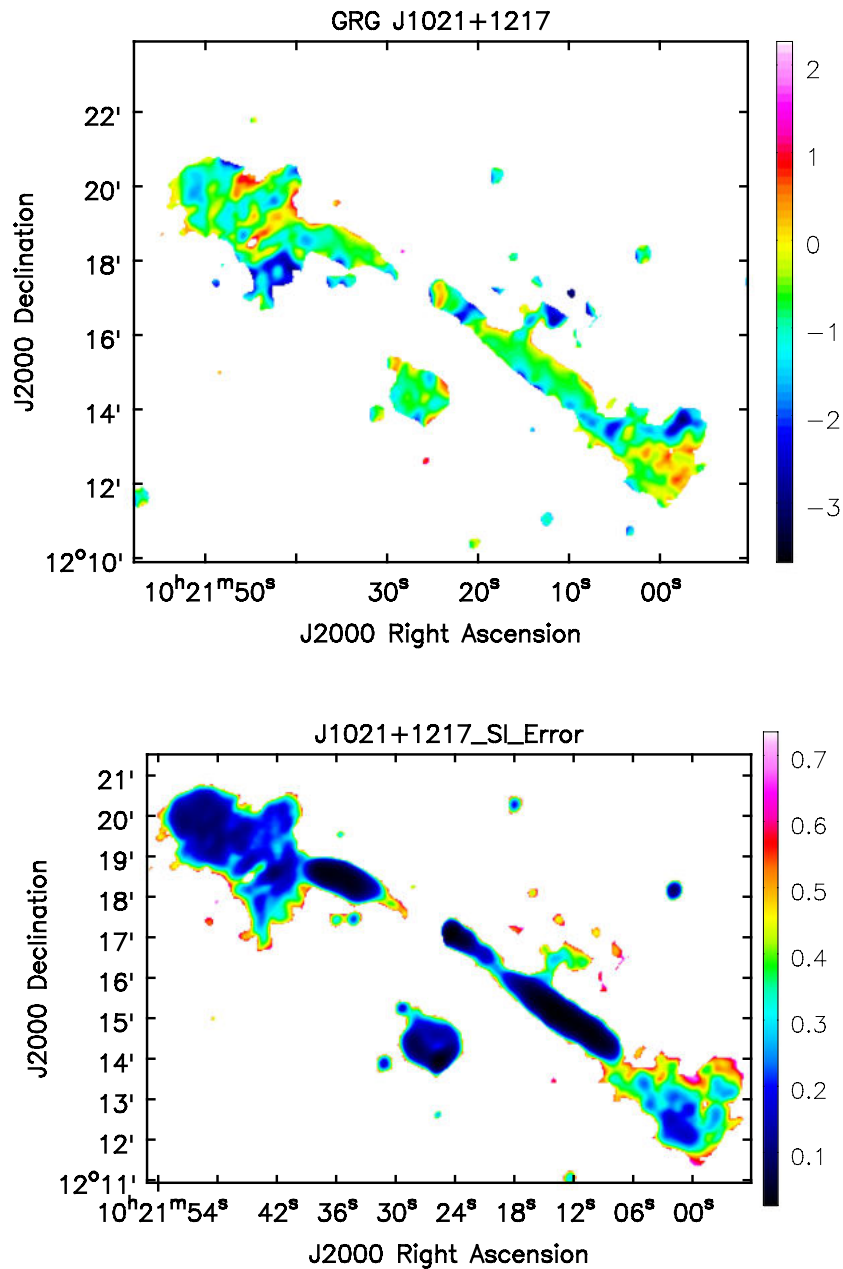


FIGURE 5.10: **Top panel:**The spectral index map generated between 610 MHz and 325 MHz GMRT images. **Bottom Panel:** The error map.

5.2.3 Jet power calculations

The jet kinetic power (\bar{Q}) of a radio source carries information regarding the state of the accreting SMBH system; its mass, spin and the magnetic field.

We have estimated the 151 MHz flux density of the outer lobe of J1021+1217 as 1.61 Jy from radio spectral index $\alpha = -1.1$. Using the calibration relation (Punsly & Zhang, 2011; Daly et al., 2012)

$$\bar{Q} \approx 1.1 \times 10^{45} [(1+z)^{1+\alpha} Z^2 F_{151}]^{6/7} \text{ ergs}^{-1} \quad (5.2)$$

where,

$$Z \equiv 3.31 - (3.65) [(1+z)^4 - 0.203(1+z)^3 + 0.749(1+z)^2 + 0.444(1+z) + 0.205]^{-0.125} \quad (5.3)$$

and F_{151} is the flux density from the lobes. \bar{Q} which is likely to be a lower limit, is estimated as $\bar{Q} \approx 6.0 \times 10^{43} \text{ erg s}^{-1}$ for the (time-averaged) jet kinetic power in J1021+1217. We have not corrected for the (unknown) loss of energy in the outer radio lobes. This indicates that (as $\bar{Q} \geq 5 \times 10^{43} \text{ erg s}^{-1}$), J1021+1217 is an FR II source (Rawlings & Saunders, 1991).

5.2.4 WISE mid infrared colours

The elliptical galaxy J1021+1217 is strongly detected in mid-IR bands centered at 3.4, 4.6, 12 and 22 μm (W1, W2, W3 and W4 bands) observed by the WISE satellite Wright et al. (2010). The signal to noise ratio (SNR) ranges from 42.7 in 3.4 μm band to 3.5 in 22 μm band. The MIR magnitudes, errors, luminosities and SNR are listed in Table 5.4. It had been shown that WISE

MIR colours can distinguish AGN from star forming and passive galaxies. The WISE colour-colour plots distinguishes the LERGs and HERGs as two distinct populations (Gürkan et al., 2014). The derived MIR colours for this source are:

$$[W1 - W2] = 0.305, [W2 - W3] = 1.848, [W2 - W4] = 4.785 \quad (5.4)$$

TABLE 5.4: WISE mid-infrared magnitudes and luminosities for J1021+1217 is shown below. The second row shows the derived luminosities in ergs s^{-1} . The third row shows the signal-to-noise ratios of detection in four bands.

WISE band (Wavelength)	W1 3.4 μm	W2 4.6 μm	W3 12 μm	W4 22 μm
Magnitude	13.338 ± 0.025	13.033 ± 0.029	11.185 ± 0.159	8.248 ± 0.312
Luminosity	5.60×10^{43}	3.04×10^{43}	1.18×10^{43}	2.54×10^{43}
SNR	42.7	36.9	6.8	3.5

The Figure 5.11 shows the wise colour-colour plots comprising of LERGs, HERGs, NLRGs, BLRGs and QSOs. From the position of J1021+1217, in the WISE colour- colour plot of W1-W2 vs W2-W3, it can be identified as a LERG. Similarly in the W1-W2 vs W2-W4 plot the source position is in the region, where LERGs cluster (Gürkan et al., 2014).

The 22 μm luminosity of J1021+1217 is $2.54 \times 10^{43} \text{erg s}^{-1}$, which is much below the threshold value ($5 \times 10^{43} \text{erg s}^{-1}$) between LERGs and HERGs. From the integrated spectral index of $\alpha = 0.95$ the radio luminosity of J1021+1217 at 151 MHz is calculated as $L_{151} = 7.7 \times 10^{40} \text{ergs S}^{-1}$. In the 22 μm luminosity versus L_{151} radio luminosity plot, also J1021+1217 falls in the group of LERGs (see Figure 5.12)(Gürkan et al., 2014).

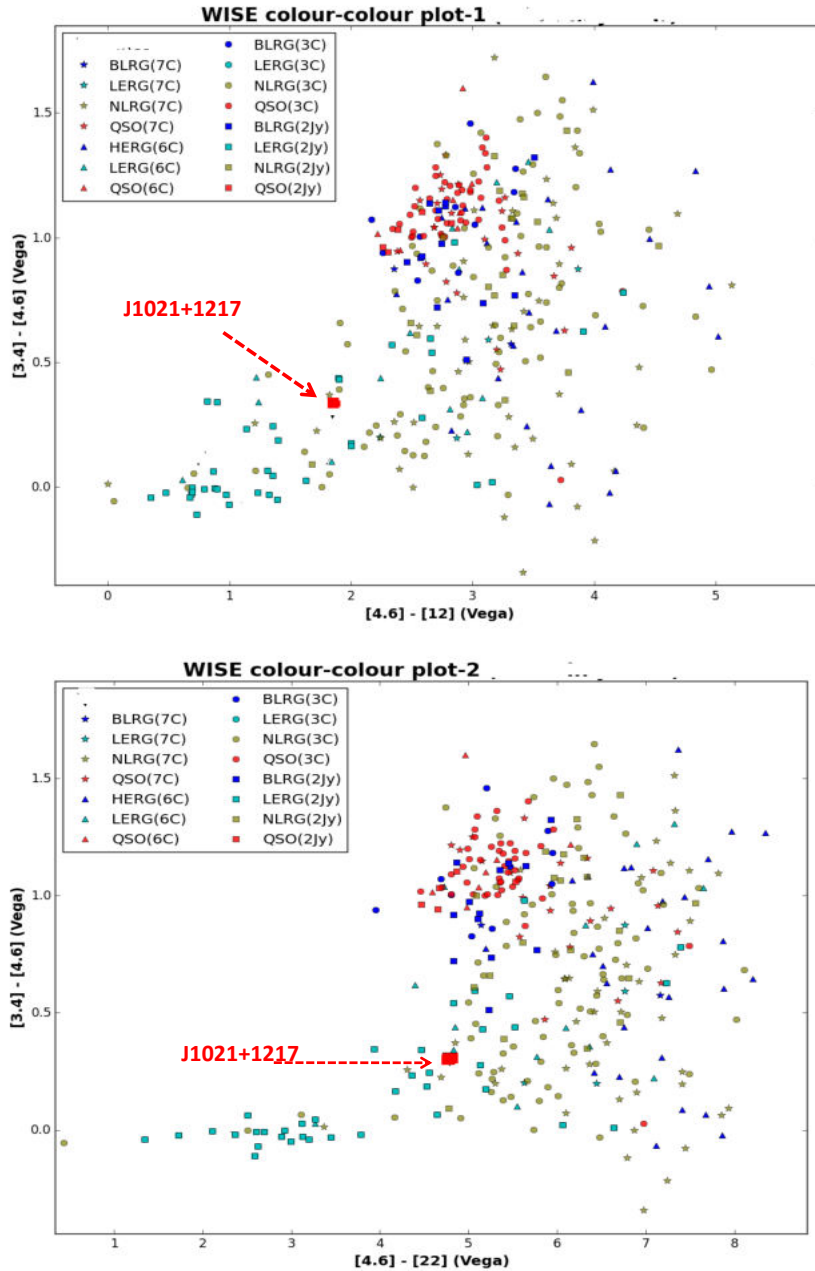


FIGURE 5.11: Top panel: WISE colour-colour plot between W1-W2 and W2-W3. Bottom Panel: WISE colour-colour plot between W1-W2 and W2-W4. In both the plots red square shows the position of J1021+1217 (Wright et al., 2010; Gürkan et al., 2014).

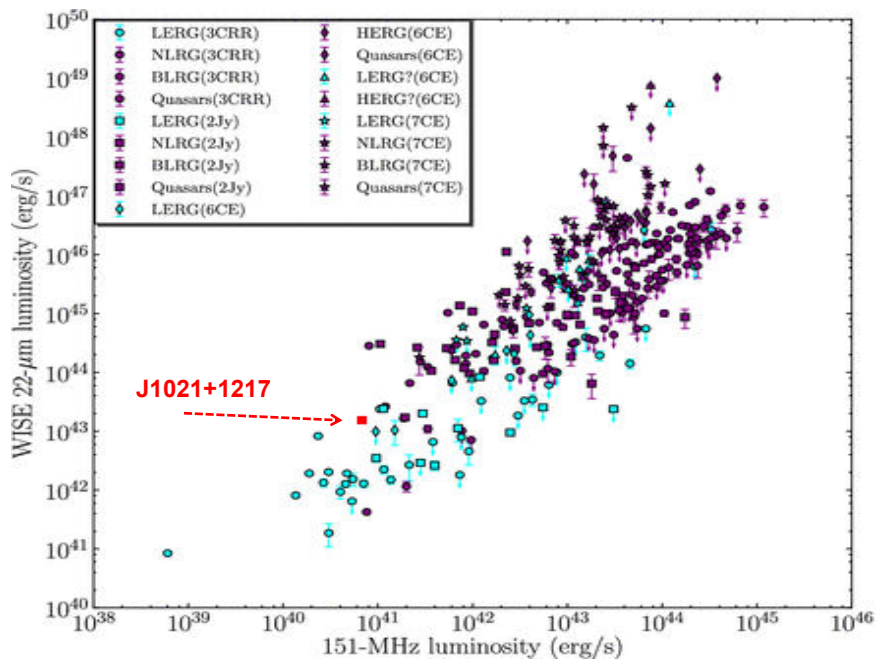


FIGURE 5.12: $22\ \mu\text{m}$ luminosity versus L_{151} radio luminosity plot. The position of J1021+1217 is marked in red (Gürkan et al., 2014).

The optical spectroscopic results discussed in the next section also shows that J1021+1217 is a LERG hosted by an elliptical galaxy. The central black hole may be ADAF state, accreting at low Eddington rates (Narayan & Yi, 1994, 1995).

5.2.5 Optical spectroscopic results

We studied the optical emission line parameters of J1021+1217 using spectroscopic data available in SDSS. From the optical spectrum shown in Fig. 5.13, it is observed that, the Balmer H_α $\lambda 6564\text{\AA}$ line is blended with forbidden lines [N II] $\lambda 6548\text{\AA}$

TABLE 5.5: Optical emission line parameters

Parameter	NVSS J102124+121702	
	flux ($\times 10^{-15}$ ergs $\text{cm}^{-2}\text{s}^{-1}$)	FWHM (km s^{-1})
H_α	1.30 ± 0.004	714
[N II] λ 6583	1.36 ± 0.006	716
[S II] λ 6716	0.47 ± 0.005	561
[S II] λ 6731	0.46 ± 0.009	560
[O I] λ 6300	0.26 ± 0.002	894
$H\beta$	0.24 ± 0.004	526
[O III] λ 5007	0.45 ± 0.007	664

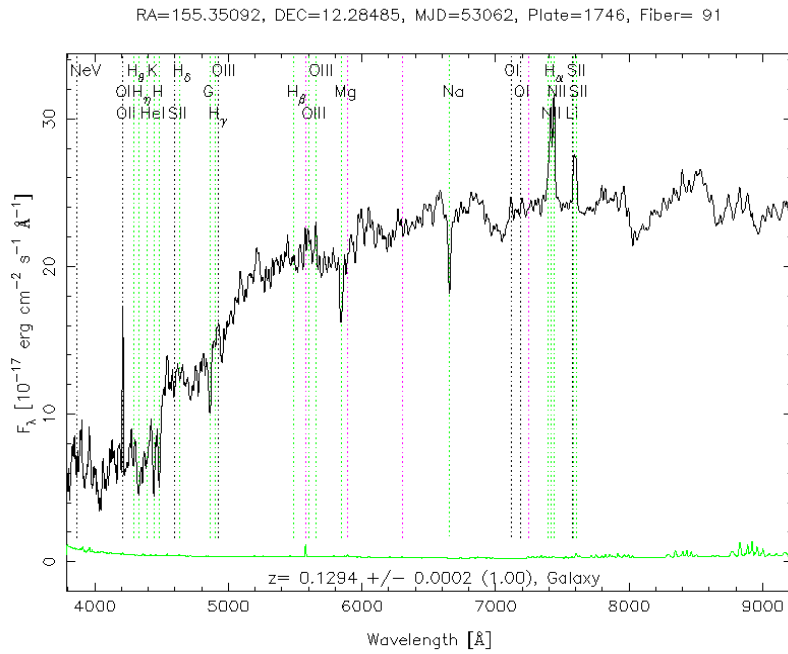


FIGURE 5.13: The optical spectrum of J1021+1217, from SDSS

and [N II] λ 6583 \AA and the Balmer H_β line is very weak. Parameters of the prominent emission lines are measured and are listed in Table 5.5. The FWHM of the H_α -line is similar to those of forbidden lines [N II], and [S II] within the errors. This shows that only a narrow component of H_α is present in the spectrum of J1021+1217.

The H_α luminosity of this source is estimated as $4.24 \times 10^{40} \text{ erg s}^{-1}$. According to Ho et al. (1997), an H_α luminosity $\leq 10^{40} \text{ erg s}^{-1}$ and weak emission lines are the characteristic features of an LLAGN. We have also estimated the Excitation Index (EI) of the source, and is obtained as -0.56, confirming its LERG nature ($\text{EI} \leq 0.95$) (see section 1.2.1.2; equation 1.1) (Buttiglione et al., 2010).

From the Estimated stellar velocity dispersion of $221 \pm 13 \text{ km s}^{-1}$, the mass of the SMBH is calculated using the formula

$$\log_{10}(M_{BH}/M_\odot) = 8.38 + 4.53 \log_{10}(\sigma/200 \text{ km s}^{-1}) \quad (5.5)$$

where σ is the velocity dispersion in km/s (McConnell et al., 2011). It is obtained is $3.77 \pm 1.0 \times 10^8 M_\odot$.

The mass of the central black hole can also be determined by the M_K (K band absolute magnitude) vs M_{BH} relation (Graham, 2007)

$$\log_{10}(M_{BH}/M_\odot) = -0.38(\pm 0.06)(M_K + 24) + 8.26 \pm 0.11 \quad (5.6)$$

This gives a value of $3.69 \pm 1.05 \times 10^8 M_\odot$ comparable with the previous estimate. These black hole mass values are more than the minimum value suggested for the production of large scale relativistic jets in radio galaxies and radio quasars is $\geq 10^8 M_\odot$ (Laor, 2000; Gopal-Krishna et al., 2008; Sikora et al., 2007).

5.3 Discussion

The observed presence of narrow emission lines in the optical spectrum and the low values of the H_α luminosity and the Excitation Index indicates that the radio AGN belongs to a low-luminosity and low-excitation class (LLAGN/LERG). This is also confirmed by the WISE colour-colour plots and the radio luminosity at 1.4GHz. The jet power of this source is estimated as $\bar{Q} \approx 6.0 \times 10^{43} \text{erg s}^{-1}$, which is comparatively high. Here, though the radio AGN is radiatively inefficient, the jet output power is high. Such a situation happens in AGNs which are in ADAF states.

ADAF state of an AGN is characterised by the geometrically thick and optically thin accretion disk. Here the radiative cooling efficiency of the accretion disk will be small, and hence the energy will be liberated through jetted outflows (See the section 4.4.4). In BZ process, the jet power relates to the black hole and magnetic properties as given in equation 3.4 as,

$$\bar{Q}_{44} \approx 0.2 M_8^2 a^2 B_4^2, \quad (5.7)$$

where, $\bar{Q}_{44} = \bar{Q}/10^{44} \text{ erg s}^{-1}$, the BH mass $M_8 = M_{\text{BH}}/10^8 M_\odot$, the poloidal magnetic field $B_4 = B/10^4 \text{ Gauss}$ and the dimensionless spin parameter $a = cJ_{\text{BH}}/GM_{\text{BH}}^2$, J_{BH} is BH's angular momentum (Blandford & Znajek, 1977; MacDonald & Thorne, 1982a; Tchekhovskoy et al., 2010).

The BH mass of this source is $3.77 \times 10^8 M_\odot$ and the magnetic field required to produce the estimated jet power ($\approx 6.0 \times 10^{43} \text{erg s}^{-1}$) through BZ mechanism (Blandford & Znajek, 1977) for a slow spinning ($a=0.1$) black hole is $\sim 5 \times 10^4 \text{ Gauss}$. The maximum magnetic field that can be created is the Eddington magnetic field when the AGN accretes in the Eddington rate, and which is obtained

as $1.1 \times 10^5 Gauss$. So for this source, a slow spinning black hole is sufficient to produce a radio jet with the observed jet power.

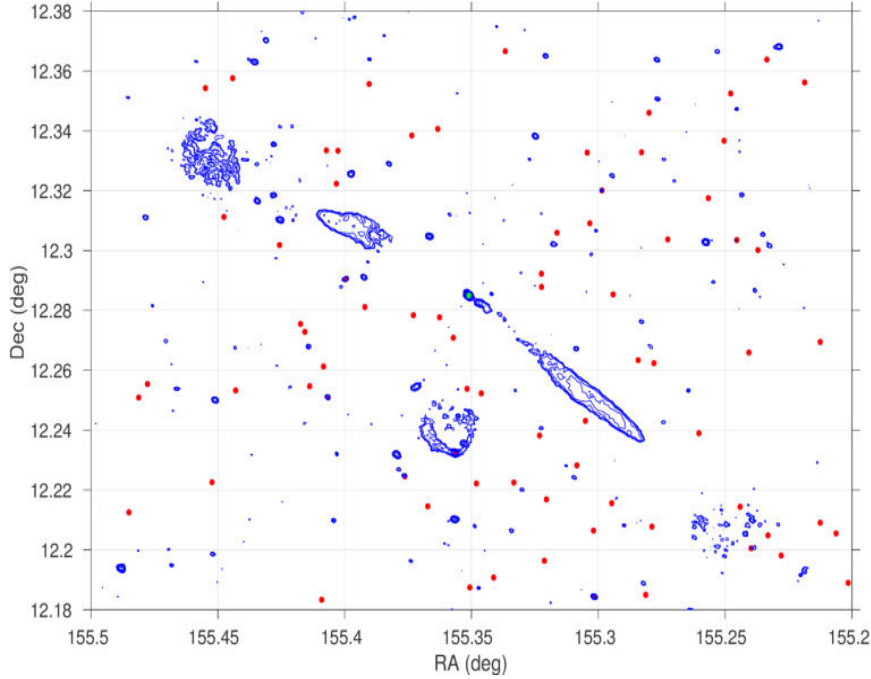


FIGURE 5.14: Galaxies around the GRGs plotted. Blue lines are radio contours, red dots are galaxies around the GRG, and the green dot is the host galaxy of the GRG

The high value of \bar{Q} in J1021+1217 is clearly above the FR I/FR II dividing value suggestive of a highly efficient, supersonic jet ejection (Rawlings & Saunders, 1991). The electron spectral age calculations for the relic plasma give an age of $(47-90) \times 10^6$ years. The dynamic age calculated with a plasma velocity of $\sim 0.5c$ gives a value of $\sim 7 \times 10^6$ years. Also, spectral index plots show a flat spectrum region in the extremities of the southern outer lobe which is an indication that the jet from the previous episode of activity may be still reaching the outer lobes or had been reaching there very recently. In such a case when the second episode of activity starts without much OFF period of the central AGN,

the newly generated jet will advance through a medium which is relatively less dense than the ICM, as it is propagating through the same channel of the former jet. For the jets to form a lobe, the medium should be sufficiently dense. As a result of which the jet of the second episode can advance more distance in shorter period. We conclude this as the reason for the formation of the uninterrupted long jet in J1021+1217.

In addition to the points discussed above, we have also plotted the 610 MHz radio map of this source with the surrounding galaxies (Figure 5.14), to study the environment of the radio source. We have chosen all nearby galaxies which are having redshift values between 0.0176 and 0.076 (i.e. between 0.126 ± 0.05). But as the number of galaxies in this field having spectroscopic redshift is less, we have selected galaxies from SDSS, having the photometric redshifts. The figure shows that, the host galaxy is residing away from the cluster centers, in a sparse environment. It is clear that environment also has played a role, in the production of such a large scale jet of ~ 650 kpc in length.

5.4 Conclusions

The results of the radio and optical studies of J1021+1217 can be summarised as below.

1. The GMRT images at 610 and 325 MHz reveal the complete structure of the radio source J1021+1217, with a linear size $\sim 2.4 Mpc$.
2. In the southern side of the source, there is an uninterrupted radio jet, starting from the core to a length of ~ 650 kpc, up to a resolution of

- $6'' \times 6''$. This is the longest uninterrupted jet found so far in any radio source.
3. The total flux density of the source at 325 MHz is 527mJy with a radio luminosity of $L_{325} = 2.8 \times 10^{32} \text{ ergs s}^{-1} \text{ Hz}^{-1}$. At 610 MHz The flux density and luminosity are respectively 340mJy and $L_{610} = 1.9 \times 10^{32} \text{ ergs s}^{-1} \text{ Hz}^{-1}$.
 4. The mass of the SMBH estimated from stellar velocity dispersion and, K band magnitude gives the value $\sim 3.8 \times 10^8 M_{\odot}$.
 5. The overall spectral index of the source is obtained as -0.95, while that for the outer relic regions it is found to be ~ -1.08 . For the inner regions, the spectral index is found to be -0.88. This indicates that the two regions are from different epochs of AGN activity.
 6. The spectral age of the relic plasma is estimated as $(48 - 99) \times 10^6$ years.
 7. The presence of flat-spectrum regions at the outer lobes shows that the jet from the previous epoch may be still reaching there or had been reaching there very recently.
 8. For this source, the AGN OFF time can be relatively small. Therefore the jet from the second episode of activity may be advancing through the same channel of the previous jet. This can be the reason for the well-collimated uninterrupted jet seen in this source. As the radio source is residing outside the cluster environment, which also may favour the formation of large-scale jets.
 9. The jet power of J1021+1217 is $\sim 6 \times 10^{43} \text{ erg/s}$, which is above the FRI/FRII dividing value. The luminosity of the source at 178 MHz also

indicates ($L_{178} = 4.34 \times 10^{25} \text{ W Hz}^{-1}$) the FR II nature of the radio source.

10. The WISE colour-colour plots and absence of strong emission lines confirm the LERG nature of the radio source.
11. The LERG nature of the source is further confirmed by the radio luminosity at 1.4GHz ($L_{1.4} = 6.33 \times 10^{24} \text{ W Hz}^{-1} < 10^{26} \text{ W Hz}^{-1}$) and the excitation index value ($\lesssim 0.95$) from spectroscopic results.
12. The value of the H_α luminosity classifies it as an LLAGN.
13. The low luminosity and low excitation nature of the radio source, as evident from the absence of strong emission lines and infrared properties, suggests that the AGN is possibly in an ADAF state.

Chapter 6

Four Giant Radio Galaxies with diffuse relic regions.

In this chapter, we study four Giant Radio Galaxies (GRGs), which are observed for the first time at low radio frequencies using GMRT. We found in chapter 1 (section 1.2.1.4) that, the number of GRG's discovered so far is around 300. (Subrahmanyam et al., 1996; Ishwara-Chandra & Saikia, 1999; Lara et al., 2001; Schoenmakers et al., 2001; Machalski et al., 2001; Saripalli et al., 2005; Machalski et al., 2006, 2007; Kuźmicz & Jamrozy, 2012; Dabhade et al., 2017). But Proctor (2016), provided a sample of 1600 candidate GRGs, using pattern recognition techniques from the data in the NVSS catalogue. He has selected source pairs (radio lobes) having a maximum separation of $20'$ and a minimum component area of 1.87 square arc minutes at the 1.4 mJy level. However, the GRG nature of many of these sources is yet to be confirmed, with detailed observations. Among the known GRGs, those with linear sizes more than 2 Mpc are very rare (Ishwara-Chandra & Saikia, 1999; Machalski et al., 2007; Konar et al., 2008).

Also, only a few GRGs have been observed and studied at multi-frequencies (Dabhade et al., 2017; Konar et al., 2004). So the absence of multi-frequency observations of GRGs does not permit on the detailed statistical analysis of their properties.

Even though the total sample and the observational data are limited, some important studies have been conducted to investigate the formation and evolution of giant radio sources (GRSs). The main factors which influence the formation of GRSs are as discussed below.

1. Effect of the environment: The low density of the Intergalactic Medium (IGM), which offers less resistance for the expansion of relativistic plasma is a favourable factor for the formation of GRGs (Subrahmanyam et al., 2008). There are examples of compression of the lobes in the direction of larger galaxy density, combined with off-axis distortions in the direction of decreasing galaxy density (Safouris et al., 2009).
2. The age of the radio sources: According to this the GRGs are much older sources than radio galaxies of smaller sizes. Jamrozy et al. (2008), studied the spectral ages of GRSs having different linear sizes. They have grouped the sample into three groups according to their linear sizes. In the first group, they have taken GRSs of average linear size ~ 1.3 Mpc, and found that their ages are between ~ 6 Mega years and ~ 48 Mega years, with a median value of ~ 23 Mega years. In the second sample with 16 smaller sources with average linear size ~ 0.35 Mpc, the average spectral ages obtained are between ~ 2.5 Mega years and ~ 26 Mega years, with a median value of ~ 8 Mega years. For the third sample with 14 radio sources with average linear sizes ~ 0.1 Mpc, the spectral ages are obtained between ~ 0.3 Mega years and ~ 5.3 Mega years with a median value of

~ 1.7 Mega years. This study shows that there is a trend indicating that the linear sizes increase with their respective spectral ages. By this, they could not find much influence of the environment on the jet sizes. Based on P-D diagram [Kuźmicz & Jamrozy \(2012\)](#), also found that GRGs could have evolved over a longer period from smaller sized sources.

3. Recurrent radio activity: [Subrahmanyan et al. \(1996\)](#) postulated that recurrent activity could influence the linear size of radio sources. The reason they put forward is that, since the jets from the restarted activity will be travelling through a medium of less density as compared to jets from the previous epoch. This enables the jets to travel unhindered through longer distances. However, observationally, many sources with signatures of recurrent activity show inner lobes, whose formation is possible only when the intergalactic environment is sufficiently dense ([Kuźmicz et al., 2017](#)). DDRGs are typical examples of radio galaxies with recurrent activity. These are radio galaxies with two pairs of lobes emerging from the same radio core and aligned along a common axis ([Schoenmakers et al., 2000c,a](#)). At present, the available sample of radio galaxies with recurrent activity is ~ 80 ([Kuźmicz et al., 2017](#); [Saikia & Jamrozy, 2009a](#); [Nandi & Saikia, 2012](#)). [Kuźmicz et al. \(2017\)](#) selected a sample of 74 galaxies with recurrent activity, of which only ~ 15 are GRGs. Also many studies on the ages of radio galaxies with recurrent activities, it is found that, those galaxies with sizes $\geq 1\text{Mpc}$ have ages of the order of $\sim \text{few} \times 10^7\text{years}$ ([Machalski et al., 2011, 2010](#); [Konar et al., 2012, 2013](#); [Hunik & Jamrozy, 2016](#)). These results indicate that the radio galaxies, which are more evolved in time are more probable to be GRGs. Also a large number of Mpc-sized radio sources are not showing any signatures of recurrent activity ([Schoenmakers et al.,](#)

2000c). This shows that intermittent activity is not a requirement for the formation of GRGs.

4. The properties of the central engine: [Kuźmicz & Jamrozy \(2012\)](#) compared the black hole masses of a sample containing 45 GRSs and almost the same number of radio sources of smaller sizes. They have estimated the black hole masses using the MgII emission line in the optical spectra of these sources. They found that the black hole masses of GRSs are in the range from $1.6 \times 10^8 M_{\odot}$ to $12.2 \times 10^8 M_{\odot}$. Whereas, black hole masses of the smaller sources are obtained as between $1.0 \times 10^8 M_{\odot}$ and $20.3 \times 10^8 M_{\odot}$. It shows that the BH masses are not the sole factor for the large sizes of GRGs/GRS.

All the four sources discussed in this chapter are observed at 325 MHz and 610 MHz radio frequencies using GMRT. We have also used the 1.4 GHz NVSS survey maps for this study. All these GRGs are characterised by the presence of very diffuse relic regions and, two of them are having linear sizes of ~ 2 Mpc. The multifrequency observations of these four GRGs and those discussed in chapters 4 and 5 will contribute to the radio properties of GRGs. The following are the GRGs discussed in this chapter.

1. 2MASX J102131.5+0519011 (hereafter J1021+0519): This is a double-lobed radio source with an angular size $\sim 916''$ and with a linear size of ~ 2.2 Mpc, at a redshift of 0.156. It is identified as an FR II radio source by [Kozieł-Wierzbowska & Stasińska \(2011\)](#).
2. 2MASX J15261183+2939048 (hereafter J1526+2939): This source is at a redshift of 0.1166, with an angular size $\sim 900''$, and with a linear size of ~ 2.0 Mpc.

3. 2MASX J22561507-361789 (hereafter J2256-3617): This source is at a redshift of 0.090 and has diffuse relic lobes. It is having an angular size $\sim 880''$ and a corresponding linear size of $\sim 1.5\text{Mpc}$.
4. 2MASX J12070524-2741466 (hereafter J1207-2741): This source is at a redshift of 0.025, with very diffuse relic lobes. It is having an angular size $\sim 2000''$ and a corresponding linear size of $\sim 1\text{Mpc}$. The radio morphology shows that this is a Wide Angle Tail (WAT) source.

All these radio sources are studied for the first time at lower radio frequencies (610MHz & 325 MHz).

6.1 Previous observations

Two of the above sample of four GRGs (J1021+0519 and J1526+2939) are observed in SDSS, and the r band images of them are shown in Figure 6.1(Left Panel). The right panel of Figure 6.1 (top and bottom) gives the optical image overlaid with the radio contours. Similarly, the DSS2 images overlaid with radio contours for the sources J2256-3617 and J1207-2741 are shown in Figure 6.2. These will enable us to detect the host galaxy and to understand the extent of the radio source into the ICM. The global parameters of the sources are given in Table 6.1 and Table 6.2. These sources are also detected in WISE and 2MASS wavelength bands. SDSS magnitudes and colours of J1021+0519 and J1526+2939 are listed in Table 6.3

The radio images of all the sources at 1.4GHz are available in the NVSS VLA data base with a resolution of 45×45 arc seconds (Condon et al., 1998).

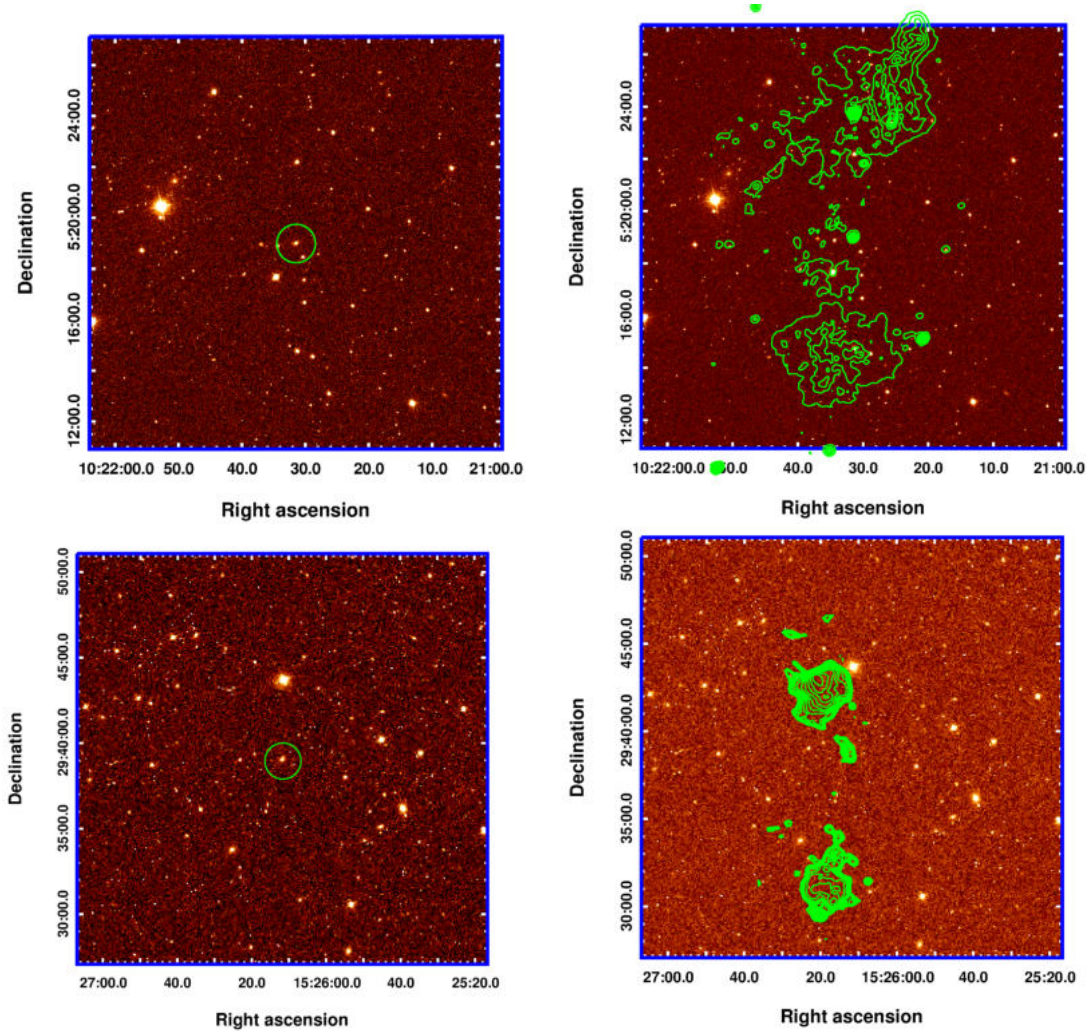


FIGURE 6.1: SDSS r band images of the galactic environment around J1021+0519 and J1526+2939 are shown in the left top and left bottom panels respectively. The galaxy positions are marked with green circles. In the right top and right bottom panels, 610 MHz GMRT radio contours are overlaid on SDSS r band images.

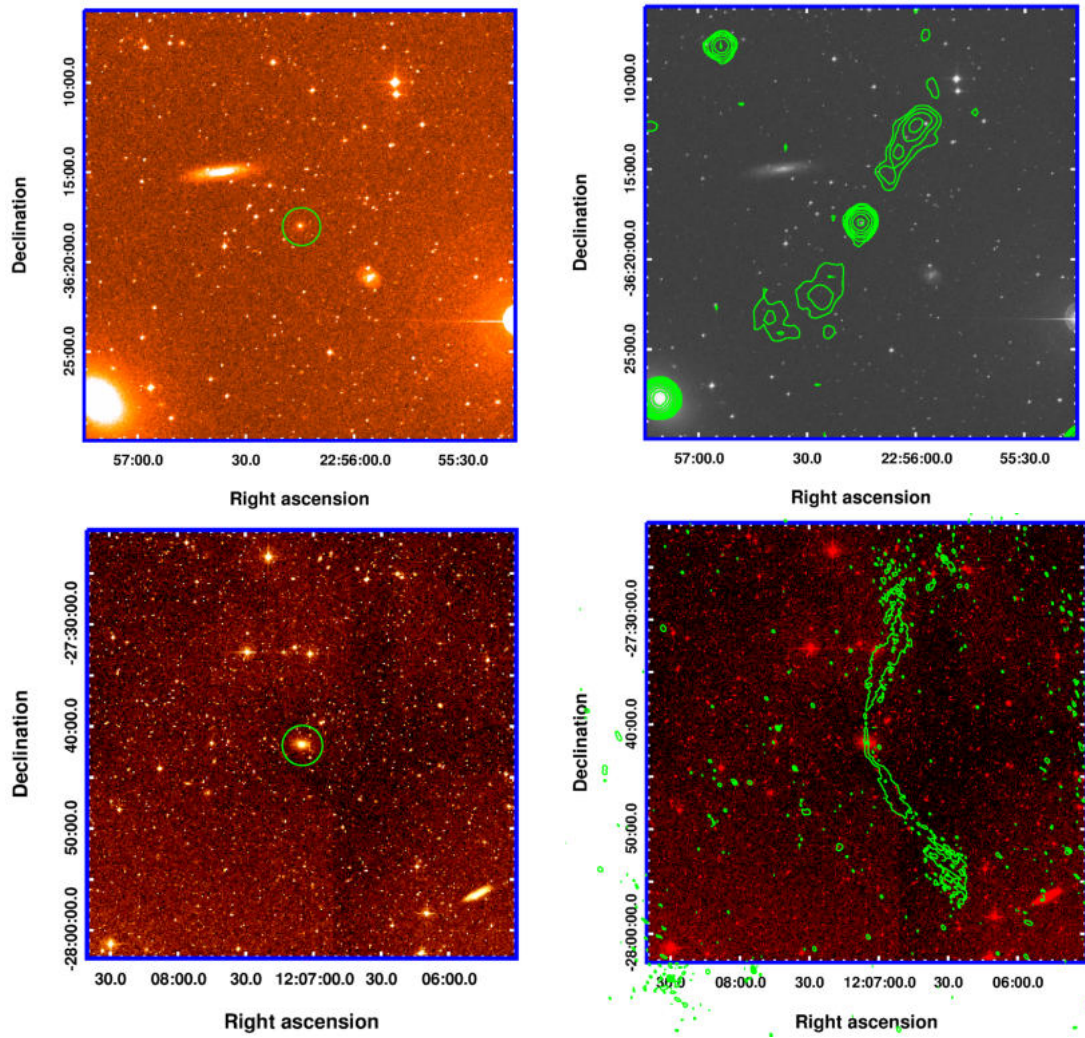


FIGURE 6.2: DSS2 r band images of the galactic environment around J2256-3617 and J1207-2741 are shown in the left top and left bottom panels respectively. The galaxy positions are marked with green circles. In the right top and right bottom panels, 610 MHz GMRT the radio contours are overlaid on the DSS2 r band images.

The radio contour plots of all the four sources are shown in Figure 6.3. The 1.4 GHz radio fluxes and radio luminosities of all these sources are given in Table 6.4. The radio luminosities of all of them are below the dividing value ($\sim 10^{26} W Hz^{-1}$) between LERGs and HERGs (Best & Heckman, 2012). Further studies also confirm the low excitation nature of these galaxies.

TABLE 6.1: Global parameters of Sources J1021+0519 and J1526+2939. Ref. <https://ned.ipac.caltech.edu/>; (Abazajian et al., 2009; Best & Heckman, 2012; Koziel-Wierzbowska & Stasińska, 2011; Skrutskie et al., 2006b; Wegner et al., 2001)

	J1021+0519	J1526+2939
RA& DEC	$10^h 21^m 31.5^s$; $+05^d 19^m 01^s$	$15^h 26^m 11.8^s$; $+29^d 39^m 05^s$
Galaxy Morphology	E2	E3
Magnitude(<i>SDSSg</i>)	17.82	16.41
Galaxy size	$0.25' \times 0.19'$	$0.47' \times 0.31'$
b/a	0.76	0.66
Luminosity distance(Mpc)	750	548
Redshift(z)	0.156	0.1169
Angular size scale (kpc/arc sec)	2.721	2.138
Radial Velocity(km s ⁻¹)	46831	35059

6.2 GMRT observations

The details of the GMRT observations of all the four GRGs discussed in this chapter are given in Table 6.5. All these observations were of 5 hours duration. Flux calibrators from among 3C147, 3C48 and 3C286 were observed for ten minutes each at the beginning and end of the observations. Phase calibrators

TABLE 6.2: Global parameters of Sources J2256-3617 and J1207-2741.
 Ref.<https://ned.ipac.caltech.edu/>;(Jones et al., 2009; Skrutskie et al., 2006b;
 Kaldare et al., 2003; de Vaucouleurs et al., 1991)

	J2256-3617	J1207-2741
RA& DEC	$22^h56^m15.1^s$; $-36^d17^m58.9^s$	$12^h07^m05.2^s$; $-27^d41^m46.6^s$
Galaxy Morphology	E1	SA0
Magnitude(visual)	16.85*	12.51
Galaxy size	$0.38' \times 0.33'$	$1.7' \times 1.4'$
b/a	0.86	0.82
Luminosity distance(Mpc)	415	110
Redshift(z)	0.0903	0.0251
Angular size scale (kpc/arc sec)	1.7	0.508
Radial Velocity(km s ⁻¹)	27057	7516

TABLE 6.3: SDSS magnitudes and SDSS colours of J1021+0519 and J1526+2939.
 Ref: SDSS database <http://www.sdss.org>

SDSS Magnitudes					SDSS Colours		
<i>u</i>	<i>g</i>	<i>r</i>	<i>i</i>	<i>z</i>	<i>g - r</i>	<i>r - i</i>	<i>i - z</i>
19.88±0.07	17.82 ±0.01	16.6±0	16.1±0	15.72 ± 0.01	1.21	0.51	0.38
19.88±0.07	17.82 ±0.01	16.6±0	16.1±0	15.72 ± 0.01	1.21	0.51	0.38

TABLE 6.4: Radio fluxes in mJy for all the four sources from NVSS. The last row gives the radio luminosity $L_{1.4GHz}$ in *Watts Hz*⁻¹.(* The source J1207-2741 alone is having two lobes each on either side). All the flux values are measured above 3σ .

	J1021+0519	J1526+2939	J2256-3617	J1207-2741
Northern outer lobe	84	105± 6	51±2.7	88±1.7
Northern inner lobe*	NA	NA	NA	108±4
Core	8	4.2± 0.9	100±24	49±6
Southern Inner lobe*	NA	NA	NA	50± 2.5
Southern outer lobe	58	40 ± 1.2	53±1	72±2.5
Total Flux (mJy)	150	150	204	367
Luminosity	1×10^{25}	5.39×10^{24}	4.2×10^{24}	5.3×10^{23}

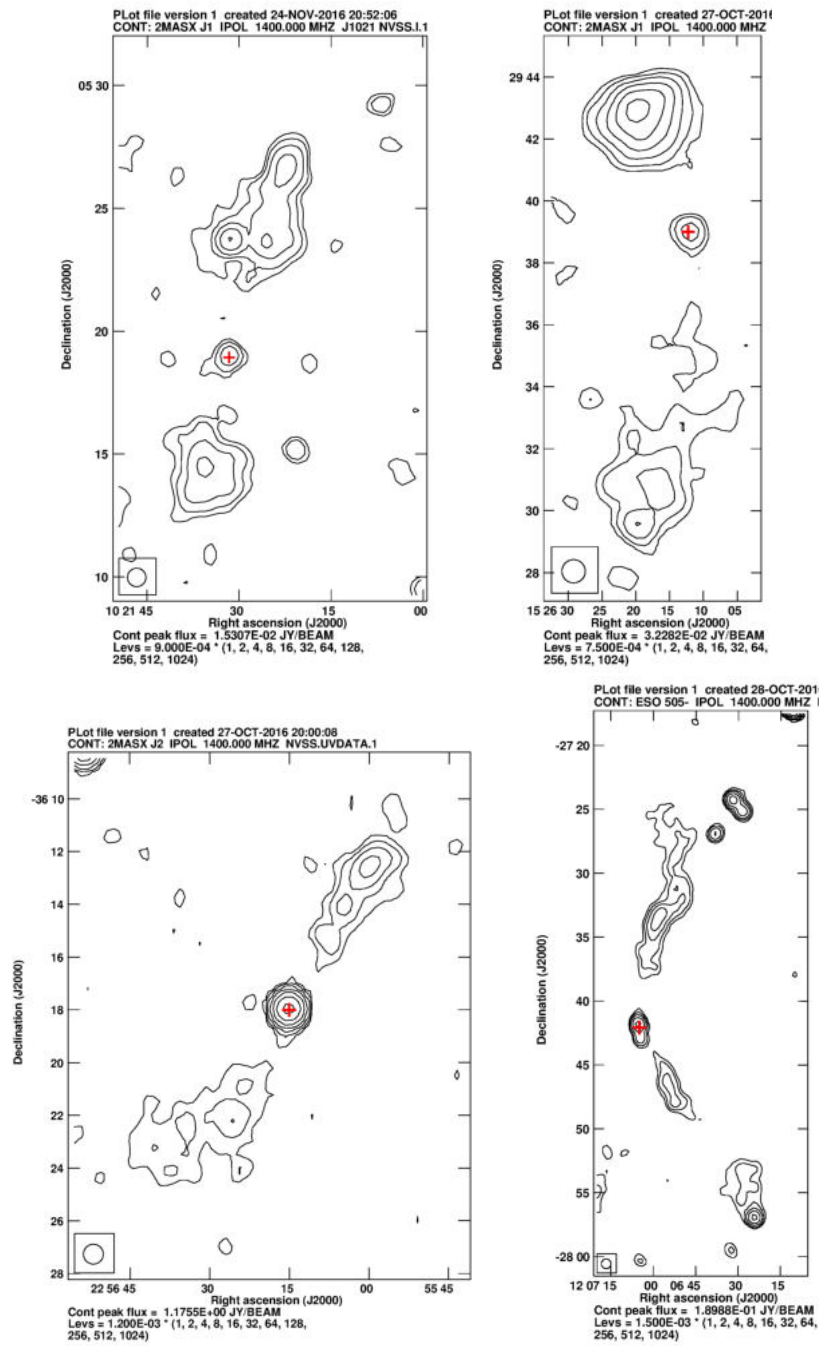


FIGURE 6.3: NVSS VLA radio contours at 1.4GHz with resolution $45'' \times 45''$. Top Panels: Sources J1021+0519 (left) and J1526+2939 (Right). Bottom panel: sources J2256-3617 (Left) and J1207-2741 (Right). The radio core positions are marked with +

TABLE 6.5: Details of the GMRT observations

Project code	Source	frequency MHz	Band width MHz	No: of Channels	Phase Calibrator	Date of observation
25_065	J1021+0519	610	32	512	1123+055	06-01-2014
25_065	J1021+0519	325	32	512	1123+055	12-01-2014
26_008	J1526+2939	610	32	256	1609+266	08-11-2014
26_008	J1526+2939	325	32	256	1609+266	03-11-2014
26_008	J2256-3617	610	32	256	2206-185	30-08-2014
26_008	J2256-3617	325	32	256	2206-185	25-08-2014
26_008	J1207-2741	610	32	256	1248-199	25-04-2014
26_008	J1207-2741	325	32	256	1248-199	18-01-2014

were selected from the VLA calibrators list which is close to the target source. The target source was observed for 30 minutes in each scan which was alternated by 5 minutes scan on phase calibrators. The data analysis details are given in chapter 2

6.3 RESULTS

6.3.1 GMRT radio images and map parameters

In this section, we discuss the GMRT radio maps at 610 MHz and 325 MHz for the sources. The details of the radio maps produced for each of the objects is discussed in this section. The total radio flux of the sources at different frequencies are tabulated in Table 6.10 at the end of this section. All the flux values are measured above 3σ .

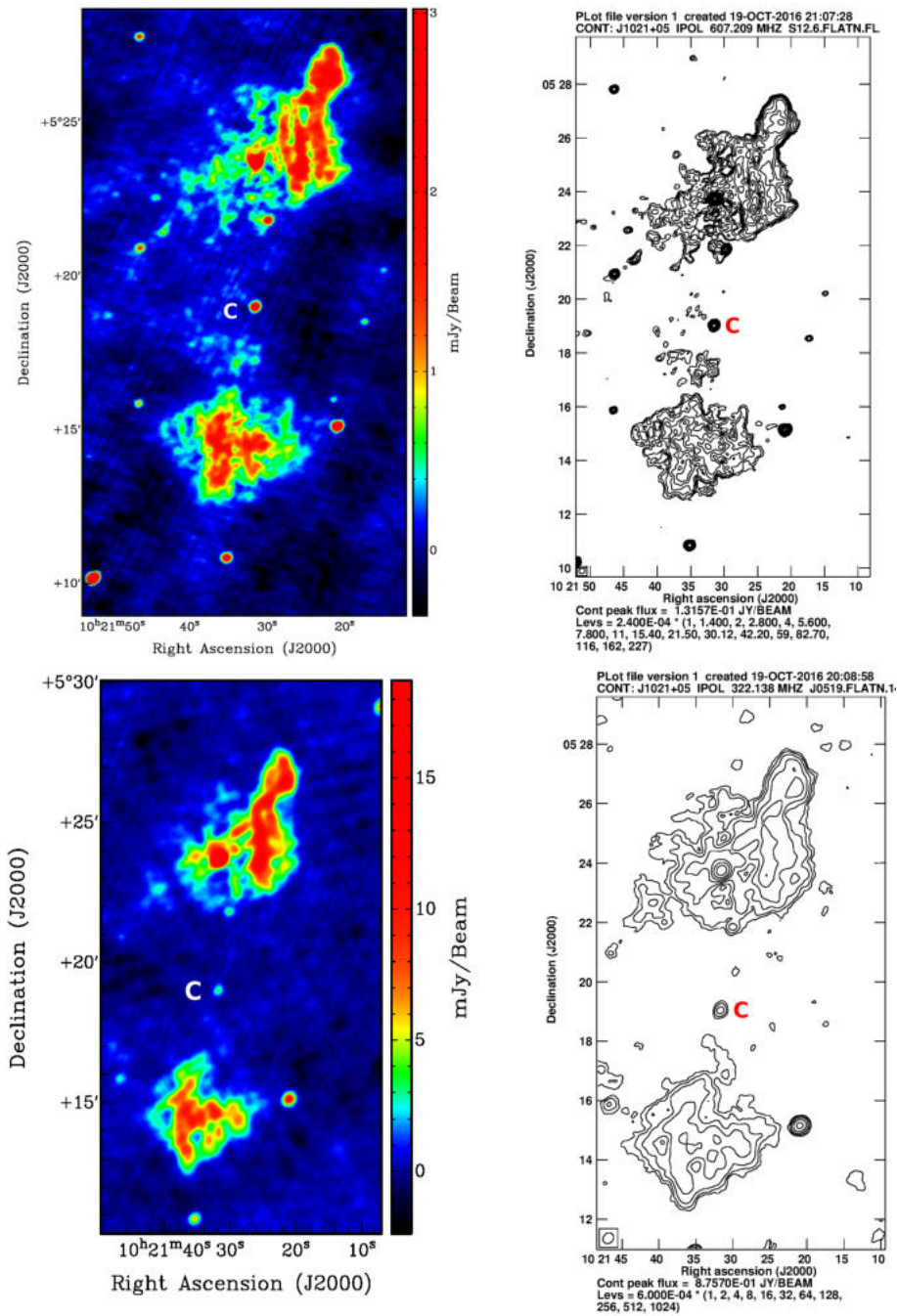


FIGURE 6.4: GMRT maps of J1021+0519; Top panel :610 MHz GMRT map with resolution $13'' \times 13''$ (Left) and contour plots $[1, 1.4, 2, 2.8, 5.6, \dots] \times 240 \mu j y$ (Right). Bottom panel:325 MHz GMRT map with resolution $20'' \times 20''$ (Left) and contour plots $[1, 2, 4, 8, 16, \dots] \times 600 \mu j y$ (Right). The radio core is labelled as 'C'.

Source J1021+0519: The GMRT radio maps and the contour plots of the source J1021+0519 are shown in Figure 6.4. The 610 MHz map is with a resolution of $13'' \times 13''$ and has an rms noise level (σ) of $90 \mu Jy$. The total flux at this frequency is 451.5 mJy . The flux in the northern and southern lobes are found to be 285 and 162 mJy respectively. Core flux is obtained as 4.5 mJy. 610 MHz contour plot is shown in Figure 6.4 (Top Panel:Right) where the first contour level is taken as $270 \mu Jy$ (3σ).

The 325 MHz, GMRT image and contour plot, are shown respectively in the bottom Left and bottom right panels of Figure 6.4. Images were produced to a resolution of $20'' \times 20''$ and with an rms of (σ) = $200 \mu Jy$. In the 325 MHz contour plot, the first contour level is taken as $600 \mu Jy$ (3σ). The total flux density at 325 MHz is obtained as 854.5 mJy . The fluxes along the northern and southern lobes are found to be 522 mJy and 330 mJy respectively. And the core flux is found to be 2.5 mJy. The core flux is found to increase with frequency (i.e. from 2.5mJy at 325 MHz to 7.5 mJy at 1.4 GHz). Indicating an inverted spectrum for the core region. This is usually observed in compact cores and can be explained as due to synchrotron self-absorption.

TABLE 6.6: Radio Map parameters of J1021+0519

freq- uency MHz	reso- lution <i>arcsec</i> ²	rms μJy	flux values (mJy)			Total flux mJy	Lumi- nosity $\times 10^{25}$ W Hz ⁻¹	Linear size Mpc
			core	northern lobe	southern lobe			
325	20x20	200	2.5	522	330	854.5	5.75	2.49
610	13x13	90	4.5	285	162	451.5	3.04	2.49
1400	45x45	500	8.0	84	58	150	1.0	2.2

The radio maps of J1021+0519 show an almost symmetric diffuse relic lobes with a faint core. The core size is estimated as $12.91'' \times 7.57''$ (see section 2.1.1.4).

Also it is observed that in both the images (610 MHz and 325 MHz) northern lobe is more extended than the southern lobe. At both the frequencies the total angular size of the source is found to be $916''$, which corresponds to a linear size of 2.49 Mpc. From the images, it seems that the northern lobe of the source is contaminated by a background point source (Quasar?) at $10^h 21^m 31.4^s + 05^d 23^m 42.8^s$. So we have subtracted the flux associated with this background source while estimating the flux of J1021+0519.

We have also estimated the luminosity of the source at 610 MHz and 325 MHz as $L_{610} = 3.04 \times 10^{25} \text{ W Hz}^{-1}$ and $L_{325} = 5.75 \times 10^{25} \text{ W Hz}^{-1}$ respectively. All the map parameters are consolidated in Table 6.6.

Source J1526+2939: This source is at a redshift of 0.1166 and is detected in the FIRST survey at 21cm (Becker et al., 1995) and the NRO VLA sky survey (Condon et al., 1998). The angular size of the radio source is $14'$ (NVSS) with core flux density 4.5mJy and total flux of 150 mJy at 1400 MHz (Table 6.4). The source has a double lobed morphology with a core. The northern lobe is close to the core and is brighter than the much diffused southern lobe. A very faint and slightly curved bridge emission is visible in the NVSS map between the core and the southern lobe .

The Figure 6.5, Top panel (Left) shows the GMRT image of J1526+2939 at 610 MHz with a resolution of $13'' \times 11''$. The map is produced to an rms noise level of $70 \mu\text{Jy}$. The total flux of the source at this frequency is obtained as 293 mJy . The Top panel (right) gives the radio contour plots at this frequency with $210 \mu\text{Jy}$ as the first contour level. The bottom Panel (left) of Figure 6.5 shows the 325 MHz GMRT map of J1526+2939, with a resolution of $23'' \times 19''$. The rms noise level of the map is $300 \mu\text{Jy}$. The total flux at this frequency is obtained as 465 mJy. The contour plots at 325 MHz is shown in the bottom

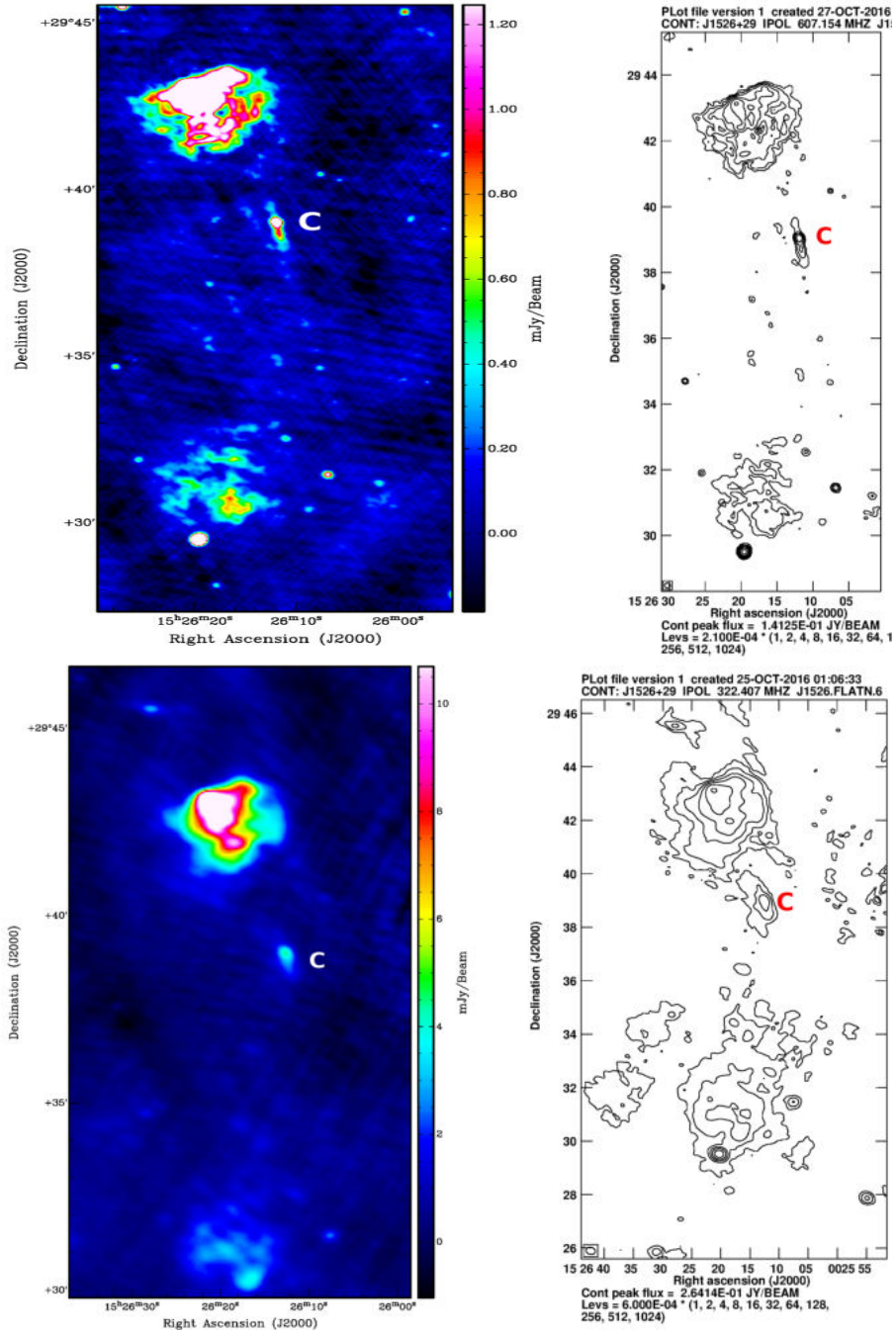


FIGURE 6.5: GMRT maps of J1526+2939; Top panel :610 MHz map with a resolution of $13'' \times 11''$ (Left) and contour plots (Right). Bottom panel:325 MHz map with a resolution of $23'' \times 19''$ (Left) and contour plots (Right).In both the contour maps the levels are $[1,2,4,8,16,\dots,1028] \times 3\sigma$. The radio core is labelled as 'C'.

right panel, where the first contour level is taken as $900 \mu \text{ Jy}$. The total linear size of the source is obtained as 2.2 Mpc with a core size of $11.14'' \times 5.42''$ (see section 2.1.1.4).

From the radio maps, we observe that the northern lobe is much brighter than the southern lobe and a hot spot is visible on it. The southern lobe, on the other hand, is very diffused. The flux values at different frequencies and at different regions are given in Table 6.7.

TABLE 6.7: Radio Map parameters of J1526+2939

freq- uency MHz	reso- lution arcsec^2	rms $\mu \text{ Jy}$	flux values (mJy)			Total flux mJy	Lumi- nosity $\times 10^{25}$ W Hz^{-1}	Linear size Mpc
			core	northern lobe	southern lobe			
325	23x19	300	16	330	119	465	1.67	2.2
610	13x11	70	8.0	215	70	293	1.01	2.2
1400	45x45	500	5.0	105	40	150	0.54	2.0

The luminosity of the source at 610 MHz and 325 MHz are obtained as $L_{610} = 1.01 \times 10^{25} \text{ Watts Hz}^{-1}$ and $L_{325} = 1.67 \times 10^{25} \text{ Watts Hz}^{-1}$ respectively.

Source J2256-3617: This is a radio source with a very diffuse, faint lobes and a strong core. From the NVSS map with $45'' \times 45''$ resolution, doesnot indicate the presence of jets feeding the plasma. At 1.4 GHz (Table 6.4) the upper (North) and lower (south) lobes have almost the same flux of $\sim 50 \text{ mJy}$, but the flux associated with the core is $\sim 100 \text{ mJy}$.

The 610 MHz radio map and contour plots of this source are shown in Figure 6.6. This radio map is having a resolution of $41'' \times 36''$ and the background rms noise level is $700 \mu \text{ Jy}$. To bring out the diffuse relic regions we have used a

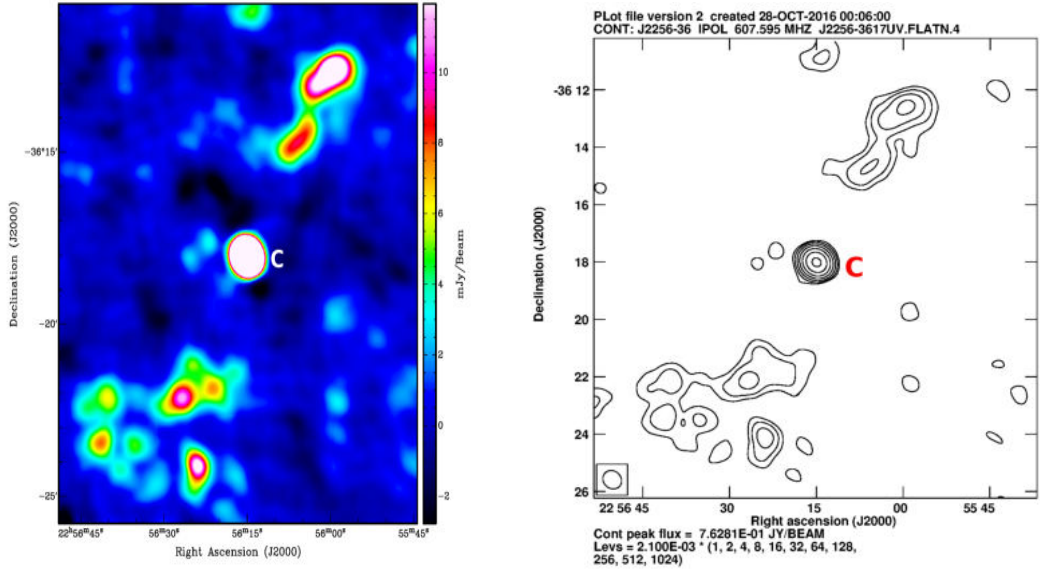


FIGURE 6.6: 610 MHz GMRT map with a resolution of $41'' \times 36''$ (Left), and contour plots (Right). The radio core is labelled as ‘C’.

TABLE 6.8: Radio Map parameters of J2256-3617

frequency	reso- lution	rms	flux values			Total flux	Lumi- nosity $\times 10^{25}$ W Hz^{-1}	Linear size
			core	northern lobe	southern lobe			
MHz	arcsec^2	μJy				mJy		Mpc
610	13x11	700	153	78	125	356	0.74	1.5
1400	45x45	500	100	51	53	204	0.42	1.5

robust parameter of ‘5’, while imaging the data using AIPS. This results in a high background rms value of $\sim 700 \mu\text{Jy}$ for this radio map. Usually for a 600 MHz radio map (\sim with 5 hours of GMRT observation) the rms noise level of $\sim 100 \mu\text{Jy}$ can be achieved. At 610 MHz the total flux is obtained as 356 mJy, with fluxes of upper lobe, core and lower lobe being 78 ± 4.7 mJy, 153 ± 40 mJy and 125 ± 3 mJy respectively. The luminosity of the source at 610 MHz is obtained

as $L_{610} = 7.34 \times 10^{24} \text{ W Hz}^{-1}$. All the radio parameters are consolidated in Table 6.8.

For this source at all the frequencies the lobes on either side are very faint, showing that they are made up of old plasma. But at the same time, the core is very strong at 1.4GHz and 610 MHz GMRT frequencies. The core size of this source is obtained as $2.91'' \times 2.80''$ (see section 2.1.1.4. It may be a case of very recently restarted AGN after a sufficiently long period of OFF state.

Though we have observed this source at 325 MHz also, due to high RFI, we couldnot produce a proper map of the source.

Source J1207-2741: Radio sources whose jets are bend into a wide C, are classified as Wide-angle tail (WAT) radio sources. WATs are generally found to be associated with dominant galaxies, often cD galaxies in clusters (Owen & Rudnick, 1976). From the NVSS image, the radio source J1207-2741 appears as a WAT source. Usually, WAT sources are characterised by the presence of jets, plumes and occasionally hot spots. The bending of the jet structure is assumed as due to the interaction of the jet system with the environment (Begelman et al., 1979). According to this model when the host galaxy moves in a cluster environment, the ram pressure resulting from it sweep the jet back, producing this type of morphology (Begelman et al., 1979; Burns et al., 1981; Smolčić et al., 2007). But this model requires very high velocities for the host galaxies, relative to the ICM, so as to produce high ram pressure capable of bending the jets. Later on, many studies have suggested that the ram pressure may be provided by cluster mergers(Pinkney et al., 1994; Loken et al., 1995; Sakelliou & Merrifield, 2000). In another model, buoyancy forces are proposed to play a role in the formation of WATs. Here as the jet density is lower compared to the surrounding medium,

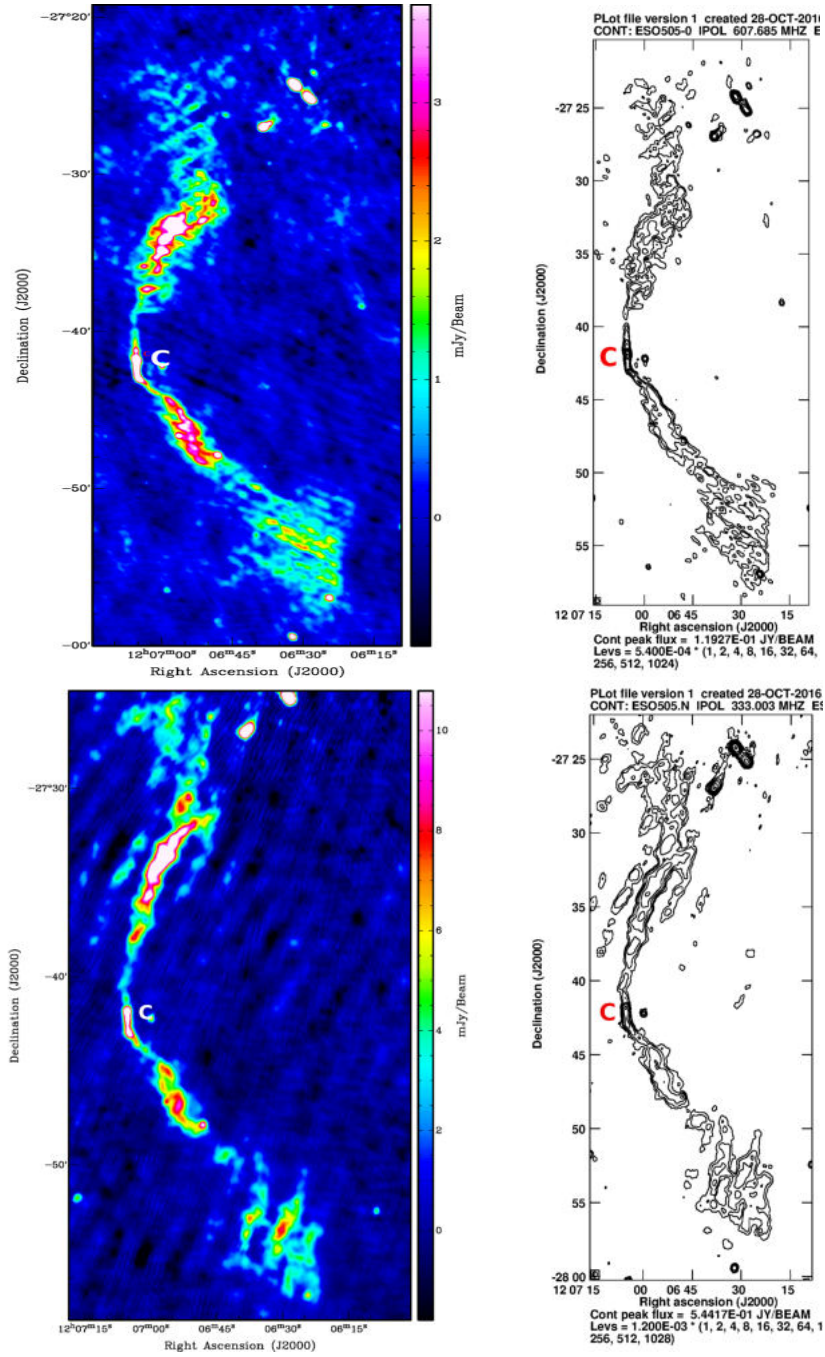


FIGURE 6.7: GMRT maps of J1207-2741; Top panel :610 MHz GMRT map with resolution of $17'' \times 15''$ (Left) and contour plots (Right). Bottom panel:325 MHz GMRT map with resolution of $21'' \times 18''$ (Left) and contour plots (Right).

The radio core is labelled as 'C'.

buoyancy forces will drag the jets to regions of the ICM, where the densities are equal (Gull & Northover, 1973; Sakelliou et al., 1996).

As WAT sources are usually associated with galaxy clusters, we searched for the clusters near to the source in NED. We found that the clusters SCL113 ($12^h08^m58.9^s, -27^d58^m42^s$), Abell S0687 ($12^h06^m40.6^s, -28^d16^m42^s$), [MHS2013] 085 ($12^h09^m46.5^s, -28^d17^m55^s$), Abell 3502 ($12^h04^m10.2^s, -28^d14^m42^s$) and Abell 3499 ($12^h02^m52^s, -27^d53^m42^s$) are the clusters within 60 arcmin, in projection, around this object. SCL 113 and Abell 0687 are the nearest clusters, which are respectively at 30.31 arcmin and 35.35 arcmin away from the host galaxy. Unfortunately, no redshift information of these clusters is available. The other clusters are more than 50 arcmin away from J1207-2741. In the case of this WAT source, the host galaxy may be moving towards the cluster center under the influence of the cluster potential. The ram pressure due to this movement depends on the velocity of the galaxy and the density of the Intra Cluster Medium (ICM). The jet pressure, on the other hand, depends on the jet velocity. In WAT sources, jets will be straight near the core and will begin to bend at a distance from the core. In jets close to the core the jet pressure will be more than the ram pressure, and hence the ram pressure will not have much effect on the jet direction. As the distance from the core increases jet pressure decreases and at some point, it becomes equal to ram pressure. After this point, jet bends prominently from their directions. At the extreme points, the ram pressure will be much higher than the jet pressure where the jet begins to diffuse into plumes.

In this case, the host galaxy is identified with a Lenticular galaxy SA0 (de Vaucouleurs et al., 1991), Figure 6.2. The jets on either side of the core are found to be straight up to $\sim 80''$ ($\sim 40\text{kpc}$). After this distance, the jet bends and ends up in plumes at the extremities, as expected in the case of any WAT source.

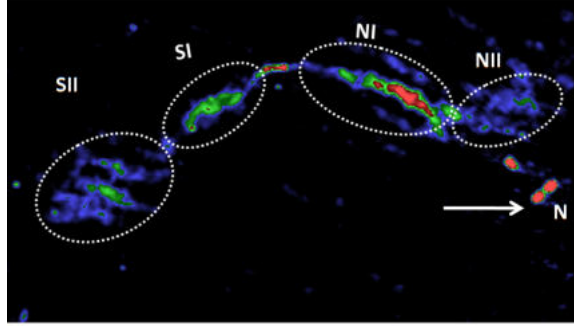


FIGURE 6.8: 325 MHz GMRT map of J1207-2741, with image positions marked. The map is rotated 90^0 in the clock-wise direction. The flux associated with the marked regions are shown in Table 6.9

TABLE 6.9: Radio Map parameters of J1207-2741. The regions mentioned in the table are shown in Figure 6.8

frequency MHz	reso- lution $arcsec^2$	rms μJy	flux values (mJy)					Total flux mJy	Lumi- nosity $\times 10^{24}$ $W Hz^{-1}$	Linear size Mpc
			core	NII region	NI region	SI region	SII region			
325	21x18	400	74.0	502	528	268	530	1902	3.75	1.0
610	17x15	150	71.0	157	386	212	325	1151	1.67	1.0
1400	45x45	500	49.0	88	108	50	72	367	0.53	1.0

The GMRT images and contour plots of J1207-2741 at 610 and 325 MHz frequencies are shown in the upper and lower panels of Figure 6.7, respectively. The 610 MHz map is having a resolution of $17'' \times 15''$ with an rms noise level of $150 \mu Jy$. The 325 MHz map has a resolution of $21'' \times 18''$, and the rms noise level is $400 \mu Jy$. The total source flux at 610 and 325 MHz are respectively 1151 ± 8 mJy and 1902 ± 15 mJy. The flux values corresponding to different regions of the source are given in table 6.9. The source is observed to have an angular size of $\sim 2000''$, which corresponds to a linear size of 1Mpc. The core size is determined as $14.32'' \times 4.26''$ (see section 2.1.1.4). The luminosity of the source at 610 MHz and 325 MHz are $L_{610} = 1.67 \times 10^{24} Watts Hz^{-1}$ and $L_{325} = 3.75 \times 10^{24} Watts Hz^{-1}$.

The observed radio flux densities and linear sizes of all the sources are given in the Table 6.10.

TABLE 6.10: Radio flux densities at different frequencies of the GRGs

source	1.4 GHz mJy	610 MHz mJy	325 MHz mJy	Linear size Mpc
J1021+0519	150	451.5	860	2.49
J1526+2939	150	292	465	2.2
J2256-3617	204	356	NA	1.5
J1207-2741	367	1151.8	1902	1.0

6.3.2 Spectral index maps and radio spectral properties

In this section, we discuss the radio spectral index properties of all the four sources. The integrated spectral index plots are prepared from the fluxes of the sources at different frequencies. We have used the 1.4 GHz data point from NVSS and the 610 and 325 MHz data points from GMRT. We have also estimated the integrated spectral index values at different regions of the source. For a better understanding of the physical nature of the source, the spectral index maps are created by convolving the radio maps to the same resolution.

Source J1021+0519: The integrated spectrum of J1021+0519 shows an overall steep spectrum from 1.4 GHz to 325 MHz. The best fit integrated spectral index is obtained as -1.19 ± 0.08 . The spectral index of the northern diffuse lobe is estimated as -1.26 ± 0.14 , and that of the southern lobe is obtained as -1.19 ± 0.03 (see Figure 6.9 top and middle panels). Table 6.6 shows the flux values corresponding to different regions of the source at various frequencies.

The steep spectral nature of the outer relic region can be seen from the figure 6.9 bottom panel, where we have plotted the data from Table 6.6 and

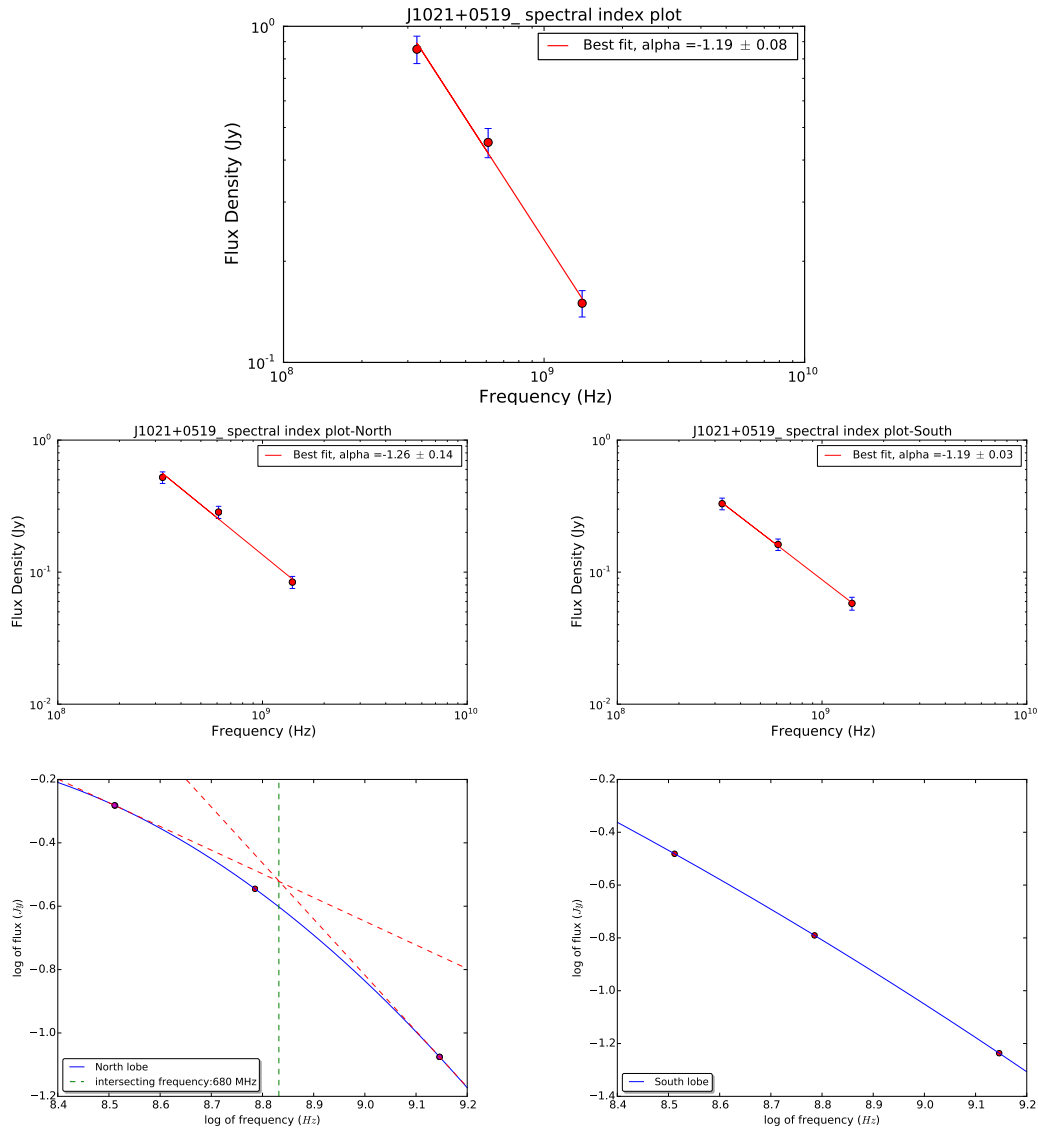


FIGURE 6.9: Source: J1021+0519; Top panel: The integrated spectral index plot produced using 1.4 GHz NVSS, 325 MHz and 610 MHz GMRT data. Middle Panel: The integrated spectral index plot for the north (Left Panel) and south lobes (Right Panel). Bottom panel: Second order polynomial fit for North and south regions (Left and Right panel). (See Table 6.6)

fitted with second order polynomial to illustrate the aged plasma. The spectrum corresponding to the Northern lobe shows a clear curvature, but that for the southern lobe is almost straight. This indicates that for the northern lobe the break frequency is most probably between 1.4 GHz and 325 MHz. An approximate estimate of the spectral break from the slope change in the curve is obtained as ~ 680 MHz (see Figure 6.9 bottom panel).

The electron spectral age t_{sp} of the source estimated from the synchrotron radio spectrum using the equation 3.1 (Murgia et al., 2011).

$$t_{sp} = 1.59 \times 10^9 \left[\frac{B^{1/2}}{[B^2 + B_{IC}^2] [\nu_b(1+z)]^{1/2}} \right] yrs \quad (6.1)$$

With the break frequency of $\nu_b = 0.68$ GHz, and magnetic field range $B = 1 - 10 \mu G$ (as applicable to relic plasma regions), the electron spectral age is obtained to be $t_{sp} = (90 - 47) \times 10^6$ years.

We have also estimated a lower limit to the age by assuming the speed of the plasma head as $\sim 0.5 c$ (Schoenmakers et al., 2000c; Konar et al., 2006). The northern and southern lobes are at angular distances 534 and 380 arc sec respectively from the core. This gives the lower limit to the age as $\sim 9.5 \times 10^6$ years and $\sim 5.5 \times 10^6$ years respectively. So the age of the plasma can be from $\sim (5.5 - 90) \times 10^6$ years.

The spectral index map between 1.4GHz vs 325 MHz with error map is shown in Figure 6.10. In the map a flat spectral index can be observed in the core region. Lobes on either side of the core have spectral indices from -0.8 to -1.6. The outer extremities of both the lobes show flat spectrum regions indicating the presence of hot spots.

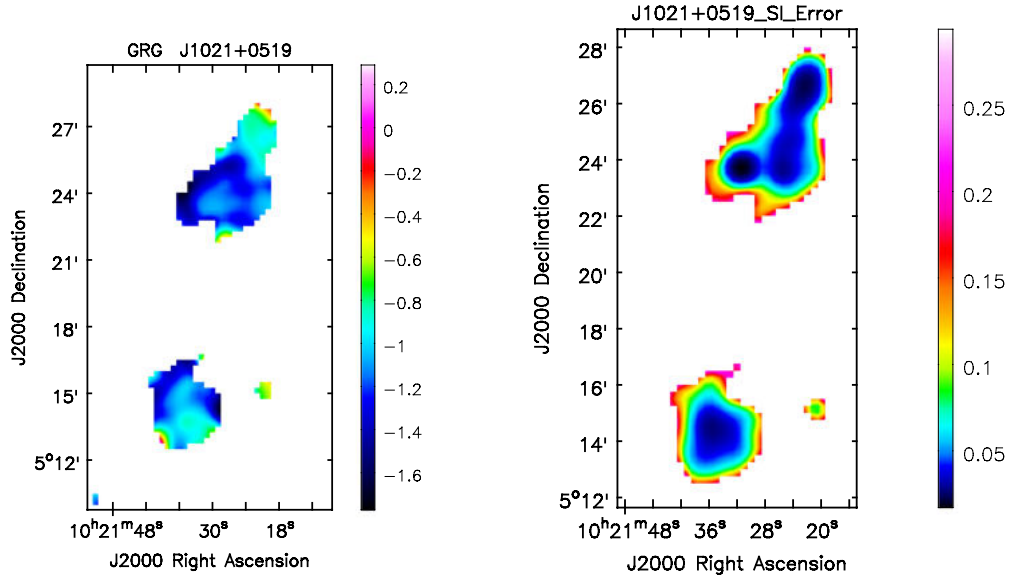


FIGURE 6.10: Source: J1021+0519; The spectral index map produced between 1.4 GHz and 325 MHz GMRT images (Left). The error map (Right).

Using the overall spectral index $\alpha = -1.19$ the luminosity of the sources at 178 MHz is estimated as $L_{178} = 1.17 \times 10^{26} \text{ WHz}^{-1}$. As this value of L_{178} is $> 2 \times 10^{25} \text{ WHz}^{-1}$, the source can be classified as an FR II radio source (Fanaroff & Riley, 1974).

Source J1526+2939: The integrated spectrum of J1526+2939 from 1.4 GHz to 325 MHz gives a spectral index value of -0.8 ± 0.02 , which is the value observed in radio sources with lobes. The spectral indices of the northern and southern diffuse lobes are estimated as -0.79 ± 0.05 and -0.75 ± 0.05 respectively (see Figure 6.11 top and bottom panels). Table 6.7 shows the flux values corresponding to different regions of the source at various frequencies. When we have plotted this data for the north and south lobes and fitted with second order polynomial, the plots are almost straight in the frequency interval from 1.4 GHz to 325 MHz, showing that there is no spectral break between these frequencies.

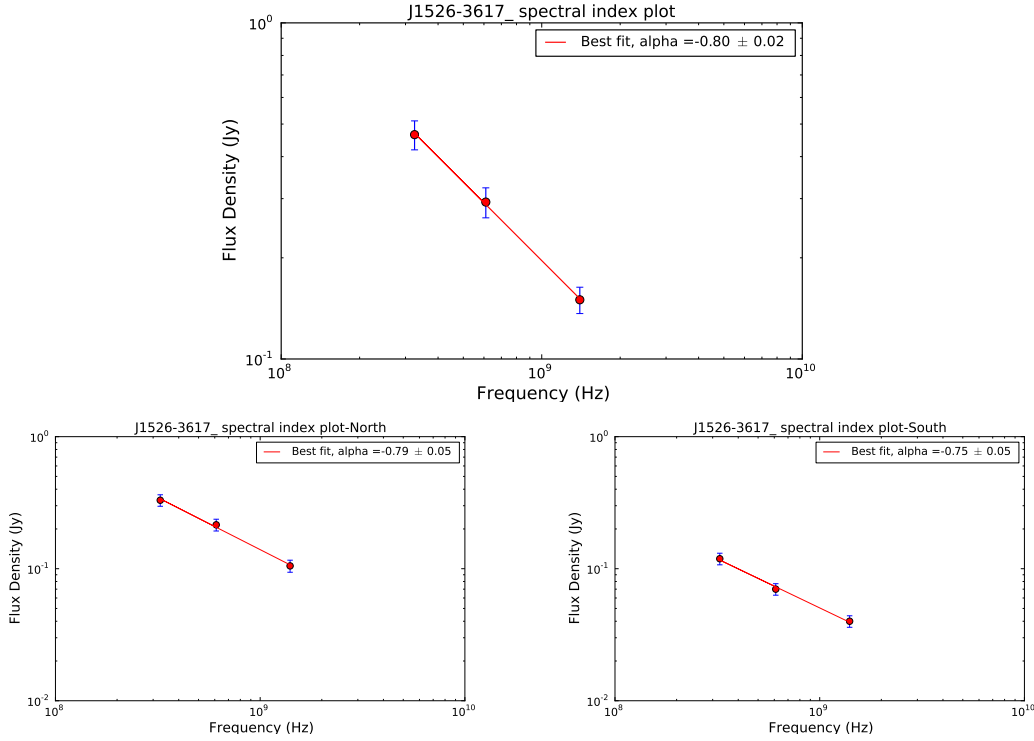


FIGURE 6.11: Top panel: The integrated spectral index plot produced using 1.4 GHz NVSS, 325 MHz and 610 MHz GMRT data. Bottom Panel: The integrated spectral index plot for the north (Left Panel) and south lobes (Right Panel).

Also, it is observed that the spectral index of the lobes are not so steep (~ -0.78), indicating that the spectral age of the plasma is relatively small and the break frequency is beyond 1.4 GHz. We have estimated a lower limit to the age of the source by assuming the speed of the plasma head as $\sim 0.5 c$ (Schoenmakers et al., 2000c; Konar et al., 2006). The southern lobe is at a farther projected distance from the core than the northern lobe. The angular distance between the core and the southern lobe is obtained as $541''$. At the scale of $2.318 \text{ kpc/arc sec}$ at redshift 0.1169, this gives the lower limit to spectral age as $\sim 4.0 \times 10^6$ years.

To estimate the age of the plasma from equation 6.1, we need the spectral break frequency which can be obtained only by observations at more frequencies.

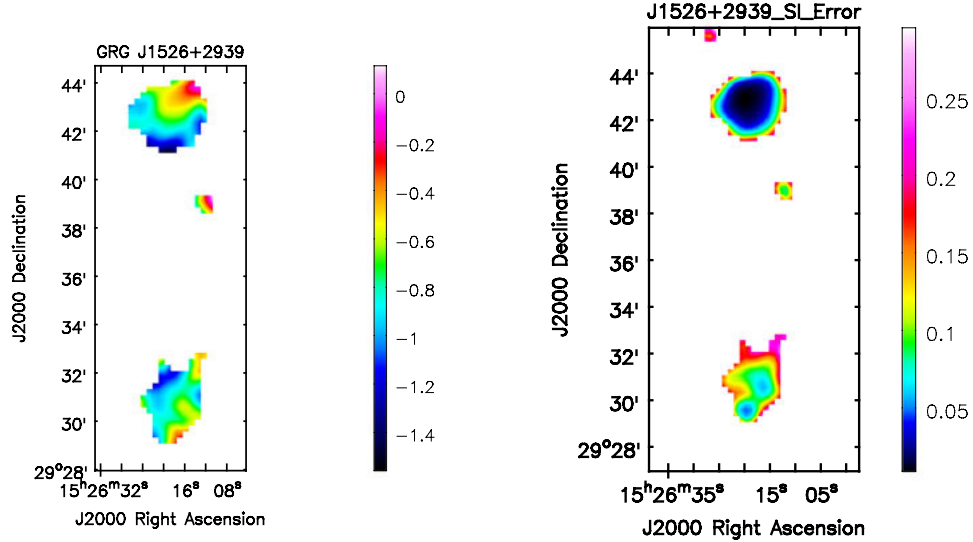


FIGURE 6.12: Left panel: The spectral index map between 1.4 GHz and 325 MHz GMRT images. Right Panel: The error map. (Source J1526+2939)

The spectral index map produced between 1.4 GHz vs 325 MHz with error map is shown in figure 6.12. In the map, a flat spectral index of ~ -0.5 can be seen in the core region. In the lobes on either side of the core the value of spectral indices are varying between -0.5 and -1.1. The outer extremities of both the lobes have flat spectrum regions, indicating the presence of hot spots.

Using the overall spectral index $\alpha = -0.8$ the luminosity of the sources at 178 MHz is estimated as $L_{178} = 2.81 \times 10^{25} WHz^{-1}$. So J1526+2939 can be classified as an FR II radio source (Fanaroff & Riley, 1974).

Source J2256-3617: The integrated spectrum of J2256-3617 from 1.4 GHz to 610 MHz gives a spectral index value of -0.67. The spectral indices of the core

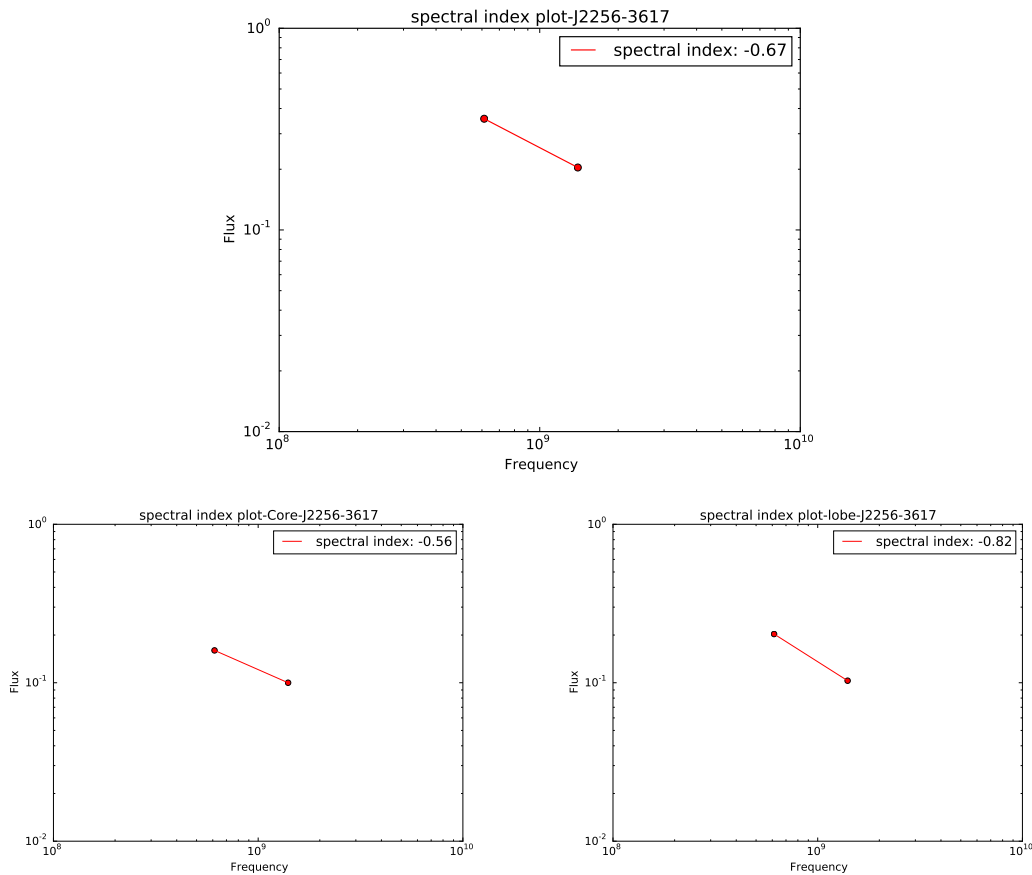


FIGURE 6.13: Source: J2256-3617; Top panel: The integrated spectral index plot produced using 1.4 GHz NVSS and 610 MHz GMRT data. Bottom Panel: The integrated spectral index plot for the core (Left) and lobes (Right).

and diffuse lobes are estimated as ~ -0.57 and -0.82 (see Figure 6.13 bottom Left and bottom right) respectively. Table 6.8 shows the flux values corresponding to different regions of the source at two frequencies. We could not produce good quality maps from 325 MHz observation, due to the high value of RFI and phase errors in the data. Due to lack of sufficient data points, we have not attempted to estimate the age of the plasma

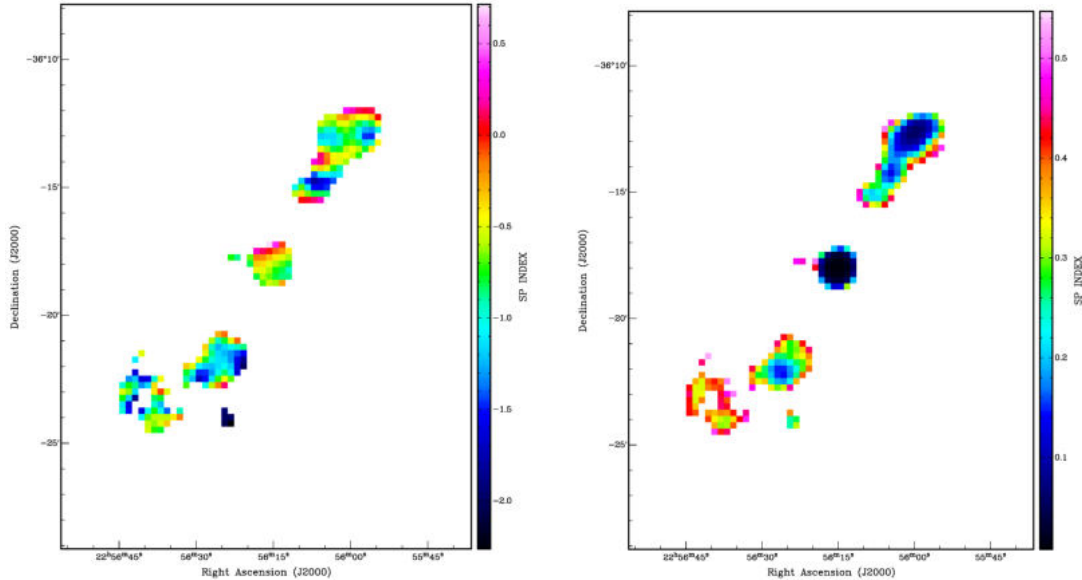


FIGURE 6.14: Left panel: The spectral index map between 1.4 GHz and 610 MHz images. Right Panel: The error map. (Source J2256-3617)

The spectral index map between 1.4GHz vs 610 MHz along with error map is shown in Figure 6.14. It is observed that in the core region itself spectral index value varies from -0.4 to -1.1. The lobes on either side of the core have spectral indices varying from -0.5 to -1.1. The spectral index map of the southern lobe is showing high error values, as evidenced by the error map. As discussed in the previous section, this radio source may be associated with an AGN which was in an OFF state for a long time and restarted its activity very recently. The energy from the central AGN is only about to reach the lobes, which are almost faded off.

Using the overall spectral index $\alpha = -0.67$ the luminosity of the sources at 178 MHz is estimated as $L_{178} = 1.67 \times 10^{25} \text{ WHz}^{-1}$. This source can be classified as an FRI radio source (Fanaroff & Riley, 1974).

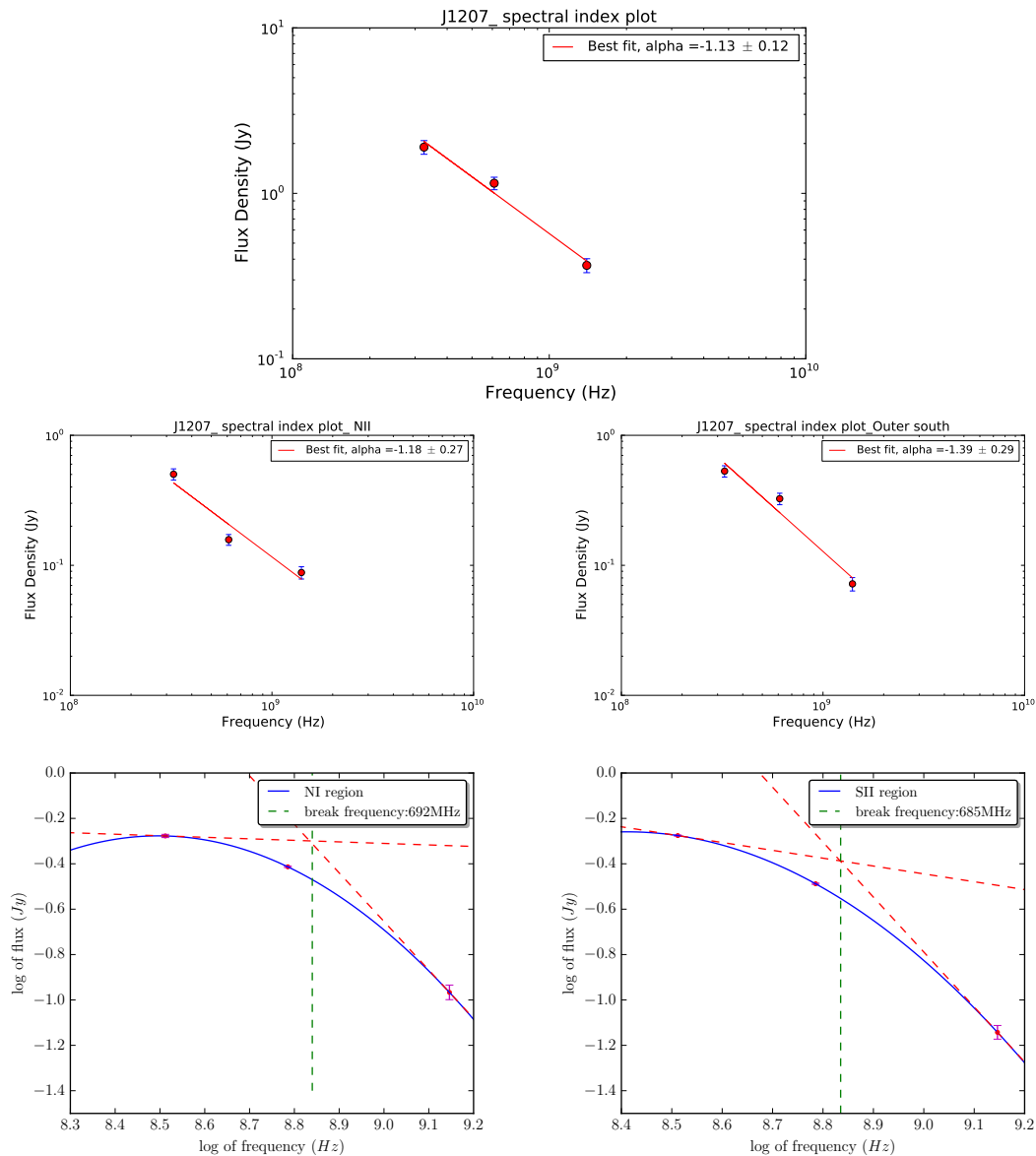


FIGURE 6.15: Top panel: The integrated spectral index plots of J1207-2741 produced using 1.4 GHz NVSS, 325 MHz and 610 MHz GMRT data. Middle Panel: The integrated spectral index plot for the NII (Left Panel) and SII (Right Panel) regions. Bottom panel: Second order polynomial fit for NII and SII regions (Left and Right panel). (See Table 6.9 and Figure 6.8.)

Source J1207-2741: The integrated spectrum of J1207-2741 shows an overall steep spectrum from 1.4 GHz to 325 MHz. The best fit integrated spectral index is obtained as -1.13 ± 0.12 . The spectral indices of the NII and SII diffuse regions are estimated as $\sim -1.18 \pm 0.27$ and -1.39 ± 0.29 (Refer Figure 6.15 and Figure 6.8) respectively. The spectral index of the regions NI and SI are obtained as $\sim -1.10 \pm 0.28$ and $\sim -1.18 \pm 0.38$ respectively. The spectral index of the core region is found to be ~ -0.29 .

The steep spectral nature of the outer relic region can be seen from the figure 6.15 bottom panel, where we have plotted the data from Table 6.9 and fitted with a second order polynomial to illustrate the aged plasma. The spectrum corresponding to the northern and southern lobes show clear curvatures, indicating that the break frequency is most probably between 1.4 GHz and 325 MHz. We obtain a rough estimate of the spectral break as ~ 680 MHz (see Figure 6.15 bottom panel). From this break frequency, the radiative age of the relic plasma is obtained using equation 6.1 and assuming a magnetic field between 1-10 μ Gauss) as $1.8-4.8 \times 10^6$ years.

The spectral index map produced between 1.4GHz vs 610 Mhz with error map is shown in figure 6.16. In the map, a flat spectral index of ~ -0.4 can be observed in the core region. In the lobes on either side of the core have spectral indices -1.0 to -1.4. In the outer extremities of both the lobes, flat spectrum regions can be seen. In WAT sources, radio-bright features like hot spots are visible at the ends (??). Such regions are not hot spots observed in radio sources, but the intrinsic variations in jet speeds are considered as responsible for it (?).

Using the overall spectral index $\alpha = -1.13$ the luminosity of the sources at 178 MHz is estimated as $L_{178} = 6.63 \times 10^{24} WHz^{-1}$, which is less than

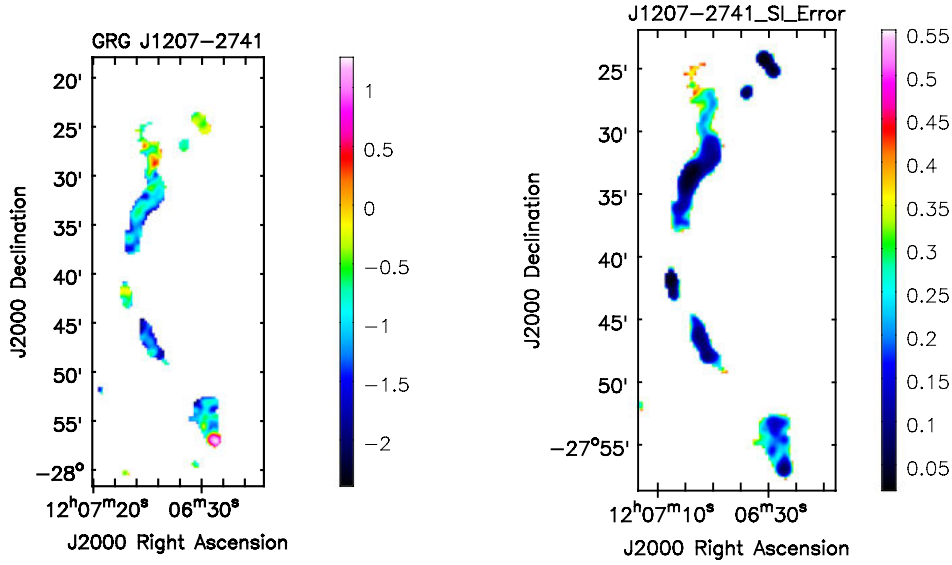


FIGURE 6.16: Left panel: The spectral index map produced between 1.4 GHz and 610 MHz images. Right Panel: The error map. (Source J1207-2741)

the dividing value between FRI and FRII radio galaxies. Accordingly, the source can be classified as an FRI radio source (Fanaroff & Riley, 1974).

6.3.2.1 Jet power

The jet power of all the sources has been calculated from the estimated low frequency ($\nu \sim 150\text{MHz}$) radio flux. We have estimated the 151 MHz lobe flux density using the observed radio spectral index associated with the lobes of the sources. We used the following relation by Punsly & Zhang (2011) to obtain the time-averaged kinetic jet power.

$$\bar{Q} \approx 1.1 \times 10^{45} [(1+z)^{1+\alpha} Z^2 F_{151}]^{6/7} \text{ergss}^{-1} \quad (6.2)$$

where,

$$Z \equiv 3.31 - (3.65) \left[(1+z)^4 - 0.203(1+z)^3 + 0.749(1+z)^2 + 0.444(1+z) + 0.205 \right]^{-0.125} \quad (6.3)$$

and F_{151} is the flux density from the lobes. The jet power obtained for all the for sources are tabulated in Table 6.11.

TABLE 6.11: Jet kinetic power in ergs s⁻¹.

Source	α	F_{151} Jy	\bar{Q}
J1021+0519(S1)	1.2	2.2	1.14×10^{44}
J1526+2939(S2)	0.8	0.896	2.92×10^{43}
J2256-3617(S3)	0.8	1.22	2.43×10^{43}
J1207-2741(S4)	1.2	5.4	9.81×10^{42}

The kinetic jet power \bar{Q} of FR II radio sources are generally found to be $\geq 5 \times 10^{43}$ ergs S⁻¹. All these sources except J1021+0519 have \bar{Q} values below this. So FR II nature of J1021+0519 is clearly verified from the value of the jet power.

6.3.3 WISE mid infrared colours

All the four galaxies discussed here are detected in the WISE mid-IR bands (W1, W2, W3 and W4) Wright et al. (2010). The MIR magnitudes, errors, luminosities and SNR are listed in Table 6.12. The MIR colours of all the four galaxies are given in Table 6.13

The Figure 6.17 shows the wise colour-colour plots of LERGs, HERGs, NLRGs, BLRGs and QSOs (Gürkan et al., 2014). In the WISE colour- colour plot of W1-W2 vs W2-W3, all the four galaxies falls in an area which is well separated

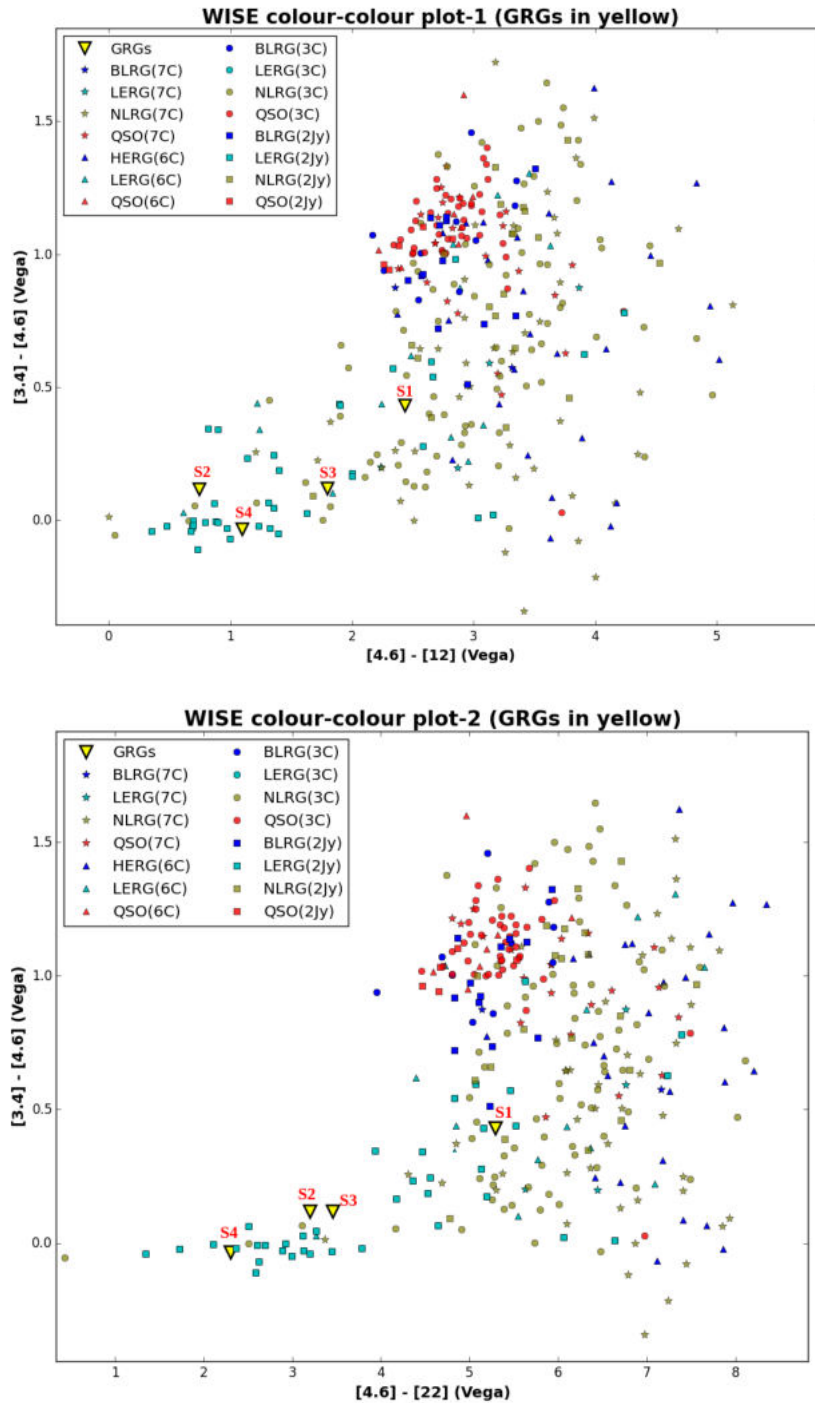


FIGURE 6.17: Top panel: WISE colour-colour plot between W1-W2 and W2-W3. Bottom Panel: WISE colour-colour plot between W1-W2 and W2-W4. In both the plots the yellow triangle shows the position of GRGs G1, G2, G3 and G4.

TABLE 6.12: WISE mid-infrared magnitudes, luminosities (in ergs s^{-1}) and signal-to-noise ratios of detection in four bands of the four sources are shown below.

Source	WISE band (Wavelength)	W1 3.4 μm	W2 4.6 μm	W3 12 μm	W4 22 μm
S1	Magnitude	13.50 ± 0.025	13.07 ± 0.04	10.64 ± 0.18	7.78 ± 0.0
	Luminosity	7.3×10^{43}	4.46×10^{43}	2.97×10^{43}	5.90×10^{43}
	SNR	42.9	30.7	6.2	1.3
S2	Magnitude	12.59 ± 0.02	12.48 ± 0.02	11.74 ± 0.15	9.27 ± 0.0
	Luminosity	8.99×10^{43}	4.12×10^{43}	5.75×10^{42}	7.99×10^{42}
	SNR	46.8	47.5	7.3	0.4
S3	Magnitude	12.48 ± 0.02	12.36 ± 0.02	10.56 ± 0.09	8.91 ± 0.0
	Luminosity	5.73×10^{43}	2.62×10^{43}	9.71×10^{42}	6.42×10^{42}
	SNR	46.9	48.7	12.6	0.5
S4	Magnitude	10.75 ± 0.02	10.78 ± 0.02	09.69 ± 0.041	8.48 ± 0.29
	Luminosity	1.99×10^{43}	7.9×10^{42}	1.53×10^{42}	6.70×10^{41}
	SNR	48.2	53.9	26.4	3.8

TABLE 6.13: WISE mid-infrared colours for all the four sources.

Source	W1-W2	W2-W3	W2-W4
J1021+0519(S1)	0.431	2.434	5.29
J1526+2939(S2)	0.118	0.739	3.201
J2256-3617(S3)	0.119	1.798	3.453
J1207-2741(S4)	-0.034	1.095	2.301

from the area of HERGs. (Gürkan et al., 2014). The W1-W2 vs W2-W4 plot also give similar results. Only the source J1021+0519 is found to be more closer to the region of HERGs.(Gürkan et al., 2014).

From the 22 μm luminosity versus L_{151} radio luminosity plot, Gürkan et al. (2014) found that the empirical cutoff between LERGs and HERGs corresponds

TABLE 6.14: Optical emission line parameters J1021+0519

Parameter	J1021+0519	
	flux ($\times 10^{-17}$ ergs cm $^{-2}$ s $^{-1}$)	FWHM (km s $^{-1}$)
H_{α}	62.09	798
[N II] λ 6583	141.7	710
[S II] λ 6716	39.96	710
[S II] λ 6731	37.41	710
[O I] λ 6300	28.68	710
$H\beta$	-14.58	-
[O III] λ 5007	93.22	710

to a 22 μm luminosity of 5×10^{43} erg s^{-1} . The 22 μm luminosity of J1021+0519 is 5.9×10^{43} ergs S^{-1} , which is just above the cutoff value. For the other sources J1526+2939, J2256-3617 and J1207-2741 these values are 7.99×10^{42} ergs S^{-1} , 6.42×10^{42} ergs S^{-1} , and 6.70×10^{41} ergs S^{-1} respectively. As per this correlation, these three sources are clearly LERGs.

From the integrated spectral index of $\alpha = -1.19$, the radio luminosity of J1021+0519 at 151MHz is calculated as $L_{151} = 2.18 \times 10^{41}$ ergs s^{-1} . In the 22 μm luminosity versus L_{151} radio luminosity plot J1021+0519 falls above the region which separates out LERGs (see Figure 6.18). Further discussions on the optical spectrum also show that it is an NLRG. For the other sources J1526+2939, J2256-3617 and J1207-2741 the 151MHz luminosities are calculated as $L_{151} = 5.0 \times 10^{40}$ ergs S^{-1} , $L_{151} = 2.99 \times 10^{40}$ ergs s^{-1} , and $L_{151} = 9.73 \times 10^{39}$ ergs s^{-1} respectively. In the Figure 6.18 these three sources are found to occupy the positions of LERGs.

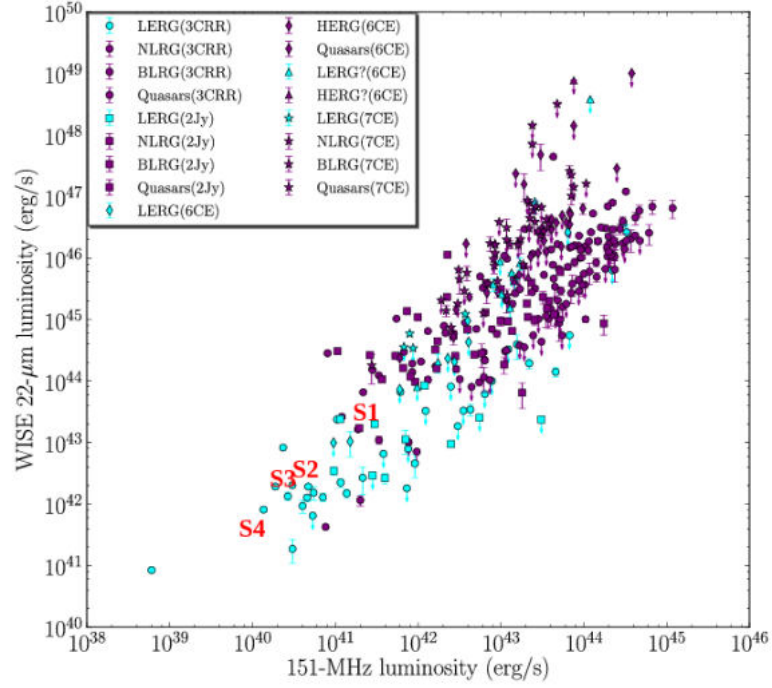


FIGURE 6.18: $22\ \mu\text{m}$ luminosity versus L_{151} radio luminosity plot. The position of all the four galaxies J1021+0519, J1526+2939, J2256-3617 and J1207-2741 marked.

TABLE 6.15: Optical emission line parameters of J1526+2939

Parameter	J1526+2939	
	flux ($\times 10^{-17}$ ergs $\text{cm}^{-2}\text{s}^{-1}$)	FWHM (km s^{-1})
H_{α}	7.52	504
[N II] λ 6583	85.64	1073
[S II] λ 6716	30.17	1073
[S II] λ 6731	8.412	1073
[O I] λ 6300	-2.347	1073
$H\beta$	2.962	504
[O III] λ 5007	16.17	1073

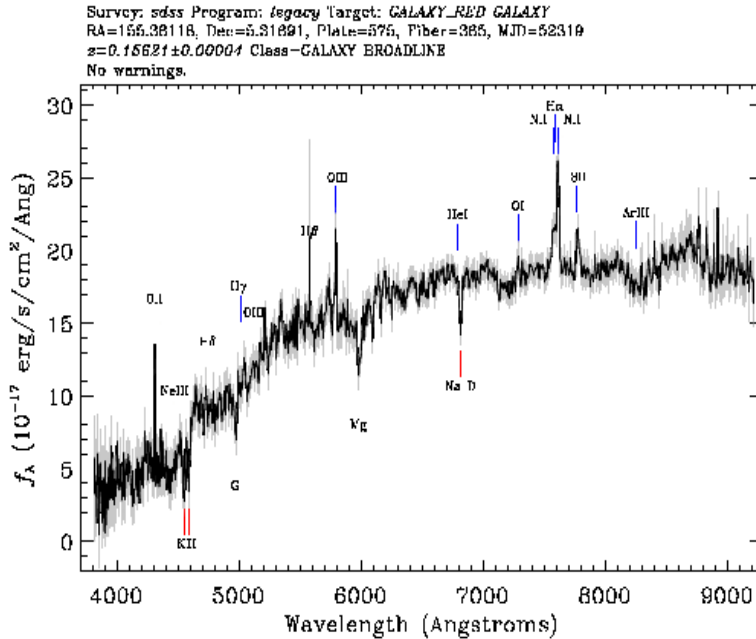


FIGURE 6.19: The optical spectrum of J1021+0519, from SDSS

6.3.4 Optical spectroscopic results

The optical spectrum of two of the galaxies J1021+0519 and J1526+2939 are available in SDSS and are shown in Figure 6.19 and Figure 6.20 respectively. The emission line parameters of these galaxies are shown in Tables 6.14 and 6.15. The spectrum of J1021+0519 shows narrow emission lines while that of J1526+2939 is almost devoid of any emission lines. From the flux values, H_α luminosities of both are estimated as 4.1×10^{40} ergs s^{-1} and 2.69×10^{39} ergs s^{-1} respectively. An H_α luminosity $\leq 10^{40}$ ergs s^{-1} and weak emission lines are characteristics of a low luminosity AGN. The low radio luminosity at 1.4 GHz ($< 10^{26}$ Watts/Hz) and the WISE colour-colour plots also support the low excitation nature of these sources.

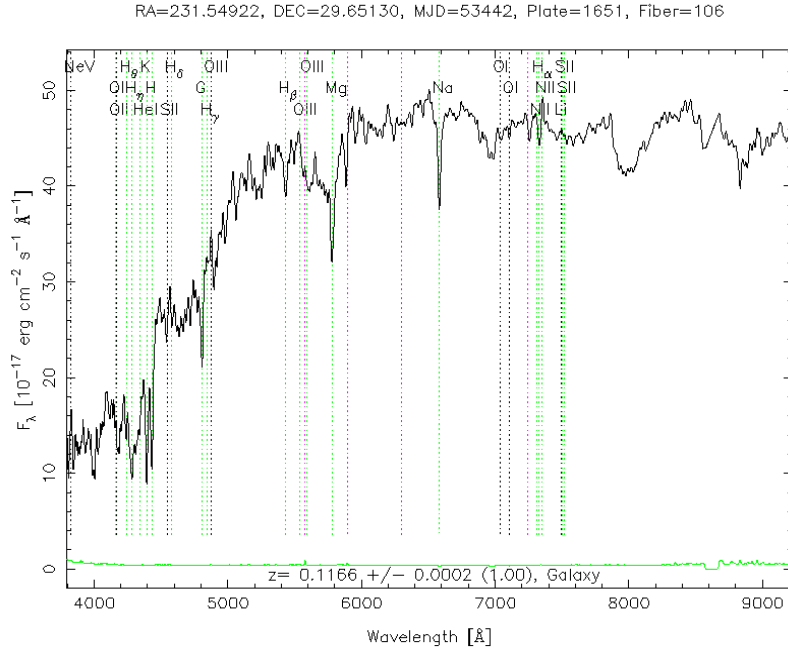


FIGURE 6.20: The optical spectrum of J1526+2939, from SDSS

This nature of these galaxies is further confirmed by the excitation index values (Buttiglione et al., 2010). For J1021+0519 the excitation index EI is obtained as ~ -0.75 and for J1526+2939 it is estimated as ~ 0.438 (both are < 0.95 the dividing value between LERGs and HERGs; see section 1.2.1.2; equation 1.1).

The stellar velocity dispersion of the source J1021+0519 is estimated from the absorption lines as $257.71 \pm 14.5 \text{ km s}^{-1}$, and the mass of the SMBH at its centres were calculated using the formula

$$\log_{10}(M_{BH}/M_{\odot}) = 8.38 + 4.53 \log_{10}(\sigma/200 \text{ km s}^{-1}), \quad (6.4)$$

where σ is the velocity dispersion in km/s (McConnell et al., 2011). The black

hole mass is obtained as $7.56 \pm 1.9 \times 10^8 M_\odot$. Similarly, the stellar velocity dispersion and black hole mass of sources J1526+2939 is obtained as $282.89 \pm 8.45 \text{ km s}^{-1}$ and $1.15 \pm 0.15 \times 10^9 M_\odot$ respectively.

The spectra of the remaining two sources J2256-3617 and J1207-2741 are not available in SDSS. As these sources have large negative declination, there are constraints in getting the spectra using Indian optical telescopes. However, we have estimated the black hole masses of these sources using their k band magnitudes.

The black hole masses calculated from the k band magnitude for all the four sources are tabulated in Table 6.16. The masses of the central black holes are determined by the M_K (K band absolute Magnitude) vs M_{BH} relation (Graham, 2007)

$$\log_{10}(M_{BH}/M_\odot) = (0.38 \pm 0.06)(M_K + 24) + 8.26 \pm 0.11 \quad (6.5)$$

TABLE 6.16: Black hole masses of all the four sources from K band absolute magnitudes

Source	Absolute magnitude	Black hole mass $\times 10^8 M_\odot$
J1021+0519(S1)	-24.98 ± 0.103	4.3 ± 1.3
J1526+2939(S2)	-25.448 ± 0.053	6.7 ± 2.1
J2256-3617(S3)	-25.11 ± 0.051	4.79 ± 1.43
J1207-2741(S4)	-23.25 ± 0.007	0.944 ± 0.26

The masses of the black holes at the centers of all these galaxies are sufficiently massive to produce large-scale jets ($\geq 10^8 M_\odot$) (Laor, 2000; Gopal-Krishna et al., 2008; Sikora et al., 2007). The black hole mass values obtained from K band absolute magnitudes are a little lower than that estimated through stellar velocity dispersion.

6.4 Discussion

6.4.1 Black hole mass and linear size of GRG

The radio jet formation in an AGN is related to the conditions in the region closer to the central engine (Blandford & Payne, 1982; Blandford & Znajek, 1977). So the central black hole properties will have a huge influence on making a galaxy loud in radio frequencies. Also, many studies have shown that galaxies with SMBH masses $\geq \text{few} \times 10^8 M_{sun}$, only are producing large-scale ($\geq 100\text{kpc}$) radio jets (Bagchi et al., 2014; Laor, 2000; Gopal-Krishna et al., 2008; Sikora et al., 2007; Chiaberge & Marconi, 2011). Recently Dabhade et al. (2017) published 25 GRGs, and all of them are found to host SMBHs of masses above this limit. Table 6.17 shows the black hole masses of all the six GRGs in this thesis (four from this chapter and one each from chapter 4 and 5). All these six GRGs are having black hole masses, which is required for launching radio jets.

TABLE 6.17: Black hole masses of the GRGs and the linear sizes

Source	Black holemass From M-Sigma $\times 10^8 M_{\odot}$	Black holemass From K Mag $\times 10^8 M_{\odot}$	linear size Mpc
J2345-0449	21 ± 7.0	10.1 ± 3.7	1.6
J1526+2939	11.5 ± 1.5	6.7 ± 2.1	2.2
J1021+0519	7.56 ± 1.9	4.3 ± 1.3	2.49
J2256-3617	NA	4.79 ± 1.43	1.5
J1021+1217	3.77 ± 1.0	3.69 ± 1.05	2.2
J1207-2741	NA	0.944 ± 0.26	1.0

Kuźmicz & Jamroz (2012) studied a sample of 45 radio sources with linear sizes ranging from ~ 0.1 Mpc to ~ 1.3 Mpc. In this study, they found that the

TABLE 6.18: The galactic environment of host galaxies: The columns 4 and 5 give the number of galaxies within 10' and 20', in the redshift range mentioned in column 3.

source	Red-shift	Redshift range ($\equiv \pm 20\text{Mpc}$)	Number of galaxies within 10'	Number of galaxies within 20'	linear size (Mpc)
J2345-0449	0.0755	0.070-0.080	01	02	1.6
J2256-3617	0.090	0.085-0.095	00	00	1.5
J1207-2741	0.025	0.020-0.030	05	08	1.0
J1021+0519	0.156	0.151-0.170	7	14	2.4
J1021+1217	0.129	0.124-0.134	13	27	2.2
J1526+2939	0.116	0.112-0.120	29	67	2.2

masses of the central black holes of giant sources and smaller sources are in the same range. For their sample, they got SMBH masses in the range from $1 \times 10^8 M_\odot$ to $1 \times 10^9 M_\odot$, irrespective of the linear sizes. So it appears that it is not the mass of the black hole alone, which decides how long the jet should go.

6.4.2 Effect of environment on linear size

Using NED, we have searched for the number of galaxies within a luminosity distance of $\pm 20\text{Mpc}$ and a projected separation of 10 and 20 arcmin, from each of the six GRGs. The results are summarised in the table 6.18. The results show that the first two GRGs in the table are from extremely sparse environments, and the last two are belonging to dense galactic environments. However, there is a caveat that, all the galaxies in that region may not have known redshift values.

The clusters nearer to the sources, with redshift and angular separation, is shown in Table 6.19. It appears that the three GRGs (J1021+0519, J1021+1217 and J1526+2939) are from cluster environments. But from chapter 5, we found

TABLE 6.19: Nearest galaxy clusters to the host galaxies

source	Red-shift	Nearest clusters	cluster red-shift	Angular separation arcmin
J2345-0449	0.0755	MCXCJ2344.2-0442	0.0786	33.095
J2256-3617	0.090	XMMXCSJ2256.5-3631	Unknown	14.14
J1207-2741	0.025	SCL 113	Unknown	30.307
J1021+0519	0.156	MSPM 10048	0.1558	1.366
J1021+1217	0.129	GMBCG J155.22187+12.13025	0.127	11.925
J1526+2939	0.116	MSPM 08857	0.1169	5.5

that the galaxy J1021+1217 is outside the virial radius of the cluster. Similarly the galaxies J2345-0449 and J1207-2741 are much away from the cluster centers. So it appears that at least these three GRGs belong to a less dense galactic environment.

6.4.3 Spectral age and linear sizes

In this work, we have estimated the spectral ages of four GRGs (i) J1021+1217 (Discussed in chapter 5) (ii) J1021+0519 and (iii) J1207-2741 (iv) J2345-0449 (GRG from a spiral host-chapter 4), from the radio spectral break frequencies.

In the paper by [Jamrozy et al. \(2008\)](#), the spectral ages of radio sources of different linear sizes are studied, and all the samples they have selected are from quasars. (The details are described in the at the beginning of this chapter). Sources with average linear sizes ~ 1.3 Mpc, have spectral ages between ~ 6 Mega years and ~ 48 Mega years and those with linear sizes ~ 0.35 Mpc have their average spectral ages are obtained as in between ~ 2.5 Mega years and ~ 26 Mega years. Objects much smaller than this is found to have in between ~ 0.3

TABLE 6.20: Spectral ages of the GRGS.

No:	Name	spectral age B= 10 μ Gauss (10^6 Years)	spectral age B= 1 μ Gauss (10^6 Years)	Linear size Mpc
1	J2345-0449	50	120	1.6
2	J1021+1217	48	99	2.4
3	J1021+0519	47	90	2.2
4	J1207-2741	1.8	4.8	1.0

Mega years and ~ 5.3 Mega years. The same trend can be seen in our sample, except the GRG with spiral host. However, for the spectral break calculations we could use only three frequencies, and hence its estimation is approximate. This necessitates the observation of GRGs at more frequencies.

6.4.4 PD diagram

The evolution of the GRGs can be studied by plotting them in a power-linear size or P-D diagram with radio galaxies of smaller linear sizes (Dabhade et al., 2017; Ishwara-Chandra & Saikia, 1999). Recently Dabhade et al. (2017) have plotted 82 GRGs along with 83 radio galaxies of linear sizes in between 100kpc and 700kpc. As obtained in the earlier studies (Ishwara-Chandra & Saikia, 1999; Dabhade et al., 2017), it is found that the luminosity of the sources decreases with the linear size. The five GRGs discussed in this thesis are plotted in the P-D diagram (see Figure 6.21) plotted with the full sample used by Dabhade et al. (2017). The dotted vertical line is drawn at 700kpc. It can be seen from the figure that there is a deficit of GRGs on the right top and bottom corners of the plot. The absence of GRGs in the right top corner proposes that GRGs are less luminous radio sources, or their luminosity decreases as they evolve in

time. It is suggested in earlier studies that (Baldwin 1982; Cotter, Rawlings & Saunders 1996; Kaiser & Alexander 1997; Kaiser et al. 1997) as time elapses the energy of the lobes will loose due to inverse Compton scattering, adiabatic expansion losses and synchrotron losses. The absence of GRGs in the bottom right corner (ie. GRGs with very low luminosity) is also expected as they can not be detected in low sensitivity sky surveys (Dabhade et al., 2017). So very high sensitivity low-frequency observations are needed to bring out such GRGS.

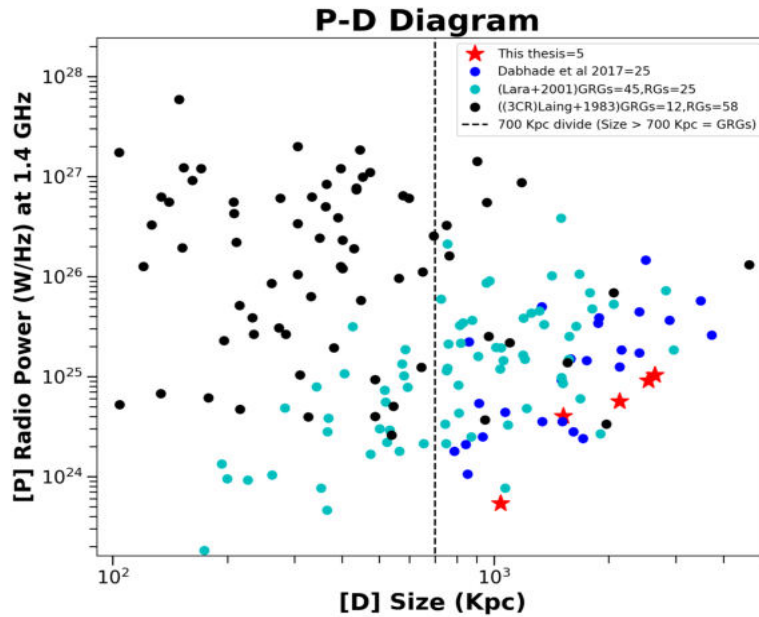


FIGURE 6.21: The 5 GRGs discussed in this thesis are plotted in the P-D diagram with the 82 GRGs and 83 RGs used in the P-D diagram produced by Dabhade et al. (2017)

6.4.5 LERG nature of the GRGs

The WISE colour-colour plots and the $L_{22\mu m}VsL_{151}$ luminosity plot discussed in section 6.3.3 show that all the four GRGs are of LERG nature. The radio luminosities of these sources also support this. Two GRGs in this sample, which are having optical spectra, show very narrow emission lines and H_α luminosity values, characteristics of low luminosity and low excitation AGNs (LLAGN/LERGs). The Excitation index of these galaxies also supports this. So we have enough factual evidence to support the LERG nature of these galaxies.

Even though all the four GRGs discussed here are having low-luminosity and low-excitation AGNs; they are hosting Mpc scale radio jets, with high jet power values (section 6.3.2.1). This indicates that the energy is released from the AGNs, mainly through radio jets. This is usually associated with AGNs in ADAF state, which are characterised by the geometrically thick accretion disks that are radiatively inefficient. However, they will release their energy through strong jets (Narayan & Yi, 1994, 1995). This strongly suggests that in these GRGs, the AGNs may be in ADAF states.

6.5 Conclusions

We summarise the radio and optical studies of four giant radio galaxies here.

1. The three giant radio galaxies J1021+0519, J1256+2939 and J1207-2741, are imaged using GMRT at 325 and 610 MHz frequencies, while the source J2256-3617 is imaged at 610 MHz frequency only and the structural details are studied, and the various parameters are estimated.

2. Two sources J1021+0519 and J1526+2939 have linear sizes 2.49 Mpc and 2.2 Mpc respectively.
3. Out of the four GRGs discussed here, radio source J1021+0519 is found to have FR II nature, from the Jet power and 178 MHz radio luminosity. All the other GRGs are found to be FR I sources.
4. The core region of the source J1021+0519 shows inverted spectrum, due to synchrotron self-absorption, which is usually observed in very compact core sources.
5. The integrated spectral indices of the sources J1021+0519 and J1207-2741 are observed to be steep, with values of -1.19 ± 0.8 and -1.13 ± 0.12 respectively. At the same time, the spectral indices of the sources J1526+2939 and J2256-3617 are found with values -0.08 ± 0.02 and -0.67 ± 0.00 respectively. The source J2256-3617 has a very strong radio core, and the core spectral index is -0.56 ± 0.00 .
6. The spectral indices of the diffused regions in J1021+0519 and J1207-2741 are found to be ~ -1.2 and ~ -1.3 respectively. For the other two sources, these are ~ -0.8 . This shows that the diffused lobes of these sources are not showing extremely steep spectral nature (~ -2).
7. The galaxy J2256-3617 is found to have very faint and diffuse lobes, with possibly in a fading away stage without having any supply of energy from the central engine. At the same time the source has a very strong core. It may be a case of very recently restarted AGN after a sufficiently long period of OFF state.
8. The radio morphology of the WAT source J1207-2741 indicates two episodes of AGN activity. The average spectral index of the inner region of the

source is observed to be -1.1, and that of the outer diffused region is -1.29. Though the difference in spectral index is small, it may be an indication of episodic AGN activity.

9. The black hole mass estimation of all the sources gives masses of the SMBHs of the order of $10^8 M_{\odot}$. On comparing the black hole masses with linear sizes of all the six GRGs discussed in this thesis, no correlation is found.
10. We have estimated the spectral ages of two sources, J1021+0519 and J1207-2741, and are obtained as (47-90)Mega years and (1.8-4.8) Mega years respectively.
11. When the linear sizes of the GRGs, discussed in this thesis are compared with their spectral ages, it is observed that there is an indication of the increase in size with the increase in spectral ages.
12. All the six GRGs are discussed in this thesis are marked in the P-D diagram, and they are observed to occupy, low-luminosity positions.
13. On examining the galactic environment of these GRGs, it is found that three of them are residing in less dense environments.
14. The 1.4 GHz radio luminosities, WISE colour-colour plots, WISE $22\mu\text{m}$ luminosity vs 151 MHz radio luminosity (L_{151}) and the optical spectra, show that all these four GRGs are LERGs.
15. Two of these sources J1021+0519 and J1526+2939 are having optical spectra, and the H_{α} luminosities of these sources are observed to be $\leq 10^{40} \text{ergs s}^{-1}$, showing that the AGNs are of low luminosity class (LLAGNs).

-
16. The low luminosity and low excitation nature of the sources and the large-scale jets propose that the AGNs in these sources may be in an ADAF state.

Chapter 7

Conclusion and Future Work

In this thesis, we have undertaken a detailed study of the radio source 4C 35.06 associated with the ‘Zwicky’s Nonet’ at the centre of the galaxy cluster Abell 407 and six GRGs. All these sources are observed at different radio frequencies using GMRT. The optical spectra of all the galaxies in the ‘Zwicky’s Nonent’ and that of J2345-0449 are observed using IGO and Palomar 200 inch Hale Telescopes. For three GRGs we have obtained the optical spectrum from SDSS. We also made use of WISE and 2MASS data for this study. The major results of our study and future works are summarised below.

We have made the deepest yet radio observations of 4C 35.06 at 150, 235 and 610 MHz with GMRT, which reveals the complete radio structure of the source. A complex central core region along with a helically twisted and kinked bipolar radio jet structure extend to ~ 400 kpc, which terminates into diffuse, ultra-steep spectrum regions at the jet extremities. Sources with such ultra-steep spectrum regions (~ -2) are rare. The spectral age of the source is estimated as between $(2.11-0.79) \times 10^8$ years.

An important feature of this system is the helically twisted and kinked jet system, revealed from the GMRT radio maps. This is similar to the precessing radio jets associated with the galactic micro-quasar SS433. 4C 35.06 is from a system of very tight condensation of nine galactic nuclei. This suggests possible gravitational perturbation effects of multiple black holes in closely interacting galaxies. This can be verified only by X-ray observations.

The GMRT map at 610 MHz shows three radio peaks at the central region of ‘Zwicky’s Nonet’, and the one falls in the middle of the jet, coincides with the optical position of a fainter member in the group. So this fainter member appears as the most probable host of this large-scale radio jet. However, in our present radio observations, we can not pin-point conclusively which one (or more) of the nine close galaxies gives rise to the overall large scale radio jet system.

We estimated the black hole masses of the constituent galaxies by two methods. The black hole mass ratio from the two methods, i.e. $M_{BH,\sigma}/M_{BH,K}$, is found to be > 2 for galaxies with well-determined masses. This suggests that possibly $M_{BH}-M_K$ method gives systematically smaller black hole masses due to the stripping of the outer envelope of some galaxies and thus a reduction in their K-band absolute magnitude. This is indicative of strong evolution in a hostile galactic environment where violent mergers and stripping of stars in multiple tidal encounters are common, as clearly evidenced by the formation of a large-scale stellar halo of stripped matter in ‘Zwicky’s Nonet’.

Further high sensitivity and higher resolution radio observations are needed to provide a complete spectral analysis and obtain detailed resolved central morphology of this complex source and to map the full extent of its relic regions. Deep X-ray observation of the hot, X-ray emitting gas around the cD galaxy in

formation and detection of the various AGN and their X-ray spectra would be very informative.

The giant radio source J2345-0449 discussed in chapter 4 is a very rare case of a megaparsec-scale radio jet launched by a spiral host. So far this is the longest radio source associated with any spiral galaxy. The spiral nature of this galaxy is revealed by deriving the rotation curve from the optical spectroscopic studies. The inclination corrected rotation velocity of this galaxy is found as 429 ± 25 km/s, which is very high compared to normal spirals. Also, this galaxy is found as very massive, ~ 7 times more massive than our Milky Way. The estimated SMBH mass from stellar velocity dispersion is obtained as $> 3.88(\pm 0.40) \times 10^8 M_{\odot}$. Such massive black holes are usually observed only in giant elliptical galaxies. Further studies are required to understand the formation of such a massive black hole in a spiral galaxy.

Another interesting feature about this source is the absence of any central bulge. A spiral galaxy with no central bulge or psuedo bulge, hosting a massive black hole at its center poses many challenges to theoretical models. Also, in standard rotation curves of galaxies, the velocity sharply increases to a peak value at some distance from the center and then flattens out. In our case, the peak of the velocity is not resolved, and only the flattened region is visible. This implies that the maximum of the rotation velocity of this galaxy can be much more than 430 km/s, close to the galactic centre. This can be confirmed only with high-resolution spectroscopic observations.

The morphology, jet power and luminosity values of this radio source are typical of FR II radio galaxies. The optical spectroscopic studies and the WISE colour plots reveal the low excitation nature of the galaxy.

GMRT observations reveal that the radio source J1021+1217 is a 2.2 Mpc scale GRG, with two episodes of AGN activity. The most important feature of this radio source is its 650 kpc scale uninterrupted radio jet towards the south, which is visible above 3σ noise level in the GMRT 610 MHz map at $6'' \times 6''$ resolution. This is the longest uninterrupted jet found so far in any radio source. The mass of the SMBH estimated from stellar velocity dispersion, and K band magnitude gives the value $\sim 3.8 \times 10^8 M_{\odot}$. The FRII class and LERG nature of the source is confirmed by the studies.

The presence of flat-spectrum regions at the outer lobes of the source in the spectral index map is an indication that the jet from the previous epoch of activity may be still reaching the hot spots or had been reaching there very recently. This can happen only when the AGN off time is relatively small. Therefore, in this case, the jet from the second episode of activity may be advancing through the same channel of the earlier jet. We propose that such a condition may favour a well collimated uninterrupted jet as seen in J1021+1217.

In this thesis, we also studied four other giant radio galaxies, J1021+0519, J1256+2939, J2256-3617 and J1207-2741. We have imaged these sources using GMRT and revealed the radio structural details. The galaxy J2256-3617 is found to have very faint and diffuse lobes, in a fading away stage, as if it is not energised by the central engine. But this source has a very strong core, with the core flux more than the total flux density of the lobes, indicating the possibility of a restarted AGN. The values of jet power and luminosities at 178 MHz show that all these sources except J1021+0519 are FRI sources. The WISE colour magnitudes, L_{151} luminosities and the optical spectra all indicate the low excitation nature of these galaxies.

In studying all these six GRGs, we found that the spectral indices of the diffuse lobes are steep, with $\alpha \lesssim -1.3$. Out of these six GRGs three sources J2345-0449, J1021+1217 and J1207-2741 are exhibiting two episodes of AGN activity. The sources J2345-0449 is a DDRG and J1207-2741 is a WAT source.

From the optical, WISE and radio studies it is confirmed that all the six GRGs discussed in this thesis are LERGs. While being in a low excitation state, all are hosting giant radio sources. This is usually seen in AGNs in ADAF state, where the accretion will be in sub-Eddington rate. ADAF state of the AGN is characterised by geometrically thick accretion disks, which have low radiative cooling efficiency, and as a result, most of the energy will be released in radio jets. So AGNs in ADAF states will have low radiative luminosities but can host powerful jetted outflows. This is the situation expected in all the six GRGs.

At least three of these six GRGs are not residing in dense galactic environments. All of them have SMBHs of masses $> 10^8 M_\odot$, but there is no observed correlation between linear sizes and black hole masses. An important indication from the study is that the linear size of the sources increases with increase in spectral age. The lack of multi-frequency observations of these GRGs makes the detailed statistical analysis of the sample difficult.

7.1 Future works

We are planning X-ray observations of 4C 35.06 using XMM Newton and Chandra, to detect the presence of binary black holes. We have also observed the ‘Zwicky’s Nonet’, using the 3.6-meter Devasthal Optical Telescope (DOT), Nainital, and the photometric studies are in progress.

We are also planning to use an 8-meter class telescope, like Gemini or Subaru to obtain high-resolution optical spectrum, of J2345-0449. This will help to get more information on the rotation velocity of the galaxy. Study of the stellar halo of ‘Zwicky’s Nonet’ and similar sources using high-resolution telescopes is also planned.

Giant Radio Sources give a lot of insight into the formation and evolution of radio-loud AGNs. A systematic search for such sources using recently released TIFR GMRT Sky Survey(TGSS) in combination with other large surveys at different frequencies and resolutions in radio and the optical band is required to unearth such population. Such sources will have steep radio spectra and can be seen prominently in low-frequency surveys like TGSS. We are planning follow-up studies of such sources using GMRT.

Bibliography

- Abazajian K. N. et al., 2009, ApJS, 182, 543
- Abell G. O., Corwin, Jr. H. G., Olowin R. P., 1989, ApJS, 70, 1
- Abell G. O., Margon B., 1979, Nature, 279, 701
- Adams T. F., 1977, ApJS, 33, 19
- Amirkhanyan V. R., 2016, Astrophysical Bulletin, 71, 384
- Argence B., Lamareille F., 2009, A&A, 495, 759
- Arp H., 1973, ApJ, 183, 411
- Baars J. W. M., Genzel R., Pauliny-Toth I. I. K., Witzel A., 1977, A&A, 61, 99
- Bagchi J., Gopal-Krishna, Krause M., Joshi S., 2007, ApJ, 670, L85
- Bagchi J., Jacob J., Gopal-Krishna, Werner N., Wadnerkar N., Belapure J., Kumbharkhane A. C., 2009, MNRAS, 399, 601
- Bagchi J., Kapahi V. K., 1994, Journal of Astrophysics and Astronomy, 15, 275
- Bagchi J. et al., 2014, ApJ, 788, 174

-
- Bardeen J. M., Petterson J. A., 1975, *ApJ*, 195, L65
- Barway S., Wadadekar Y., Kembhavi A. K., Mayya Y. D., 2009, *MNRAS*, 394, 1991
- Becker R. H., White R. L., Helfand D. J., 1995, *ApJ*, 450, 559
- Beckwith K., Hawley J. F., Krolik J. H., 2008, *ApJ*, 678, 1180
- Begelman M. C., Blandford R. D., Rees M. J., 1980, *Nature*, 287, 307
- Begelman M. C., Blandford R. D., Rees M. J., 1984, *Reviews of Modern Physics*, 56, 255
- Begelman M. C., Rees M. J., Blandford R. D., 1979, *Nature*, 279, 770
- Bell M. R., Roberts D. H., Wardle J. F. C., 2011, *ApJ*, 736, 118
- Best P. N., Heckman T. M., 2012, *MNRAS*, 421, 1569
- Best P. N., Kauffmann G., Heckman T. M., Brinchmann J., Charlot S., Ivezić Ž., White S. D. M., 2005, *MNRAS*, 362, 25
- Best P. N., von der Linden A., Kauffmann G., Heckman T. M., Kaiser C. R., 2007, *MNRAS*, 379, 894
- Biju K. G. et al., 2017, *MNRAS*, 471, 617
- Biju K. G., Pandey-Pommier M., Sunilkumar P., Dhurde S., Bagchi J., Ishwara-Chandra C. H., Jacob J., 2014, in *Astronomical Society of India Conference Series*, Vol. 13, *Astronomical Society of India Conference Series*, pp. 155–156
- Blandford R. D., Payne D. G., 1982, *MNRAS*, 199, 883
- Blandford R. D., Znajek R. L., 1977, *MNRAS*, 179, 433

- Blundell K. M., Bowler M. G., 2004, *ApJ*, 616, L159
- Bogdán Á., Forman W. R., Kraft R. P., Jones C., 2013, *ApJ*, 772, 98
- Bondi M., Gregorini L., Padrielli L., Parma P., 1993, *A&AS*, 101, 431
- Brocksopp C., Kaiser C. R., Schoenmakers A. P., de Bruyn A. G., 2007, *MNRAS*, 382, 1019
- Burbidge E. M., Burbidge G. R., 1961, *AJ*, 66, 541
- Burns J. O., Schwendeman E., White R. A., 1983, *ApJ*, 271, 575
- Burns J. O., White R. A., Hough D. H., 1981, *AJ*, 86, 1
- Buttiglione S., Capetti A., Celotti A., Axon D. J., Chiaberge M., Macchetto F. D., Sparks W. B., 2010, *A&A*, 509, A6
- Capetti A., Zamfir S., Rossi P., Bodo G., Zanni C., Massaglia S., 2002, *A&A*, 394, 39
- Carilli C. L., Perley R. A., Harris D. E., 1994, *MNRAS*, 270, 173
- Chandrasekhar S., 1943, *ApJ*, 97, 255
- Chiaberge M., Marconi A., 2011, *MNRAS*, 416, 917
- Cohen A. S., Lane W. M., Cotton W. D., Kassim N. E., Lazio T. J. W., Perley R. A., Condon J. J., Erickson W. C., 2007, *AJ*, 134, 1245
- Condon J. J., Cotton W. D., Greisen E. W., Yin Q. F., Perley R. A., Taylor G. B., Broderick J. J., 1998, *AJ*, 115, 1693
- Condon J. J., Mitchell K. J., 1984, *ApJ*, 276, 472

- Conway R. G., Garrington S. T., Perley R. A., Biretta J. A., 1993, *A&A*, 267, 347
- Costero R., Osterbrock D. E., 1977, *ApJ*, 211, 675
- Cotton W. D., Condon J. J., Arbizzani E., 1999, *ApJS*, 125, 409
- Courteau S., 1997, *AJ*, 114, 2402
- Cowie L. L., Binney J., 1977, *ApJ*, 215, 723
- Crawford C. S., Fabian A. C., Sanders J. S., Ettori S., 2003, *New Astron. Rev.*, 47, 239
- Dabhade P., Gaikwad M., Bagchi J., Pandey-Pommier M., Sankhyayan S., Raychaudhury S., 2017, *MNRAS*, 469, 2886
- Daly R. A., Sprinkle T. B., O’Dea C. P., Kharb P., Baum S. A., 2012, *MNRAS*, 423, 2498
- David L. P., Jones C., Forman W., Nulsen P., Vrtilik J., O’Sullivan E., Giacintucci S., Raychaudhury S., 2009, *ApJ*, 705, 624
- De Lucia G., Springel V., White S. D. M., Croton D., Kauffmann G., 2006, *MNRAS*, 366, 499
- de Vaucouleurs G., de Vaucouleurs A., Corwin, Jr. H. G., Buta R. J., Paturel G., Fouqué P., 1991, *Third Reference Catalogue of Bright Galaxies*. Volume I: Explanations and references. Volume II: Data for galaxies between 0^h and 12^h . Volume III: Data for galaxies between 12^h and 24^h .
- De Young D. S., 1993, *ApJ*, 405, L13
- Deane R. P. et al., 2014, *Nature*, 511, 57

- Dressler A., 1980a, *ApJS*, 42, 565
- Dressler A., 1980b, *ApJ*, 236, 351
- Dubner G. M., Holdaway M., Goss W. M., Mirabel I. F., 1998, *AJ*, 116, 1842
- Ebeling H., Edge A. C., Bohringer H., Allen S. W., Crawford C. S., Fabian A. C., Voges W., Huchra J. P., 1998, *MNRAS*, 301, 881
- Fabian A. C., 1994, *ARA&A*, 32, 277
- Fabian A. C., Nulsen P. E. J., 1977, *MNRAS*, 180, 479
- Fanaroff B. L., Riley J. M., 1974, *MNRAS*, 167, 31P
- Farouki R. T., Shapiro S. L., 1982, *ApJ*, 259, 103
- Ferrarese L., Merritt D., 2000, *ApJ*, 539, L9
- Gallimore J. F., Axon D. J., O'Dea C. P., Baum S. A., Pedlar A., 2006, *AJ*, 132, 546
- Garijo A., Athanassoula E., Garcia-Gomez C., 1997, *A&A*, 327, 930
- Ge J. P., Owen F. N., 1993, *AJ*, 105, 778
- Gebhardt K. et al., 2000, *ApJ*, 539, L13
- Giovanelli R., Haynes M. P., Rubin V. C., Ford, Jr. W. K., 1986, *ApJ*, 301, L7
- Gopal-Krishna, Mangalam A., Wiita P. J., 2008, *ApJ*, 680, L13
- Govoni F., Feretti L., 2004, *International Journal of Modern Physics D*, 13, 1549
- Gower A. C., Gregory P. C., Unruh W. G., Hutchings J. B., 1982, *ApJ*, 262, 478

-
- Graham A. W., 2007, MNRAS, 379, 711
- Graham A. W., Onken C. A., Athanassoula E., Combes F., 2011, MNRAS, 412, 2211
- Gull S. F., Northover K. J. E., 1973, Nature, 244, 80
- Gültekin K. et al., 2009a, ApJ, 698, 198
- Gültekin K. et al., 2009b, ApJ, 698, 198
- Gürkan G., Hardcastle M. J., Jarvis M. J., 2014, MNRAS, 438, 1149
- Hao J. et al., 2010, ApJS, 191, 254
- Hardcastle M. J., Evans D. A., Croston J. H., 2006, MNRAS, 370, 1893
- Hardcastle M. J., Sakelliou I., 2004, MNRAS, 349, 560
- Häring N., Rix H.-W., 2004, ApJ, 604, L89
- Hausman M. A., Ostriker J. P., 1978, ApJ, 224, 320
- Hawley J. F., Krolik J. H., 2006, ApJ, 641, 103
- Hine R. G., Longair M. S., 1979, MNRAS, 188, 111
- Ho L. C., Filippenko A. V., Sargent W. L. W., 1997, ApJS, 112, 315
- Hocuk S., Barthel P. D., 2010, A&A, 523, A9
- Hodges-Kluck E. J., Reynolds C. S., Miller M. C., Cheung C. C., 2010, ApJ, 717, L37
- Hota A. et al., 2011, MNRAS, 417, L36

- Hu J., 2008, *MNRAS*, 386, 2242
- Hunik D., Jamrozy M., 2016, *ApJ*, 817, L1
- Ishwara-Chandra C. H., Saikia D. J., 1999, *MNRAS*, 309, 100
- Jamrozy M., Konar C., Machalski J., Saikia D. J., 2008, *MNRAS*, 385, 1286
- Janiuk A., Proga D., Kurosawa R., 2008, *ApJ*, 681, 58
- Jetha N. N., Hardcastle M. J., Sakelliou I., 2006, *MNRAS*, 368, 609
- Jones D. H. et al., 2009, *MNRAS*, 399, 683
- Jordán A., Côté P., West M. J., Marzke R. O., Minniti D., Rejkuba M., 2004, *AJ*, 127, 24
- Kaldare R., Colless M., Raychaudhury S., Peterson B. A., 2003, *MNRAS*, 339, 652
- Katz J. I., 1997, *ApJ*, 478, 527
- Kauffmann G., Heckman T. M., Best P. N., 2008, *MNRAS*, 384, 953
- Kawakatu N., Kino M., Nagai H., 2009, *ApJ*, 697, L173
- Kellermann K. I., Owen F. N., 1988, *Radio galaxies and quasars*, Kellermann K. I., Verschuur G. L., eds., pp. 563–602
- Kennicutt, Jr. R. C., 1998, *ARA&A*, 36, 189
- Konar C., Hardcastle M. J., Jamrozy M., Croston J. H., 2013, *MNRAS*, 430, 2137
- Konar C., Hardcastle M. J., Jamrozy M., Croston J. H., Nandi S., 2012, *MNRAS*, 424, 1061

- Konar C., Jamrozy M., Saikia D. J., Machalski J., 2008, *MNRAS*, 383, 525
- Konar C., Saikia D. J., Ishwara-Chandra C. H., Kulkarni V. K., 2004, *MNRAS*, 355, 845
- Konar C., Saikia D. J., Jamrozy M., Machalski J., 2006, *MNRAS*, 372, 693
- Kormendy J., Bender R., Cornell M. E., 2011, *Nature*, 469, 374
- Kormendy J., Djorgovski S., 1989, *ARA&A*, 27, 235
- Kormendy J., Ho L. C., 2013, *ARA&A*, 51, 511
- Kormendy J., Richstone D., 1995, *ARA&A*, 33, 581
- Kozieł-Wierzbowska D., Stasińska G., 2011, *MNRAS*, 415, 1013
- Kulkarni G., Loeb A., 2012, *MNRAS*, 422, 1306
- Kuźmicz A., Jamrozy M., 2012, *MNRAS*, 426, 851
- Kuźmicz A., Jamrozy M., Kozieł-Wierzbowska D., Weżgowiec M., 2017, *MNRAS*, 471, 3806
- Laing R. A., Jenkins C. R., Wall J. V., Unger S. W., 1994, in *Astronomical Society of the Pacific Conference Series*, Vol. 54, *The Physics of Active Galaxies*, Bicknell G. V., Dopita M. A., Quinn P. J., eds., p. 201
- Lal D. V., Hardcastle M. J., Kraft R. P., 2008, *MNRAS*, 390, 1105
- Laor A., 2000, *ApJ*, 543, L111
- Lara L., Cotton W. D., Feretti L., Giovannini G., Marcaide J. M., Márquez I., Venturi T., 2001, *A&A*, 370, 409

- Leahy J. P., Williams A. G., 1984, MNRAS, 210, 929
- Ledlow M. J., Owen F. N., Keel W. C., 1998, ApJ, 495, 227
- Lequeux J., 1983, A&A, 125, 394
- Lin Y.-T., Shen Y., Strauss M. A., Richards G. T., Lunnan R., 2010, ApJ, 723, 1119
- Liuzzo E., Giovannini G., Giroletti M., Taylor G. B., 2010, A&A, 516, A1
- Loken C., Roettiger K., Burns J. O., Norman M., 1995, ApJ, 445, 80
- Lu J. F., 1990, A&A, 229, 424
- Lugger P. M., 1984, ApJ, 286, 106
- Lynden-Bell D., 1969, Nature, 223, 690
- MacDonald D., Thorne K. S., 1982a, MNRAS, 198, 345
- MacDonald D., Thorne K. S., 1982b, MNRAS, 198, 345
- Machalski J., Jamrozy M., Konar C., 2010, A&A, 510, A84
- Machalski J., Jamrozy M., Stawarz Ł., Koziel-Wierzbowska D., 2011, ApJ, 740, 58
- Machalski J., Jamrozy M., Zola S., 2001, A&A, 371, 445
- Machalski J., Jamrozy M., Zola S., Koziel D., 2006, A&A, 454, 85
- Machalski J., Koziel-Wierzbowska D., Jamrozy M., 2007, Acta Astronomica, 57, 227

-
- Machalski J., Koziel-Wierzbowska D., Jamrozny M., Saikia D. J., 2008, *ApJ*, 679, 149
- Magorrian J. et al., 1998, *AJ*, 115, 2285
- Mann A. W., Ebeling H., 2012, *MNRAS*, 420, 2120
- Marconi A., Hunt L. K., 2003a, *ApJ*, 589, L21
- Marconi A., Hunt L. K., 2003b, *ApJ*, 589, L21
- McConnell N. J., Ma C.-P., 2013, *ApJ*, 764, 184
- McConnell N. J., Ma C.-P., Gebhardt K., Wright S. A., Murphy J. D., Lauer T. R., Graham J. R., Richstone D. O., 2011, *Nature*, 480, 215
- McKinney J. C., 2005, *ApJ*, 630, L5
- McKinney J. C., Tchekhovskoy A., Blandford R. D., 2013, *Science*, 339, 49
- McNamara B. R., Nulsen P. E. J., 2007, *ARA&A*, 45, 117
- McNamara B. R., Nulsen P. E. J., 2012, *New Journal of Physics*, 14, 055023
- Meier D. L., 2001, *ApJ*, 548, L9
- Merrifield M. R., Kent S. M., 1991, *AJ*, 101, 783
- Merritt D., 1983, *ApJ*, 264, 24
- Merritt D., 1985, *ApJ*, 289, 18
- Merritt D., Ekers R. D., 2002, *Science*, 297, 1310
- Merritt D., Ferrarese L., 2001, *ApJ*, 547, 140

- Mguda Z., Faltenbacher A., Heyden K. v. d., Gottlöber S., Cress C., Vaisanen P., Yepes G., 2015, *MNRAS*, 446, 3310
- Miley G., De Breuck C., 2008, *A&A Rev.*, 15, 67
- Miley G. K., Perola G. C., van der Kruit P. C., van der Laan H., 1972, *Nature*, 237, 269
- Milgrom M., 1979, *A&A*, 76, L3
- Murgia M. et al., 2011, *A&A*, 526, A148
- Nandi S., Saikia D. J., 2012, *Bulletin of the Astronomical Society of India*, 40, 121
- Narayan R., Yi I., 1994, *ApJ*, 428, L13
- Narayan R., Yi I., 1995, *ApJ*, 452, 710
- Negroponte J., White S. D. M., 1983, *MNRAS*, 205, 1009
- Nelson C. H., 2000, *ApJ*, 544, L91
- Oemler, Jr. A., 1976, *ApJ*, 209, 693
- Osterbrock D. E., Koski A. T., Phillips M. M., 1976, *ApJ*, 206, 898
- Ostriker J. P., Hausman M. A., 1977, *ApJ*, 217, L125
- Ostriker J. P., Tremaine S. D., 1975, *ApJ*, 202, L113
- Owen F. N., O’Dea C. P., Inoue M., Eilek J. A., 1985, *ApJ*, 294, L85
- Owen F. N., Rudnick L., 1976, *ApJ*, 205, L1
- Paul S., Iapichino L., Miniati F., Bagchi J., Mannheim K., 2011, *ApJ*, 726, 17

-
- Pearson T. J., Readhead A. C. S., 1984, *ARA&A*, 22, 97
- Penna R. F., Narayan R., Sądowski A., 2013, *MNRAS*, 436, 3741
- Piffaretti R., Arnaud M., Pratt G. W., Pointecouteau E., Melin J.-B., 2011, *A&A*, 534, A109
- Pinkney J., Burns J. O., Hill J. M., 1994, *AJ*, 108, 2031
- Proctor D. D., 2016, *ApJS*, 224, 18
- Punsly B., 2005, *ApJ*, 623, L9
- Punsly B., Zhang S., 2011, *ApJ*, 735, L3
- Rawlings S., Saunders R., 1991, *Nature*, 349, 138
- Rees M. J., Begelman M. C., Blandford R. D., Phinney E. S., 1982, *Nature*, 295, 17
- Rigopoulou D., Franceschini A., Aussel H., Genzel R., Thatte N., Cesarsky C. J., 2002, *ApJ*, 580, 789
- Riley J. M., 1975, *MNRAS*, 170, 53
- Roettiger K., Burns J. O., Loken C., 1996, *ApJ*, 473, 651
- Rottmann H., 2001, PhD thesis, Thesis (Ph.D.) – University Bonn, 2001, 180 pages
- Rowan-Robinson M., 1977, *ApJ*, 213, 635
- Rykoff E. S. et al., 2008, *ApJ*, 675, 1106
- Safouris V., Subrahmanyan R., Bicknell G. V., Saripalli L., 2009, *MNRAS*, 393, 2

- Saikia D. J., Jamrozy M., 2009a, *Bulletin of the Astronomical Society of India*, 37
- Saikia D. J., Jamrozy M., 2009b, *Bulletin of the Astronomical Society of India*, 37
- Sakelliou I., Merrifield M. R., 2000, *MNRAS*, 311, 649
- Sakelliou I., Merrifield M. R., McHardy I. M., 1996, *MNRAS*, 283, 673
- Saripalli L., Hunstead R. W., Subrahmanyam R., Boyce E., 2005, *AJ*, 130, 896
- Schneider D. P., Gunn J. E., 1982, *ApJ*, 263, 14
- Schoenmakers A. P., de Bruyn A. G., Röttgering H. J. A., van der Laan H., 2000a, *MNRAS*, 315, 395
- Schoenmakers A. P., de Bruyn A. G., Röttgering H. J. A., van der Laan H., 2000b, *MNRAS*, 315, 395
- Schoenmakers A. P., de Bruyn A. G., Röttgering H. J. A., van der Laan H., 2001, *A&A*, 374, 861
- Schoenmakers A. P., de Bruyn A. G., Röttgering H. J. A., van der Laan H., Kaiser C. R., 2000c, *MNRAS*, 315, 371
- Seyfert C. K., 1951, *PASP*, 63, 72
- Shakura N. I., Sunyaev R. A., 1973, *A&A*, 24, 337
- Shankar F., Marulli F., Mathur S., Bernardi M., Bournaud F., 2012, *A&A*, 540, A23
- Shulevski A. et al., 2015, *A&A*, 579, A27

-
- Sikora M., Stawarz Ł., Lasota J.-P., 2007, *ApJ*, 658, 815
- Singh V., Ishwara-Chandra C. H., Sievers J., Wadadekar Y., Hilton M., Beelen A., 2015, *MNRAS*, 454, 1556
- Sirothia S. K., Gopal-Krishna, Wiita P. J., 2013, *ApJ*, 765, L11
- Skrutskie M. F. et al., 2006a, *AJ*, 131, 1163
- Skrutskie M. F. et al., 2006b, *AJ*, 131, 1163
- Smolčić V. et al., 2007, *ApJS*, 172, 295
- Sofue Y., Rubin V., 2001, *ARA&A*, 39, 137
- Soltan A., 1982, *MNRAS*, 200, 115
- Stern D. et al., 2012, *ApJ*, 753, 30
- Subrahmanyan R., Saripalli L., Hunstead R. W., 1996, *MNRAS*, 279, 257
- Subrahmanyan R., Saripalli L., Safouris V., Hunstead R. W., 2008, *ApJ*, 677, 63
- Tadhunter C., 2016, *A&A Rev.*, 24, 10
- Tadhunter C. N., Morganti R., Robinson A., Dickson R., Villar-Martin M., Fosbury R. A. E., 1998, *MNRAS*, 298, 1035
- Tchekhovskoy A., Narayan R., McKinney J. C., 2010, *ApJ*, 711, 50
- Thuan T. X., Puschell J. J., 1989, *ApJ*, 346, 34
- Tonry J. L., 1987, in *IAU Symposium, Vol. 127, Structure and Dynamics of Elliptical Galaxies*, de Zeeuw P. T., ed., pp. 89–96
- Toomre A., Toomre J., 1972, *ApJ*, 178, 623

-
- Tovmassian H. M., Andernach H., 2012, *MNRAS*, 427, 2047
- Tremaine S. et al., 2002, *ApJ*, 574, 740
- Urry C. M., Padovani P., 1995, *PASP*, 107, 803
- van Breugel W., Heckman T., Miley G., 1984, *ApJ*, 276, 79
- van den Bosch R. C. E., Gebhardt K., Gültekin K., van de Ven G., van der Wel A., Walsh J. L., 2012, *Nature*, 491, 729
- Volonteri M., Haardt F., Madau P., 2003, *ApJ*, 582, 559
- Vorontsov-Velyaminov B. A., 1959, in *Atlas and catalog of interacting galaxies (1959)*
- Walker R. C., Dhawan V., Romney J. D., Kellermann K. I., Vermeulen R. C., 2000, *ApJ*, 530, 233
- Wegner G. et al., 2001, *AJ*, 122, 2893
- Willis A. G., Strom R. G., Perley R. A., Bridle A. H., 1982, in *IAU Symposium, Vol. 97, Extragalactic Radio Sources*, Heeschen D. S., Wade C. M., eds., pp. 141–144
- Willis A. G., Strom R. G., Wilson A. S., 1974, *Nature*, 250, 625
- Wilson A. S., Colbert E. J. M., 1995, *ApJ*, 438, 62
- Wright E. L., 2006, *PASP*, 118, 1711
- Wright E. L. et al., 2010, *AJ*, 140, 1868
- Yokosawa M., Inoue M., 1985, *PASJ*, 37, 655

Zirbel E. L., 1997, ApJ, 476, 489

Zirbel E. L., Baum S. A., 1995, ApJ, 448, 521

Zwicky F., Humason M. L., 1961, ApJ, 133, 794

Zwicky F., Zwicky M. A., 1971, Catalogue of selected compact galaxies and of post-eruptive galaxies